



FACULTY OF ELECTRICAL ENGINEERING
UNIVERSITY OF BANJA LUKA

ELECTRONICS

VOLUME 16, NUMBER 1, JUNE 2012

FACULTY OF ELECTRICAL ENGINEERING UNIVERSITY OF BANJA LUKA

Address: Patre 5, 78000 Banja Luka, Bosnia and Herzegovina

Phone: +387 51 211824

Fax: +387 51 211408

ELECTRONICS

Web: www.electronics.etfbl.net

E-mail: electronics@etfbl.net

Editor-in-Chief:

Branko L. Dokić, Ph. D.
Faculty of Electrical Engineering
University of Banja Luka, Bosnia and Herzegovina
E-mail: bdokic@etfbl.net

International Editorial Board:

- Goce Arsov, St. Cyril and Methodius University, Skopje, Republic of Macedonia
- Petar Biljanović, University of Zagreb, Croatia
- Milorad Božić, University of Banja Luka, Bosnia and Herzegovina
- Đemal Kolonić, University of Banja Luka, Bosnia and Herzegovina
- Vladimir Katić, University of Novi Sad, Serbia
- Vančo Litovski, University of Niš, Serbia
- Danilo Mandić, Imperial College, London, United Kingdom
- Vojin Oklobdžija, University of Texas at Austin, USA
- Zorica Pantić, Wentworth Institute of Technology, Boston, USA
- Aleksandra Smiljanić, University of Belgrade, Serbia
- Slobodan Vukosavić, University of Belgrade, Serbia
- Volker Zerbe, Technical University of Ilmenau, Germany
- Mark Zwoliński, University of Southampton, United Kingdom
- Deška Markova, Technical University of Gabrovo
- Chakresh Kumar, Galgotias College of Engineering and Technology, Greater Noida, India

Secretary:

Mladen Knežić, M.Sc.
E-mail: mladen_knezic@etfbl.net

Željko Ivanović, M.Sc.
E-mail: zeljko@etfbl.net

Publisher:

Faculty of Electrical Engineering
University of Banja Luka, Bosnia and Herzegovina
Address: Patre 5, 78000 Banja Luka, Bosnia and Herzegovina
Phone: + 387 51 211824
Fax: + 387 51 211408
Web: www.etfbl.net

Number of printed copies: 100

Guest Editorial

THE International journal "Electronics", published by University of Banja Luka, is devoting its special issue to the 16th International Symposium on Power Electronics - Ee2011. The editor of the journal Prof. Dr. Branko Dokić has invited me, as a guest-editor, to present the most interesting papers of the symposium. The Symposium was held in Novi Sad from October 26-28, 2011 (<http://www.dee.uns.ac.rs>). It was co-organized by Power Electronic Society (Serbia) sited in Novi Sad, Faculty of Technical Sciences from Novi Sad, Institute "Nikola Tesla" from Belgrade and Novi Sad Fair. Ministry of Science of Republic of Serbia, Provincial Secretariat for Science and Technological Development of AP Vojvodina, Serbian Academy of Science and Art (SANU), IEEE Serbia & Montenegro Section and Engineering Chamber of Serbia co-sponsored it.

Symposium "Power Electronics", widely known as **Ee** (this shortcut comes from title in Serbian - "Energetska elektronika"), is now in its 40-ties. Still it is a young, full of new ideas, excellent meeting place for researchers, university professors, engineers, manufacturers, students and other experts in the field of Power Electronics. This significant event shows constant interest of researchers, university professors, engineers, manufacturers, students and other experts in the field of Power Electronics, which more widely comprise power electronics switches, power electronics converters, electrical machines, electric drives, control & measurement in power engineering, power electronics in communications, electric power quality and renewable energy sources.

The first gathering Ee was held in Belgrade in 1973 with 47 presented papers from all over ex-Yugoslavia, while the current Ee 2011 symposium, as a fully international, was host of 102 papers. Papers came from research institutes, industry and university centers of 19 countries: Austria, Bosnia & Herzegovina, Bulgaria, Canada, Croatia, Germany, Hungary,

Iran, Italy, Japan, Republic of Macedonia, Montenegro, Poland, Romania, Serbia, Switzerland, Turkey, United Kingdom and USA and gathered more than 200 participants. All papers were published in electronic form (USB), which also contains multimedia presentations of the organizers and commercial sponsors, facts about Power Electronics Society, as well as complete bibliography from all symposiums on Power Electronics (1973-2011).

The symposium highlighted the problems and practical or virtual solution in many fields. Six topics were put forward: Power Converters, Electrical Drives, Electrical Machines, Control & Measurement in Power Engineering, Power Electronics in Telecommunications and Power Quality. The most interesting contribution were in the areas of power electronics application, industrial motor drives, vector control, distributed power generation, new or improved power electronic converters, power quality, etc.

The selection of the papers presented in this issue is the guest editor's choice and only one of several possible selections. All papers passed additional reviews and represent the state-of-the-art in wide field of Power Electronics. We would like to emphasize our thanks to the authors who have accepted our request for prompt respond and fast adaptation of the papers to journal requirements..

We would also like to invite all readers of the "Electronics" journal to take active participation by submitting the papers or attending the next the 17th International Symposium on Power Electronics - Ee 2013, when we will celebrate 40 years and which will be organized in NOVI SAD, SERBIA in October 2013.

Prof. Vladimir Katić, Ph.D.
Guest Editor

Prof. dr Vladimir Katić Biography



Vladimir Katić is a *Professor* of the Faculty of Technical Sciences at the University of Novi Sad, Novi Sad, Serbia. He received B.Sc. degree from University of Novi Sad in 1978, and M.Sc. and Ph.D. degrees from University of Belgrade in 1981 and 1991, respectively, all in electrical engineering. From 1978 he is with Department for Power, Electronics & Communication Engineering of the Faculty of Technical

Sciences, University of Novi Sad, where he is currently Professor, Vice-Dean of the Faculty of Technical Sciences and Head of Power Electronics and Converters Group.

The main fields of scientific and research interest of Prof. Katić are power quality, renewable energy sources, power electronics converters and standardization in electrical engineering.

He is the author or co-author of several scientific monograph and text books: "Real/Time Modelling of Power Electronics Converters" (2011), "Power Quality" (2007), "Renewable Sources of Electrical Energy" (2007), "Microprocessor Applications in Power Engineering" (2006), "Control of Power Converters" (2006), "Electric Power Quality - Harmonics" (2002), "Power Electronics – Laboratory Practice" (2000), "Power Electronics - Worked Problems" (1998), and the editor of the book "Modern Aspects of Power Engineering" (1995).

Prof. Katić published research results in more than 350 scientific papers as author or co-author in international and national journals and conferences proceedings. He has participated or was the main researcher in 54 national and international R&D projects.

He is in the Editorial Boards of *International Journal on Electrical Engineering Education* (U.K.), *International Journal of Power and Energy Systems* (USA-Canada-CH), *Advances in Electrical and Computer Engineering* (Romania), *Electronics Journal* (BIH), *Engineering-Electrical Engineering* (Serbia) and was a Member of Program or Steering Committees of more than 75 International Conferences around the World. He chaired numerous international and national conferences, on which biannual International Symposium on Power Electronics – Ee and EPE-PEMC 2012 ECCE Europe are the most known. He is also reviewer, member of international programme committees and session chairman of many international or national journals and conferences.

Prof. Katić is a Senior member of the IEEE and currently serving as IEEE PELS Chapter Development Chair, IEEE R8 Technical Committee Liaison, Past-chair of IEEE Serbia and Montenegro Section and Chairman of the IEEE Joint Chapter on Industrial Electronics/Power Electronics/Industry Application Society of IEEE Serbia and Montenegro Section.

He is also Founder and the President of the Power Electronic Society of Serbia, a Member of the Presidency of National Society of ETRAN, a Member of CIGRE (Paris), an Observer Member in the SC C4 of CIGRE (Paris), a Member of National Committee of CIGRE (Serbia), and a Founder and a Member of the Executive Board of National Committee of CIRED.

Bidirectional AC-DC Converter for Regenerative Braking

Predrag Pejovic, Johann W. Kolar, and Yasuyuki Nishida

Abstract—In this paper, a bidirectional AC DC converter is analyzed. The converter applies a half bridge thyristor rectifier and a recuperating thyristor bridge instead of a braking resistor. Recuperating mode of the converter is focused in the analysis, and it is shown that the converter exposes two operating modes within the recuperating mode, one characterized by negligible, and the other one characterized by significant distortion of the input voltages. Theoretical results are experimentally verified on a 10 kW converter.

Index Terms—About four key words or phrases in alphabetical order, separated by commas.

I. INTRODUCTION

IN this paper, a half-bridge three-phase thyristor rectifier intended for application in machine drives, presented in Fig. 1, is analyzed. In many applications, like crane [1] or elevator drives, a machine drive that presents the load operates in generating mode, and the generated energy requires to be taken care of. One method to do this is to dissipate the generated power on a pulse width modulated braking resistor ([2], page 421). This method is reliable, simple, and robust, but requires additional cooling effort, significantly reduces the converter power density, and increases the energy cost. To avoid these drawbacks, bidirectional power converters are of interest. Full-bridge thyristor rectifiers are simple and robust, and provide bidirectional power flow, but in the inverting mode the output voltage has to be reversed [3], [4]. Refinements of this approach can be found in [5], [6], and [7]. To keep the voltage polarity in the inverter mode, auxiliary thyristor bridge accompanied by a free-wheeling diode (Fig. 1) is proposed to replace the braking resistor voltage by the highest of the line voltages available at given time instant [8], [9]. Results presented in this paper are an extension of the results presented in [8] and [9], in theoretical direction, with

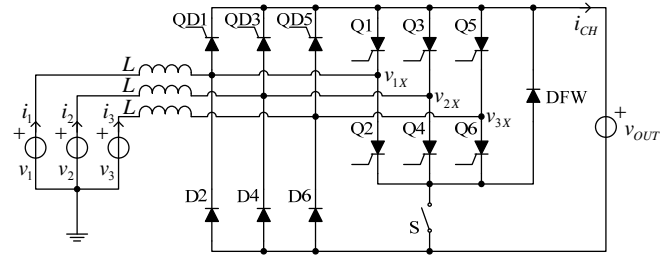


Fig. 1. The converter.

the converter control and operating modes subjected to detailed analysis.

II. NOTATION AND NORMALIZATION

Let us assume that the converter is supplied by an undistorted symmetrical three-phase voltage system

$$v_k = V_m \cos\left(\omega t - (k-1)\frac{2\pi}{3}\right) \quad (1)$$

for $k \in \{1, 2, 3\}$. The supply lines are assumed to have leakage inductance L per phase, connected in series to the ideal voltage sources v_1 , v_2 , and v_3 . To simplify the notation, let us introduce two waveforms, one of them being the waveform of the voltage equal to the maximum of the phase voltages,

$$v_A = \max(v_1, v_2, v_3) \quad (2)$$

while the other one being the waveform of the voltage equal to the minimum of the phase voltages,

$$v_B = \min(v_1, v_2, v_3) \quad (3)$$

Since the phase voltages add up to zero,

$$v_1 + v_2 + v_3 = 0 \quad (4)$$

waveform of the voltage defined to be equal to the phase voltage that is neither minimal nor maximal at a considered time point can be obtained as

$$v_C = -v_A - v_B \quad (5)$$

According to the definitions of v_A , v_B , and v_C , phase angle segments over the line period could be identified where indices of the phase voltages that represent v_A , v_B , and v_C do not change. There are six such segments, and they are given in Table 1. Table 1 also contains values of the index variables A , B , and C . For example, consider maximum of the line voltages $v_{AB} = v_A - v_B$ on the segment $\pi/3 < \omega t < 2\pi/3$; in that segment, $v_{AB} = v_2 - v_3$, since $A=2$ and $B=3$ over the segment. Besides the values of the phase voltage index variables, Table I also contains values of semiconductor index

Manuscript received 30 May 2012. Accepted for publication 10 June 2012. Some results of this paper were presented at the 16th International Symposium Power Electronics, Novi Sad, Serbia, October 26-28, 2012.

P. Pejović is with the Faculty of Electrical Engineering, University of Belgrade, Belgrade, Serbia (phone: +381-11-3218-313; fax: +381-11-324-8681; e-mail: peja@etf.rs).

J. W. Kolar is with Swiss Federal Institute of Technology, Zürich, Switzerland (e-mail: kolar@lem.ee.ethz.ch).

Y. Nishida is with the Chiba Institute of Technology, Japan (e-mail: nishida_yas@nifty.com).

TABLE I
DEFINITIONS OF INDEX VARIABLES, A, B, C, a , AND b

range	A	B	C	a	b
$0 < \omega t < \pi/3$	1	3	2	1	6
$\pi/3 < \omega t < 2\pi/3$	2	3	1	3	6
$2\pi/3 < \omega t < \pi$	2	1	3	3	2
$\pi < \omega t < 4\pi/3$	3	1	2	5	2
$4\pi/3 < \omega t < 5\pi/3$	3	2	1	5	4
$5\pi/3 < \omega t < 2\pi$	1	2	3	1	4

variables a and b , where a is the index of the semiconductor component connected to the highest of the phase voltages, while b is the index of the of the semiconductor component connected to the lowest of the phase voltages.

Since numerical methods were extensively used to provide the results presented in this paper, to generalize the results normalization of variables is introduced. The voltages are normalized taking amplitude of the phase voltage as a basis, providing normalized value m_X of the voltage v_X as

$$m_X = \frac{v_X}{V_m} \quad (6)$$

The currents are normalized taking amplitude of the short-circuit phase current as a base current for normalization

$$j_X = \frac{\omega L}{V_m} i_X \quad (7)$$

The base current for normalization is high, thus all the currents in the analysis would be characterized by relatively low per unit values. For example, the RMS value of the phase short-circuit current is

$$I_{SC\,RMS} = \frac{1}{\sqrt{2}} \frac{V_m}{\omega L} \approx 0.707 \text{ p.u.} \quad (8)$$

A consequence is that the powers in the system would also be characterized by low per unit quantities, thus the short circuit apparent power is

$$S_{SC} = \frac{3}{2} \frac{V_m^2}{\omega L} = 1.5 \text{ p.u.} \quad (9)$$

Applying normalization defined by (6) and (7), the equation that characterizes the line inductance

$$v_L = L \frac{di_L}{dt} \quad (10)$$

in normalized terms becomes

$$m_L = \frac{dj_L}{d\omega t} \quad (11)$$

In analyses that follow, time variable t will be frequently represented by the phase angle variable ωt , like it has already been done in (11).

III. ANALYSIS OF THE CONVERTER OPERATION

Fundamental idea discussed in this paper is how to replace the voltage across the braking resistor with the maximum of the line voltages, v_{AB} , obtained applying the recuperating thyristor bridge of Fig. 1? Besides the voltage v_{AB} , the

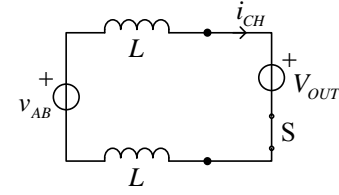


Fig. 2. Equivalent circuit of the converter during the recuperation interval.

recuperating thyristor bridge provides connection to two L inductors that represent the line inductance, connected in series to v_{AB} , as depicted in Fig. 2. In the analysis, it is assumed that the output voltage is constant. Thus, the output of the converter, including the output capacitor, is replaced by a constant voltage source V_{OUT} in the circuit diagram of Fig. 1, being supplied by the charging current i_{CH} , as depicted in Fig. 2.

According to the phase voltages (1), on the phase angle segment $0 < \omega t < \pi/3$ maximum of the line voltages is given by its normalized value

$$m_{AB}(\omega t) = \sqrt{3} \sin\left(\omega t + \frac{\pi}{3}\right) \quad (12)$$

reaching the minimum of $m_{AB}(0) = m_{AB}(\pi/3) = 1.5$. Now, let us assume that in the phase angle interval $0 < \omega t < \alpha$ the braking switch of Fig. 1 is on, and that $M_{OUT} > m_{AB}$, which results in the recuperation interval. During the interval, normalized equation that characterizes the charging current is

$$\frac{dj_{CH}}{d\omega t} = \frac{1}{2} (m_{AB} - M_{OUT}) \quad (13)$$

Assuming that $j_{CH}(0) = 0$, the waveform of j_{CH} is given by

$$j_{CH}(\omega t) = -\frac{1}{2} \left[\sqrt{3} \cos\left(\omega t + \frac{\pi}{3}\right) + M_{OUT} \omega t - \frac{\sqrt{3}}{2} \right] \quad (14)$$

which for $M_{OUT} > \sqrt{3}$ reaches maximum of its magnitude for $\omega t = \alpha$, $j_{MAX} = -j_{CH}(\alpha)$.

Average of the charging current is computed performing averaging over the phase angle of $\pi/3$, which is the phase angle interval that corresponds to the fundamental period of the charging current,

$$J_{CH} = \frac{3}{\pi} \int_0^{\alpha} j_{CH}(\omega t) d\omega t \quad (15)$$

resulting in

$$J_{CH} = \frac{3}{4\pi} \left(2\sqrt{3} \sin\left(\alpha + \frac{\pi}{3}\right) + M_{OUT} \alpha^2 - \sqrt{3} \alpha - 3 \right) \quad (16)$$

In steady state, the converter output current is equal to the average of the charging current, $J_{OUT} = J_{CH}$, according to the charge balance over the filtering capacitor connected in parallel to the load. This is not shown in Fig. 1, but being assumed.

The charging current (16) is negative, which corresponds to the converter operation in the inverting mode. Normalized

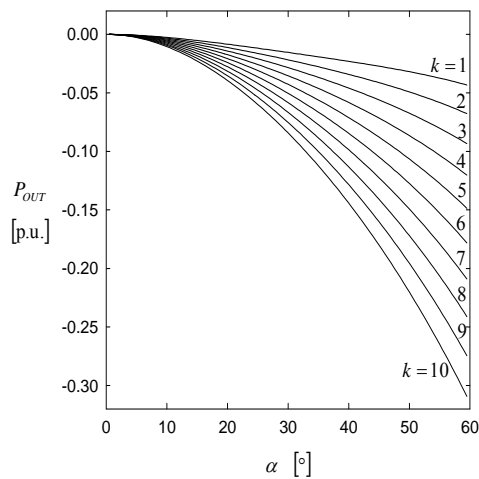


Fig. 3. Dependence of P_{OUT} on α for $M_{OUT} = 1.7 + 0.05k$.

power in the inverting mode is given by $P_{OUT} = M_{OUT} J_{CH}$, and for various values of M_{OUT} and α it is depicted in Fig. 3. From the curves of Fig. 3 it can be observed that relatively high power could be recuperated, and that the process could be controlled varying the switch on-angle α , being also dependent on the converter output voltage.

Averaged equation over the output capacitor voltage governs the converter output voltage, and in normalized form it is given by

$$\frac{d m_{OUT}}{d \omega t} = j_{CH}(m_{OUT}, \alpha) - j_{OUT} \quad (17)$$

Thus, dynamics of the converter in the recuperation mode is given by the first order nonlinear differential equation.

The analysis performed this far covers only the recuperating interval. However, at the end of the interval substantial amount of energy might remain stored in the inductors of

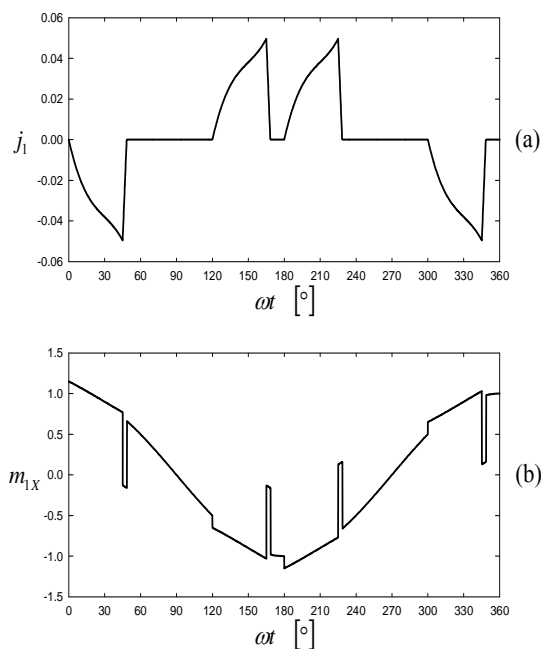
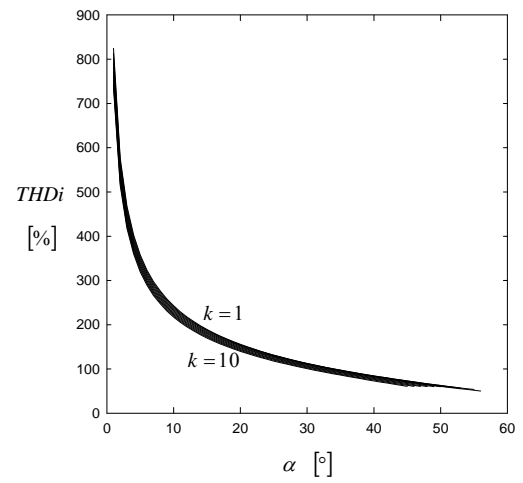
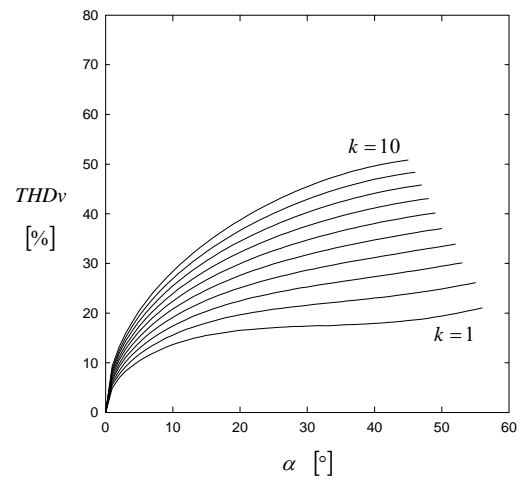


Fig. 4. Waveforms of j_1 and m_{1X} for $M_{OUT} = 1.8$ and $\alpha = 45^\circ$.



(a)



(b)

Fig. 5. Dependence of the input current (a) and the coupling point voltage (b) THD on α for $M_{OUT} = 1.7 + 0.05k$.

Fig. 2. For example, for $M_{OUT} > \sqrt{3}$ the maximum of $|i_{CH}|$ flows through the inductors at the time instant when S is being turned off. This energy will be discharged through the free-wheeling diode (DFW in Fig. 1) during the discharge interval that follows the recuperating interval. Equivalent circuit for this interval corresponds to the circuit diagram of Fig. 2 with V_{OUT} replaced by a short circuit, and the governing equation for the current of the inductors i_L is

$$\frac{d j_L}{d \omega t} = \frac{1}{2} m_{AB} \quad (18)$$

where i_L is oriented in the same direction as i_{CH} . This interval lasts while $i_L < 0$. The discharge interval does not contribute to the recuperated power, since the voltage source that represents the load, is open during the interval. Typical waveforms of j_1 and m_{1X} in the recuperating mode are shown in Fig. 4.

Dependence of the input current THD and the THD of the voltages at the converter coupling points, just after the inductors that represent leakage inductances of the line, are

presented in Fig. 5. The converter is characterized by high distortions of the currents and voltages, which might not be a fact of relevance in isolated local networks.

IV. CONTROL OF THE CONVERTER

In the analysis presented this far, it was shown that the output voltage could be controlled adjusting the switch on angle α , and that the governing equation is a nonlinear first order differential equation (17). In this section, the analysis is extended to the output voltage below $M_{OUT} = \sqrt{3}$, down to $M_{OUT} = 1.5$, which is the bottom limit to turn the thyristors Q1 to Q6 on. In this case, the charging current i_{CH} may reach zero spontaneously, causing the thyristors of the recuperating

bridge to turn off, without any need for hard switched turn off of S. This operating mode is named soft discharge mode.

According to (13), at low output voltages, lower than $\sqrt{3}$ p.u., recuperating current grows in magnitude as long as $m_{AB} < M_{OUT}$, while it starts to decrease when $m_{AB} > M_{OUT}$. For the output voltages lower than about 1.67 p.u., the recuperating current reaches to zero during the recuperating interval, and the thyristors Qa and Qb turn off spontaneously. Exact limit of this operating mode is $M_{OUT} < M_{SDM}$, where M_{SDM} is obtained as a solution of

$$M_{SDM} \arcsin \frac{M_{SDM}}{\sqrt{3}} + \sqrt{3 - M_{SDM}^2} - \frac{2\pi}{3} M_{SDM} + \frac{\sqrt{3}}{2} = 0 \quad (19)$$

Numerical solution of (19) is $M_{SDM} \approx 1.673436$. In the case $M_{OUT} < M_{SDM}$, the line inductance discharge is spontaneously performed. In this manner, the voltage spikes related to the discharge process after the hard turn off of S are avoided, and the THD of the input voltages remains moderate. In the first two diagrams of Fig. 6, the input current and the input voltage are presented for the converter operating in this mode, at $M_{OUT} = 1.65$ and $\alpha = 45^\circ$, corresponding to $J_{OUT} = -0.023$. The THD of the input current, presented in Fig. 6(a), was expectedly high, equal to 127%. However, the THD of the input voltage waveform, presented in Fig. 6(b), was only 2.73%, which is a consequence of the absence of the voltage spikes that characterize the discharge process caused by hard

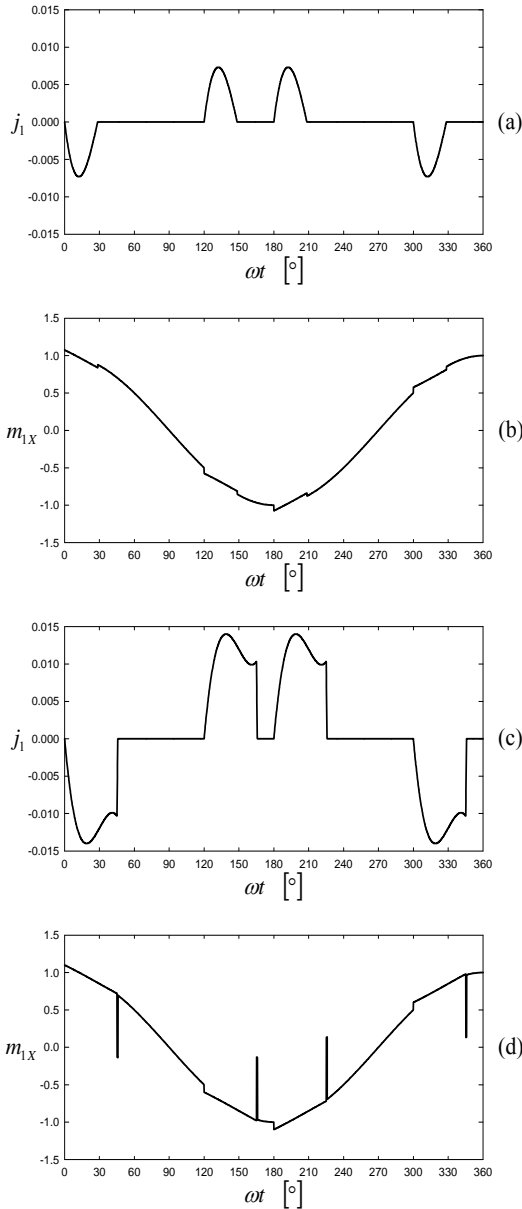


Fig. 6. Waveforms of the input current and the input voltage for $\alpha = 45^\circ$: (a) and (b) soft discharge mode at $M_{OUT} = 1.65$; (c) and (d) hard discharge mode at $M_{OUT} = 1.7$.

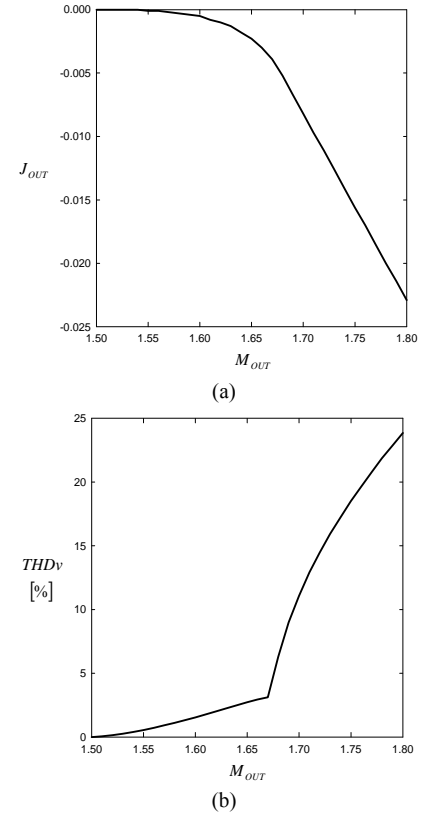


Fig. 7. (a) Dependence of J_{OUT} on M_{OUT} for $\alpha = 45^\circ$; (b) dependence of the input voltage THD on M_{OUT} for $\alpha = 45^\circ$.

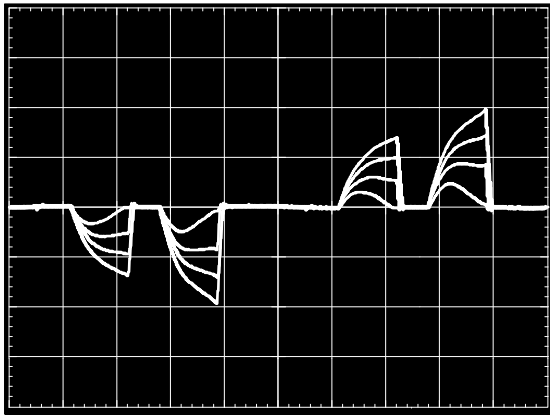


Fig. 8. Waveforms of the input current for the output voltages of 590 V, 580 V, 570 V, and 550 V. Scales: 20 A/div, 2 ms/div.

turn off of S. Applying numerically obtained value for M_{SDM} , maximum of the recuperated current absolute value in the soft discharge mode is obtained as $J_{OUT} = -0.004291$, which corresponds to the recuperated power of $P_{OUT} = -0.007181$ p.u., or in the terms of the short circuit apparent power at the point of coupling

$$\frac{P_{OUT}}{S_{SC}} = -0.4787\% \quad (20)$$

Output current of recuperating mode increased above the soft discharge limit forces the converter to operate in the hard discharge mode. The input current and the input voltage waveforms that correspond to this operating mode at $M_{OUT} = 1.7$ and $\alpha = 45^\circ$, corresponding to $J_{OUT} = -0.0081$, are presented in the last two diagrams of Fig. 6, labeled (c) and (d). The THD of the input current is reduced to 69.44%, while the THD of the input voltage is increased to 11.77%.

In order to compare the converter behavior in the soft discharge mode to the operation in the hard discharge mode, a set of numerical simulations is performed. In Fig. 7(a) dependence of the recuperated current J_{OUT} on the output voltage M_{OUT} is presented. It can be observed that for normalized output voltages lower than M_{SDM} absolute value of the recuperated output current is relatively low in magnitude, lower than the limit of 0.00429 p.u. Increased output voltage causes the converter to operate in the hard discharge mode, resulting in increased absolute value of the recuperated current. In Fig. 7(b), dependence of the input voltage THD on the output voltage is presented. Point where the converter switches from soft discharge mode to the hard discharge mode is readily observable by sudden increase of the input voltage THD.

It can be concluded that the converter at low output voltages and relatively low recuperating power could be operated in the soft discharge mode, which is characterized by absence of the input voltage spikes and moderate distortions of the input voltages. Besides, hard switched turn off of S is avoided in this mode. In the case the load tolerates the output voltage variations of about 20%, it is possible to operate the

converter with a constant on-angle of S. In that case, at higher recuperating power the converter would operate in the hard discharge mode, while at lower recuperating power the converter would operate in the soft discharge mode.

V. EXPERIMENTAL RESULTS

In order to verify feasibility of the proposed concept, a laboratory model of the converter with the rated power of 10 kW was built applying IXYS VVZB 120 module for the half controlled thyristor bridge and the controlled switch, and six discrete thyristors IXYS CS 30-120i, for the recuperating thyristor bridge. The converter is intended to operate at the three-phase voltage system with the phase voltage RMS value of 230 V, at 50 Hz. The line inductance was 1 mH. The output voltage of the converter was impressed by an external DC source, which is applied to provide the power to be recuperated to the mains. To analyze the effects caused by the supplying three-phase voltage system unbalance, voltage at one of the phases is increased for about 4% by an adjustable transformer.

To illustrate the converter operation at different output voltages, while keeping the switch on-angle constant, a set of measurements is performed, and obtained waveforms of the input currents are presented in Fig. 8. The measurements are performed for four values of the output voltage: 590 V, 580 V, 570 V, and 550 V. These output voltages correspond to the recuperating power of 9.3 kW, 7.2 kW, 5.4 kW, and 1.6 kW, respectively. Operation of the converter in the soft discharge mode at the lowest of the power is clearly observable.

VI. CONCLUSIONS

In this paper, a bidirectional AC-DC converter intended for application in machine drives to provide regenerative braking is analyzed. The converter is derived replacing the braking resistor by a thyristor bridge that provides the maximum of the line voltages at its output in order to recuperate the braking energy. Appropriate normalization is introduced to generalize the results. Operation of the converter is analyzed in detail, and it is shown that the converter in the recuperating mode can operate in two sub-modes: soft discharge mode and the hard discharge mode. The soft discharge mode is shown to provide recuperation with negligible distortion of the input voltages. Limits for this operating mode are derived. Constant on angle control strategy for the recuperating switch is analyzed, and it is shown to be applicable for the loads that tolerate 20% variation of the supply voltage. The analyses are experimentally verified on a 10 kW converter laboratory model.

REFERENCES

- [1] R. Belmans, F. Busschots, R. Timmer, "Practical design considerations for braking problems in overhead crane drives," in IEEE Industry Applications Society Annual Meeting, 1993, pp. 473-479.

- [2] N. Mohan, T. M. Undeland, W. P. Robbins, *Power Electronics: Converters, Applications and Design*, 2nd Edition. New York: John Wiley & Sons, 1995.
- [3] R. M. Davis, "A bidirectional AC DC power converter for fixed polarity DC loads," in 3rd International Conference on Power Electronics and Variable Speed Drives, London, UK, 1988, pp. 142-145.
- [4] D. Milly, "An AC to DC converter with output reversal," in Record of the 3rd European Conference on Power Electronics and Applications, Aachen, Germany, 1989, pp. 813-817.
- [5] J. C. Clare, P. R. Mayes, W.F. Ray, "Bidirectional power converter for voltage fed inverter machine drives," in 23rd Annual IEEE Power Electronics Specialists Conference Record, 1992, pp. 189-194.
- [6] K. Matsui, K. Tsuboi, S. Muto, "Power regenerative controls by utilizing thyristor rectifier of voltage source inverter," *IEEE Transactions on Industry Applications*, vol. 28, pp. 816-823, July/Aug. 1992.
- [7] K. Matsui, U. Mizuno, Y. Murai, "Improved power regenerative controls by using thyristor rectifier bridge of voltage source inverter and a switching transistor," *IEEE Transactions on Industry Applications*, vol. 28, pp. 1010-1016, Sep./Oct. 1992.
- [8] J. W. Kolar, H. Ertl, F. C. Zach, "A novel concept for regenerative braking of PWM-VSI drives employing a loss-free braking resistor," in 12th Annual Applied Power Electronics Conference and Exposition APEC '97 Conference Proceedings, 1997, pp. 297-305.
- [9] J. W. Kolar, H. Ertl, F. C. Zach, "Design and experimental evaluation of the loss-free braking resistor concept for applications in integrated converter machine systems," in Proceedings of the 24th Annual Conference of the IEEE Industrial Electronics Society, IECON '98, 1998, pp. 626-629.

Analysis of Single Coil PM-BLDC Motor

Boguslaw Grzesik and Mariusz Stepień

Abstract—The aim of the paper is FEM analysis of single coil BLDC motor operated as drive of small piston pump. The paper contains analysis of design, distribution of magnetic field, forces and torque under static and dynamic conditions. Voltages, currents, signals waveforms are also given as the results of analysis. The cogging torque and total torque are discussed in the paper.

Index Terms—ANSYS, BLDC motor, FEM analysis, single coil motor.

I. INTRODUCTION

PERMANENT magnet DC brushless motors are broadly used in small drives. They have many advantages, such as high efficiency, reliability, low production costs and simple control.

Permanent magnet BLDC motors are used in mechatronic, electronic devices like CD-rooms in range of power from tens of milliwatts to hundred watts and range of rotational speed from hundred to several thousand rpm. The motor presented in the paper is dedicated to drive small liquid piston pump. Usually brushless DC motors are made of three or more windings (coils) supplied by electronic full bridge commutator. PM single coil motor is supplied by only single coil, sectioned and distributed along stator circumference, where each subsequent section is wound in opposite direction. Rotor of the motor is made of sectioned permanent magnet. The idea of design of this type of motor and method of its control is known [1]. It is also described in details in the next section. For proposed application it needs detailed analysis of magnetic field, torques and power properties. The main work in this paper is analysis of magnetic field in the motor and its properties at given dimensions and power using ANSYS software (based on FEM method) [2]. Obtained results of FEM analysis are compared with results of measurement. It is necessary to underline that analyzed motor is characterized by its extremely simple power electronic control system of four transistor bridge

Manuscript received 30 May 2012. Accepted for publication 10 June 2012. Some results of this paper were presented at the 16th International Symposium Power Electronics, Novi Sad, Serbia, October 26-28, 2012.

B. Grzesik is with the Faculty of Electrical Engineering, Silesian University of Technology, Gliwice, Poland (e-mail boguslaw.grzesik@polsl.pl).

M. Stepień is with Faculty of Electrical Engineering, Silesian University of Technology, Gliwice, Poland (corresponding author to provide phone: +48-32-237-1247; fax: +48-32-237-1304; e-mail:mariusz.stepien@polsl.pl).

II. IDEA OF SINGLE COIL BLDC MOTOR

The rotor of PM-BLDC contains sectioned permanent magnet (Fig. 1) where number of section is equal to number of poles in the stator. Stator is made of even number of coils connected in series and wound, each in opposite direction in respect of neighbor one. The idea of considered rotor is shown in Fig. 1. The most important is direction of coil winding. It is marked in Fig. 2 with arrows. Also direction of coil current is marked by signs (“+” and “-”) and proper color. Control of the stator current is based on the signals of Hall sensors H located in the stator (Fig. 1). They detect magnetic field generated by rotor magnets.

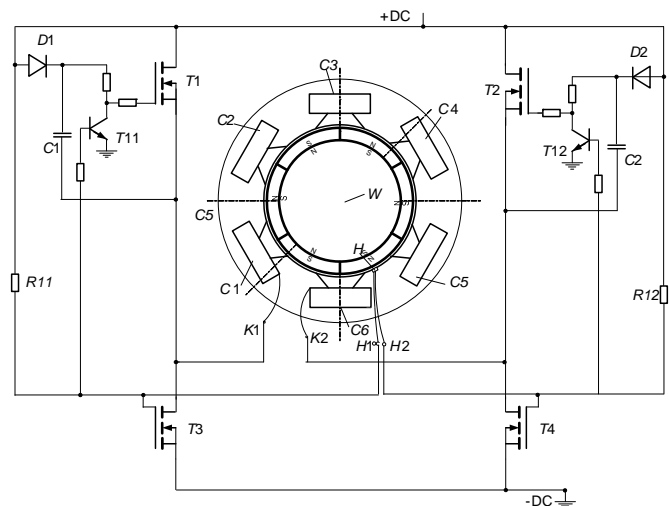


Fig. 1. Schematic diagram of control circuit of PM BLDC single coil motor.

The control circuit of the system with PM-BLDC is depicted in fig. 1. The bridge T1- T4 is switched in pairs (T1-T4) and (T2-T3). Due to the state of the bridge the each half of the stator coils change its polarity. For the state (T1-T4) the coils C1, C3, C5 attract relevant permanent magnet of the rotor while the coils C2, C4, C6 are repulse their counterpart permanent magnets. The direction of the motion is determined with special symmetry of stator. The control is based on Hall sensors that senses the position of the rotor. The rotational speed is proportional to the DC supply voltage that is delivered between +DC and -DC terminals. It is necessary to notice that control circuit having limited number of electronic parts is cheaper than the circuit designed for instance for three phase solution.

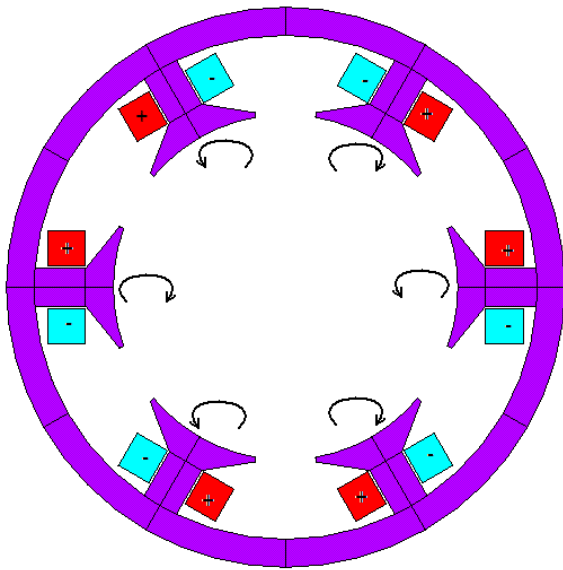


Fig. 2. Stator windings in single coil PM- BLDC motor; opposite marked direction of coil winding and resulted current in coil.

III. COMPUTATIONAL MODEL

Analysis of magnetic field in described motor is calculated using ANSYS software which is based on FEM. Calculations were carried out using 2D planar magnetic model. It is assumed that stator magnetic material operates with linear H-B characteristic. The part of the geometry of 2D ANSYS model with mesh displayed is shown in Fig. 3.

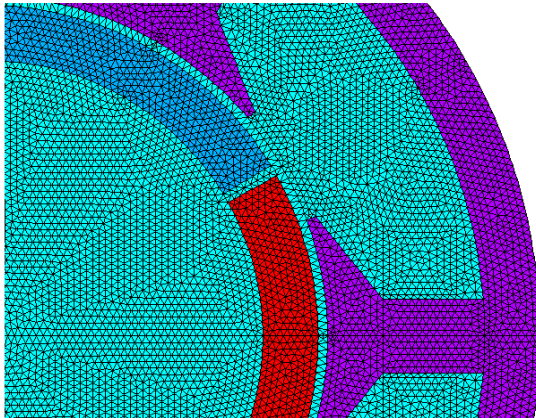


Fig. 3. Stator windings in single coil PM- BLDC motor; opposite marked direction of coil winding and resulted current in coil.

IV. FEM ANALYSIS OF MAGNETIC FIELD

The analysis of magnetic field allows to optimize design in respect of the motor performance and calculate magnetic forces existing between stator and rotor. Magnetic flux lines in motor with no coil current at 0 deg and 20 deg of rotor position are shown in Fig. 4 and Fig. 5 respectively. One can observe symmetrical flux lines distribution at 0 deg rotor position and closed loops of flux inside of stator pole at 20 deg. Flux distribution influences on cogging torque of motor.

Magnetic flux distribution and current distribution in coils

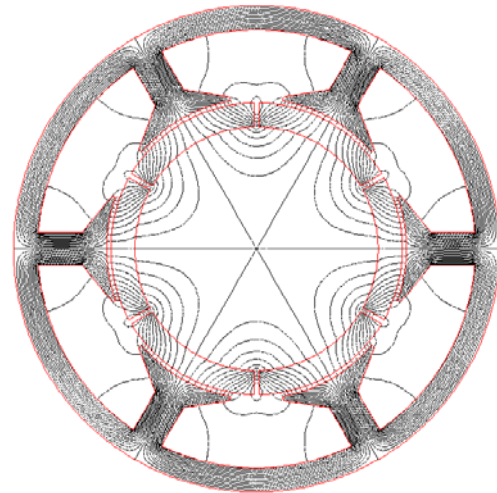


Fig. 4. 2D flux lines in PM BLDC single coil motor ($\alpha=0$ deg).

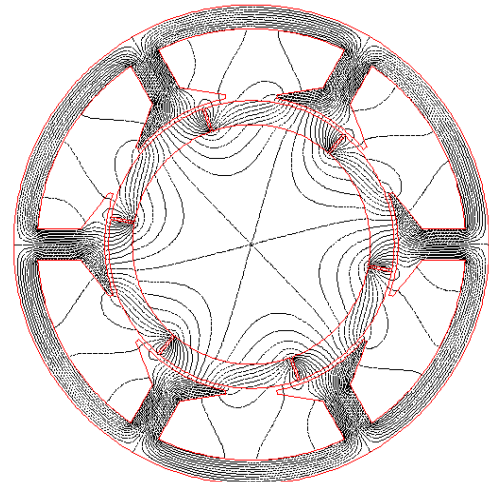


Fig. 5. 2D flux lines in PM BLDC single coil motor ($\alpha=0$ deg).

at load current 4 A/turn is shown in Fig. 6. Presented distribution of magnetic field produces no torque at 0 deg position at any current flowing in stator coils.

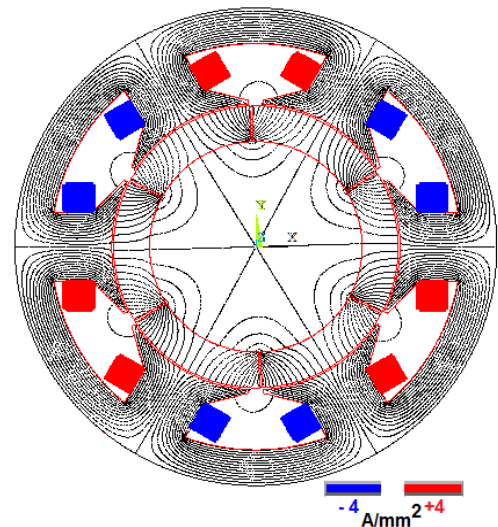


Fig. 6. Magnetic flux density distribution and current distribution at 0 deg of rotor position and 4 A/turn of coil current.

V. FEM ANALYSIS OF TORQUE

Analysis of magnetic field at each position allows to calculate characteristics of torque vs. rotor position at given load current. Both cogging torque and total torque were calculated.

The characteristic of cogging torque vs. rotor position is shown in Fig 7. One can observe high value near 0 deg position and at every 60 deg rotation. Cogging torque hold rotor in proper location in case of no load current. Characteristic of total torque at two different values of load current is shown in Fig. 8 (cogging torque shown for the reference). One can observe no torque at 0 deg and each 60 deg multiple. Because of no load current hold position is the same as for zero torque position at given current. It means that there is no starting torque in the motor.

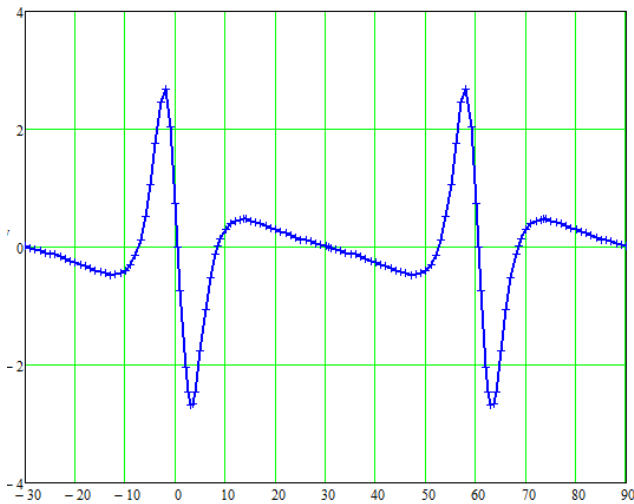


Fig. 7. Cogging torque vs. position of rotor.

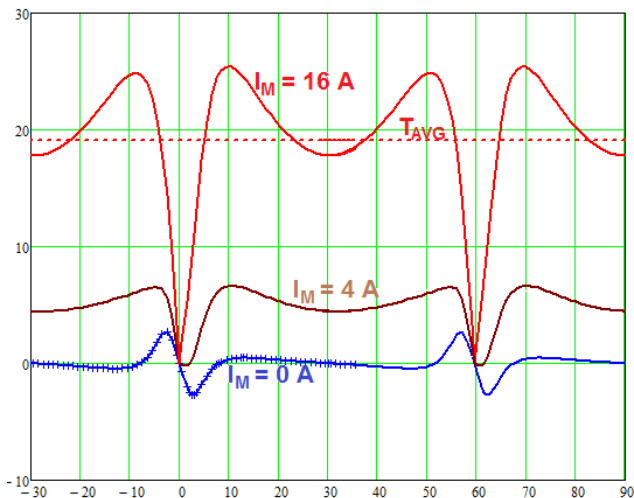


Fig. 8. Total torque vs. position of rotor at different value of load current (16 A/turn, 4 A/turn and 0 A/turn – only cogging torque); T_{AVG} – average value of total torque at 16 A/turn.

VI. THE DENT INFLUENCE ON STARTING TORQUE

In order to obtain non-zero torque at 0 position under non-zero load current modification of stator pole was applied. It consists in inserting of dent for unsymmetrical field

distribution. The dent location and magnetic field distribution is shown in Fig. 9. Characteristics of torque vs. rotor position in vicinity of 0 deg is shown in Fig. 10. Two cases are compared, with dent and without dent. One can observe that zero cogging torque is at 1 deg, while torque at load current at this position is non-zero. It means torque produced by current at hold position is non-zero and it allows to start rotation of motor in clockwise direction.

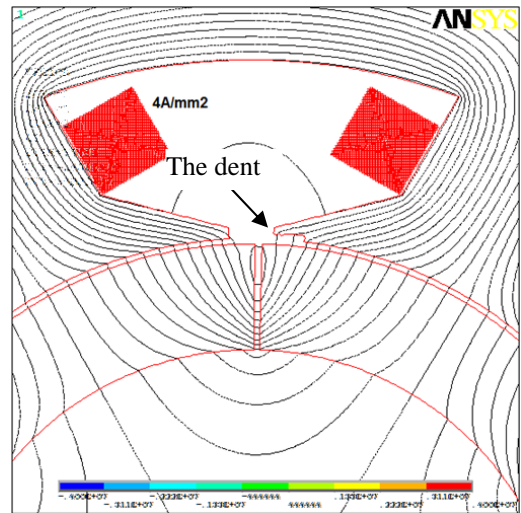


Fig. 9. Magnetic flux density and current density – motor with dent and angle 0 deg and 4 A/turn ($4A/mm^2$).

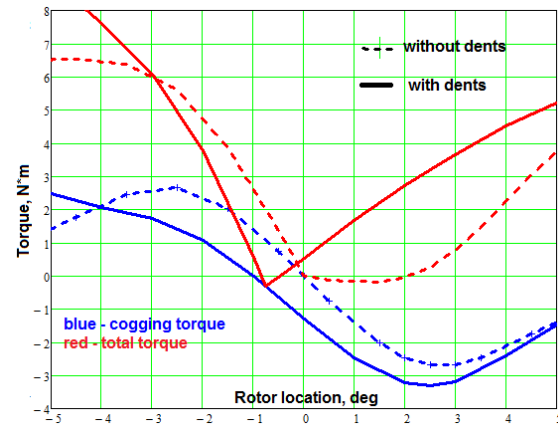


Fig. 10. A torque vs. position of rotor in vicinity of 0 deg position, comparison of motor poles with dents and without dents at 4 A/turn.

VII. CONCLUSIONS

- Permanent magnet brushless single coil DC motor described in [1] is analyzed.
- Features of the analyzed single coil DC motor are slightly different comparing with standard three phase motor.
- Future works will be concentrated on analysis of circuit model based on FEM.

REFERENCES

- [1] Gerfast S. R.: "Single coil, direct current permanent magnet brushless motor with voltage boost", US Patent 6940238, September 2005
- [2] ANSYS Software Manual

IPMSM Model Including Magnetic Saturation and Cross-Coupling

Darko P. Marčetić, Roberto M. Varga, and Mile B. Božić

Abstract—This paper presents a modified IPMSM model suitable for use with carrier-signal-injection-based sensorless methods. The suggested model includes magnet saturation of both d- and q- axis and cross-coupling which all result in more accurate description of high frequency test signal propagation. The model is verified by comparing experimental results of a sensorless method based on HF test signal with simulation results from standard and modified model.

Index Terms—IPMSM, model, HF test signal sensorless.

NOMENCLATURE

v_d, v_q	– stator d - and q - axis voltages
i_d, i_q	– stator d - and q - axis currents
v_{dh}, v_{qh}	– stator d - and q - axis high frequency voltage components
i_{dh}, i_{qh}	– stator d - and q - axis high frequency current components
ψ_d, ψ_q	– stator d - and q - axis fluxes
ψ_f	– permanent magnet flux
R_s	– stator phase resistance
L_d, L_q	– stator d - and q - axis self inductances
L_{dh}, L_{qh}	– stator d - and q - axis incremental self inductances
L_{dqh}, L_{qdh}	– stator d - and q - axis incremental mutual inductances
θ_r, θ_r^e	– actual and estimated rotor electrical position
ω_r	– actual rotor electrical angular frequency
T_e	– electromagnetic torque
P	– number of pole pairs

I. INTRODUCTION

INTERIOR Permanent Magnet Synchronous Machine (IPMSM) is used in many motor drive applications mostly due to its cost, high efficiency and high torque-to-inertia ratio [1]. Further drive system cost reduction is only possible if shaft position sensor is eliminated. The most popular methods for IPMSM rotor position estimation are a carrier-signal-injection-based methods. Those methods bypass fundamental

Manuscript received 30 May 2012. Accepted for publication 10 June 2012. Some results of this paper were presented at the 16th International Symposium Power Electronics, Novi Sad, Serbia, October 26-28, 2012.

This work was supported by Ministry of Education and Science of the Republic Serbia within project III 42004.

D. Marčetić is with the Faculty of Faculty of Technical Sciences, University of Novi Sad, , Serbia:(phone: +381-21-485-2504; e-mail: darmar@uns.ac.rs).

R. Varga is with Neotech Ltd, Novi Sad, Serbia (e-mail: neotech@open.telekom.rs).

M. Božić is with Nidec Motor Corporation, Chicago, USA (e-mail: mile.bozic@nidec-motor.com).

BEMF limitations by injecting a HF voltage signal into the phase windings and by measuring the machine response detecting corresponding HF current. The HF signal can be injected as rotating carrier in the stationary reference frame [2], [3] or as pulsating signal into the estimated d-axis [4], [5]. Usage of test signal injection helps but does not fully cancel the methods dependence on motor parameters variation. It has been reported that both saturation and cross-coupling effects introduce load dependent rotor position error [6] – [10].

This paper presents improved IPMSM model that helps explaining motor load dependence of HF test signal based methods. The model includes magnet saturation of both d- and q- axis and cross-coupling magnetic saturation. Experimental results show that only suggested model modifications bring model results close to experimental results under the heavy loading conditions.

II. MATHEMATICAL MODEL OF IPMSM WITH AND WITHOUT SATURATION AND CROSS-COUPLING

Electrical subsystem of IPMSM can be modeled using voltage balance equations (1), flux linkage equations (2) and electromagnetic torque formula (3).

$$\begin{bmatrix} v_d \\ v_q \end{bmatrix} = \begin{bmatrix} R_s & 0 \\ 0 & R_s \end{bmatrix} \begin{bmatrix} i_d \\ i_q \end{bmatrix} + \begin{bmatrix} p & -\omega_r \\ \omega_r & p \end{bmatrix} \begin{bmatrix} \psi_d \\ \psi_q \end{bmatrix} \quad (1)$$

$$\begin{bmatrix} \psi_d \\ \psi_q \end{bmatrix} = \begin{bmatrix} L_d & 0 \\ 0 & L_q \end{bmatrix} \begin{bmatrix} i_d \\ i_q \end{bmatrix} + \begin{bmatrix} \psi_f \\ 0 \end{bmatrix} \quad (2)$$

$$T_e = \frac{3}{2} P [\psi_f i_q + (L_q - L_d) i_d i_q] \quad (3)$$

The state space model of IPMSM is given in (4)

$$p \begin{bmatrix} i_d \\ i_q \end{bmatrix} = [A] \begin{bmatrix} i_d \\ i_q \end{bmatrix} + [B] \begin{bmatrix} v_d \\ v_q \\ \omega_r \psi_f \end{bmatrix} \quad (4)$$

where

$$[A] = \begin{bmatrix} -\frac{R_s}{L_d} & \frac{\omega_r L_q}{L_d} \\ -\frac{\omega_r L_d}{L_q} & -\frac{R_s}{L_q} \end{bmatrix} \quad [B] = \begin{bmatrix} \frac{1}{L_d} & 0 & 0 \\ 0 & \frac{1}{L_q} & -\frac{1}{L_q} \end{bmatrix}$$

This is basic model that does not include d- and q-axis magnetic saturation nor cross-coupling saturation. The magnet saturation can be included by altering L_d and L_q parameter with current level using following functions.

$$\begin{aligned} L_d &= L_d(i_d, i_q) \\ L_q &= L_q(i_d, i_q) \end{aligned} \quad (5)$$

L_d and L_q variation can be mapped for different current levels using finite-element analysis or experimental results. Experimental results for tested motor for $L_d(i_d, i_q)$ and $L_q(i_d, i_q)$ are given on the Fig 1 and Fig 2.

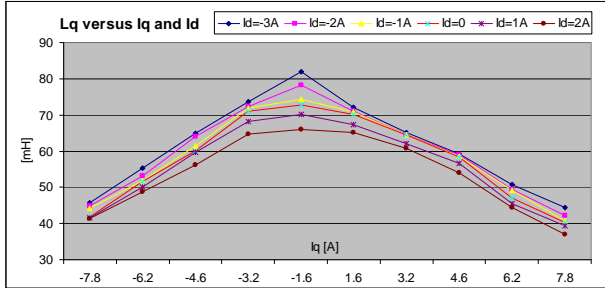


Fig. 1. Measured $L_q = L_q(i_d, i_q)$.

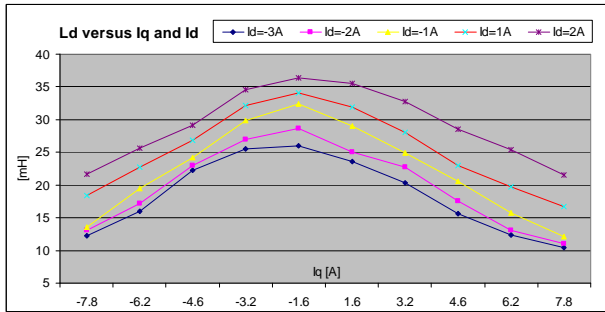


Fig. 2. Measured $L_d = L_d(i_d, i_q)$.

The cross coupling magnet saturation can be also built-in in IPMSM model using L_{dq} inductance parameter

$$\begin{bmatrix} \psi_d \\ \psi_q \end{bmatrix} = \begin{bmatrix} L_d & L_{dq} \\ L_{dq} & L_q \end{bmatrix} \begin{bmatrix} i_d \\ i_q \end{bmatrix} + \begin{bmatrix} \psi_f \\ 0 \end{bmatrix} \quad (6)$$

One way to include L_{dq} is to alter the state space IPMSM model as shown in (7) and on Fig 3.

$$\begin{bmatrix} \dot{i}_d \\ \dot{i}_q \end{bmatrix} = \frac{1}{p} \left(\begin{bmatrix} A \\ B \end{bmatrix} \begin{bmatrix} i_d \\ i_q \end{bmatrix} + \begin{bmatrix} v_d \\ v_q \\ \omega_r \psi_f \end{bmatrix} \right) + \begin{bmatrix} 0 & -L_{dq}/L_d \\ -L_{dq}/L_q & 0 \end{bmatrix} \begin{bmatrix} i_d \\ i_q \end{bmatrix} \quad (7)$$

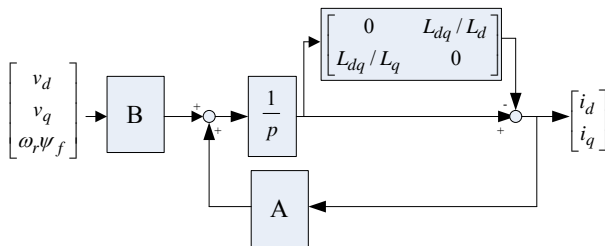


Fig. 3. Modified IPMSM model with build in cross-coupling saturation – suitable for MATLAB/ Simulink.

Cross coupling also changes with saturation and therefore L_{dq} parameter also has to vary with d- and q-axis current level. Measured $L_{dq} = L_{dq}(i_d, i_q)$ is given on the Fig 4. The data was collected experimentally, using approach suggested in [10].

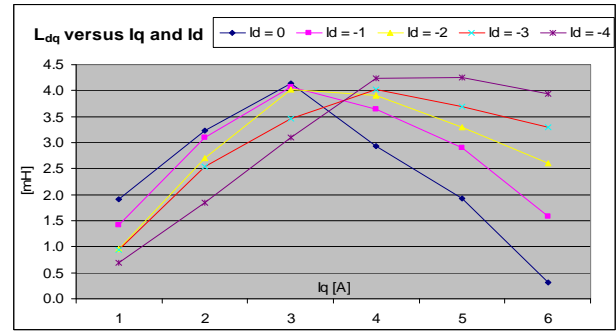


Fig. 4. Measured $L_{dq} = L_{dq}(i_d, i_q)$.

III. IPMSM MODEL EXCITED WITH INJECTED HF TEST SIGNAL AND UNDER DIFFERENT LOAD CONDITIONS

HF test signal based methods inject high frequency voltage signal into the phase windings and measure the machine response by detecting corresponding HF current signal. The HF q-axis current signal is compared to d-axis HF current signal and rotor position error signal is created, Fig 5.

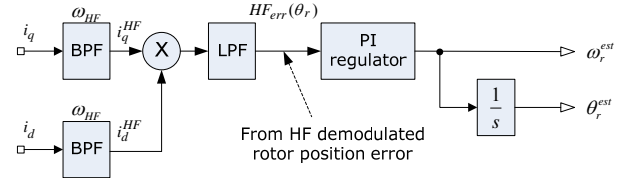


Fig. 5 The rotor position and speed estimation using demodulated HF current signal.

If only HF signals are considered, the model (1) and (6) reduces to

$$\begin{bmatrix} v_{dh} \\ v_{qh} \end{bmatrix} = \begin{bmatrix} L_{dh} & L_{dqh} \\ L_{qd} & L_{qh} \end{bmatrix} \cdot p \begin{bmatrix} i_{dh} \\ i_{qh} \end{bmatrix} \quad (8)$$

Equation (8) is valid in rotor position reference frame θ_r . However, the DSP can see only the quantities in used (estimated) rotor position reference frame, θ_r^e .

$$[T]^{-1} \begin{bmatrix} v_{dh}^e \\ v_{qh}^e \end{bmatrix} = \begin{bmatrix} L_{dh} & L_{dqh} \\ L_{qd} & L_{qh} \end{bmatrix} \cdot p [T]^{-1} \begin{bmatrix} i_{dh}^e \\ i_{qh}^e \end{bmatrix} \quad (9)$$

where $[T] = \begin{bmatrix} \cos(\theta_{err}) & \sin(\theta_{err}) \\ -\sin(\theta_{err}) & \cos(\theta_{err}) \end{bmatrix}$ transforms from θ_r to θ_r^e reference frame (Fig. 6).

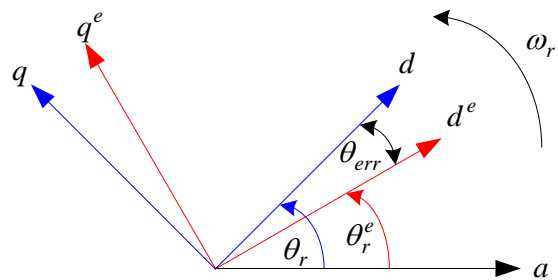


Fig. 6. Actual dq and estimated dq^e (DSP) rotating reference frames.

Therefore, if HF test signal v_{sig} is injected in d^e -axis only ($v_{dh}^e = v_{sig}$, $v_{qh}^e = 0$), in the estimated rotor position reference frame is valid (10)

$$\begin{bmatrix} v_{sig} \\ 0 \end{bmatrix} = \begin{bmatrix} L_{avg} - \hat{L}_{diff} \cos(2\theta_{err} + \theta_m) & \hat{L}_{diff} \sin(2\theta_{err} + \theta_m) \\ \hat{L}_{diff} \sin(2\theta_{err} + \theta_m) & L_{avg} + \hat{L}_{diff} \cos(2\theta_{err} + \theta_m) \end{bmatrix} p \begin{bmatrix} i_{dh}^e \\ i_{qh}^e \end{bmatrix}$$

where

$$L_{avg} = (L_{qh} + L_{dh})/2, L_{diff} = (L_{qh} - L_{dh})/2, \hat{L}_{diff} = \sqrt{L_{diff}^2 + L_{dq}^2}$$

$$\theta_m = \arctan(L_{dq} / L_{diff})$$

Solution of (10) for current d^e - and q^e -axis components available in DSP (estimated position reference frame) are

$$i_{dh}^e = \frac{v_{sig}}{p(L_{avg}^2 - \hat{L}_{diff}^2)} (L_{avg} + \hat{L}_{diff} \cos(2\theta_{err} + \theta_m)) \quad (11)$$

$$i_{qh}^e = -\frac{v_{sig}}{p(L_{avg}^2 - \hat{L}_{diff}^2)} (\hat{L}_{diff} \sin(2\theta_{err} + \theta_m))$$

Most of sensorless algorithms have estimated rotor position regulators that ultimately force i_{qh} signal to zero. If that is the case, according to (11) sensorless algorithm ends up with rotor position error equal to:

$$\theta_{err} = -\frac{\theta_m}{2} \quad (12)$$

Because of high dependence of relevant parameters (L_d , L_q and L_{dq}) of dc current levels in rotor position reference frame (Figures 1, 2, and 4) it is not easy to predict what will be the finally position error for giving load conditions. The only way to exam the nature of position error is to use modified simulation model which uses all inductance parameters as variables. Simulation results are given for no load $I_d = 0A$, $I_q = 0A$ (Fig. 7) and full load conditions $I_d = -4.5A$, $I_q = 5.5A$ (Fig. 8). The later pair is calculated using maximum torque per ampere approach. Both figures show trajectories of demodulated HF error signal (Fig 5.) for standard (dashed red) and for modified (solid blue) IPMSM model. Figures also show sawtooth signal of estimated rotor position which was artificially moved full circle around rotor position at stand still.

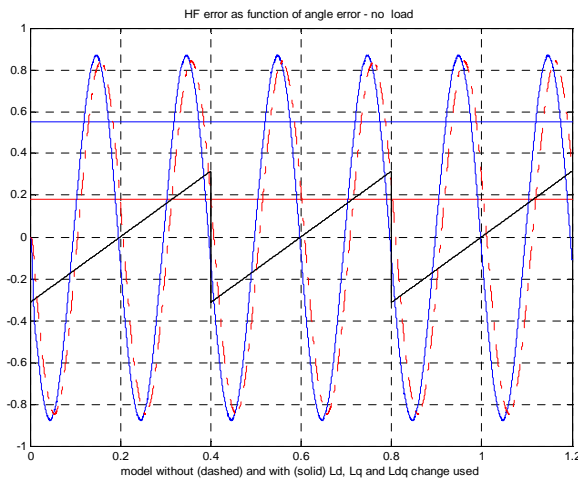


Fig. 7. Demodulated HF error signal as function of rotor position error for no load condition – model with (solid) and without (dashed) variable parameters.

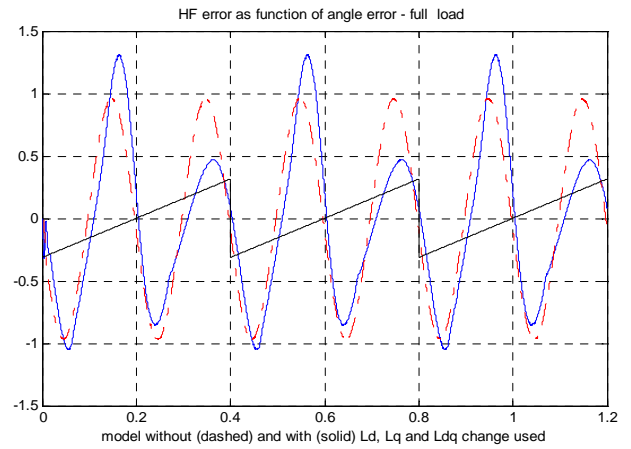


Fig. 8. Demodulated HF error signal as function of rotor position error for full load condition – model with (solid) and without (dashed) variable parameters.

Demodulated HF error signal holds position error information and drives sensorless position regulator. Standard IPMSM model predicts almost unchanged error signal trajectory for full circle of position error and therefore similar behavior of sensorless algorithm for different load conditions. On the other hand, modified IPMSM model predicts completely different nature of position error signal when load condition changes. Modified IPMSM model holds the reason for error signal deviation, the change is driven by significant L_d , L_q and L_{dq} inductance parameter variation with position error, as shown on Figure 9 for full load condition. While I_d^{DSP} and I_q^{DSP} for given load condition stay the same in DSP reference frame, the actual I_d and I_q vary with actual position error signal (in this case full circuit) and entirely change the model behavior and resulting error signal.

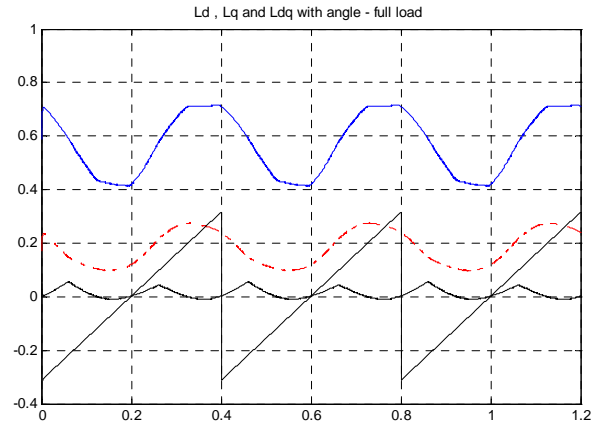


Fig. 9. Trajectories of L_d , L_q and L_{dq} inductances for full circle of rotor position errors and maximum current.

IV. EXPERIMENTAL RESULTS

The proposed IPMSM model was verified by using an experimental setup consisting vector controlled 1kW IPMSM machine, Fig. 10. The IPMSM parameters are – rated power $P_n = 750W$, with 36.5 V_{L-L} peak BEMF at 1000 rpm, star connected stator, $P = 4$, $R_s = 3.8\Omega$, and inductance parameters as given in figures 1, 2 and 4.

Motor was kept at stand still with lock rotor bracket. The magnet and encoder position was preset to zero. HF test

signal, amplitude 0.2 A and frequency 250 Hz, was injected in slowly rotating estimated rotor position, DSP d-axis. Shown demodulated rotor position error signal is calculated using model at Figure 5. The data from DSP was transferred into PC via fast GUI interface.



Fig.10. Experimental setup.

Fig. 11. shows the demodulated error signal relatively to sawtooth estimated position signal. With real magnet position kept at zero that sawtooth is also position error signal. Dashed red line shows data collected for zero current condition $I_d=0A$, $I_q=0A$ and shows very close match to both IPMSM models. Solid blue line for full load condition ($I_d = -4.5A$, $I_q = 5.5A$) shows complex nature of demodulated error signal. While original IPMSM model show no change with load (Fig 7.) modified IPMSM model (Fig 8.) shows similar output HF error distortion.

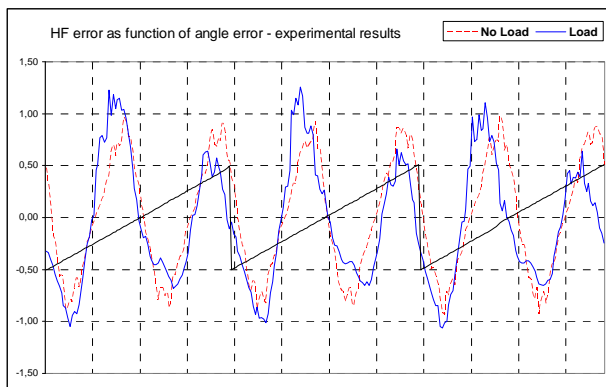


Fig. 11. Demodulated HF error signal as function of rotor position error for no load (dashed) and full load (solid) –experimental results.

V. CONCLUSION

This paper describes a modified IPMSM model that includes all known saturation effects. The motivation for this

model development was HF test signal based sensorless instability at ultra high load condition. The modified IPMSM model results suggest the reason for that unwanted sensorless behavior. It shows large distortion of demodulated position error signal which can lead to 1. significant estimated position error (the zero crossing of error signal and actual zero position error differ) or 2. regulator instability, especially if error signal offsets from zero and loses zero-crossing. In that case regulator runs through actual zero position and runs to next available zero crossing where it settles erroneously.

REFERENCES

- [1] Angus Murray, Marco Palma and Ali Husain, "Performance Comparison of Permanent Magnet Synchronous Motors and Controlled Induction Motors in Washing Machine Applications using Sensorless Field Oriented Control", Energy Saving Products Division International Rectifier El Segundo, CA 90245.
- [2] Y.-S. Jeong, R. D. Lorenz, T. M. Jahns and S.-K. Sul, "Initial Rotor Position Estimation of an Interior Permanent Magnet Synchronous Machine using Carrier-Frequency Injection Methods," IEEE Intern. Electric Machines and Drives Conf. IEMDC, Madison, WI, June 1-4, 2003, pp. 1218–1223; later in IEEE Trans. Industry Appl., Vol. 41, No. 1, Jan./Feb. 2005, pp. 38-45.
- [3] M. J. Corley and R. D. Lorenz, "Rotor position and velocity estimation for a salient-pole permanent magnet synchronous machine at standstill and high speed," IEEE Trans. Ind. Appl., vol. 34, no. 4, pp. 784–789, Jul./Aug. 1998.
- [4] G. Foo and M. F. Rahman, "Sensorless sliding-mode MTPA control of an IPM synchronous motor drive using a sliding-mode observer and HF signal injection," IEEE Trans. Ind. Electron., vol. 57, no. 4, pp. 1270–1278, Apr. 2010.
- [5] Chan-Hee Choi and Jul-Ki Seok, "Pulsating Signal Injection-Based Axis Switching Sensorless Control of PMSM for Minimal Zero Current Clamping Effects", School of Electrical Engineering, Yeungnam University DaeDong, Kyungsan, Kyunbuk, Korea (ZIP : 712-749)
- [6] Y. Li, Z. Q. Zhu, D. Howe, and C. M. Bingham, "Modeling of Cross-Coupling Magnetic Saturation in Signal-Injection-Based Sensorless Control of Permanent-Magnet Brushless AC Motors", IEEE Transactions on Magnetics, vol. 43, no. 6, June 2007.
- [7] H. W. De Kock, M. J. Kamper, and R. M. Kennel, "Anisotropy comparison of reluctance and PM synchronous machines for position sensorless control using HF carrier injection," IEEE Trans. Power Electron., vol. 24, no. 8, pp. 1905–1913, Aug. 2009.
- [8] P. Guglielmi, M. Pastorelli, and A. Vagati, "Impact of cross-saturation in sensorless control of transverse-laminated synchronous reluctance motors," IEEE Trans. Ind. Electron., vol. 53, no. 2, pp. 429–439, Apr. 2006.
- [9] N. Bianchi and S. Bolognani, "Influence of rotor geometry of an interior PM motor on sensorless control feasibility," IEEE Trans. Ind. Appl., vol. 43, no. 1, pp. 87–96, Jan./Feb. 2007.
- [10] Y. Li, Z. Q. Zhu, D. Howe, C.M. Bingham, and D. Stone, "Improved rotor position estimation by signal injection in brushless AC motors, accounting for cross-coupling magnetic saturation," IEEE Trans. Ind. Appl., vol. 45, no. 5, pp. 1843–1849, Sep./Oct. 2009.

Comparison of Methods for On-Line Harmonic Estimation

Jovan M. Knežević and Vladimir A. Katić

Abstract—The aim of this paper is to present a comparison of some popular methods for online harmonic estimation. The well-known methods Discrete Fourier Transform (DFT), Enhanced Phase Locked Loop (EPLL), Adaptive Notch Filter (ANF) and method based on Extended Kalman Filter (EKF) are simulated and compared. The methods are compared in critical phases, such as the fast change of harmonic amplitudes and the change of the system frequency.

Index Terms—Power Electronics/Harmonic estimation /Simulation

I. INTRODUCTION

THE number of sensitive devices that require high power quality, i.e. high quality of power supply is constantly increasing [1]. On the other hand the use of applications of nonlinear loads, mostly consisting of power electronics devices, is growing even at faster pace. Such loads and devices are distorting supply waveforms and therefore polluting power system grid. The development of tools for accurate harmonic estimation enables a proper operation of the devices for mitigation of power quality imperfections.

The Fourier Transform (FT) and its discrete form the Discrete FT (DFT) have been the most common tool used by researchers and practitioners over last several decades [2]. The DFT decomposes signals into fundamental and higher order harmonics. Many problems of the DFT such as spectral leakage, picket fence effects and sensitivity to the variations of the system frequency are limiting its accuracy. To preserve time information in the signal the windowed DFT known also as Short Time Fourier Transform has been developed [2].

In recent years, in order to overcome above mentioned problems, the researchers have been developing methods that can adaptively track changes in the system. The methods based on the Enhanced Phase Locked Loop have been presented [3]-[5]. They use one EPLL block to adaptively track an amplitude and the phase of the particular harmonic.

Manuscript received 30 May 2012. Accepted for publication 10 June 2012. Some results of this paper were presented at the 16th International Symposium Power Electronics, Novi Sad, Serbia, October 26-28, 2012.

This paper is supported by the Ministry of Education and Science of Republic of Serbia, through project No. III 42004, Smart Electricity Distribution Grids Based on Distribution Management System and Distributed Generation (2011-2014).

J. M. Knežević is with BMW Peugeot Citroen GmbH, Munich, Germany (e-mail: jovan.knezevic@bpc-electrification.com).

V. A. Katić is with Faculty of Technical Sciences, University of Novi Sad, Novi Sad, Serbia. (e-mail: katav@uns.ac.rs).

The method of [3]-[5] makes a fundamental assumption that the existing frequency components in the signal are in the form of harmonics [2]. The Adaptive Notch Filter (ANF) presented in [6], on the other hand, relaxes that assumption and presents a major improvement of the methods presented in [7] and [8] which enables direct detection and extraction of arbitrary frequency components. Such methods are very accurate in a non-stationary environment but they have slower dynamic response than the DFT [6].

To achieve a higher resolution and better estimation accuracy and still to preserve adaptive feature, the Kalman Filter (KF) have been suggested [10]. The KF is a mathematical model that uses noisy and inaccurate measurement data and provides an efficient computational (recursive) means to estimate the past, present or future values in a way that minimizes the mean of the squared error. In order to achieve higher accuracy an accurate model is required. For nonlinear model, the extended KF is used [9].

In this paper several methods for online harmonic estimation are simulated and compared. The most common tool - the DFT, methods based on gradient descent method EPLL and ANF and ECKF are tested in the typical environment with fast dynamical changes of system parameters.

II. METHODS

A. Discrete Fourier Transform

The FT is one of the most frequently used techniques of signal analysis [1], [2]. The FT $X(f)$ of the continuous signal $x(t)$ is defined in (1). Considering the periodical nature of the electrical current and voltage as well as the use of the digital signal processing, the DFT is used as a conventional tool.

$$X(f) = \int_{-\infty}^{\infty} x(t)e^{-j2\pi ft} dt \quad (1)$$

The DFT $X[k]$ of the sampled signal $x[n]$ is defined as:

$$X[k] = \sum_{n=0}^{N-1} x[n]e^{-j\frac{2\pi kn}{N}} \quad (2)$$

$x[n]$ is the sampled value of the continuous signal $x(t)$ at time instant nT

$$x[n] = x(nT), \quad n = 0, 1, 2, \dots, N-1 \quad (3)$$

The recursive algorithm of the DFT can be easily represented by equations (4) and (5) assuming that the DFT is

implemented as the windowed DFT with the square window of the width equal to the period of the fundamental harmonic.

$$a_i[n] = a_i[n-1] + \frac{2}{N} (x[n] - x[n-N]) \cos\left(\frac{2\pi ni}{N}\right) \quad (4)$$

$$b_i[n] = b_i[n-1] + \frac{2}{N} (x[n] - x[n-N]) \sin\left(\frac{2\pi ni}{N}\right) \quad (5)$$

where N is the number of samples per period of the fundamental component of the signal, i is the order of the harmonic and a_i and b_i are the real and imaginary coefficients of the DFT. Fig. 1 presents MATLAB-Simulink model of the DFT. It shows how many calculations are necessary to obtain a_i and b_i coefficients of the DFT.

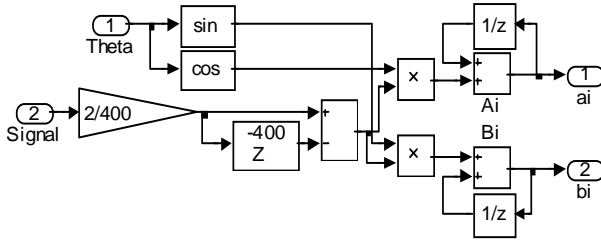


Fig. 1. MATLAB-Simulink model of the DFT.

It is obvious that it is very easy to calculate these Fourier coefficients, but if it is necessary to have the amplitude and the phase of a certain harmonic, such calculations require additional computational effort of the digital processor as given in (6) and (7).

$$A_i = \sqrt{a_i^2 + b_i^2} \quad (6)$$

$$\delta_i = \arctan\left(\frac{b_i}{a_i}\right) \quad (7)$$

After the amplitude and the phase are obtained, reconstruction of the particular harmonic is given as:

$$h_i(t) = A_i \sin(i\omega_1 t + \delta_i) \quad (8)$$

Some sources of errors in the DFT can be recognized as aliasing, spectral leakage, picket fence, etc. [2]. These errors are particularly enhanced in cases of fast varying signals of transients. In those cases the signal frequency is changing even with the pace faster than one period of the fundamental harmonic (20ms in 50Hz systems) [2].

B. The Enhanced Phase Locked Loop

Continuous signal can be represented as:

$$x(t) = \sum_{i=1}^N x_i \quad (9)$$

$$x_i(t) = A_i \sin(\omega_i t + \delta_i) \quad (10)$$

where i is the order of the harmonic so that ω_1 represents the fundamental frequency component (the first harmonic) and higher harmonic components are defined by $i > 1$. Usually $\omega_i = i\omega_1$, but this is not necessarily true in all cases. The task of the EPLL is to extract individual harmonic components of the signal $x(t)$. The least squares error between the input of the EPLL $x(t)$ and the estimated signal $x_i(t)$ is

minimized by the method of gradient descent [5]. The cost function is defined as:

$$J(t, A_i(t), \phi_i(t)) = \frac{1}{2} [x(t) - x_i(t, A_i(t), \phi_i(t))]^2 = \frac{1}{2} e^2(t, A_i(t), \phi_i(t)) \quad (11)$$

If it is assumed that $\Theta \in R^N$ is the vector of parameters $A_i(t), \phi_i(t)$ the gradient descent method can be written as:

$$\frac{\partial}{\partial t} \Theta(t) = -\mu_i \frac{\partial}{\partial \Theta} J(t, \Theta(t)) \quad (12)$$

The gradient descent method provides a method of adjusting the parameter Θ so that the cost function J converges to its minimum point. The EPLL is developed as an adaptive notch filter and is described by the following differential equations:

$$\frac{dA_i(t)}{dt} = \mu_{1i} e_i(t) \sin \phi_i(t) \quad (13)$$

$$\frac{d\omega_i(t)}{dt} = \mu_{2i} e_i(t) \cos \phi_i(t) \quad (14)$$

$$\frac{d\phi_i(t)}{dt} = \mu_{3i} \mu_{3i} e_i(t) \cos \phi_i(t) + \omega_{0i} \quad (15)$$

$$y_i(t) = A_i(t) \sin \phi_i(t) \quad (16)$$

$$e_i(t) = x(t) - y_i(t) \quad (17)$$

$$\phi_i(t) = \omega_{0i} t + \delta_i \quad (18)$$

Detailed derivations and stability analysis can be found in [5]. Fig. 2 shows a very simple implementation of the computational unit in the MATLAB/Simulink of the EPLL.

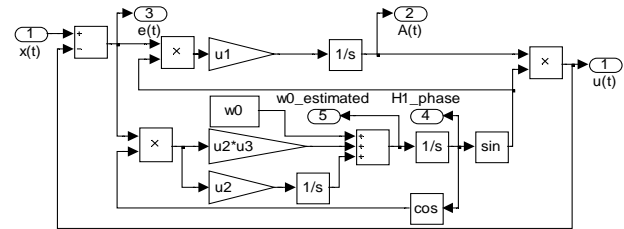


Fig. 2. MATLAB-Simulink model of the EPLL.

A proper setting of the parameters μ_{1i} , μ_{2i} and μ_{3i} ensures the convergence of the solution to differential equations. The parameter μ_{1i} controls the amplitude and the others control the phase and frequency tracking properties. Larger μ_{1i} guarantees a faster step response of the amplitude, but also introduces a higher steady state error. It is a trade-off between accuracy and speed. In order to reduce ripple in the response of the EPLL, it is possible to introduce filters for the amplitude and frequency, but this further decreases the time response.

C. Adaptive Notch Filter

An ANF has been recently proposed in [6]-[8]. The dynamic behaviour of the ANF is defined by following set of differential equations:

$$\ddot{y}_k + \theta_k^2(t) y_k = 2\zeta_k \theta_k(t) \dot{y}_k \quad (19)$$

$$\dot{\theta}_k(t) = -\gamma_k \theta_k(t) e(t), k = 1, \dots, n \quad (20)$$

$$e(t) = x(t) - \sum_{k=1}^n \dot{y}_k(t) \quad (21)$$

where $x(t)$ is the input signal, θ_k is the estimated frequency of the k th component, and γ_k and ζ_k are both real and positive numbers which determine the behaviour of the k th subfilter of the ANF in terms of accuracy and convergence speed.

It can be found that for the input signal $x(t)$ the dynamical system (19)-(21) has a unique quasi orbit given by:

$$P(t) = \left(P_1^T(t) \dots P_n^T(t) \right)^T \quad (22)$$

where $P_k(t)$ is given by

$$P_k(t) = \begin{pmatrix} \bar{y}_k \\ \dot{\bar{y}}_k \\ \bar{\theta}_k \end{pmatrix} = \begin{pmatrix} -\frac{A_k}{\omega_k} \cos \phi_k(t) \\ A_k \sin \phi_k(t) \\ \omega_k \end{pmatrix}, \quad k = 1, \dots, n \quad (23)$$

This means that the k th constituting component of the input signal as well as its frequency are directly provided by the k th set of the differential equations (19)-(21), and hence, a full decomposition is achieved if a sufficient number of filters are employed.

Detailed derivations and stability analysis can be found in [6]. Fig. 3 shows a very simple implementation of the subfilter unit of the ANF in the MATLAB/Simulink and its full decomposition of the parallel structure in fig.4..

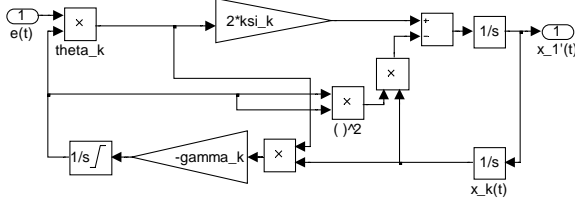


Fig. 3. MATLAB-Simulink model of one Subfilter of the ABF.

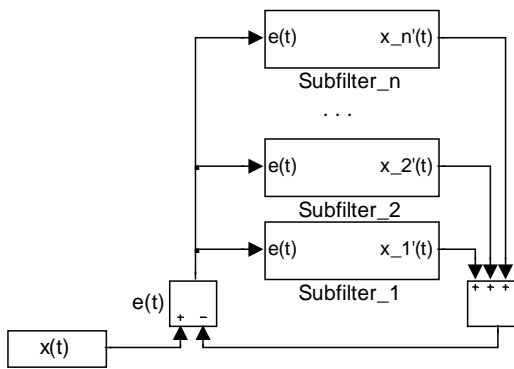


Fig. 4. Full Decomposition of the parallel structure of the ANF.

Similar to the DFT, the amplitude and phase shift of particular harmonic can be calculated as:

$$A_k = \sqrt{\bar{\theta}_k^2 \bar{x}_k^2 + \dot{\bar{x}}_k^2} \quad (24)$$

$$\phi_k = \arctan\left(\frac{\dot{\bar{x}}_k}{\bar{\theta}_k \bar{x}_k}\right) \quad (25)$$

D. The Extended Complex Kalman Filter

An observed signal at time k can be described in a power system as a sum of N of x_i sinusoids (9) with white noise v_i :

$$x_k = \sum_{i=1}^N (x_i + v_i) \quad (26)$$

$$v_i \approx N(0, R_i)$$

The observation noise v_i is a Gaussian white noise with zero mean and variance σ_v^2 . The covariance of measured errors is $R_k = E[v_k v_k^{*T}]$. For the sake of simplicity, let us consider only single complex sinusoid x with the angular frequency ω_l and the amplitude a_l . Complex type state variables are defined as [10]:

$$x_{k(1)} = e^{j\omega_l T_s}$$

$$x_{k(2)} = a_1 e^{j(k\omega_l T_s + \phi_1)} \quad (27)$$

$$x_{k(3)} = a_1 e^{-j(k\omega_l T_s + \phi_1)}$$

The state – space model is written as:

$$x_{k+1} = f(x_k) \quad (28)$$

$$y_k = Hx_k + v_k$$

where:

$$x_k = [x_{k(1)} \quad x_{k(2)} \quad x_{k(3)}]^T \quad (29)$$

$$f(x_k) = \begin{bmatrix} x_{k(1)} & x_{k(1)}x_{k(2)} & \frac{x_{k(3)}}{x_{k(2)}} \end{bmatrix}^T \quad (30)$$

$$H = [0 \quad -0.5i \quad 0.5]^T \quad (31)$$

The recursive process of the ECKF is then:

State Prediction

$$\tilde{x}_{k+1|k} = f(\hat{x}_{k|k}) \quad (32)$$

the symbols \sim and $\hat{\cdot}$ stand for the estimated and predicted values, respectively.

$$P_{k+1|k} = F_k P_{k|k} F_k^{*T} + Q_k \quad (33)$$

$$F_k = \frac{\partial f(x_k)}{\partial x_k} \quad (34)$$

$$F_k = \begin{bmatrix} 1 & 0 & 0 \\ x_{k(2)} & x_{k(1)} & 0 \\ -x_{k(3)}/x_{k(1)}^2 & 0 & 1/x_{k(1)} \end{bmatrix} \quad (35)$$

State Filter

$$\hat{x}_{k|k} = \tilde{x}_{k|k-1} + K_k (y_k - H\tilde{x}_{k|k-1}) \quad (36)$$

and the Kalman filter gain is calculated as:

$$K_k = P_{k|k-1} H^T [HP_{k|k-1} H^T + R_k]^{-1} \quad (37)$$

$$P_{k|k} = P_{k|k-1} - K_k H P_{k|k-1} \quad (38)$$

The parameters of the frequency f_k , and amplitude a_k at time k can be obtained as:

$$f_k = \frac{1}{2\pi T_s} \left[\text{Im}(\ln(\hat{x}_{k(1)})) \right] \quad (39)$$

$$a_k = \hat{x}_{k(2)} \quad (40)$$

More details about the ECKF can be found in [9] and [10].

III. SIMULATION

All of the mentioned methods have been simulated in the MATLAB/Simulink environment. In this paper these methods have been tested in the case of fast changes of system parameters, amplitude and the frequency. In order to do this, two test signals have been defined:

$$x_1(t) = A_1(t) \sin(\omega_1 t) \quad (41)$$

$$A_1(t) = \begin{cases} 1 & t \leq 100\text{ms} \\ 1.2 & t > 100\text{ms} \end{cases} \quad (42)$$

$$\omega_1 = 2 \cdot \pi \cdot 50$$

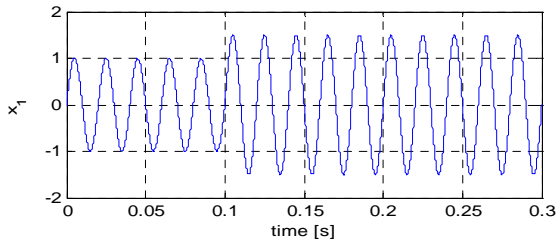


Fig. 5. Test signal x_1 .

and the second.

$$x_2(t) = A_2 \sin(\omega_2(t)t) \quad (43)$$

$$\omega_2(t) = \begin{cases} 2 \cdot \pi \cdot 50 & t \leq 100\text{ms} \\ 2 \cdot \pi \cdot 60 & t > 100\text{ms} \end{cases} \quad (44)$$

$$A_2 = 1$$

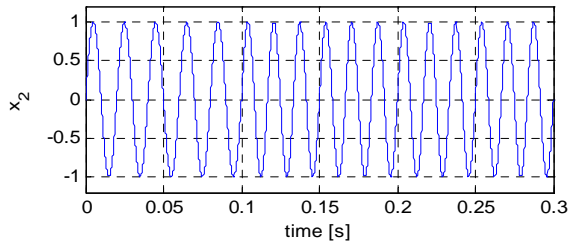


Fig. 6. Test signal x_2 .

A. Change of the amplitude

In fig.7 to fig.10 analysis of the signal x_1 is shown. A sudden step of the signal amplitude is analysed. As it is well known the DFT and ECKF have a faster step response while the EPLL and ANF are significantly slower.

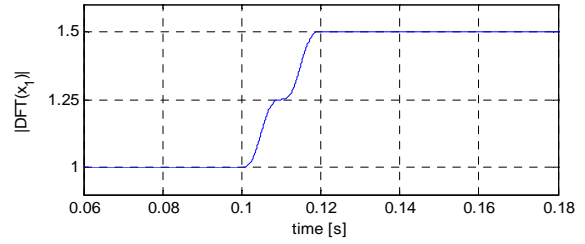


Fig. 7. Amplitude of the signal x_1 using DFT.

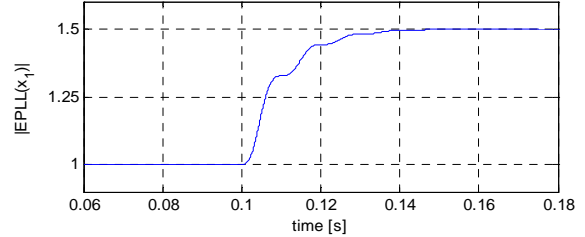


Fig. 8. Amplitude of the signal x_1 using EPLL.

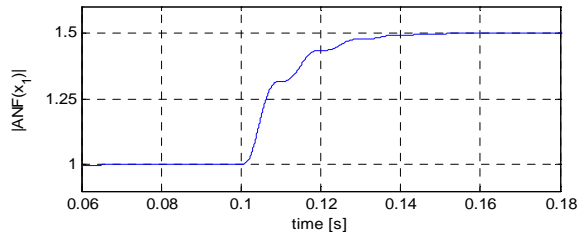


Fig. 9. Amplitude of the signal x_1 using ANF.

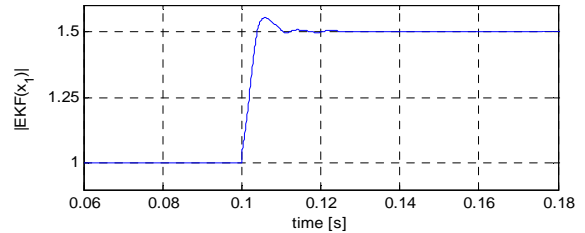


Fig. 10. Amplitude of the signal x_1 using ECKF.

B. Change of the frequency

In fig.11 to fig.14 analysis of the signal x_2 is shown. In the signal x_2 a sudden change of the frequency can be seen. A known problem of the DFT can be seen in fig.11. The DFT doesn't work properly in the case of variable frequency. The EPLL and ANF needed some time to converge to the new value of the signal frequency while the ECKF is obviously faster.

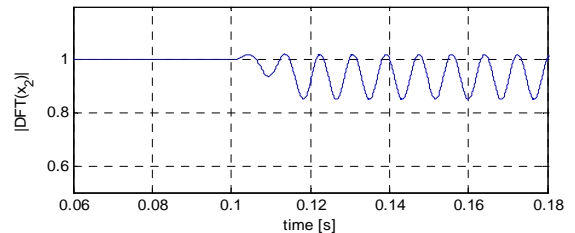
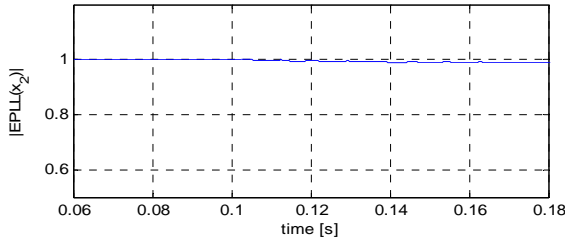
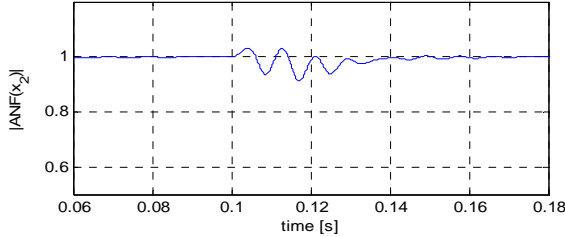
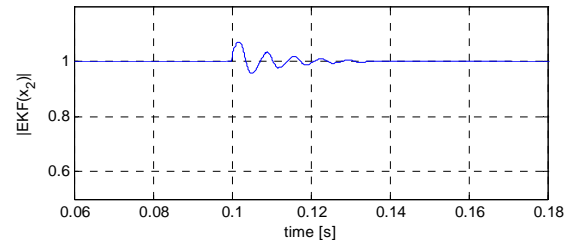


Fig. 11. Amplitude of the signal x_2 using DFT.

Fig. 12. Amplitude of the signal x_2 using EPLL.Fig. 13. Amplitude of the signal x_2 using ANF.Fig. 14. Amplitude of the signal x_2 using ECKF.

C. Example

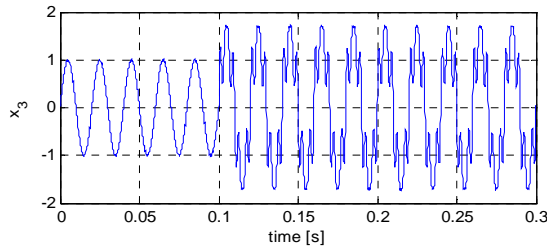
In fig.15 the test signal x_3 is shown. It has a main harmonic as well as the 5th and 7th harmonic and white noise $n(t)$.

$$x_3(t) = A_1 \sin(\omega_0 t) + A_5 \sin(5 * \omega_0 t) + A_7 \sin(7 * \omega_0 t) + n(t) \quad (45)$$

$$A_1 = \begin{cases} 1 & t \leq 0.1 \\ 1.5 & t > 0.1 \end{cases} \quad (46)$$

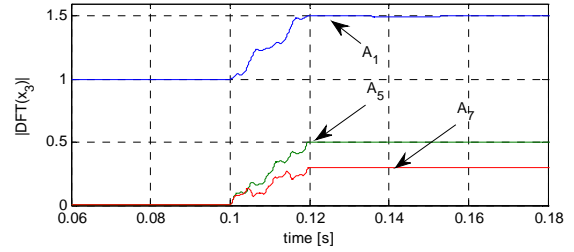
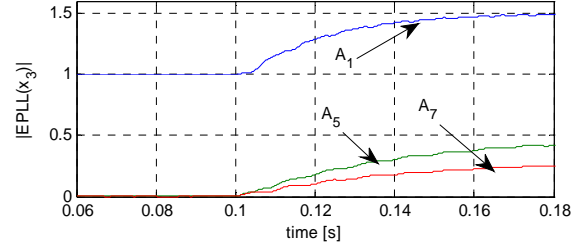
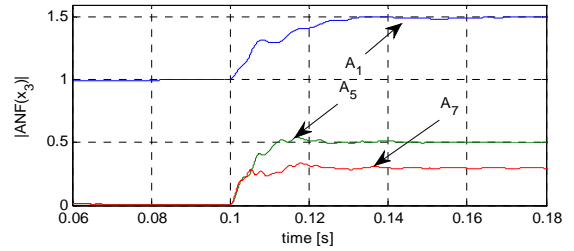
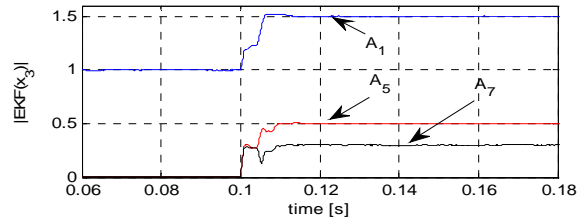
$$A_5 = \begin{cases} 0 & t \leq 0.1 \\ 0.5 & t > 0.1 \end{cases}$$

$$A_7 = \begin{cases} 0 & t \leq 0.1 \\ 0.3 & t > 0.1 \end{cases}$$

Fig. 15. Test signal x_3 .

The analysis of the signal x_3 is shown in fig.16 to fig.19. In the case of several harmonics and constant system frequency the DFT is very accurate with the delay of 20ms. The ECKF is

even faster if the parameters of the noise are known. Methods based on the gradient descent method need more time to converge to the steady state values.

Fig. 16. DFT analysis of the signal x_3 .Fig. 17. EPLL analysis of the signal x_3 .Fig. 18. ANF analysis of the signal x_3 .Fig. 19. ECKF analysis of the signal x_3 .

IV. CONCLUSION

In this paper several methods for harmonic analysis are compared. The DFT, methods based on the gradient descent method the EPLL and ANF and ECKF are simulated in the typical environment with fast dynamical changes of system parameters. The DFT and ECKF are fast and accurate. In the case of the variable system frequency the DFT can produce significant errors. In the case of slow changes the EPLL and ANF can adaptively and accurately track the parameters of the system. The EPLL and ANF are simple and easy to implement while the ECKF is very complex and requires powerful processor.

REFERENCES

- [1] D. Sabin and A. Sandaram, "Quality Enhances Reliability," *IEEE Spectrum*, vol.33, no.2, pp.34-41, Feb.1996.
- [2] Sachin K. Jain and S.N. Singh, "Harmonics estimation in emerging power system: Key issues and challenges," *Electric Power Systems Research*, vol.81, pp.1754-1766, June 2011.
- [3] A.K. Ziarani and A. Konrad, "A method of extraction of non-stationary sinusoids," *Signal Processing*, vol. 84, no. 8, pp. 1323–1346, 2004.
- [4] M. Karimi-Ghartemani and M.R. Iravani, "Measurement of harmonics/inter-harmonics of time-varying frequencies," *IEEE Trans. on Power Delivery*, vol. 20, no. 1, pp. 23–31, Jan. 2005.
- [5] M. Karimi-Ghartemani and A.K. Ziarani, "Performance characterization of a nonlinear system as both an adaptive notch filter and a phase-locked loop," *Int. Journal on Adaptive Control Signal Processing*, vol. 18, pp. 23–53, 2004.
- [6] M. Mojiri, M. Karimi-Ghartemani and A. Bakhshai "Processing of harmonics and interharmonics using an adaptive notch filter," *IEEE Trans. on Delivery*, vol. 25, pp. 534–542, 2010.
- [7] M. Mojiri, M. Karimi-Ghartemani and A. Bakhshai "Time-domain signal analysis using adaptive notch filter," *IEEE Trans. on Signal Process*, vol. 55, pp. 85–93, Jan. 2007.
- [8] M. Mojiri and A. Bakhshai "Estimation of n frequencies usign adaptive notch filter," *IEEE Trans. Circuits Syst. II*, vol. 54, pp. 338–342, Apr. 2007
- [9] C.I. Chen, G.W. Chang, R.C. Hong and H.M. Li, "Extended Real Model of Kalman Filter for Time Varying Harmonic Estimation," *IEEE Trans. on Power Delivery*, vol. 25, pp. 17–28, Jan. 2010.
- [10] C.H. Huang, C.H Lee, K.J. Shih and Y.J. Wang, "Frequency Estimation of Distorted Power System Signals Using a Robust Algorithm," *IEEE Trans. on Power Delivery*, vol. 23, pp. 41–52, Jan. 2008.

PWM Algorithms for Multilevel Inverter Supplied Multiphase Variable-Speed Drives

Martin Jones, Obrad Dordevic, Nandor Bodo, and Emil Levi

Abstract—Multiphase variable speed drives are nowadays regarded as serious contenders for various applications, due to the certain advantages that they possess when compared to three-phase drives. On the other hand, the multilevel (predominantly three-level) voltage source inverter (VSI) has become an industrially accepted technology for medium-voltage three-phase drives. The logical next step is to integrate multilevel VSI and multiphase drive technologies, since benefits of each can then be combined. This paper will review recent advances in this area. Two different topologies of the multiphase supply will be considered and the emphasis will be placed on appropriate pulse width modulation (PWM) techniques that can be used in conjunction with the supply structure. The first topology utilises multilevel (three-level) VSI and the machine's stator multiphase winding is star-connected with an isolated neutral point. In the second topology the winding is left open-ended and each side of the winding is connected to an isolated two-level VSI. This topology can also achieve three-level operation. Carrier-based and space vector based PWM strategies are considered and the obtainable performance is illustrated using experimental results.

Index Terms—Multiphase drives, multilevel voltage source inverters, open-end winding topology.

I. INTRODUCTION

THE requirements that a VSI modulation algorithm should satisfy are numerous. Most importantly, the output phase voltages must match the commanded references on average and the undesired harmonics should appear only around the multiples of the switching frequency. The resulting voltage total harmonic distortion (THD) should be as low as possible and the switching sequence should be arranged symmetrically, in a way that gives each inverter leg equal and constant switching frequency. The resulting voltage waveforms should have maximal dc-link utilisation. Some requirements are in contradiction to each other. For instance, switching losses can be minimised by lowering the switching frequency, however this impacts negatively on the THD and electro-magnetic interference (EMI).

Manuscript received 30 May 2012. Accepted for publication 10 June 2012. Some results of this paper were presented at the 16th International Symposium Power Electronics, Novi Sad, Serbia, October 26-28, 2012.

This paper was made possible by NPRP grant 4-152-02-053 from the Qatar National Research Fund (a member of Qatar Foundation). The statements made herein are solely the responsibility of the authors.

M. Jones, O. Dordevic, N. Bodo and E. Levi are with School of Engineering, Technology and Maritime Operations, Liverpool John Moores University, Liverpool, United Kingdom (e-mails: m.jones2@ljmu.ac.uk, o.dordevic@2009.ljmu.ac.uk, n.bodo@2009.ljmu.ac.uk, e.levi@ljmu.ac.uk).

Three-phase modulation methods are well established in terms of both carrier-based and space vector techniques. With properly chosen zero sequence that is added to the reference, the same voltage waveforms are achievable with both types of the modulation strategies [1]. The space vector techniques use the three nearest space vectors to the reference, which are the vertices of the triangle in which the reference is positioned. In the two-level case this means that two active and zero space vectors are used to achieve the reference during each switching period.

The advantages of multiphase variable speed drives over the three-phase ones are numerous [2]. An increase of fault tolerance is achieved, since the rotating field inside the stator winding can be obtained with only three phases. Thus, the machine can continue its operation with several faulted phases, as long as there are at least three healthy ones left [3]. Multiphase machines can be built with concentrated or distributed windings. With the distributed winding machines only the first harmonic of the supply contributes to torque production. However, there is a possibility to have several multiphase machines connected in series and drive them independently with a single VSI [3]-[4]. When the machine is equipped with a concentrated winding, other, higher harmonics can also be used for torque production. Therefore, a higher amount of torque is producible with a better iron utilisation than with its three-phase counterpart [2].

Three-phase multilevel topologies have been drawing increased attention in the past two decades [5]. The numerous advantages of multilevel supply include [6]: good power quality (low voltage distortion and dv/dt), good electromagnetic compatibility, operation with a lower switching frequency (lower switching losses), high voltage capability, smaller common mode (CM) voltage (reducing the stress in the motor bearings), and the possibility for fault tolerant operation in some, modular configurations. There are various topologies of multilevel converters. The main ones are the neutral point clamped (NPC), the flying capacitor (FC) and the cascaded converters [5]-[6].

Among the cascaded converters, the dual two-level inverter configuration supplying an open-end winding machine has received growing attention due to its simple structure [7]. Typically, three-phase VSIs are utilised. Application of such a dual-inverter supply enables drive operation with voltage waveform equivalent to the one obtainable with a three-level VSI in single-sided supply mode. Three-phase open-end

winding drive systems are currently considered as possible alternative supply solutions in EVs/HEVs [8]-[9], propulsion [10] and rolling mills [11].

Over the years many modulation algorithms have been presented for the three-phase multilevel converter. A general space vector based approach is given in [12] which, with some modifications, can be made applicable to any single-sided three-phase converter topology.

Although combination of a multilevel converter and a multiphase machine appears advantageous, there are relatively few examples of the multiphase multilevel drives [13]-[24]. The focus is on the three-level five-phase NPC drive [13]-[15]. The initial space vector modulation (SVM) methods for multiphase VSIs were based on the simple extension of the three-phase multilevel SVM approaches, so that only the three vectors were utilised. Such an extension from the three-phase to five-phase system, that divides each sector into four equal triangles, is given for three-level inverter in [14]. An optimal SVM switching strategy, based on a discrete particle swarm optimisation (PSO) algorithm, is presented in [13]. In principle, the number of applied vectors must equal the number of phases [3]. Utilisation of three instead of five space vectors during the switching period disregards this basic rule; consequently, only the first plane of the multiphase system is controlled. Hence numerous low-order harmonics are generated, which map into the second plane. Another similar concept, again based on the three-phase principles, is also used in [14].

A SVM method, which controls both planes, has been developed in [15] for the three-level NPC five-phase drive and is extended to the seven-phase case in [16]. Further details of this SVM technique will be presented later on in the paper. A different approach to the SVM of multilevel multiphase system is given for a general case of an m -level, n -phase VSI in [17]. The algorithm is based on the considerations of the multidimensional (n -dimensional) space and therefore does not include decomposition of the n -dimensional space into 2-D planes. A somewhat similar method, in the sense that decomposition into 2-D planes is not utilised, is the one in [18], where a multiphase multilevel PWM is developed using n single-leg modulators.

Initial interest in the multiphase drive systems in open-end winding configuration was limited to an asymmetrical six-phase induction motor drive. In [19] the supply is provided by means of two isolated two-level six-phase VSIs. The goal was, in essence, low-order harmonic reduction rather than the multilevel operation. As a consequence, the converter is not operated in multilevel mode. The scheme considered in [20] employs four three-phase two-level inverters, with four isolated dc sources to prevent circulation of zero sequence currents. The SVM control is performed in the same way as for a standard three-level three-phase converter, using the nearest three vector (NTV) approach in conjunction with three-level NPC inverter. The work is focused towards controlling the power sharing between the four converters. Recently, modulation techniques have been proposed for the five-phase [21]-[23], seven-phase and nine-phase [24] open-end winding topologies. These modulation algorithms will be

discussed in detail in this paper and their performance examined using two experimental set-ups.

II. TWO-LEVEL MULTIPHASE SPACE VECTOR MODULATION

Before considering multilevel multiphase modulation techniques it is beneficial to review the two-level SVM method [25]. This method serves as a benchmark for other modulation methods and it comprises the basic ideas that are used further in the development of other modulation techniques. Similarly to the three-phase inverters, the ones with more phases also consider space vectors to calculate the switching states and their application times.

Common for all n -phase (where n is an odd number) sinusoidal SVM schemes is the need to use $n-1$ active space vectors per switching period. Once when the set of $n-1$ active space vectors is identified and the reference space vector magnitude and position are known, it is necessary to solve an algebraic set of $n-1$ equations, in order to obtain duty cycles of each active space vector. These equations are generated considering positions and magnitudes of the selected active space vectors in all of the $(n-1)/2$ 2-D planes. The aim is to generate the fundamental in the first plane, while zero average value is imposed as the restriction in all the other planes.

Fig. 1 shows the two-level VSI five-phase space vector pattern, which is the same in both of the planes of the topology. Space vectors are labeled with decimal numbers, which, when converted into binary, reveal the values of the switching functions of each of the inverter legs. Active (non-zero) space vectors belong to three groups in accordance with their magnitudes - small, medium and large space vector groups. The magnitudes are identified with indices s , m , and l and are given as $|\underline{v}_s| = 4/5\cos(2\pi/5)V_{dc}$, $|\underline{v}_m| = 2/5V_{dc}$, and $|\underline{v}_l| = 4/5\cos(\pi/5)V_{dc}$, respectively. The switching states that produce large vectors in the α - β plane map into small vectors in the x_1 - y_2 plane and vice-versa. The space vectors clearly divide the plane in ten sectors, each occupying a 36° angle around the origin. The next step in the multiphase SVM is to choose the space vectors to be applied. The aim is to apply the space vectors with the largest magnitudes in the first plane, and the smallest magnitudes in the other plane(s) [25]. The solution for five-phase case is depicted in Fig. 2 with the mapping of the space vectors in the first and the second plane. The projections of the reference signal to the axis of the applied space vectors in both planes enable the derivation of their dwell times according to:

$$t_{bl} = \frac{2 \sin(2\pi/5)}{V_{dc}} \sin[\vartheta - (s-1)\pi/5] |\underline{v}^*| t_s \quad (1)$$

$$t_{bm} = \frac{2 \sin(\pi/5)}{V_{dc}} \sin[\vartheta - (s-1)\pi/5] |\underline{v}^*| t_s$$

$$t_{al} = \frac{2 \sin(2\pi/5)}{V_{dc}} \sin(s\pi/5 - \vartheta) |\underline{v}^*| t_s$$

$$t_{am} = \frac{2 \sin(\pi/5)}{V_{dc}} \sin(s\pi/5 - \vartheta) |\underline{v}^*| t_s \quad (2)$$

where t_s is the switching period, ϑ is the reference position and indices a and b are defined in Fig. 2. Total time of application

of the zero space vector $t_0 = t_s - (t_{a1} + t_{am} + t_{bl} + t_{bm})$ is equally shared between zero space vectors \underline{v}_0 and \underline{v}_{31} . The vectors are then arranged in a switching sequence that is symmetrical and gives equal switching frequency in each inverter leg.

As an example of the performance of this method, an experimental result is presented in Fig. 3. The switching frequency is 2kHz, the modulation index is $M = 1$ and the dc-link voltage is 600V. Inverter dead time is 6μs and the load is a five-phase R-L type. Clearly the algorithm generates practically no low order harmonics with the dominant harmonics positioned around multiples of the switching frequency. Furthermore, the target fundamental frequency (50Hz) and amplitude are met.

III. MULTIPHASE MULTILEVEL TOPOLOGIES

Multiphase machines can be built using two different concepts for the torque production. In the one considered throughout this paper, the winding is wound in such a way that the magneto-motive force distribution can be regarded as near-sinusoidal. As a consequence, the supply is required to provide only fundamental harmonic, without any low-order harmonics in the motor voltage waveform. Thus, the reference phase voltages are sinusoidal.

In the first considered topology three-level NPC VSI is used to supply the machine with, in principle, n -phase stator winding and single isolated neutral point. The topology is

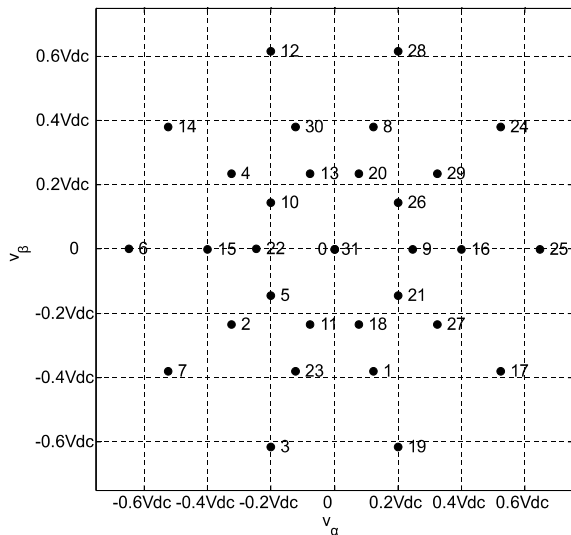


Fig. 1. Two-level five-phase VSI space vector pattern.

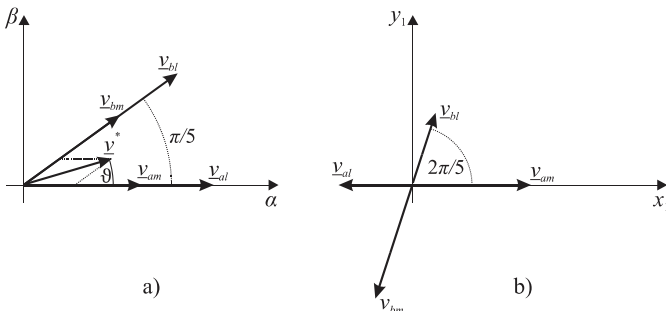


Fig. 2. Reference and applied space vectors in the first sector of the five-phase two-level VSI supply in (a) the first and (b) the second plane.

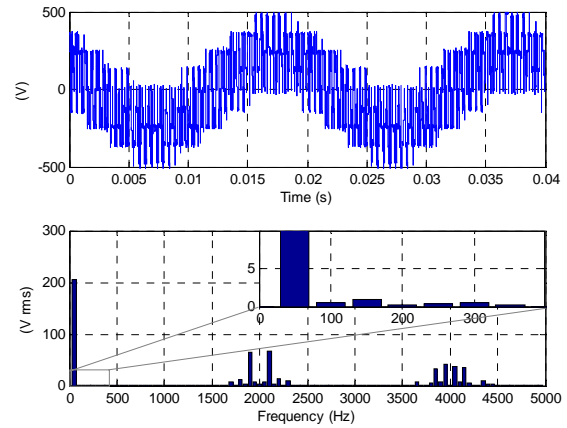


Fig. 3. Experimental result: phase voltage for five-phase two-level SVM with R-L load ($M = 1$).

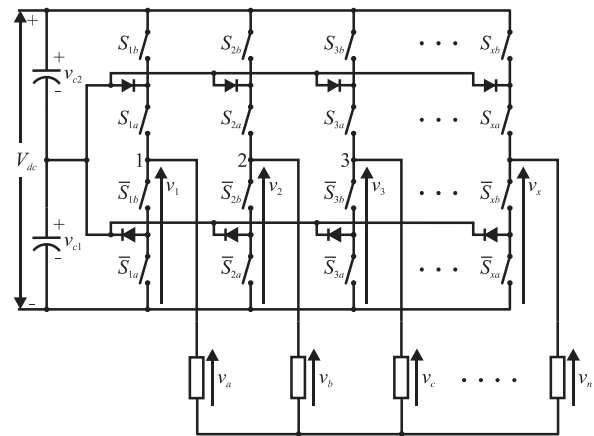


Fig.4. Multiphase (n -phase) three-level NPC inverter supplying a star connected load.

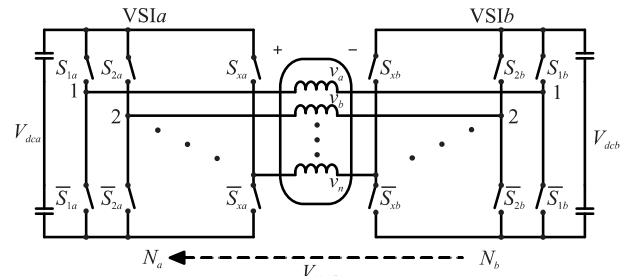


Fig. 5. Open-end winding supply structure.

shown in Fig. 4. This paper considers predominantly five-phase (and, to some extent seven-phase) topology, although the same principles of PWM control can be extended to symmetrical multiphase machines with a composite phase number and machines with an asymmetrical multiphase winding (e.g., two three-phase windings mutually shifted by 30 degrees).

The second discussed topology, with an open-end winding structure and dual-inverter supply, is shown in Fig. 5. Two dc sources are isolated, so that the circulating current does not appear. When the dc sources are of the same voltage, as it is assumed throughout this paper, the supply configuration of Fig. 5 becomes analogous to the three-level inverter supply of Fig. 4 with doubled input dc-link voltage.

The control of multiphase multilevel converters increases in complexity with the increase of phase and level numbers of the topology. To emphasise the complexity of the problem, an illustration of the relationships between numbers of levels m and phases n , in conjunction with the number of inverter switching states and voltage space vectors, is given in Table I for the NPC VSI topology. It can be seen from Table I that an increase in the number of phases dramatically increases the number of switching states, the number of space vectors and the number of redundant switching states (the difference between the total numbers of switching states and space vectors).

Table II shows the number of space vectors and switching states for the open-end topology for odd phase numbers. It is considered, for the sake of simplicity, that the open-end topology comprises two inverters with m levels each. The increase in the space vector and switching state number is far more evident in the open-end topology, for the given phase number and the number of levels, when compared to the single-sided supply (Table I). Simultaneous increase of both leads to practically exponential rise in the number of switching states and voltage space vectors.

Comparison of Table I and Table II shows that the number of switching states in the open-end winding topology, when two-level inverters are applied at both sides, coincides with the number of switching states of the four-level single-sided inverter. On the other hand, the number of space vectors equals the number obtained with the three-level inverter. This can be explained using Table III (discussed later), which shows that, although there are four possible switching states to apply, the two-level open-end supply gives inverter states equivalent to the three-level inverter. The same can be observed in conjunction with the three-level open-end topology and the nine- and five-level single-sided inverters.

Distribution of the phase voltage space vectors in the α - β plane is depicted in Figs. 6 and 7 for the five-phase and seven-phase three-level topologies, respectively. It is evident that designing a suitable modulation method represents a significant challenge.

IV. SINGLE-SIDED MULTILEVEL MULTIPHASE MODULATION TECHNIQUES

In what follows the modulation techniques, suitable for multiphase three-level converters, will be discussed and their performances analysed using an experimental set-up illustrated in Fig. 8. The level-shifted phase-disposition PWM (PD-PWM) method will be reviewed since it has been proven to produce the best results in terms of voltage THD. A space vector modulation, introduced in [15], will be discussed next.

A. Carrier-Based Modulation

Fig. 9 shows three carrier-based PWM techniques, as utilised in the single-sided supply mode in conjunction with three-level VSIs. The phase-shifted PWM (PS-PWM) and the level-shifted PWM (LS-PWM) have appeared as a natural extension of the traditional carrier-based PWM for two-level inverters. The PS-PWM is well suited for the FC multilevel

TABLE I
NUMBER OF SWITCHING STATES AND VOLTAGE SPACE VECTORS (IN BRACKETS) IN SINGLE-SIDED CONFIGURATION

m/n	3	5	7	9
2	8 (7)	32 (31)	128 (127)	512 (511)
3	27 (19)	243 (211)	2,187 (2,059)	19,683 (19,171)
4	64 (37)	1024 (781)	16384 (14,197)	262,144 (242,461)
5	125 (61)	3,125 (2,101)	78,125 (61,741)	1,953,125 (1,690,981)
9	729 (217)	59,049 (26,281)	4,782,969 (2,685,817)	$\sim 3.9e+8$ ($\sim 2.5e+8$)

TABLE II
NUMBER OF SWITCHING STATES AND VOLTAGE SPACE VECTORS (IN BRACKETS) IN OPEN-END WINDING CONFIGURATION

m/n	3	5	7	9
2	64 (19)	1024 (211)	16,384 (2059)	262,144 (19,171)
3	729 (61)	59,049 (2101)	4,782,969 (61,741)	$\sim 3.9e+8$ (1,690,981)
4	4096 (127)	1,048,576 (9031)	$\sim 2.7e+8$ (543,607)	$\sim 6.9e+10$ ($\sim 3.0e+7$)
5	15,625 (217)	9,765,625 (26,281)	$\sim 6.1e+9$ (2,685,817)	$\sim 3.8e+12$ ($\sim 2.5e+8$)

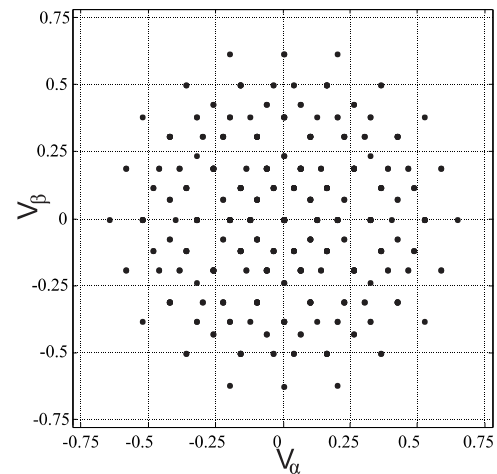


Fig. 6. Five-phase three-level VSI space vector distribution in the α - β plane.

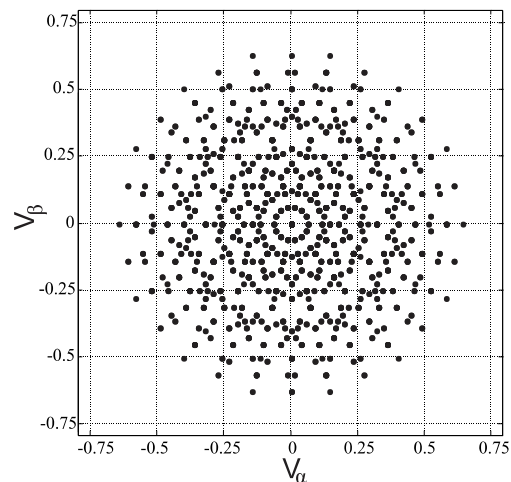


Fig. 7. Seven-phase three-level VSI space vector distribution in the α - β plane.

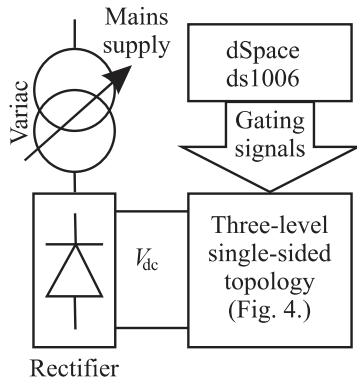


Fig. 8. Single-sided three-level VSI experimental set-up.

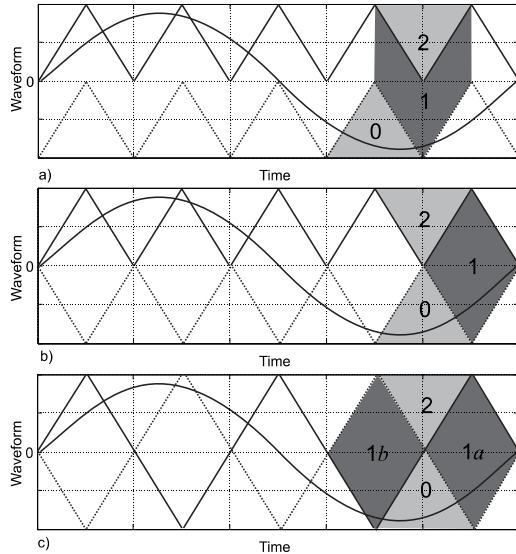


Fig. 9. Carrier and modulating signals for: a) PD-PWM, b) APOD-PWM and c) PS-PWM modulation methods.

topology because of its natural capacitor voltage balancing property. In the PS-PWM a phase shift is introduced between the carrier signals of the cells belonging to the same inverter leg, causing them to switch at different instants. A stepped multilevel waveform is created in this way [26]. The three-level structure consists of two such cells. The lowest THD is achieved when the carriers are in anti-phase. Since all the cells are effectively controlled with the same carrier that is altered only in terms of phase, i.e. the carriers occupy the same vertical position (Fig. 9c), the switch utilisation and the average power handled are evenly distributed among the cells at all times [26]. When applied to the FC topology, the capacitors are charged at the start-up. Because of the even power distribution, there will be no further unbalance produced [27]. With a topology with k cells, the output phase voltage has a switching pattern with k times the frequency of the pattern of each cell. Thus, the first higher frequency harmonics will appear at the frequencies around k (here the value is $k = 2$) times the carrier frequency [26].

Level-shifted PWM is also a natural extension of bipolar PWM. The use of a carrier signal comparison with the reference decides between the upper and lower voltage levels, which are the positive and negative dc-link rails in the case of

a two-level VSI. For a multilevel inverter, there are $(m-1)$ carriers, where m is the number of voltage levels. They are now vertically shifted rather than phase-shifted (Figs. 9a and 9b). Since each carrier determines a border between two voltage levels, the notion of ‘level-shifted’ is used. The control signals have to be sent to the appropriate switches in order to generate gating signals that correspond to the desired voltage levels and this depends on the actual inverter topology that is used.

There are several forms of the LS-PWM method. When all carriers are in phase with each other, the method is called phase disposition (PD-PWM, Fig. 9a). when all the positive carriers are in phase with each other and in phase opposition with the negative carriers, the method is known as phase opposition disposition (POD-PWM). Finally, the alternate phase opposition disposition method (APOD-PWM) is obtained by having opposite phase for each two adjacent carriers [28]. In the three-level case, POD-PWM and APOD-PWM are identical, Fig. 9b. Because of the very good characteristics and its dominance in industrial applications, PD-PWM is the method that is normally denoted as the LS-PWM in literature. LS-PWM leads to less distorted voltages, compared to PS-PWM. However, PD-PWM cannot achieve capacitor voltage balancing in the FC inverters and therefore it has to be applied to NPC inverters.

Experimental results for described five-phase PD-PWM three-level algorithm (with offset injection) are shown in Fig. 10. The data are: modulation index $M = 1$, fundamental frequency $f = 50\text{Hz}$, dc-link voltage $V_{dc} = 600\text{V}$, switching frequency $f_s = 2\text{kHz}$, and inverter dead-time $6\mu\text{s}$. Comparison with Fig. 3 shows that multilevel operation is obtained. The zero space vector is not applied in each switching period, which enables closer approximation of the reference by the applied space vectors. The number of phase voltage levels is difficult to determine from the figure but is verified as 15.

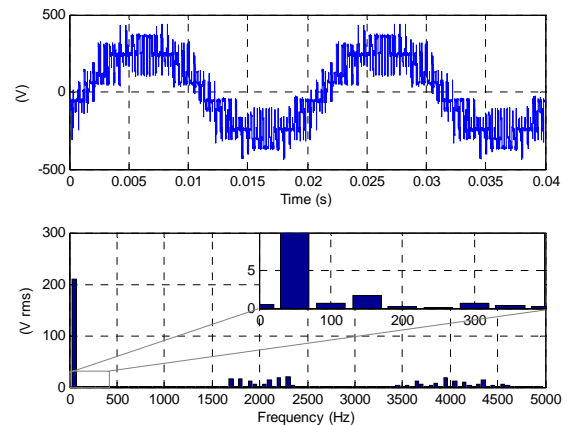


Fig. 10. Experimental result: PD-PWM carrier-based five-phase three-level case with $R-L$ load ($M = 1$).

B. Space Vector Approach

This sub-section reviews the only known SVM algorithm suitable for five-phase single-sided three-level NPC drives [15], which considers simultaneously both planes. Extension

of this algorithm to seven-phase three-level system is given in [16]. The algorithm requires a significant number of offline calculations that makes generalisation difficult. However, the final modulator structure is quite easy to implement.

The main concepts of the algorithm are briefly reviewed here. As with all space vector methods the starting point is vector space decomposition (VSD). Sinusoidal output is desired so that the reference projection into the α - β plane is circular, while projection into other planes is zero. Number of space vector projections in each plane is large (see Table I) but some of them can be omitted from further analysis. One simple rule for reduction of the number of switching states of interest is introduced in [15] and is termed the order-per-sector law [16]. Namely, the order of leg voltages must be the same as the order of the reference phase voltages in every instant of time. The order of the reference phase voltages is constant for each sector. For example, in five-phase case, order of the reference phase voltages in the first sector is $v_a^* \geq v_b^* \geq v_e^* \geq v_c^* \geq v_d^*$. The projection of the switching state 22011 belongs to the first sector in the α - β plane but it does not follow the reference order since output leg voltage v_3 is lower than v_4 ($0 < 1$). Thus, according to the order-per-sector law, this switching state can be omitted from the further analysis. The number of switching states of interest in five-phase three-level case is reduced in this way from 243 to 113, while reduction in seven-phase three-level case is from 2187 to 297.

For determination of the switching sequences one method with graphical interpretation is introduced in [16]. The one-level transition in the I^{th} leg maps into a $2/n$ scaled unit vector inclined for $(I-1) \cdot 2\pi/n$ radians with respect to α -axis. For instance, all transitions in the first sector between space vector projections after the order-per-sector law application, for five-phase three-level case, are shown in Fig. 11. Transitions in different legs are shown in different colours. Since during the switching period a transition appears in each leg, it is enough to find all closed n -angle contours (patterns) that contain each colour shown in Fig. 11. One such n -angle contour is highlighted in Fig. 11. The process of switching sequence determination is not finished at this stage, since sequence of the highlighted five transitions can start from three different switching states (10000, 11000 and 11001). In five-phase three-level case the number of patterns is 16 and there are 32 corresponding redundant switching sequences. In seven-phase three-level case these values are 64 and 128, respectively.

The space vector dwell times are calculated by solving a matrix similar to equations (1) and (2). Application of the simple rule [15], that dwell time of each switching state must be in the range from 0 to t_s , enables identification of region where the switching pattern can be applied. In other words, a number of sub-sectors are determined within each sector. In the five-phase case only 10 patterns are considered since the other six patterns have projections in x_1 - y_1 plane that cannot be cancelled in a manner similar to that shown in Fig. 2b. In seven-phase case one more non-flux/torque producing plane is present, so the situation is more difficult. There are patterns

that provide cancellation in one plane only, and patterns that provide cancellation in both planes but the dwell-time solution does not coincide. Therefore, the method of graphical elimination of some patterns is not enough, and the dwell time determination matrix has to be solved. For that purpose numerical calculations were used in [16]. After elimination of the unusable patterns, one gets that in seven-phase three-level case there are 18 patterns that divide the first sector into 18 sub-sectors. In both the five- and seven-phase case, final switching sequence per pattern is chosen by optimisation, which is simply based on the minimisation of the transitions when the reference changes sub-sector. It is preferable that all switching sequences have the same starting switching state, if it is possible. Another rule for final sequence determination is related to the inverter topology. For the best capacitor voltage balancing, those switching sequences with the maximum number of 'ones' (state when the output is determined by the mid-point of the inverter) are desirable.

To determine the sub-sector in which the reference lies, it is enough to calculate the projection of the reference to a few specified axes. These axes are determined by the borders between sub-sectors. In both five-phase and seven-phase three-level cases there are five different directions of the borders, so five projection axes are used in both cases. Comparing projections of the reference to these axes with the projection of the sub-sector borders, simple rules for sub-sector determination can be obtained.

Despite the complicated nature of the algorithm the final modulator realisation is quite straightforward, with many of the calculations performed off-line. For each sub-sector switching sequence is stored in memory. Also, dwell times calculation that requires inversion of the matrices can be calculated in advance for each switching sequence and stored in memory.

Experimental results for described five-phase three-level SVM algorithm are shown in Fig. 12. The data are: modulation index value $M = 1$, fundamental frequency $f = 50\text{Hz}$, dc-link voltage $V_{dc} = 600\text{V}$, and switching frequency $f_s = 2\text{kHz}$. Dead-time of the inverter is $6\mu\text{s}$.

The strong resemblance of the phase voltage waveform, obtained using the described SVM and carrier-based PD-

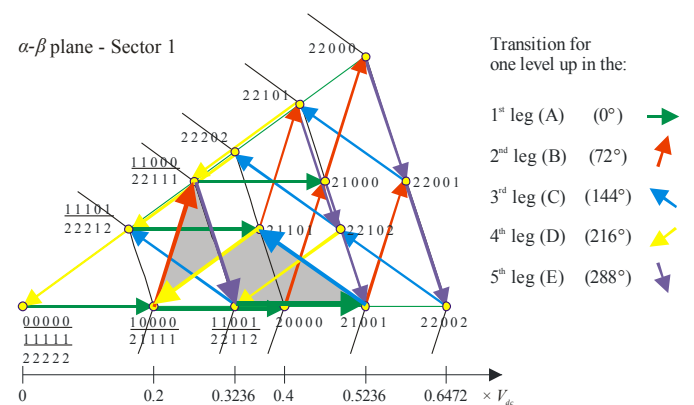


Fig. 11: All switching state transitions in the first sector after application of order-per-sector law ($n = 5$, $m = 3$).

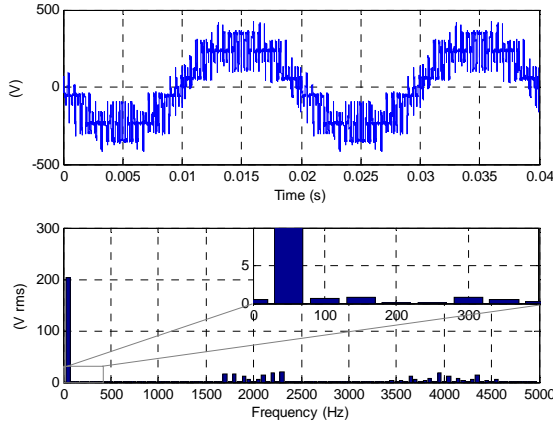


Fig. 12. Experimental result: five-phase three-level SVM with R - L load ($M=1$).

PWM methods, is evident from Figs. 10 and 12. An additional comparison, related to the phase voltage THD, is given in section 6. However, differences between the algorithms are present in the leg voltages and the CM voltage.

V. OPEN-END WINDING MULTILEVEL MULTIPHASE MODULATION TECHNIQUES

A different approach to achieve a multilevel supply is to connect two separate inverters to the ends of the stator windings, as shown in Fig. 5. There are additional benefits gained from this topology, compared to the multilevel multiphase ones. An additional degree of fault tolerance is available since the supply is realised with two independent inverters. In case one of them is faulted, the other can continue to provide power to the machine [29]. The same phase voltages can be achieved with half the dc-link voltages on the two inverter inputs compared to the single-sided supply, which can be useful in applications such as electric and hybrid electric vehicles and medium sized ships, where the dc voltage levels are limited. These applications are able to generate isolated power supplies from two sets of batteries or generators. Further, due to the construction of the topology, it can be noticed that the structure does not require additional diodes and capacitors like the NPC and FC topologies. The latter results in a further advantage: the absence of need for capacitor balancing techniques.

The easiest way to understand how the open-end topology achieves three-level operation is to compare the switching states to those of the FC converter as described in Table III. The notation for the switches for the FC topology is such that states of the upper-most and the second upper-most switch are identified with indices a and b , respectively. The notation of the switches of the open-end topology corresponds to Fig. 5, with indices a and b denoting the left and the right inverter. It can be seen that the difference between the two sets of gating signals is that those for the switches S_{xb} (x = leg number) are inverted in the open-end topology, compared to the FC. As a consequence of the topology, the load voltages are governed by the difference of voltages applied by the two inverters. In what follows three different modulation approaches will be

TABLE III
INVERTER STATES AND RELATED GATING SIGNALS

Switching function	FC VSI gating signals	Dual-inverter gating signals
2	$S_{xa}=1, S_{xb}=1$	$S_{xa}=1, S_{xb}=0$
1	1a $S_{xa}=1, S_{xb}=0$	$S_{xa}=1, S_{xb}=1$
	1b $S_{xa}=0, S_{xb}=1$	$S_{xa}=0, S_{xb}=0$
0	$S_{xa}=0, S_{xb}=0$	$S_{xa}=0, S_{xb}=1$

examined using the five-phase experimental set-up shown in Fig. A1. The equivalent total dc-link voltage is 600V, meaning 300V per inverter.

A. Space Vector Approach – URS Modulation

Due to the large number of switching states and space vectors generated by the open-end winding topology, it is prudent to try to reduce the complexity of the problem by considering the modulation in terms of two independent two-level modulators. Therefore, the two-level space vector modulation, described in section 2, can be applied to the two inverters separately.

To accommodate the fact that the inverters are located at opposite sides of the stator windings, the references applied to them are in counter-phase. This method is termed unequal reference sharing (URS) modulation since the voltage reference applied to the modulators is apportioned according to the modulation index M [21]. Initially, only $VSIa$ is operated up to its maximum modulation index ($M_1 = M_{\max} = 1.0515$ for five-phase topology), while $VSIb$ is kept in zero state. Hence the converter operates in two-level mode, since $VSIb$ output is zero (it is kept in a zero state at all times). When $M > M_{\max}/2$, $VSIa$ is held at $M_1 = M_{\max}$ and $VSIb$ output is modulated as well. The constraints of the modulation index sharing can be expressed as:

$$0 \leq M \leq M_{\max} / 2 \quad \begin{cases} M_1 = 2M \\ M_2 = 0 \end{cases} \quad (3)$$

$$M_{\max} / 2 \leq M \leq M_{\max} \quad \begin{cases} M_1 = M_{\max} \\ M_2 = 2M - M_{\max} \end{cases}$$

At lower modulation indices the second inverter is clamped to a zero vector, while the first inverter works in classical two-level modulation. Since it switches half the dc-link voltage of an equivalent single-sided two-level inverter, it is expected to give superior THD performance. In the upper modulation region the open-end topology works in multilevel mode and thus it gives better performance than the single two-level inverter.

An example of the obtained experimental results is presented in Fig. 13 where $M = 1$ and switching frequency is 1kHz. It is clear that, despite the low switching frequency, there are no low order harmonics and the target fundamental has been met.

B. SVM Approach – Decomposition Method

The complexity of selecting the proper switching states for a given command voltage can be significantly reduced if the three-level space vector decagon is decomposed into a number

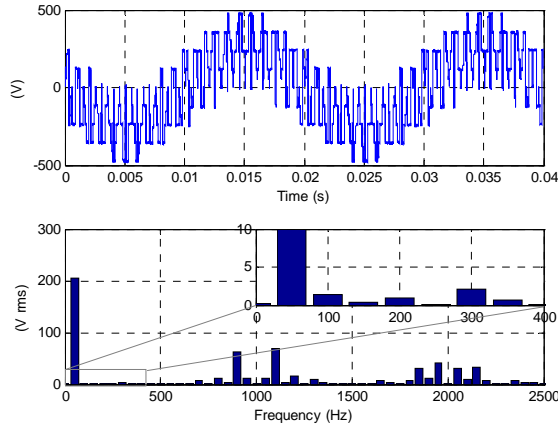


Fig. 13. Experimental result: five-phase SVM, URS method with pure R load ($M = 1$).

of two-level decagons, as illustrated in Fig. 14. The centre decagon comprises vectors which can be activated if one inverter is used up to half of the achievable maximum voltage with the other one in zero state. As a consequence, the converter is in two-level mode of operation based on four active and zero vector application, as discussed in section 2. The origins of the outer decagons are located on the outer vectors of the inner decagon, denoted by the larger dots in Fig. 14, which correspond to the outermost vectors and switching states given in Fig. 1. However, once when the magnitude of the reference voltage exceeds the maximum value obtainable with one inverter, one inverter is operated in ten-step mode while the second inverter is space vector modulated [22].

It is well known that operation of a five-phase inverter in ten-step mode without a controllable dc-link leads to uncontrollable, constant fundamental output voltage magnitude and unwanted low order harmonics. This leads to the requirement that the second inverter must be able to not only control the fundamental but also eliminate the unwanted low order harmonics, which are produced by applying only the large vector in α - β plane from the first inverter. This causes unwanted harmonics in both planes since a large vector has a corresponding non-zero value in the second, x_1 - y_1 plane. In order to achieve this objective, the second inverter modulation scheme will need to operate in both the α - β and the x_1 - y_1 planes, since references for the second inverter can be given as:

$$\begin{aligned} \underline{v}_\alpha^{**} &= -(\underline{v}_\alpha^* - \underline{v}_{i(\alpha)}) & \underline{v}_\beta^{**} &= -(\underline{v}_\beta^* - \underline{v}_{i(\beta)}) \\ \underline{v}_x^{**} &= \underline{v}_{i(x_1)} & \underline{v}_y^{**} &= \underline{v}_{i(y_1)} \end{aligned} \quad (4)$$

Here $i = 1 \dots 10$ stands for the large vector of the first VSI. A space vector modulator, which achieves simultaneous control in both the α - β and x_1 - y_1 planes, was developed in [30] in order to control multiphase multi-motor drive systems. A schematic illustration of the SVM process is shown in Fig. 15. This SVM method utilises two two-level five-phase space vector modulators, as discussed previously. Each SVM operates in a separate plane.

Fig. 16 shows the performance of the method when $M = 1$ and $f_s = 2\text{kHz}$. It is clear that a multilevel output is achieved

and that the scheme is able to completely compensate unwanted low order harmonics created by the ten-step operation of one inverter.

C. Carrier-Based Approach – PD-PWM

The carrier-based methods described in sub-section 4.1 are all applicable to the open-end winding topology. The gating signals for the two inverters are easily obtainable by associating each of the carrier signals to one inverter. Due to the differences in the inverter switching functions and their

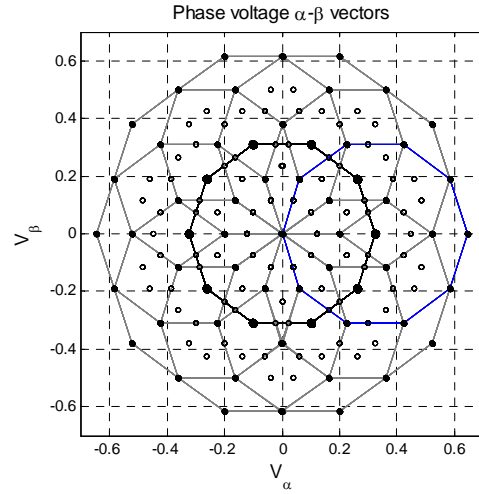


Fig. 14. Decomposed SVM method: space vector distribution in the α - β plane.

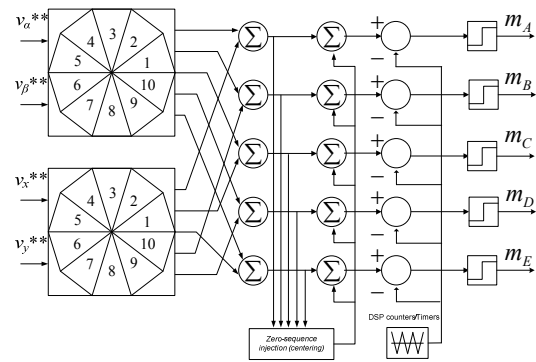


Fig. 15. Signal flow of the five-phase multi-frequency space vector modulator.

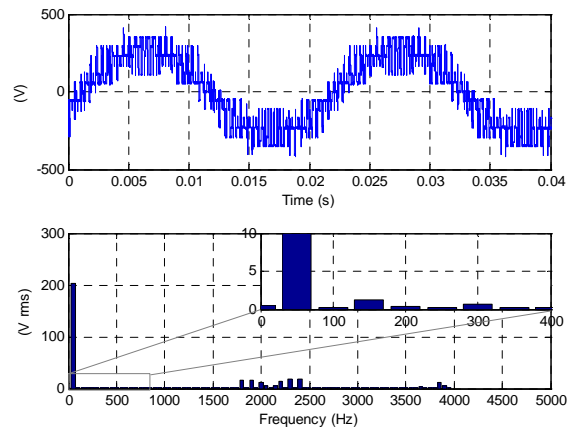


Fig. 16. Experimental result: five-phase SVM, decomposition method with R - L load ($M = 1$).

associated gating signals (Table III), one of the gating signals has to be inverted. As it was already stated, the PD-PWM gives the best results in terms of voltage THD, but it cannot be applied to the FC topology due to capacitor balancing issues. However, since there are no capacitor voltages to balance in the open-end topology, there is no restriction towards the implementation of this method.

The experimental results in Fig. 17 are obtained by applying the carrier-based PD-PWM method to the open-end winding machine. The two isolated dc-bus voltages are set to 300V. The modulation index is set to $M = 1$ and switching frequency is 2kHz. The resulting phase-voltage waveform and its harmonic spectrum are similar to the ones obtained in the previous section with the single-sided three-level inverter. These results validate the theoretical consideration that the open-end topology can work as a three-level inverter although it comprises two, more common, two-level inverters.

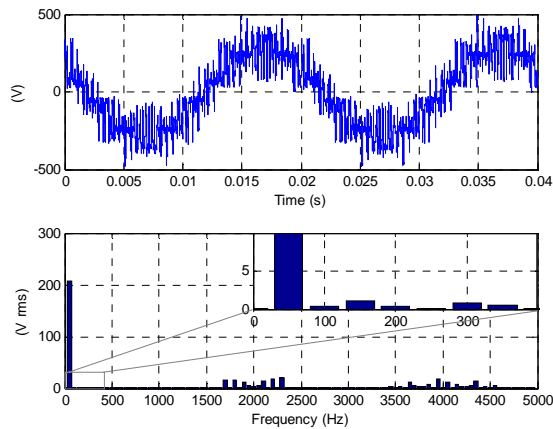


Fig. 17. Experimental result: five-phase PD-PWM method with R - L load ($M = 1$).

VI. COMPARISON OF SIMULATION AND EXPERIMENTAL RESULTS

Experimental results have been used throughout this paper to support the theory. Extensive simulation studies have, however, been also conducted and there is a very good agreement between the results obtained experimentally and via simulation. Therefore the simulation results of Fig. 18 enable a THD performance comparison between the modulation methods, investigated in the paper. As expected, the two-level VSI modulation has shown the worst performance of all the methods considered. The three-level PD-PWM and the method introduced in [15] have identical voltage THD throughout the modulation index range (the difference between them can be noticed only in the leg and CM-voltage waveforms). The URS method, developed for the open-end winding machines, has the superior performance in the low modulation region, which is the same as with the PD-PWM. However, in the upper modulation region it gradually approaches the performance of the two-level modulation. This drawback is however counter-balanced by the power-sharing capability of this method, which is important in certain applications.

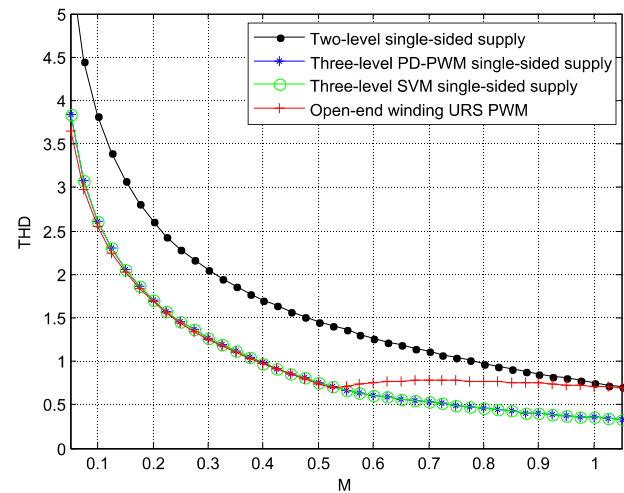


Fig. 18. Voltage THD comparison across the modulation range for a five-phase system.

VII. CONCLUSION

The combined advantages offered, by multiphase and multilevel topologies, make them an attractive proposition for high power and fault tolerant applications. However, the control of these topologies represents a considerable challenge due to the exponential increase in the number of switching states and large number of active space vectors. This paper has presented a review of some of the recently published solutions to the modulation of multiphase multilevel converters for both carrier-based modulation and SVM methods. The performance of these techniques has been examined using experimental rigs, with the THD comparison obtained by means of simulations.

REFERENCES

- [1] D. G. Holmes, "The general relationship between regular-sampled pulse-width-modulation and space vector modulation for hard switched converters," in *Proc. IEEE Industry Applications Society Annual Meeting IAS*, Houston, TX, pp. 1002-1009, 1992.
- [2] E. Levi, "Multiphase electric machines for variable-speed applications," *IEEE Transactions on Ind. Electronics*, vol. 55, no. 5, pp. 1893-1909, 2008.
- [3] E. Levi, R. Bojoi, F. Profumo, H. A. Toliyat, and S. Williamson, "Multiphase induction motor drives - A technology status review," *IET Electric Power Applications*, vol. 1, no. 4, pp. 489-516, 2007.
- [4] S. Gataric, "A polyphase cartesian vector approach to control of polyphase AC machines," in *Proc. IEEE Industry Applications Society Annual Meeting IAS*, Rome, Italy, pp. 1648-1654, 2000.
- [5] S. Kouro, M. Malinowski, K. Gopakumar, G. Franquelo, J. Pou, J. Rodriguez, B. Wu, and A. Perez, "Recent advances and industrial applications of multilevel converters," *IEEE Transactions on Industrial Electronics*, vol. 57, no. 8, pp. 2553-2580, 2010.
- [6] J. Rodriguez, S. Bernet, B. Wu, J. O. Pontt, and S. Kouro, "Multilevel voltage-source-converter topologies for industrial medium-voltage drives," *IEEE Transactions on Industrial Electronics*, vol. 54, no. 6, pp. 2930-2945, 2007.
- [7] K. A. Corzine, S. D. Sudhoff, and C. A. Whitcomb, "Performance characteristics of a cascaded two-level converter," *IEEE Transactions on Energy Conversion*, vol. 14, no. 3, pp. 433-439, 1999.
- [8] B. A. Welchko and J. M. Nagashima, "A comparative evaluation of motor drive topologies for low-voltage, high-power EV/HEV propulsion systems," in *Proc. IEEE Int. Symp. on Ind. Elec. ISIE*, Rio de Janeiro, Brazil, pp. 379-384, 2003.
- [9] C. Rossi, G. Grandi, P. Corbelli, and D. Casadei, "Generation system for series hybrid powertrain based on dual two-level inverter," in *Proc. Eur.*

- Power Elec. and Appl. Conf. EPE*, Barcelona, Spain, CD-ROM paper 0978, 2009.
- [10] G. Grandi, C. Rossi, A. Lega, and D. Casadei, "Multilevel operation of a dual two-level inverter with power balancing capability," in *Proc. IEEE Industry Applications Society Annual Meeting IAS*, Tampa, FL, pp. 603-610, 2006.
- [11] Y. Kawabata, M. Nasu, T. Nomoto, E. C. Ejiogu and T. Kawabata, "High-efficiency and low acoustic noise drive system using open-winding AC motor and two space-vector-modulated inverters," *IEEE Transactions on Industrial Electronics*, vol. 49, no. 4, pp. 783-789, 2002.
- [12] N. Celanovic and D. Boroyevich, "A fast space-vector modulation algorithm for multilevel three-phase converters," *IEEE Transactions on Industry Applications*, vol. 37, no. 2, pp. 637-641, 2001.
- [13] C. M. Hutson, G. K. Venayagamoorthy, and K. A. Corzine, "Optimal SVM switching for a multilevel multi-phase machine using modified discrete PSO," in *Proc. IEEE Swarm Intelligence Symposium*, St. Louis, MO, CD-ROM, 2008.
- [14] Q. Song, X. Zhang, F. Yu, and C. Zhang, "Research on PWM techniques of five-phase three-level inverter," in *Proc. Int. Symp. on Power Elec., Electrical Drives, Automation and Motion SPEEDAM*, Taormina, Italy, pp. 561-565, 2006.
- [15] L. Gao and J. Fletcher, "A space vector switching strategy for three-level five-phase inverter drives," *IEEE Transactions on Industrial Electronics*, vol. 57, no. 7, pp. 2332-2343, 2010.
- [16] O. Dordevic, M. Jones, and E. Levi, "A space-vector PWM algorithm for a three-level seven-phase voltage source inverter," in *Proc. Eur. Power Elec. and Appl. Conf. EPE*, Birmingham, UK, CD-ROM paper 0123, 2011.
- [17] O. Lopez, J. Alvarez, J. Doval-Gandoy, and F. D. Freijeiro, "Multilevel multiphase space vector PWM algorithm with switching state redundancy," *IEEE Transactions on Industrial Electronics*, vol. 56, no. 3, pp. 792-804, 2009.
- [18] J. I. Leon, S. Vaquez, J. A. Sanchez, R. Portillo, L. G. Franquelo, J. M. Carrasco, and E. Dominguez, "Conventional space-vector modulation techniques versus the single-phase modulator for multilevel converters," *IEEE Transactions on Industrial Electronics*, vol. 57, no. 7, pp. 2473-2482, 2010.
- [19] K. K. Mohapatra and K. Gopakumar, "A novel split phase induction motor drive without harmonic filters and with linear voltage control for the full modulation range," *EPE Journal*, vol. 16, no. 4, pp. 20-28, 2006.
- [20] G. Grandi, A. Tani, P. Sanjeevikumar, and D. Ostojsic, "Multi-phase multi-level AC motor drive based on four three-phase two-level inverters," in *Proc. Int. Symp. on Power Elec., Electrical Drives, Automation and Motion SPEEDAM*, Pisa, Italy, pp. 1768-1775, 2010.
- [21] M. Jones, W. Satiawan, and E. Levi, "A five-phase multilevel space-vector PWM algorithm for a dual-inverter supplied drive," in *Proc. IEEE Industrial Electronics Society Annual Meeting IECON*, Glendale, AZ, pp. 2461-2466, 2010.
- [22] M. Jones, W. Satiawan, and E. Levi, "A three-level five-phase space-vector modulation algorithm based on the decomposition principle," in *Proc. IEEE Int. Elec. Machines and Drives Conf. IEMDC*, Niagara Falls, Canada, pp. 1235-1240, 2011.
- [23] N. Bodo, E. Levi, and M. Jones, "Carrier based modulation techniques for five-phase open-end winding topology," in *Proc. IEEE Industrial Electronics Society Annual Meeting IECON*, Melbourne, Australia, 2011.
- [24] N. Bodo, M. Jones, and E. Levi, "A PWM method for seven and nine phase open-end winding drives," in *Proc. Int. Conf. on Modelling and Simulation of Elec. Mach., Converters and Systems ELECTRMacs*, Paris, France, CD-ROM paper 0038, 2011.
- [25] D. Dujic, M. Jones, and E. Levi, "Generalized space vector PWM for sinusoidal output voltage generation with multiphase voltage source inverters," *Int. J. Ind. Elec. and Drives*, vol. 1, no. 1, pp. 1-13, 2009.
- [26] J. Rodriguez, L. G. Franquelo, S. Kouro, J. I. Leon, R. C. Portillo, M. A. M. Prats, and M. A. Perez, "Multilevel converters: An enabling technology for high-power applications," *Proceedings of the IEEE*, vol. 97, no. 11, pp. 1786-1817, 2009.
- [27] R. H. Wilkinson, T. A. Meynard, and H. du Toit Mouton, "Natural balance of multicell converters: The general case," *IEEE Transactions on Power Electronics*, vol. 21, no. 6, pp. 1658-1666, 2006.
- [28] G. Carrara, S. Gardella, M. Marchesoni, R. Salutari, and G. Sciutto, "A new multilevel PWM method: A theoretical analysis," *IEEE Transactions on Power Electronics*, vol. 7, no. 3, pp. 497-505, 1992.
- [29] E. C. de Santos and M. Pacas, "Fault-tolerant open-end winding motor drive systems," in *Proc. IEEE Industrial Electronics Society Annual Meeting IECON*, Melbourne, Australia, 2011.
- [30] D. Dujic, G. Grandi, M. Jones, and E. Levi, "A space vector PWM scheme for multi-frequency output voltage generation with multiphase voltage-source inverters," *IEEE Transactions on Industrial Electronics*, vol. 55, pp. 1943-1955, 2008.

APPENDIX

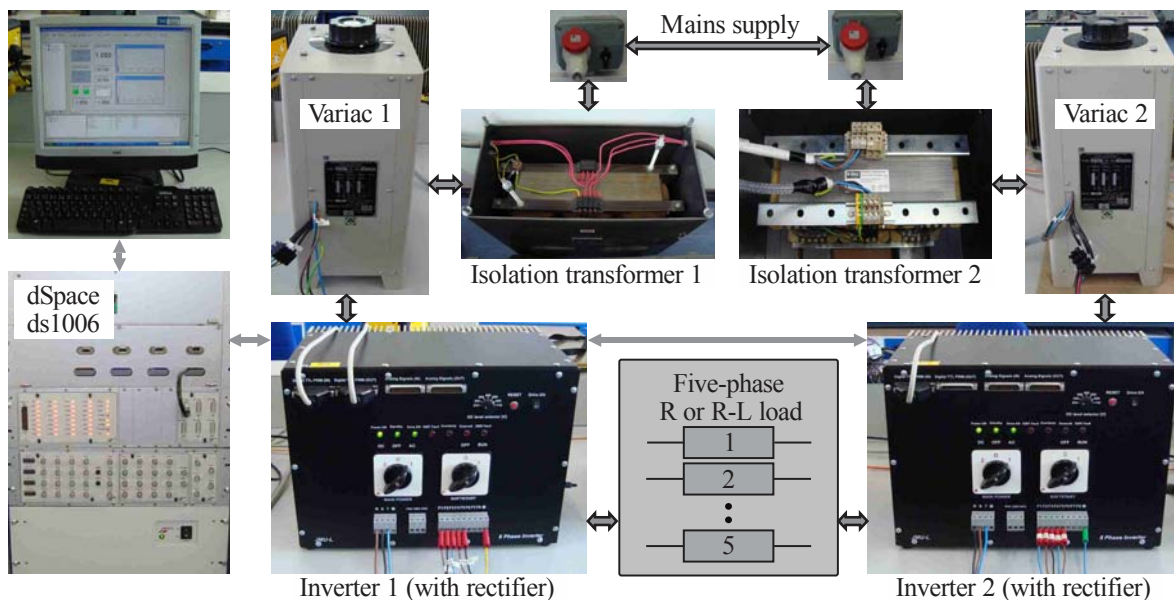


Fig. A1. Experimental set-up for the open-end winding configuration.

Some Examples that Use the FEM in PM Generators Analysis

Marian Greconici

Abstract—The present paper refers to some examples that use the finite element method (FEM) in the process of analysis, design and optimization of the permanent magnet (PM) generators used in wind applications. The 2D-FEM program Opera 13 of Vector Fields is used in the analyzed examples. These examples refer to two types of radial flux low speed PM generators of 5 KW for wind applications. Some possibilities of electrical machine optimization, using the FEM-programming packages available today, are pointed out during the present paper.

Index Terms—PM generator, finite element method, optimization, wind applications.

I. INTRODUCTION

In the last forty years, ongoing and fast developments of numerical techniques for the particular questions concerning electrical machines can be noticed. This development can be seen in parallel with the efforts and success of the software and hardware computer industry in producing powerful tools. Computers as well as commercial software are now ready to be applied to solve realistic numerical models of technical relevance. Of course, there are enough complicated problems and questions, which are not yet answered to a satisfactory extended.

At the time, when not too many computers were available yet, the design of electrical machines was performed in the classical way, by using one-dimensional model (1D). Particular electromagnetic parts of the machine are considered to form a homogenous element in a magnetic circuit approach. In this approach the knowledge of particular “design” factors is assumed. Such models enabled the calculation of specific stationary working point of the machine. Laplace transformations applied to such models made it possible to analyze the machine for dynamic operations. The refinements of 1D models yield the technique of magnetic equivalent circuit models.

A very rough figure can be drawn in saying that the development of numerical methods for electrical machines started with the finite difference method (FDM) which quickly was followed and further overtaken from the finite element method (FEM).

With the first numerical models of electrical machines, in the 70s, electromagnetic fields considering imposed current sources could be simulated by applying first order triangular elements. Further developments of the finite element method lead via the definition of external circuits to problem formulations with imposed voltage sources, which were more accurate models with respect to the realistic machine that is operated by a voltage. Today’s developments are directed to all aspects of coupled fields. There are the thermal/magnetic problems or structure dynamic field problems coupled to the electromagnetic field.

Parallel with the developments of the finite element method first attempts to numerically optimize the finite element models were made. Optimizations of realistic machine models were first performed in the late 80s and early 90s.

However, research directed to accelerate the numerical solver is going on as well. Extension of the overall machine models can be made by applying more realistic material models. Hysteresis effects and material anisotropy are still a lack in many software packages. Special winding models allow reducing the size of a numerical model significantly and therefore the computation time as well. To avoid long lasting transient simulations single-phase machines can be modeled by a time-harmonic approach by modeling separate rotor models for the rotary fields in reverse respectively rotation direction of the rotor.

However, with the developments of numerical techniques around the electrical machine analysis, it must be noticed that the classical approach cannot be replaced by the numerical models. Enormous expertise and knowledge to model the various electromagnetic effects appropriate and accurately are still required. The modeling/solving/post-processing of numerical motor models still requires substantial engineering time and cannot replace the quick and correct answer of an exercised motor design engineer. Both experts, probably in one person, numerical modeling and electromagnetic motor design engineer, are required for successful and novel developments in the engineering discipline.

Manuscript received 30 May 2012. Accepted for publication 10 June 2012. Some results of this paper were presented at the 16th International Symposium Power Electronics, Novi Sad, Serbia, October 26-28, 2012.

M. Greconici is with the Faculty of Electrical Engineering, POLITEHNICA University of Timisoara, Timisoara, Romania (corresponding author to provide phone: +40-722-690328; fax: +40-256-403392; e-mail: marian.greconici@et.upt.ro).

II. FEM ANALYSIS OF PM ELECTRICAL MACHINES

In general, a power system consists of a mechanical turbine, an electrical generator and control block. Because of the mechanical constrains, in most of the cases the rotational speed of turbines is low. Usual generators however have high nominal rotational speed (1000 rpm or higher) incompatible with the turbine's rotational speed. One of the solutions is to introduce a gearbox between the turbine and the electrical generator, with all the drawbacks of such a mechanical device. An alternative is to have the electrical generator directly coupled with the shaft of the turbine. In this case, the design of the generator must solve the problem of good performances of electrical machines at low values of rotational speed imposed by the primary source of the energy mover. Nowadays there is a trend to use electrical generators directly coupled to the wind turbine, due to the advantages in comparison with the high speed generators coupled to the turbine through mechanical gearbox.

The direct drive PM generators are preferred in the water and wind low speed turbines. They have some advantages like: no gear-box between mechanical turbine and the generator (no losses, no maintenance, no gear noise, etc.); are more efficient, more compact, than other generators; cheaper than the direct drive synchronous generator with electrical winding excitation; smaller dimensions than those of the normal speed asynchronous generator with gear-box, or of the multi-pole asynchronous generator.

The paper analysis numerically some aspects concerning two radial flux low speed PM generators of 5KW for wind applications. After the preliminary classical design of the generators, a numerical analysis using the Opera 2D of Vector Fields has been performed. The classical design process generates the geometrical quantities, the shape and the geometrical dimension of the slot, the air gap form, the number of turns in the coils, the permanent magnets pattern, etc. Using the numerical analysis by FEM programs during the design process, we can analyze and improve the performances of the PM generators. In most of cases it represents a great advantage because the project could be changed during the design process and even some performances of the generator could be optimized.

The cross-section models of the two radial flux low speed PM generators that have been simulated using the Opera 2D-FEM program of the Vector Fields, are presented in Fig. 1. The purpose was to obtain PM generators with a simple structure, good performances and very low cogging torque. The inner rotor has 32 permanent magnets (16 magnetic pair of poles) of alternatively opposite radial magnetization. The permanent magnets used are NdFeB, N35SH. Two types of stators have been used in the design process: one with 33 stator slots (Fig. 1a) and the other one with 63 stator slots (Fig. 1b).

Considering some quantities of high importance in the design process (such as the cogging torque or the back EMF waveform shape), some analysis of these quantities has been

made, performing some optimizations in the geometrical design of the generators.

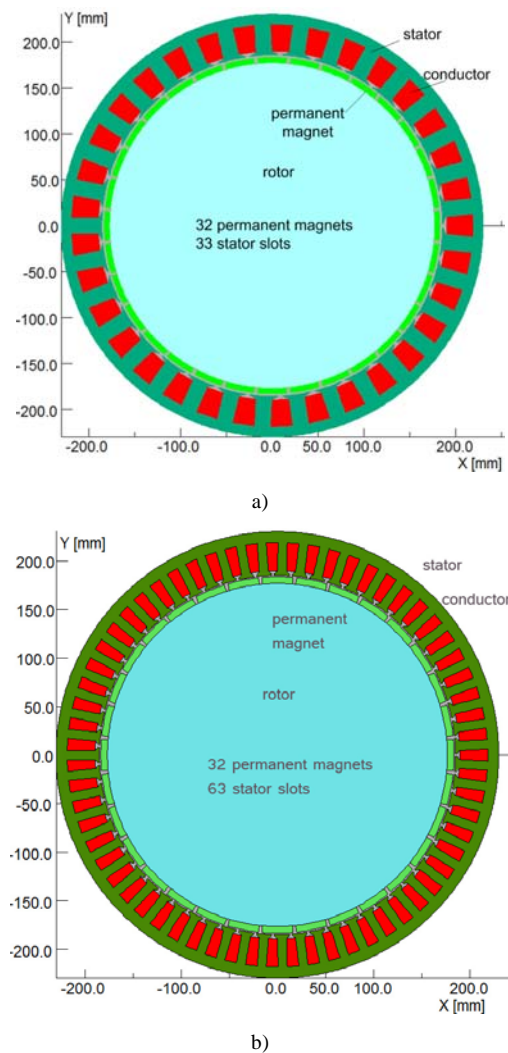


Fig. 1. The numerical models for FEM simulation.

III. MAGNETIC FIELD AND BACK EMF ANALYSIS

Due to the plan-parallel symmetry of the most electrical machines, a cross section of the machine is used for the numerical analyses that involve 2D-FEM programs.

The solution of the magnetic field generated by the FEM program allows to be analyzed some aspects concerning with the design process respectively the functioning of the electric machine, such as: identification of the possible saturated ferromagnetic area for which a reconsidered design process is necessary; the calculus of the iron losses in the main magnetic circuit or in different adjacent regions.

In order to have information about the magnetic field generated by the permanent magnets, a static analysis has been performed. Fig. 2 refers to the magnetic field generated by the permanent magnets of the generator with 33 stator poles. The field lines distribution are sketched in Fig. 2a while the Fig. 2b draw the radial component of the magnetic flux density versus the mechanical angle in the machine air-gap.

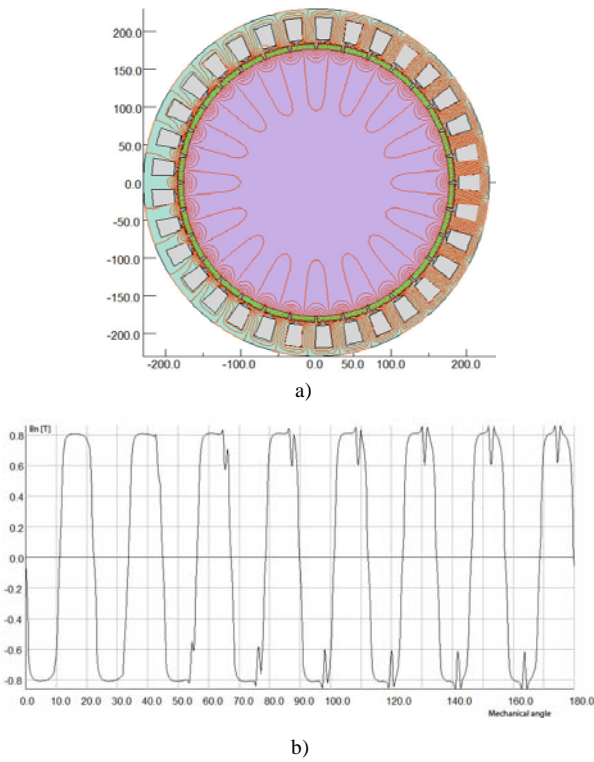


Fig. 2. The magnetic field for the generator with 33 stator slots a) field lines distributions; b) the radial component of the flux density in the air gap.

The same quantities are representing in Fig. 3 for the generator with 63 stator slots.

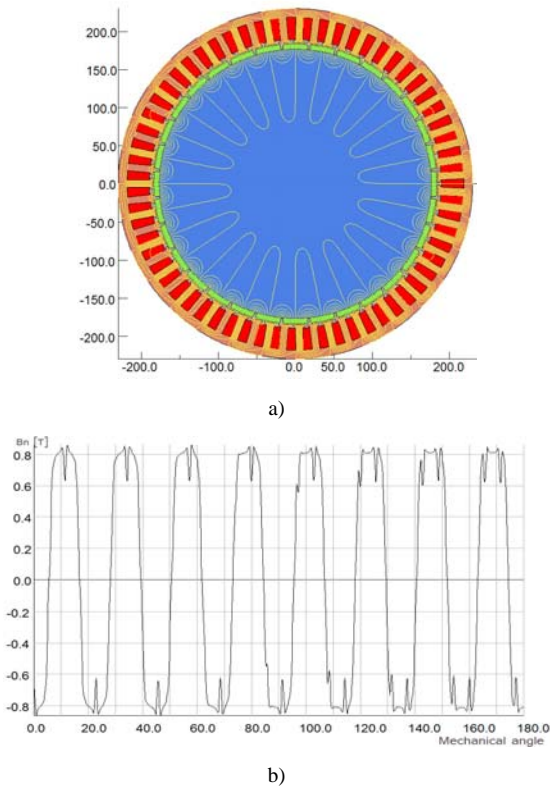


Fig. 3. The magnetic field for the generator with 63 stator slots a) field lines distributions; b) the radial component of the flux density in the air gap.

The dynamic analysis using FEM has been applied to draw the voltage shape of back EMF induced in stator windings. This analysis can take into account the non-linear characteristics of iron cores (the saturation effects), the opening of the stator slots, and the load current effects. Finally, the voltage shape, with Fourier series expansion can be analyzed. In this way, some parts of the generator could be optimized so as to achieve an acceptable waveform.

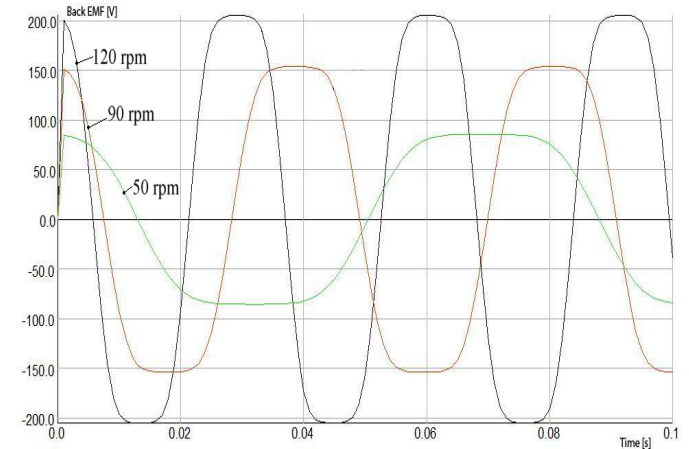


Fig. 4. The dependence back EMF versus time for different rotor speeds of the PM generator with 33 stator slots.

The back emf voltage shape for the generator with 33 stator slots is drawn in Fig. 4, for three different rotor speeds: 120 rpm (the rated speed), 90 rpm and 50 rpm. As we may expect, the magnitude and the frequency of the back emf are depending on the rotor speed. The numerical simulated shapes prove a frequency of $f=32$ Hz for a 120 rpm speed, $f=24$ Hz for 90 rpm and $f=13.33$ Hz for 50 rpm. The FFT analysis of the voltage waveform, point out the large value of the third harmonic.

The back emf voltage shape for the generator with 63 stator slots, using the same rotor speeds, is drawn in Fig. 5.

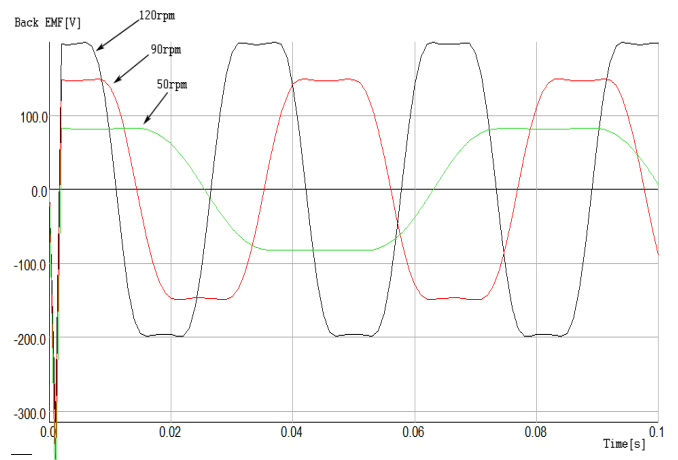


Fig. 5. The dependence back EMF versus time for different rotor speeds of the PM generator with 63 stator slots.

The influence of the pole coverage ratio over the back emf

waveform for the generator with 33 stator slots is presented in Fig. 6. There has been analyzed the back emf waveform for four different widths of magnets. This type of analyze allows an optimal value of the magnet width to be set so as to achieve the desired form of the back emf waveform.

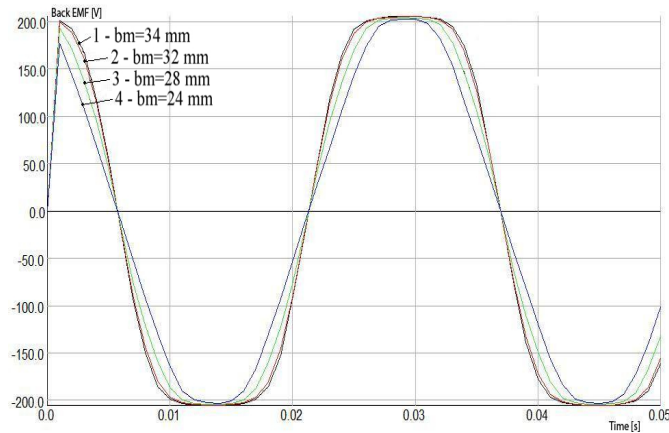


Fig. 6. The dependence back EMF versus time for different magnet widths of the PM generator with 33 stator slots.

IV. COGGING TORQUE ANALYSIS

Cogging torque is one of the most important quantities that have to be controlled during the design process of the PM generators. Due to the magnetic field generated by the permanent magnets, on the rotor acts a torque (cogging torque) even without current flows in the stator coils. The cogging torque depends on the ratio between the number of the statoric slots and the poles, the generator geometry and also on the pole coverage of the magnets. Large values of the cogging torque are unacceptable in the generator behavior. From this reason, the value of the cogging torque should be reduced during the design process of the generator by using the FEM analysis.

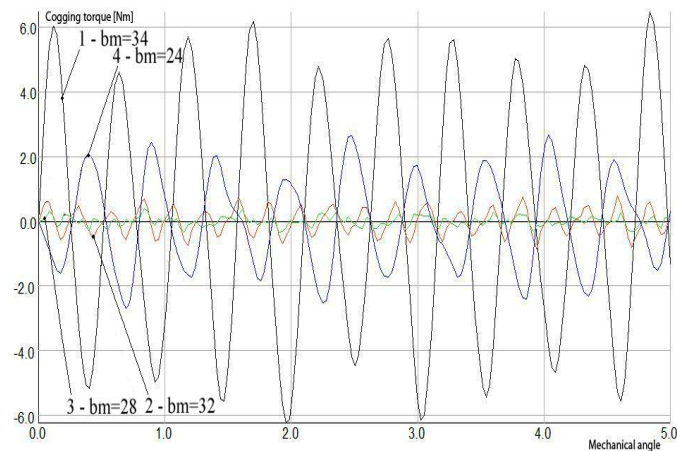


Fig. 7. The dependence cogging torque versus mechanical angle for different magnets widths of the PM generator with 33 stator slots.

The two types of generators have been designed with such a ratio between the number of the statoric slots and the magnetic

poles to generate a low cogging torque.

The dependence cogging torque versus rotor position (mechanical angle) for the generator with 33 stator slots has been drawn in Fig. 7 for different magnet widths. Due to a favorable rate between the number of the stator slots (33 slots) and the number of the rotor poles (32 permanent magnets), the generator has been design with a very low cogging torque. Even for wide values of the magnetic width, the cogging torque is less than one percent of the rated torque of the generator.

Similarly for the generator with 63 stator slots, the dependence cogging torque versus mechanical angle drawn in Fig. 8 shows low values comparing with the rated torque of the generator.

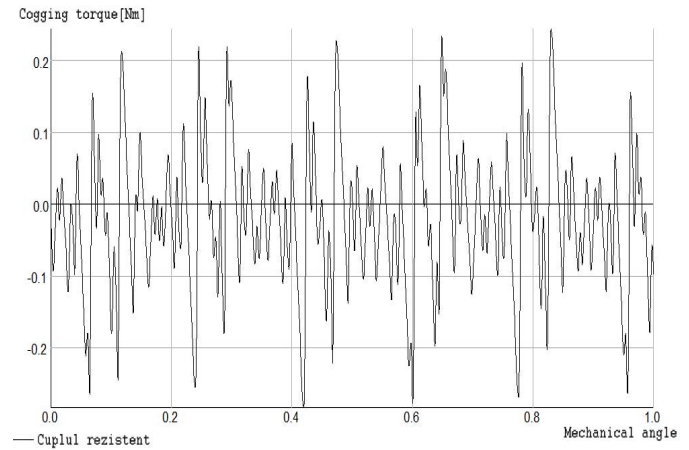


Fig. 8. The dependence cogging torque versus mechanical angle for the PM generator with 63 stator slots.

The optimization of the number of the stator slots or the number of the rotor poles, or the ratio between the two values can be done by performing a numerical analysis using a FEM program. The minimization of the cogging torque values performed by FEM analysis generates optimal dimensions in the design process of the generator.

V. CONCLUSIONS

The present paper emphasizes the great advantage of the FEM analysis used during the design process of the electrical machines, in particular PM generators. Using the numerical analysis of the PM generators during the design process avoids some errors that could be encountered and allows optimizing some performances of the machine by some corrections of the design. Such adjustments during the design process could have considerable economical benefits.

The prototype of the radial flux low speed PM generators with 33 stator slot has been realized following the classical design combined with the numerical analysis using FEM program, Fig. 9.



Fig. 9. Photo of the 5 KW PM generator.

The specification and main dimensions of the three-phase generator are presented in Table I.

The prototype was tested and analyzed on no-load and load conditions.

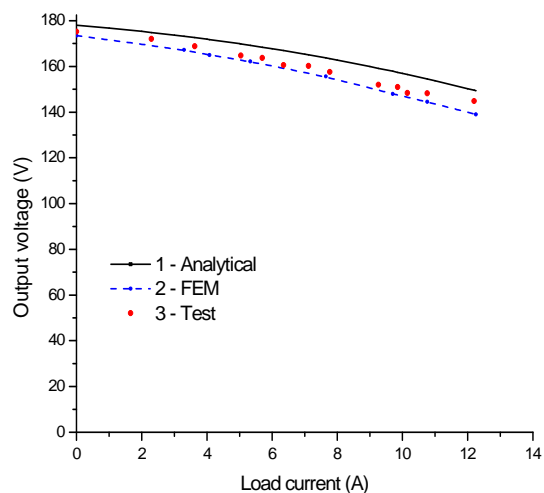


Fig. 10. The measured and estimated output voltage as function of load current for the PM generator with 33 stator slots; 1-analytical method; 2-FEM analysis; 3-measured values.

TABLE I.
SPECIFICATIONS AND DIMENSIONS OF THE GENERATOR

Rated output power (W)	5000
Rated rotational speed (rpm)	120
Rated output phase voltage (V)	145
Number of poles	32
Number of stator slots	33
Inner stator diameter (mm)	370
Stator winding factor ξ_1	0,954
Air-gap (mm)	1,4
Length of stator core (mm)	120
Magnet radial thickness (mm)	7
Magnet width (mm)	32
The stator winding resistance R (Ω)	0,98
The magnetizing reactance X_m (Ω)	1,05
The leakage reactance X_σ (Ω)	4,7
Permanent magnet NdFeB	N35SH

In Fig. 10 is presented the variation of output voltage estimated during the design process, curve 1. The curve 2 is obtained using the FEM. The measured values of the output voltage at resistive load are marked on the figure with few points. As a conclusion, there are good agreements between the analytical results, FEM results and the measured values.

REFERENCES

- [1] T.W. Preston, A.B.J. Reece, *The contribution of the finite-element method to the design of electrical machines: An industrial viewpoint*. IEEE Trans. on Magnetics, Vol.19, No.6, 1983, pp. 2375-2380.
- [2] M. Greconici, G. Madescu, C. Koch, *Advantages of FEM analysis in electrical machines optimization used in wind energy conversion systems*. Proceedings of the 3th International Symposium on Exploitation of Renewable Energy Sources, EXPRES 2011, Subotica, Serbia, 2011.
- [3] M. Biriescu, G. Madescu, M. Greconici, M. Mot, *Low speed PM generator for direct-drive wind applications* Proceedings of the International Conference on Computer as a Tool, EUROCON 2011, Lisbon, Portugal, 2011.
- [4] N. Bianchi, *Electrical Machines Analysis Using Finite Elements*, CRC Press, Taylor and Francis Group, 2005.
- [5] W. Hua, M. Cheng, Z.Q.Zhu, D. Howe, *Analysis and Optimization of Back EMF Waveform of a Flux Switching Permanent Magnet Motor*, IEEE Trans. on Energy Conversion, Vol.23, No.3, 2008, pp. 727-733.
- [6] Vector Fields, Reference manual for Opera 13, 2009.

Influence of a Thin Copper Shield on a BLDC Motor Parameters

Nándor Burány, Dejana Herceg, and Neda Pekarić-Nadž

Abstract—A simplified model of a brushless DC motor segment is studied in this work. Shielding of the ferromagnetic structure with a high conductivity layer is explored. The shield is supposed to reduce the ohmic losses of the magnets and of the entire structure, particularly at the higher frequencies. In order to verify that, both calculations and measurements of the power loss are accomplished for the model first. In conclusion, locked rotor measurements are performed on a real BLDC motor in order to validate the results.

Index Terms—Eddy current loss, BLDC rotor shielding.

I. INTRODUCTION

MAGNETIC field in a brushless DC (BLDC) motor plays the most important role not only in the torque formation, but also in the loss generation. Besides the fundamental components of the magnetic flux generated by the stator currents, there are high frequency components too, due to both the space harmonics and the time harmonics generated by chopping activity in a modern motor supply. High speed rotor losses due to the space harmonics are well documented in the literature [1-6]. The losses are mostly controlled by lamination and magnet segmentation [7]. High conductivity rotor shield is an option for the loss reduction in the case of a machine with a solid-rotor [6]. Using conductive shield is expected to reduce both losses caused by the time and space harmonics. The ohmic losses, caused by the PWM voltage supplying the stator, are not fully explained in the literature and need more attention. In this paper we study both fundamental frequency and the higher frequencies BLDC motor losses, due to the chopping nature of the supply voltage. The available motor is presented in Fig. 1. The goal of the work is first to evaluate the



Fig. 1. The explored 300W outer rotor BLDC motor.

loss on a simple model and next to extrapolate the conclusions to the real BLDC motor. In the end, some of the results for the model are verified by measurements on the available motor.

II. MATERIALS AND METHODS

A. The model

A simplified BLDC motor segment model from Fig. 2 is supposed to recreate the magnetic field similar to the one inside the motor. This flat model is studied both by numerical modeling and measurements on a physical model. Commercially available software is used for the calculations. The 2D FEM analysis results for the inductance, resistance and power loss were not satisfactory. Consequently the 3D analysis is employed. Magnetic forces in the segment model are calculated using magnetostatic analysis. In order to explore the copper layer influence, winding impedance and the ohmic losses are calculated using time harmonic analysis. The 3D model for the motor segment from Fig. 2 is explored. The copper layer thickness varies from 0.1 mm to 0.5 mm. For

Manuscript received 30 May 2012. Accepted for publication 10 June 2012. Some results of this paper were presented at the 16th International Symposium Power Electronics, Novi Sad, Serbia, October 26-28, 2012.

This work was partially supported by Project TR32019 with Serbian Ministry of Science and Technology.

N. Burány is with the College of Dunaújváros, Tácsics Mihály u. 1/A, 2400 Dunaújváros, Hungary, (e-mail: burany.nandor@gmail.com).

D. Herceg is with the Faculty of Technical Sciences, University of Novi Sad, Novi Sad, Serbia (e-mail: vuletic@uns.ac.rs).

N. Pekarić-Nadž is with the Faculty of Technical Sciences, University of Novi Sad, Novi Sad, Serbia, +381214852583 (e-mail: pekarić@uns.ac.rs).

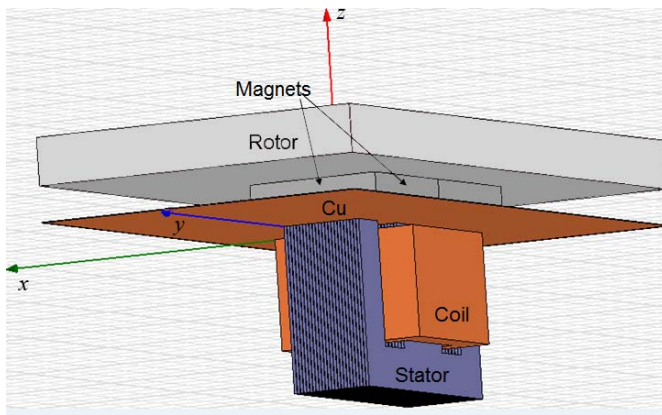


Fig. 2. Simplified model of the BLDC motor segment.

the calculations, the coil is taken to be supplied by the time harmonic current of $NI=240$ A-turns.

The model from Fig. 2 consists of the parts resembling the stator and rotor of the motor. Influence of the different copper layer thicknesses is studied on the model. The part equivalent to the “Rotor” in Fig. 2 is built from a 7 mm thick solid iron. Neodymium magnets, 5 mm thick, are combined into a flat layer and protected by a 0.1 mm thick plastic sheet. The examined layer is 0.1 mm, 0.35 mm or 0.5 mm thick copper, or alternatively plastic, covered by a 0.1 mm thick plastic protection. The “Stator” to “Rotor” separation was kept constant, but filled with appropriate varying thickness copper or plastic foil. The part representing “Stator” in Fig. 2 is built out of 24 (36x24 mm) E shaped, isolated silicon steel sheets. The individual sheets are 0.5 mm thick including the protective coating. Bulk iron conductivity assumed $\sigma=10.3 \cdot 10^6$ S/m. Copper coil is formed by twisting together seven individually insulated conductors of 0.45 mm diameter, in order to reduce skin effect. The number of turns in the coil is 24. The winding is placed around the central leg of the E core, having the cross section in the form of a 12 mm x 12 mm square. Plastic coil former around the wire package is 1 mm thick. The winding area is 16 mmx4 mm. Linearity of iron is assumed, with $\mu_r = 550$.

The stator to rotor gap has immense influence on the magnetic field distribution inside the motor. In the segment considered, the corresponding separation was kept constant and filled with copper foils of different thicknesses, which was not possible for the real motor. For this reason, the calculations are verified by measurements on the physical model of the segment.

B. The motor

The available 300 W motor from Fig. 1 is an outer rotor BLDC motor. The spacing between the stator and the rotor of the motor from Fig. 1 is measured to be about 0.4 mm. Consequently, only a very thin copper foil, 0.1 mm thick, together with two insulation layers of 0.1 mm, can be inserted. At the PWM frequency of $f=22$ kHz, the copper thickness of 0.1 mm represents less than 25% of the skin depth, $d=0.44$ mm, at the observed frequency.

III. CALCULATION RESULTS

Numerical solution to the problem is based on the magnetic vector potential, A . The current of the stator coil from Fig. 2 is circumferential. Thus, magnetic vector potential has only horizontal (“x” and “y”) components. Numerical results are obtained for the quasi-static case with “x” and “y” oriented induced currents. For the problem of interest, the governing equation for the magnetic vector potential is

$$j\omega\sigma\vec{A} + \nabla \times \left(\frac{1}{\mu_0\mu_r} \nabla \times \vec{A} \right) = \vec{J}. \quad (1)$$

Magnetic flux density is calculated first for the different frequencies. Fig. 3 represents the flux density distribution at 50 Hz. As can be observed, magnetic flux density has the greatest magnitude in the E-laminates of the stator and much lower in the rotor. At the higher frequencies the magnetic field is more and more situated in the air, outside the ferromagnetic material.

Fig. 4 represents calculated inductances of the segment model with (w) or without (w/o) the copper layer of the different thicknesses of 0.1 mm, 0.35 mm and 0.5 mm. The results for the ohmic loss in respect to the different copper

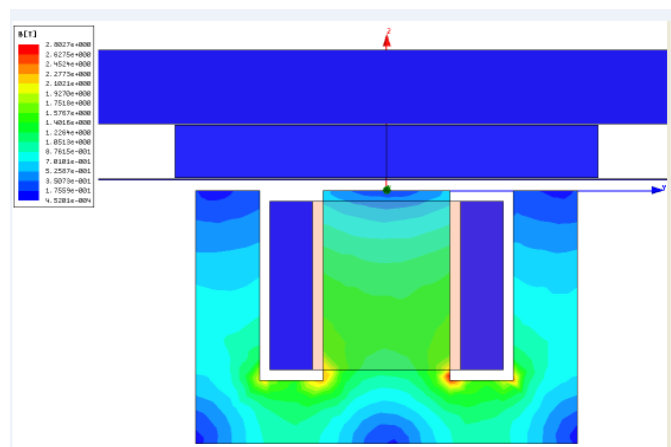


Fig. 3. Calculated values of the magnetic flux density in the model at 50Hz.

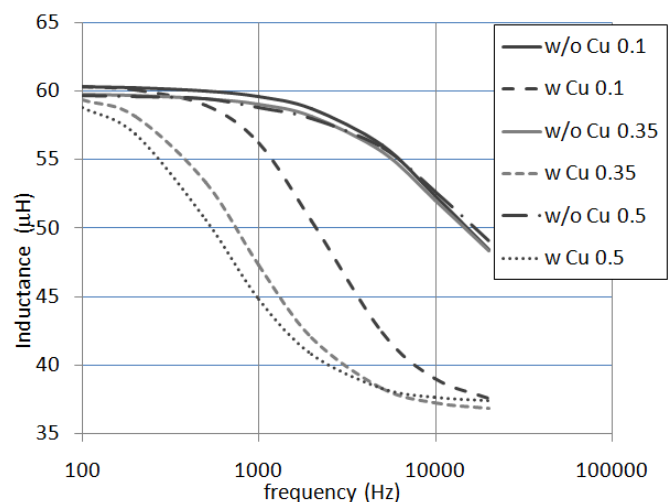


Fig. 4. Calculated values for the inductance of the model.

layer thicknesses are presented in Fig. 5.

Some values of the calculated magnetic force are listed in Table I. The force depends on the relative position of the magnets. For the sake of comparison we present only the results for the central position of the “Stator” between the “Rotor” magnets.

Please notice from Fig. 5 that a thicker layer of the copper shield enables better power loss reduction at high frequencies. In the same time, as observed from Table I, it does not significantly alter the tangential (“y”) component of the magnetic force. The vertical (“z”) component of the force for the segment is visibly reduced. As the BLDC motor torque is controlled by the tangential component only, inserting a thin layer of copper between the stator and rotor should have a little consequence on the torque in a real motor.

IV. MEASUREMENT RESULTS

A. The model measurements

The inductance and resistance measurements on the model from Fig. 6 are performed on the HP 4194A Impedance Analyzer. The Figs. 7 and 8 present some of the results for the copper shield thickness of 0.35 mm.

Measured power loss of the model, for the same copper shield thickness of 0.35 mm is presented in Fig. 9. Some results for the different thicknesses are given in Table II. The equipment used for the measurement is the same as used for the motor, described below.

B. The motor measurements

Locked rotor measurements of the power loss and torque produced by the available BLDC motor are performed

TABLE I
CALCULATED FORCES FOR THE MODEL WITH THE MAGNETS IN THE CENTRAL POSITION

Thickness (mm)	F _y (N)	F _z (N)
0.10	4.8	109
0.35	4.6	98
0.50	4.5	93

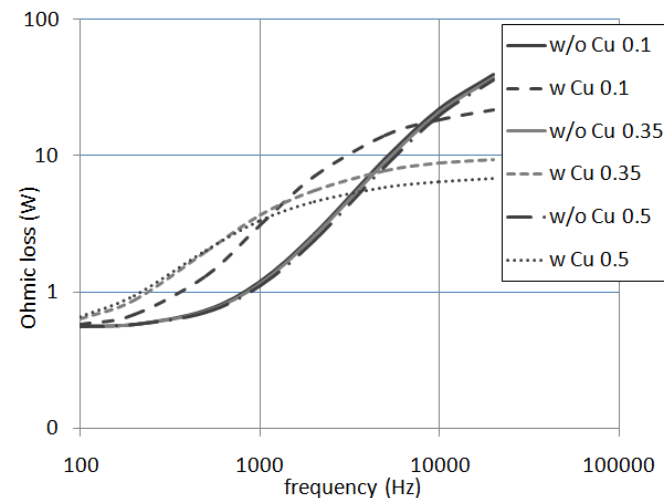


Fig. 5. Calculated values for the power loss in the model.

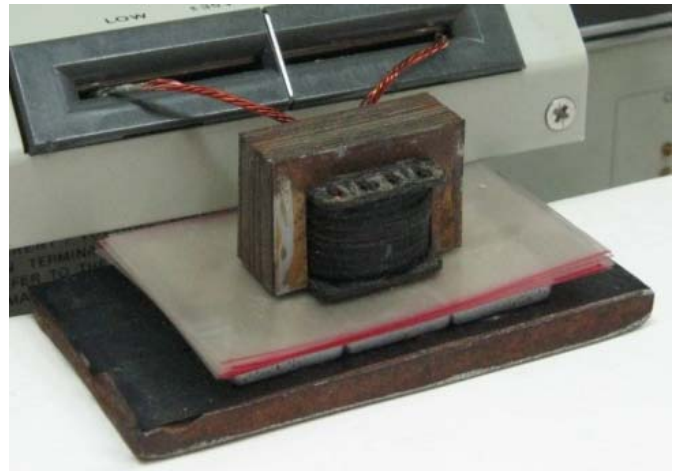


Fig. 6. Measurements on the model using HP 4194A Impedance Analyzer.

TABLE II
MEASURED POWER LOSS IN THE PHYSICAL MODEL AT 22 KHZ

Thickness (mm)	Copper layer: Power loss (W)	Plastic layer: Power loss (W)
0.10	35	31
0.35	28	30
0.50	26	29

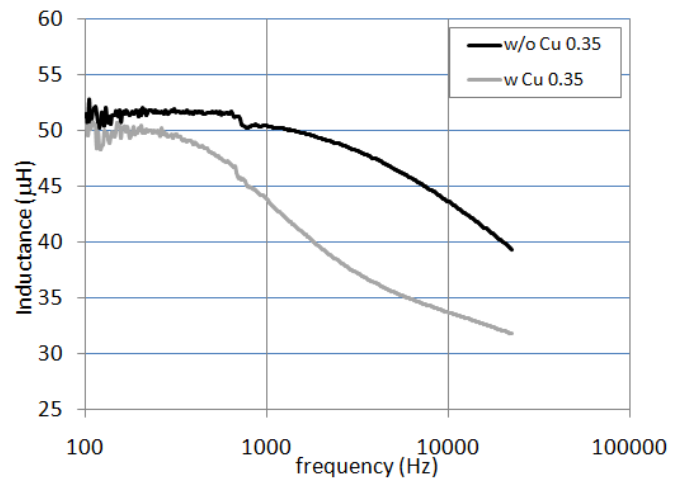


Fig. 7. Measured inductance of the physical model using HP 4194A.

according to the block diagrams from Figs. 10a and 10b. The H-bridge supplies two phases of the motor at time, as is typical with the BLDC drives. The motor terminal voltage is rectangular, with amplitude up to $V=40$ Vp-p and switching frequency $f=22$ kHz. The duty cycle varies between 35-65%, to enable the desired average current and the current ripple of approximately 20 Ap-p at the maximum supply voltage. The bridge is supplied by a DC source, signified by V_d in the Figs. 10a and 10b. Total losses of the bridge-motor cascade are measured by an electro-dynamic wattmeter, W, type EL 0120, manufactured by Iskra Co. As the loss of the H-bridge from Fig. 10b is only a small portion of the motor losses, the total losses are attributed to the motor losses.

The H-bridge is built of four MOSFETs, with low channel resistance, R_{DSon} , denoted by Q1-Q4 in Fig.10b. The drive circuits are half bridge drivers of the bootstrap type. The upper and the lower drive channels are controlled by the direct

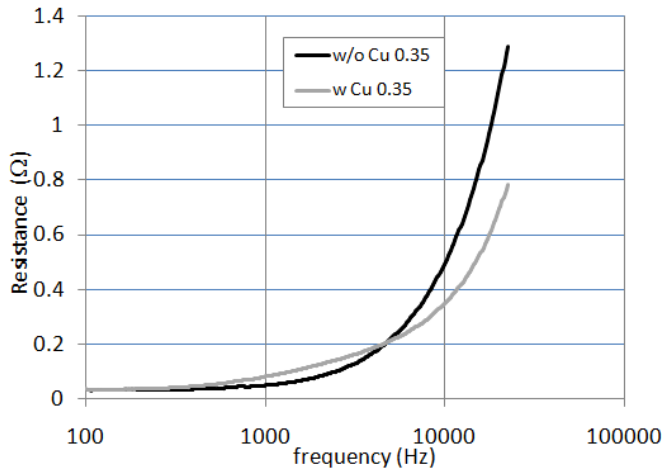


Fig. 8. Measured resistance of the physical model using HP 4194A.

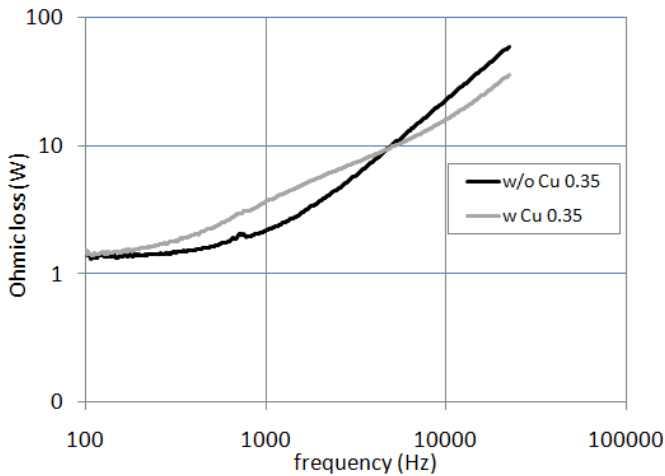


Fig. 9. Measured power loss of the physical model.

and the inverted PWM signals. The bipolar PWM bridge control is achieved by diagonal switching of the transistors, as illustrated in Fig. 10b. The measurement results of the motor loss, with and without the copper layer inserted, are presented in Fig. 11.

Measurements of the physical model power loss are performed with the same equipment from Fig. 10, used for the motor power loss measurements. Some of the results at $f=22$ kHz, for the voltage $V=30$ Vp-p, 50% duty cycle and the current ripple about $I=20$ Ap-p, are summarized in Table II and in Fig. 9.

V. DISCUSSION

As can be seen from Figs. 4 and 7, the results of the inductance calculations and measurements are in reasonably good agreement. The numerical results for the segment's inductance from Fig. 4 suggest that the inductance decays much steeper with the copper layer inserted than without. This can be a desirable feature to enable a fast response BLDC motor current control. Calculated power loss from Fig. 5 is in acceptable agreement with the physical model power measurements from Table II.

As seen from Fig. 11, insertion of the thin copper layer is found to increase the power loss for the smaller average

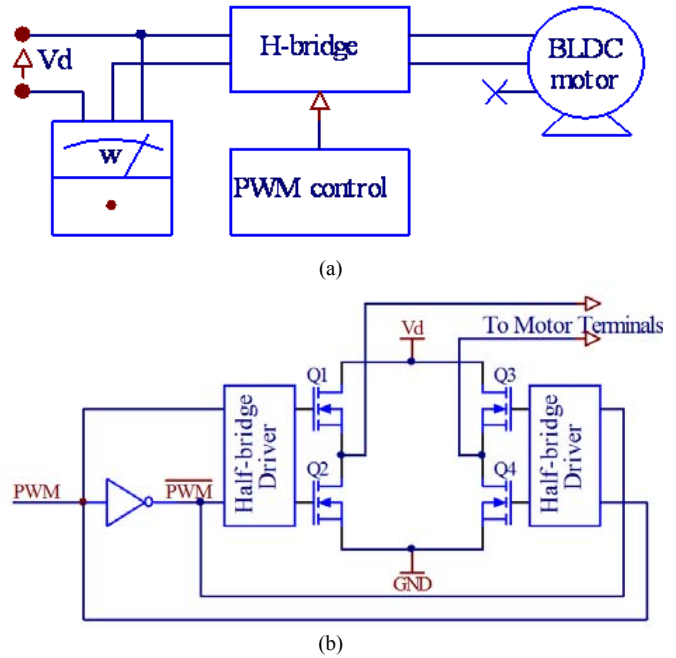


Fig. 10. (a) Diagram of the setup for the BLDC motor measurements, (b) The MOSFET H-bridge with drive circuits and control signals.

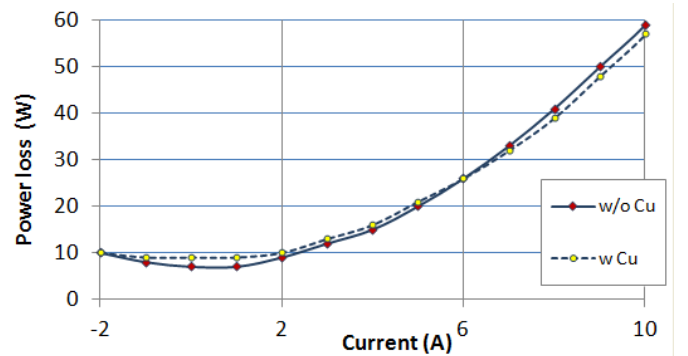


Fig. 11. Measured power loss depending on the average current in the BLDC motor, $V=40$ Vp-p, $f=22$ kHz.

current. For the larger average current, the power loss is slightly reduced in comparison to the no layer situation. Overall, insertion of the copper layer significantly thinner than the skin depth can not be considered beneficial for the motor.

When using thicker copper shield the ohmic losses are visibly reduced. Unfortunately, substantial increase in the copper layer thickness would increase the air gap between the stator and the rotor of a real BLDC motor and would inevitably affect the torque. This effect could not be measured on the model, but is possible to evaluate numerically. Some results are listed in Table I.

VI. CONCLUSION

The BLDC motor flat segment model is studied in order to explore the influence of the copper thickness on the power loss. 2D numerical analysis of the model was not applicable. Only 3D numerical model gives the results in acceptable agreement with the measurements. Lower ohmic loss is obtained for the copper shield thicknesses comparable to at

least one third of the skin depth. As the consequence of the thicker layer inclusion, the air gap between the stator and the rotor must increase. Increasing the gap between the stator and the rotor by a fraction of a millimeter in a real motor, may not reduce the motor torque dramatically, but it is a designer's decision to determine how much torque reduction can be tolerated in return for somewhat lower power loss at the higher frequencies of the motor current.

The BLDC motor losses caused by the supply voltage chopping may be reduced by a highly conductive shield of the appropriate thickness, placed between the stator and the rotor. The shield may be especially effective for the components over 10 kHz, but must have appropriate thickness related to the material skin depth. In the case of the available real BLDC motor measurements, we were limited to evaluate only one, very small thickness for the copper layer. As expected from the calculations and confirmed by the measurements, such layer increases overall ohmic loss for the smaller current magnitudes which is not desirable.

REFERENCES

- [1] Z. Fengzheng, S. Jianxin, F. Weizhong, L. Ruiguang: "Study of retaining sleeve and conductive shield and their influence on rotor loss in high-speed PM BLDC motors", IEEE Trans. Mag. Vol. 42, No. 10, Oct. 2006, pp. 3398-3400.
- [2] A. Borisavljevic, H. Polinder, J. A. Ferreira: "Minimising rotor losses in high-speed high-power permanent magnet synchronous generators with rectifier load", Proc. of PEMD 2010, April 2010, Brighton, UK, doi 10.1049/cp.2010.0141.
- [3] A. Mansouri and H. Trabelsi: "On the iron losses computation of a three phase PWM inverter-fed SMPM by using VPM and transient FEA", PIERS Proceedings, Marrakesh, MOROCCO, March 20-23, 2011, pp 866-869.
- [4] J.L.F. van der Veen, L.J.J. Offringa: "Rotor losses in a high speed synchronous generator with permanent magnet excitation and rectifier load", EUT Report 96-E-301 ISBN 90-6144-301-6 December 1996.
- [5] Yu Tang, Yong Xiang Xu, Wei Yan Liang: "Influence of permanent magnet thickness on loss of permanent magnet brushless dc motor", Advanced Materials Research Vol 204 – 210, pp 1797-1800.
- [6] [Polinder, H. and Hoeijmakers, M.J: "Effect of a shielding cylinder on the rotor losses in a rectifier-loaded PM machine", Proceedings of the IEEE Conf. on Industry Application. Vol. 1, 2000, pp. 163–170.
- [7] Y. Chen, Z. Q. Zhu, and D. Howe, J. H. Gliemann: "Rotor Eddy Current Loss in Single-Phase Permanent Magnet Brushless DC Motor", Conf. Record of the 42nd IEEE IAS Annual Meeting. 10/2007; DOI: 10.1109/IAS.2007.87. W.-K. Chen, *Linear Networks and Systems* (Book style). Belmont, CA: Wadsworth, 1993, pp. 123–135.

High frequency model of EMI filter

Szymon Pasko and Boguslaw Grzesik

Abstract—The EMI filters are usually used for suppression of electromagnetic conducted interference of range 9 kHz-30 MHz. The efficiency of electromagnetic interference filter is described by attenuation characteristics. The value of attenuation of EMI filter depends on main parameters of filter's elements and its parasitic parameters. Therefore the high frequency model of electromagnetic interference filter is analyzed in this paper.

Index Terms—Electromagnetic compatibility, EMI filter.

I. INTRODUCTION

THE EMI filters are usually used to suppress electromagnetic conducted interference of range 9 kHz - 30 MHz.

The EMI filter is inserted between main supply and devices which generates interferences (Fig. 1). The conducted interferences embrace common mode (CM) and differential mode (DM) interferences. The common mode (CM) interferences are propagated in both phases in the same direction and come back to the ground (Fig. 1). The differential mode (DM) interferences are propagated in one phase in one direction and come back via the second phase in opposite direction (Fig. 1). The direction of the interference is like the direction of respective current $-i_{CM}$, i_{DM} [1].

The structure of filter is selected so the impedance mismatch occurs. If impedance of main supply V_{AC} is big then the impedance of filter, seen from L, N terminals has to be low, and the same from devices side [1].

The CM interferences are suppressed by coupled coils L_0 , and the capacitor C_{Y1} , C_{Y2} . The impedance of coupled coils is higher than impedance of capacitors C_{Y1} , C_{Y2} so that the CM interferences flow via capacitors C_{Y1} , C_{Y2} and PE conductor (Fig. 1). The DM interferences flow by capacitors C_{X1} and C_{X2} , because the impedance of AC supply is higher than the impedance of the filter, seen from L, N terminals. It results from mismatch impedance conditions [1]. The efficiency of EMI filter suppression is determined by its attenuation A_{dB} .

$$A_{dB} = 20 \log \left(\frac{V_1}{V_2} \right) \quad (1)$$

Manuscript received 30 May 2012. Accepted for publication 10 June 2012. Some results of this paper were presented at the 16th International Symposium Power Electronics, Novi Sad, Serbia, October 26-28, 2012.

S. Pasko and B. Grzesik are with the Faculty of Electrical Engineering, Silesian University of Technology, ul Bolesława Krzywoustego 2, 44-100 Gliwice, Poland, (corresponding author to provide phone: +48 32-237 13 04; fax: +48 32 237 19 77 (e-mail: {szymon.pasko, boguslaw.grzesik}@polsl.pl).

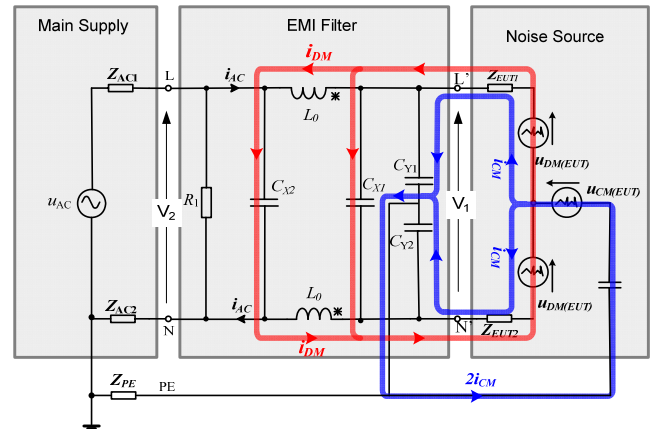


Fig. 1. Propagation of CM, DM interferences in EMI filter.

where V_1 is the voltage of source of interferences (V_{DM} , V_{CM}), while V_2 is the voltage at the output of the filter that is connected to the Noise' source [2], [3]. It is given in dB. The measured attenuation characteristic of FN2020 filter is depicted in Fig. 2.

II. HIGH FREQUENCY MODEL OF FILTER'S ELEMENTS

The EMI filters consist of coupled coils L_0 and capacitors C_X and C_Y (Fig. 1). The value of attenuation of EMI filter depends also on parasitic parameters of EMI filter elements. The value of parasitic parameters causes frequency resonances which reduces the attenuation of EMI filters.

The equivalent circuit of capacitors of EMI filters, e.g. C_{X1} , (Fig. 3b) is the series connections of: resistance R_{X1} , which represents the losses of the capacitor, inductance L_{X1} , which

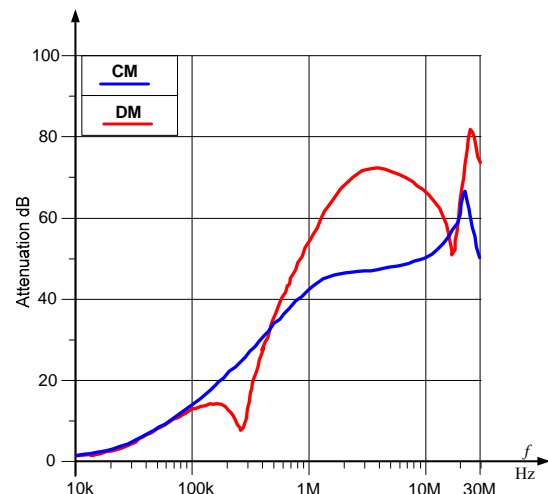


Fig. 2. The measured attenuation characteristics of FN2020 EMI filter.

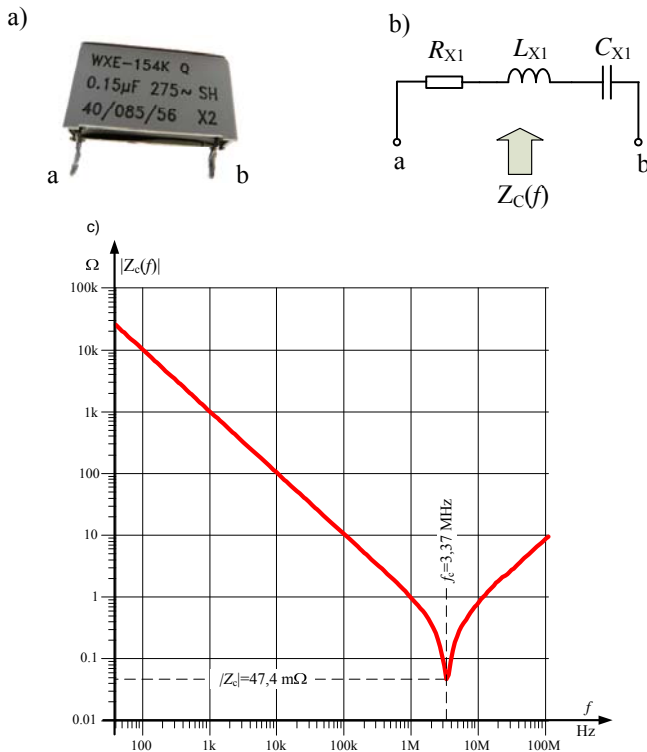


Fig. 3. The capacitor CX (0.15 μF) polyester capacitor WXE 154K: a) photograph, b) equivalent circuits, c) measured module impedance characteristic.

represents inductance of the capacitor and the actual capacitance C_{X1} of the capacitor C_{X1} Fig. 3a).

The parameters of filter's capacitors C_X , C_Y equivalent circuits are calculated basing on the modulus of impedance characteristics, which were measured by impedance analyzer Agilent 4294A [4], [5]. The measured impedance characteristic of capacitors C_X , is given in Figure 3c. The impedance $|Z_C(f)|$ of the capacitor decreases with increasing frequency, up to serial resonance frequency f_c . The value of C_X is proportional to $X_C(\omega)$ up to serial resonance frequency f_c . For the resonant frequency the impedance $|Z_C|$ is equal to the R_X , the series resistance capacitor. The impedance $|Z_C|$ increases above resonant frequency f_c . The capacitor equivalent circuit above the resonance frequency changes its character from capacitive to inductive. The parasitic inductance is calculated according equation (2).

$$f_c = \frac{1}{2\pi\sqrt{L_X C_X}} \quad (2)$$

The parasitic parameters of capacitors depend on their construction. The majority of EMI filters are based on metalized polypropylene, polyester, paper and ceramic capacitors.

The ceramic capacitors have the lowest parasitic inductance. The parasitic inductance of metalized capacitors is also small. The greatest parasitic resistance has ceramic capacitors, while among the metalized capacitors the greatest value of the parasitic resistance has paper capacitors. Metalized capacitors have self-healing properties while ceramic ones are not. Therefore ceramic capacitors are not

used as C_X capacitors. However, the metalized capacitors are characterized by larger volume and higher price in comparison with ceramic ones. [6]

The most important elements of EMI filter are coupled coils. These coupled coils are wound on toroidal core. The equivalent circuit (Fig. 4) of coupled coils consists of: L_0 inductances, leakage inductance L_r ($L_r \ll L_0$), R_p resistance which represents the losses of the coil, R_w resistance which represents the resistance of the wire, $R_w \ll R_p$, C_1 , C_2 , C_3 , C_4 parasitic capacitances of coupled coils.

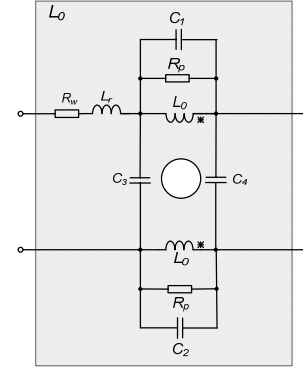


Fig. 4. The equivalent circuits of EMI filter coupled coils.

The C_1 , C_2 represents parasitic capacitances of primary and secondary winding of the coupled choke. The C_3 , C_4 represents the parasitic capacitances between primary and secondary winding.

The parameters of equivalent circuit of coupled coils are calculated basing on the modulus of impedance characteristics, which were measured by impedance analyzer Agilent 4294A. The calculation of parameters of equivalent circuit of coupled coils is more complicated than those of capacitor's one. The method is presented in details in [7].

The parasitic parameters filter elements have influence on attenuation characteristic of EMI filter. The value of choke parasitic parameters depends on design of coupled coils. The value of L_0 depends on core materials and number of turns. The core made of Mn-Zn ferrite is common practice in EMI filter. The initial permeability of Mn-Zn core is small in comparison with initial permeability of, e.g., nanocrystalline core. Therefore nanocrystalline materials offer significant advantage in attenuation performance. The high permeability permits to achieve the inductance L_0 5 times higher than for Mn-Zn for common mode case when the geometry and number of turns are similar [8]. It should be noted that inductance L_0 and resistance R_p are strongly depend on frequency. The inductance increases and resistance R_p decreases vs, frequency. The value of resistance also depends on type of core.

The value of parasitic capacitances depends on the way the winding is wound and number of turns. The lowest value of parasitic capacitance is obtained in single layer windings (Fig. 5a) and in "bifilar" windings (Fig. 5b). The "bifilar" coupled coils however must be wound with well-insulated insulated wires due to safety requirements. Moreover, the leakage inductance of L_r bifilar wound coils is minimal.

The single layer coils a larger core to achieve the larger inductance. Double layer windings increases the parasitic capacitances but can be decreases the dimension of the core [6], [8], [9].

The Actown Electrocoil Company has brought into market TIGHTpak toroidal coupled coils (Fig. 6). These are a single layer coils with wires flattened on the inner part of the core.

This manufacturing technique makes the higher number of turns in winding having the same length. This increases inductance L_0 without increasing core size [10], [11].

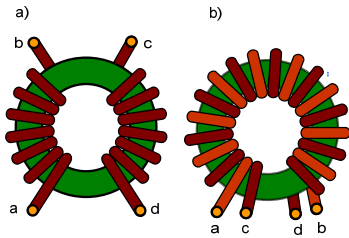


Fig. 5. EMI coupled coils: a) single layer, b) "bifilar" wound coupled coils.

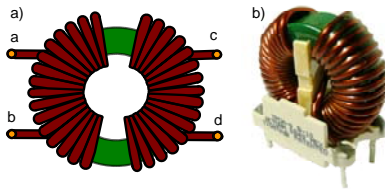


Fig. 6. TIGHTpak toroidal coupled coils.

III. HIGH FREQUENCY MODEL OF EMI FILTER

Basing equivalent circuits of filter elements its high frequency model is created – Fig. 7. The equivalent circuits of EMI filter for CM interferences takes the form shown in Fig. 8a.

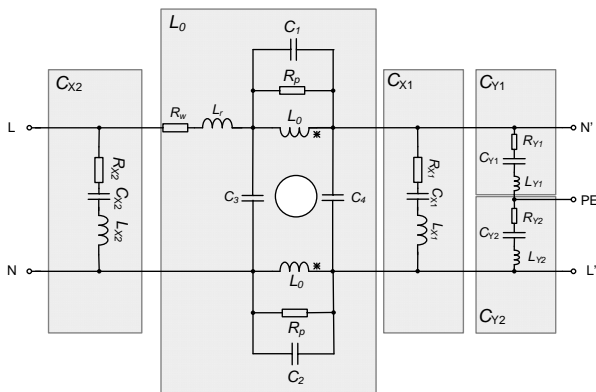


Fig. 7. The high frequency model of EMI filter.

The attenuation characteristic of CM noise depends on value of inductance L_0 , resistance $0.5 R_p$, and sum of winding parasitic capacitance $C_1 + C_2$ and also parameters of equivalent circuits of C_{Y1} , C_{Y2} .

The parameters of C_{X1} , C_{X2} have no impact on attenuation characteristic for CM noise.

The differential mode (DM) interferences are propagated in

one phase in one direction and come back via the second phase in opposite direction. Therefore the equivalent circuits of EMI filter for DM take the form shown in Fig. 8b. The attenuation characteristic of DM noise depends on value of leakage inductance L_r , resistance R_p , parasitic capacitance C_1 , C_2 , C_3 , C_4 and also parameters of equivalent circuits of C_{Y1} , C_{Y2} , C_{X1} , C_{X2} .

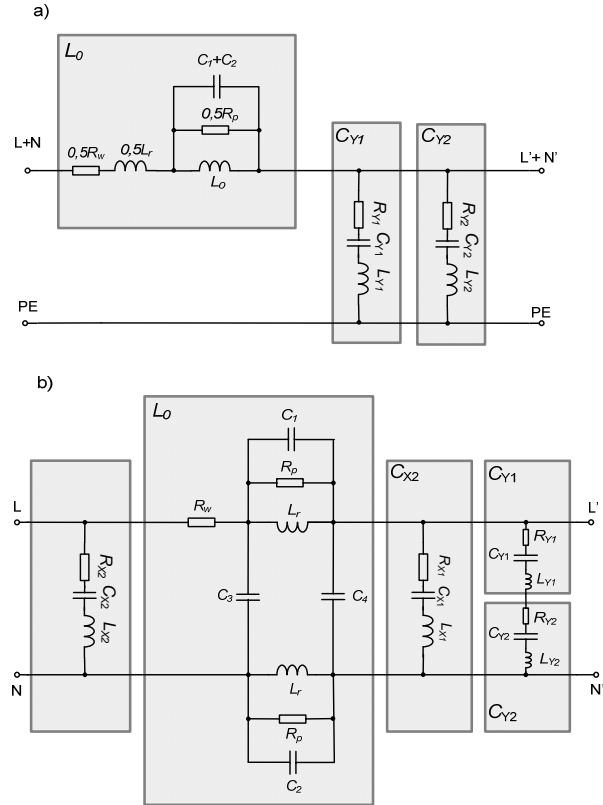


Fig. 8. The high frequency model of EMI filter for: a) CM conducted interference, b) DM conducted interference.

IV. EXAMPLES OF FILTER'S ELEMENT INFLUENCE ON EMI FILTER'S ATTENUATION

The parasitic parameters of filter's elements have predominated influence on attenuation characteristic of EMI filter. The parasitic parameters of filter's elements depend on its construction. As an example the value of L_0 depends on core materials, winding construction and number of turns. Therefore nanocrystalline materials offer significant advantage in attenuation performance. The high permeability of nanocrystalline materials permits to achieve the inductance L_0 5 times higher than for Mn – Zn for common mode in case when the geometry and number of turns are similar. The comparison of EMI filter attenuation characteristic for common mode with nanocrystalline (NC) and Mn-Zn (MnZn) materials is depicted in Fig. 9.

The value of L_0 , also depends on number of turns. The number of turns yields to decrease value of inductance L_0 and also parasitic capacitance which reduce attenuation. Therefore the method of winding of coupled coils is most important. The "bifilar" wound coupled coils has the lowest parasitic capacitance and also leakage inductance L_r as

opposed to the double layer coupled coils. Therefore the attenuation for filter with “bifilar” wound coupled coils is higher for CM noise and lower for DM in comparison on filter with double layer coupled coils. The comparison of attenuation characteristic for EMI filter with “bifilar” (BCc) wound coupled coils and double layer (DCc) one is depicted in Fig. 10.

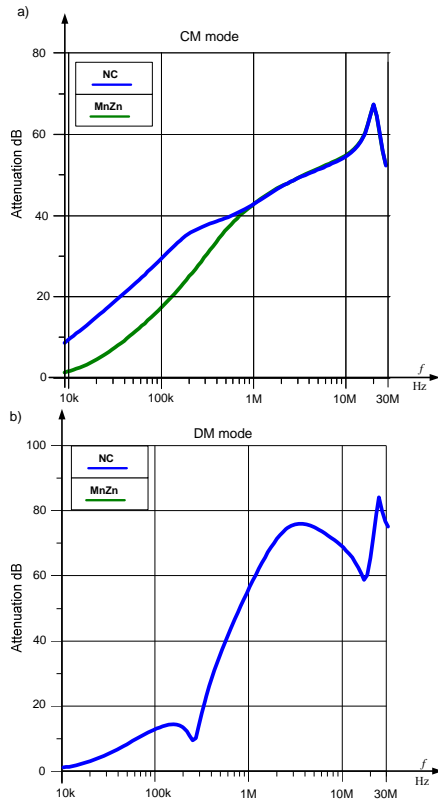


Fig. 9. Comparison of EMI filter attenuation characteristic of coupled coils with nanocrystalline (NC) and Mn-Zn (MnZn) materials: a) attenuation characteristic for CM noise, b) attenuation characteristic for DM noise.

V. CONCLUSION

The parameters of EMI filter have influence on its attenuation performance for different frequency as was shown in Fig. 9, Fig. 10. The power electronics converters generate the conducted electromagnetic interference in different range of frequency. It results from its construction. Therefore to effectively suppress electromagnetic conducted interference and EMI filter construction the high frequency model is indispensable.

The future work will be based on creating FEM (finite elements method) model of EMI filter and checking the proposed one.

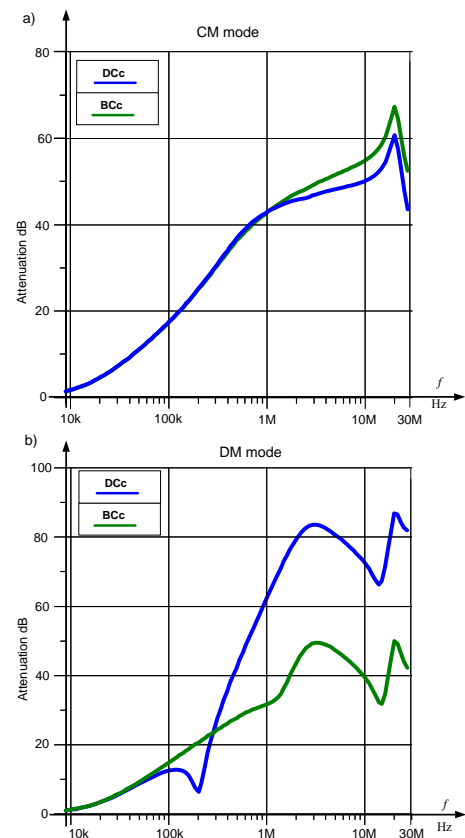


Fig. 10. Comparison of EMI filter attenuation characteristic for “bifilar”(BCc) and double layer (DCc) coupled coils: a) attenuation characteristic for CM noise, b) attenuation characteristic for DM noise.

REFERENCES

- [1] T. Williams, “EMC for product Designers”, Newnes (2001).
- [2] L. R. Ozenbaugh, EMI filter Design, Headquarters, 2001.
- [3] H.W Ott, “Electromagnetic compatibility Engineering”, John Wiley & Sons, 2009.
- [4] Agilent Technology: 4294A Precision Impedance Analyzer Operation Manual Application Note, 2003.
- [5] L. Tihanyi, “Electromagnetic compatibility in Power Electronics”, Butterworth-Heinemann, 2004.
- [6] S. Pasko, “Analysis of the impact on construction of filters of power converters’ conducted interferences”, Phd Thesis Silesian University of Technology, Gliwice 2010.
- [7] S. Pasko, F. Beck, B. Grzesik, “Parameters calculation of coupled coils equivalent circuit of EMI filter”, Electrical Review, Aug. 2009.
- [8] S. Pasko, B. Grzesik, F. Beck, “Attenuation of nanocrystalline and ferrite common mode chokes for EMI filters”, 15th International Symposium POWER ELECTRONICS Ee2009, 28th-30th October 2009, Novi Sad, Serbia.
- [9] S. Pasko, F. Beck, B. Grzesik, “Property comparisons of TIGHTpak toroidal and double layer common choke”, Electrical Review, Feb. 2010.
- [10] M. Seitz, M. Roeber “Squeeze more performance out of toroidal inductors, Power Electronics Technology Magazine, pp. 302–33, Aug 2005.
- [11] Actown Electrocoil Inc, “Magnetic core winding method, apparatus and produced there form”, Patent no. US 7.154.368 B2, Dec. 2006.

Energy Efficiency in Electric Drives

Slobodan Mirchevski

Abstract—In this paper a look at energy efficiency in electric drives is taken strongly through energy parameters - efficiency η and power factor k (in special case $\cos \varphi$). Considering electric drive as system of working machine, motor and power converter, the influence of components is evaluated. Induction motor, as the most used in industry, has been treated. The necessary of variable speed drives in dynamic states for reducing electrical losses by help of power converters is presented. The importance of energy efficiency in electric drives on improving technological process, consumed and paid electric energy and global problem of environment pollution is elaborated.

Index Terms—Adjustable Speed Electric Drives, Energy Efficiency, Induction Motor, Power Factor.

I. INTRODUCTION

ENERGY efficiency is the basis of technical systems working. The first great question of this field was DC (T. Edison's practice) or AC system (N. Tesla's invention). And normally, the system with greater possibilities (bigger power, longer distances) and evidently lower losses won. Energy efficiency is always closely related with energy crisis in the world. In the past it has been temporary event, but these days it has become continuous and global problem because of environment pollution. The name has varied from energy saving in early 80-ties, through rational use of energy in 90-ties, to (till) energy efficiency now [16], [17], [18], [19], [20]. Electric drives account for approximately 65% of the electricity consumed by EU industry. Therefore electric drives have the great energy saving potential, technical (higher) and economic (lower) [1], [2], [3], [4], [5], [6].

The efficiency of an electric drive depends on more factors, including: motor efficiency, motor speed control, proper sizing, power supply quality, distribution losses, mechanical transmission, maintenance practices, end-use mechanical efficiency (pump, compressor, fan etc.). The energy efficiency has influence on the work of electric drive, its consumption and paying of electric energy (active, reactive), the working life etc. [21], [22], [23], [24], [25], [26].

Manuscript received 30 May 2012. Accepted for publication 10 June 2012. Some results of this paper were presented at the 16th International Symposium Power Electronics, Novi Sad, Serbia, October 26-28, 2012.

Slobodan Mirchevski is with the Faculty of Electrical Engineering and Information Technologies, University of Ss. Cyril and Methodius, Skopje, Republic of Macedonia (tel: +389-2-3099-149; fax: +387-2-3064-262; e-mail: mirceslo@feit.ukim.edu.mk).

What energy efficiency practice for? The answer is simple - because of getting high quality and cheaper products, lower production costs and reducing of global pollution.

How to realize energy efficiency in electric drives? The right way is with usage of better working machines, power converters for getting variable speed to reduce power losses and energy efficient motors.

This paper strongly deals with energy efficiency in electric drives through energy parameters - efficiency η and power factor k (in special case with ideal supply without harmonics $\cos \varphi$). In fact, efficiency and power factor are in close relation and therefore their product is also used as energy parameter. The working machine as a part of an electric drive is not treated, although it is (comprising its whole distribution ducting) with the greatest savings potential (125 billion kWh/year for EU-25, [4]). It is worth mentioning that pumps, compressors and fans are the most used loads (>60% of all installed working machines), fortunately with mainly centrifugal mechanical characteristics $n(M)$ and the greatest savings potential by using power converters with simple and cheap control system. In this paper, the attention is focused on motor speed control with saving potential of 50 billion kWh/year for EU-25 and motor losses expressed through its efficiency and power factor k with saving potential of 27 billion kWh/year for EU-25, [4].

Low voltage squirrel cage induction motor is considered as "work horse" in industry. Because of its wide, dominant usage, over 65% in all installed drives [1], [8], [9], [20], [27] is taken into consideration.

II. VARIABLE SPEED DRIVE

Variable speed drives with help of power electronics converters are more effective way of improving drive energy efficiency with nearly double savings potential than HEM [4]. In Fig. 1 the losses during starting of induction motor with one speed winding (a), Dahlander's winding for two speeds in ratio 1:2 (b) and continuous changing of speed (c), are presented [9]. It is evident utility of speed control during drive starting, braking, reversing and speed changing.

Losses during starting and counter current braking (plugging) in no load regime ($M_L=0$) are expressed with eq. (1) and eq. (2)

$$A_{Cu_{st}} = J \frac{\omega^2}{2} \quad (1)$$

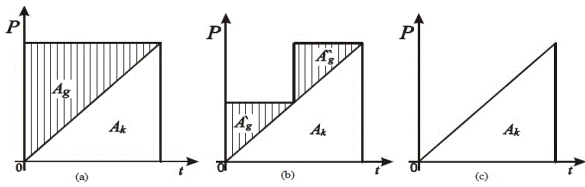


Fig. 1. Losses during starting ($M_L=0$) of IM with one speed winding (a) $\eta=0,5$; Dahlander's winding for two speeds in ratio 1:2 (b) $\eta=0,75$ and continuous changing of speed with ideal power converter neglecting losses (c) $\eta=1$. [9].

$$A_{Cu_{2br}} = 3J \frac{\omega^2}{2} \quad (2)$$

where A_{Cu2} [Ws] are copper losses in the rotor, J [kgm^2] is the moment of inertia and ω [rad/s] is the angular speed. With load the situation becomes worse. It is clear that speed changing is the right solution for reducing losses in dynamic states.

Variable speed is obtained with frequency and voltage power converters, usually of indirect type with DC circuit, called voltage source inverters (VSI). Power electronics converters are also consumers of reactive energy, because of switches nonlinearity. So, in indirect frequency converters the rectifier consumes reactive power from the grid and reactive power is generated in the circuit of the inverter and the motor, because DC circuit does not cross reactive power. The solution of these problems is in using condenser banks and filters, passive or active. However, consumption of reactive and disturbance energy (according to DIN 40110) in power converters is neglected. Objectively this consumption exists and it is approximately a few percentage of the active energy consumption, without costs for condenser banks and filters.

In Fig. 2 [4] conventional pumping system (a) and energy efficient pumping system (b) are presented with their total efficiency 31% and 72%.

The greater initial investment is covered in short period with

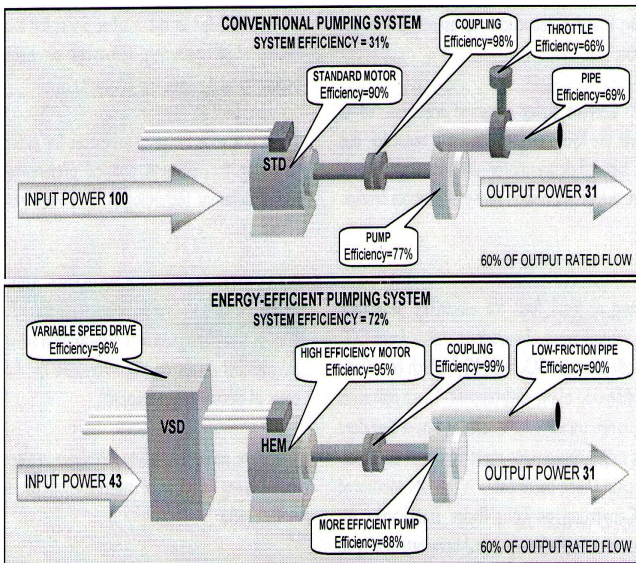


Fig. 2. Conventional pumping system 31% (a); Energy-efficient pumping system 72% (b), [4].

evident energy saving possibilities [18], [19], [20], [21], [22], [23], [24], [25,], [26], [30].

III. INDUCTION MOTOR

The low voltage induction squirrel cage motor is superior to other types of motors because of its good technical characteristics (torque, current, overloading), smaller dimensions and mass, so as lower price. In the power range up to a 100 kW it is a serial product and standards already define the categories of motors with respect to their efficiency [7], [8], [27], [28], [31].

A. Efficiency η

The concept for increasing the efficiency of the motor is to reduce power losses and at the same time achieve all other required characteristics of the machine. The tendencies are directed towards standardization of the values of efficiency required in advance. The efficiency of electric motors can be improved by: a) Reducing the losses in the windings, which is done by increasing the cross-sectional area of the conductor or by improving the winding technique to reduce the length; b) Using better magnetic steel; c) Improving the aerodynamics of the motor; d) Improving manufacturing tolerances. Assuming that we have applied all the knowledge in machine design to reduce power losses in an induction motor (sizing of the air-gap, shape and number of slots, magnetic wedges, optimal choice of the cooling fan, squirrel-cage made of copper instead of aluminium etc.), the possibility of further reduction of losses is by increasing the motor size within reasonable limits (motor frame size, shaft height).

Using the scaling laws for design of electric machines [8], [9], the equation for efficiency η can be obtained

$$\eta = \frac{P}{P + k_{Cu1} a^{(2n-5)} + k_{Fe1} a^{(3-2n)} + P_{meh} + P_{dod}} \quad (3)$$

where P is the rated mechanical shaft power and P_g are the total losses in the motor which consist of the stator and rotor copper losses P_{Cu} , the iron losses P_{Fe} , the friction and windage losses P_{meh} and the additional losses $P_{dod} = 0,005 P_1$ (P_1 is the electric power input from the grid) which are the four addends in the denominator of eq. 3. It is assumed that mechanical losses due to friction and windage will not change significantly due to increased dimensions.

The variation of efficiency is a function of changes of linear dimensions a (max 2) and of the exponent n (0-2), according to scaling laws for specific magnetic load $B=(0,4-1,2)$ [T] and specific electric load $\Gamma < 3 \cdot 10^6$ [A/mm²]. Let assume that we have induction motor with following ratings 22 kW, 380 V, 50 Hz, $2p=2$, $P_{Fe} = 597$ W, $P_{Cu} = 1098$ W, $P_{meh} = 870$ W, $P_{dod} = 110$ W. Using eq. (3) we can obtain the curves in Fig. 3 which showing efficiency η as a function of changes of linear dimensions a and of the parameter n for the motor.

The electric energy saved due to increased efficiency of an electric motor can be calculated from

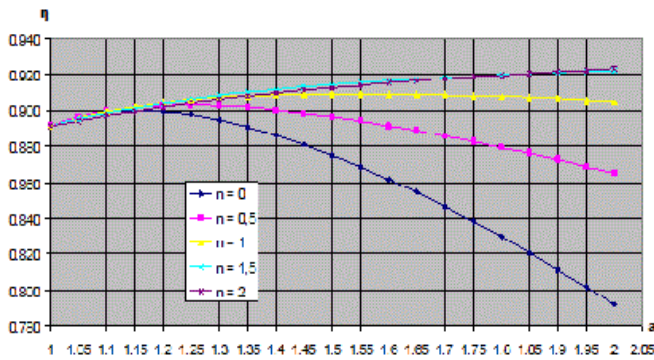


Fig. 3. Family of curves showing efficiency η as a function of changes of linear dimensions a and of the parameter n for the motor.

$$\Delta W_{year} = P_r t_r \left(\frac{1}{\eta_n} - \frac{1}{\eta_v} \right) \text{ kWh} \quad (4)$$

where ΔW_{year} is the annual energy savings in kWh, P_r is the actual power load in kW, t_r is the number of operating hours per year, η_n is the lower efficiency of the motor and η_v is the higher efficiency.

Let us consider a realistic case with presented motor. If dimensions are increased by 25% ($a = 1,25$), in Fig. 3 is shown that the efficiency can be increased at maximum from 0,89159 to 0,90611, i.e. by 1,452%. The annual energy savings thus obtained is 2016,6 kWh. If the exploitation period of the motor is 20 years, the total energy savings equals 40332 kWh. If the average price of electric energy is 0,05 EUR/kWh, the annual savings amounts to 100,83 EUR, and during exploitation period of 20 years it equals 2016,6 EUR.

Motors with improved efficiency are called "High Efficiency Motors" or HEM. Three energy efficiency classes are proposed, Fig. 4, [1], [3], [7], [8], [11], [12], [13], [27], [28], [31]. The fourth class IE4 - Super Premium as informative is also proposed. It is clear that better efficiency is result of greater dimensions (eq. 3) and therefore the price of HEM is greater. The range of payback on individual motors is between several months and several years [4].

In [29] the impact of different lubrication oils on electric motor energy consumption is given.

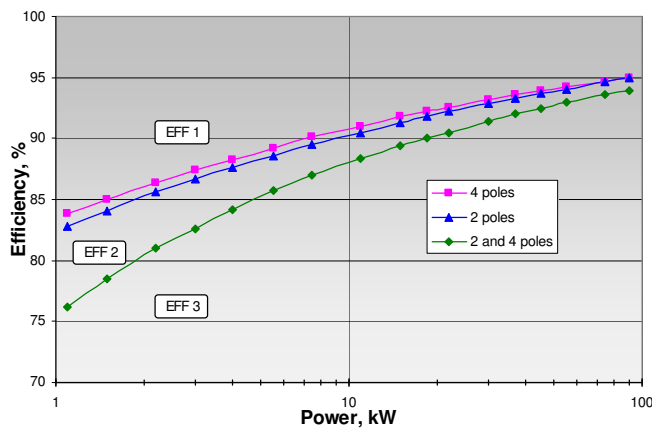


Fig. 4. Efficiency of induction motors according to EuroDEEM classification.

In [32] possibilities for enhancing reliability and efficiency are considered.

B. Power factor k

Reactive power is necessary for induction motor because of magnetization and maintaining the alternating magnetic field. Power factor is the ratio $k = P[\text{kW}]/S[\text{kVA}]$ and it is different from $\cos \varphi$ because of harmonics. The equality is only for ideal sinusoidal supply or $\cos \varphi$ relates to basic harmonic. In Fig. 5 a) and b) $\cos \varphi(P)$ for $2p = 2, 4, 6$ and $P = (0-90)$ [kW] for induction motors according [11] and [15] are presented. In Table I the values of $\cos \varphi$ for different powers of catalogue and speeds of 3000 [min^{-1}], 1500 [min^{-1}] and 1000 [min^{-1}] are shown. Power factor k depends on ratio $\mu = Q[\text{kVAr}]/P[\text{kW}]$, which is better to be lower [10].

$$\mu = Q/P = gp/D \quad (5)$$

where g [m] is air gap between stator and rotor, p is number of pair poles and D [m] is diameter of the stator. It is clear that machines with greater power and greater speed have greater power factor (Fig. 5).

It should be note that power factor is mainly less than 0,9. It means that condenser banks are needed or reactive energy must be paid. In any case, there are certainly costs for reactive energy.

IV. CONCLUSION

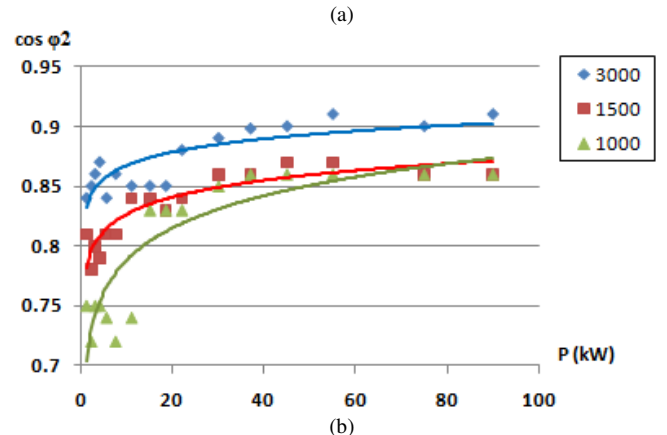
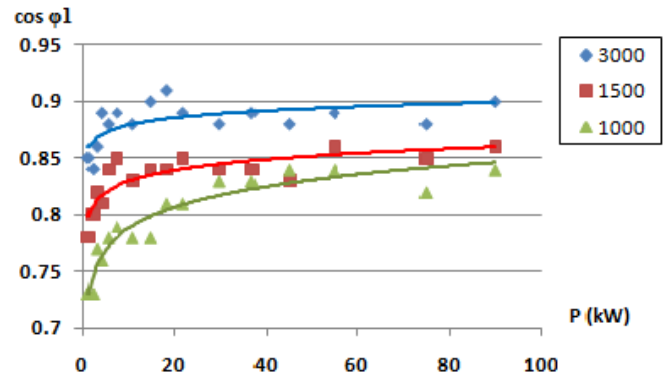


Fig. 5. Power factor ($\cos \varphi$) of fully loaded IM in function of power for different speeds: (a) – ABB ($\cos \varphi_1$), (b) – SIEMENS ($\cos \varphi_2$).

TABLE I
VALUES OF $\cos\phi$ IN FUNCTION OF POWER FOR DIFFERENT SPEEDS
(1 – ABB; 2 – SIEMENS)

$n[\text{min}^{-1}] / P[\text{kW}]$		1.1	3	5.5	11	15	22	30	45	55	75	90
3000	cos ϕ_1	0.85	0.86	0.88	0.88	0.90	0.89	0.88	0.88	0.89	0.88	0.90
	cos ϕ_2	0.84	0.86	0.84	0.85	0.85	0.88	0.89	0.90	0.91	0.90	0.91
1500	cos ϕ_1	0.78	0.82	0.84	0.83	0.84	0.85	0.84	0.83	0.86	0.85	0.86
	cos ϕ_2	0.81	0.80	0.81	0.84	0.84	0.86	0.87	0.87	0.86	0.86	0.86
1000	cos ϕ_1	0.73	0.77	0.78	0.78	0.78	0.81	0.83	0.84	0.84	0.82	0.84
	cos ϕ_2	0.75	0.75	0.74	0.74	0.83	0.83	0.85	0.86	0.86	0.86	0.86

The cost of electric energy during the exploitation period of the motor can be from 100 to 200 larger than the price of the motor [8].

Reactive and disturbance energy cannot be neglected in considerations in energy efficiency, as it is usually done.

Electric drives have great saving potential with total 202 billion kWh/year, equivalent to a reduction of 10 billion EUR per year in operating costs for industry. It would also create the following additional benefits:

- a saving of 5-10 billion EUR per year in operation costs for industry through reduced maintenance and improved operations (EU-25),
- a saving of 6 billion EUR per year in reduced environmental costs (EU-25),
- a reduction of 100 million tonne of CO₂ equivalent emissions, or approximately 30% of the EU's Kyoto target of 336 million CO₂ eq. (EU-25),
- a 45 GW reduction in the need for new power plant over the next 20 years (EU-25),
- a 6% reductions in EU's energy imports (EU-25), [4].

To achieve this a 4 year (2008-2012) package of measures is suggested, investing 400 million EUR in the electric drives market [4].

The package of measures should include stimulation of industry through national governments solutions and financial support for wide education and training possibilities in universities and industry.

REFERENCES

- [1] Anibal de Almeida, Paolo Bertoldi, Werner Leonhard (Editors), *Energy Efficiency Improvements in Electric Motors and Drives*, Springer-Verlag Berlin, Heidelberg, 1997.
- [2] Energy Efficiency, ABB Review, 2/2007.
- [3] <http://energyefficiency.jrc.cec.eu.int/eurodeem/index.htm>
- [4] <http://re.jrc.ec.europa.eu/energyefficiency/motorchallenge/index.htm>
- [5] <http://www.gefweb.org>
- [6] <http://www.cda.org.uk/megab2/elecapps/casestud/index.htm>
- [7] Miloje M. Kostic, *Efficiency Classes Induction Motors and Saving Energy*, (invited paper IP4-1), 14-th International Symposium on Power Electronics Ee 2007, Novi Sad, Serbia, 7-9 November, 2007.
- [8] Drago Ban, Damir Zarko, Slobodan Mircevski, *State of the Art and Tendency for Increased Power Efficiency of Electric Machines and Drives*, 6-th Conference of Mako CIGRE, Ohrid, Macedonia, 4-6 October, 2009.
- [9] Berislav Jurkovic, *Electric Drives*, School Book, Zagreb, 1987 (3-rd ed. in Croatian).
- [10] Leonid Geiler, *Basic Electric Drives*, Minsk, 1972 (in Russian).
- [11] Catalogue ABB, *BU/Process performance motors*, GB 09-2003.
- [12] <http://www.abb.com/motors&drives>
- [13] <http://online.abb.com/motors&drives>
- [14] Katalog M 11 SIEMENS, *Drehstrom-Niederspannungsmotoren Kfifglauermotoren*, 1994/95.
- [15] <http://www.siemens.com/motors>
- [16] T. D. Jakimov, S. Mircevski, *The influence of voltage reducing on the on the work of drives with induction motors*, II conference Electric Drives, Trogir, 24-26 april, 1984 (pp. 331-340, in Serbian).
- [17] S. Mircevski, R. Ackovski, *Determination of satisfactory power factor for under loaded electric drives with induction motors*, III conference Electric Drives, Dubrovnik, 22-24 april, 1986 (pp. 419-425, in Serbian).
- [18] S. Mircevski, G. Arsov, D. Manov, M. Sarevski, Z. Andonov, G. Rafajlovski, D. Andonov, *Rational use of electric energy in AC drives*, (invited paper), 8-th Ee'95 (pp. 45-53), Novi Sad, Yugoslavia, September 27-29, 1995.
- [19] S. Mircevski, Z. Kostic, *Energy saving possibilities with pump's AC adjustable speed drives*, Proceedings of the IASTED international conference High technology in the power industry, Banff, Canada, 6-8 June, 1996 (pp. 164-167).
- [20] S. Mircevski, D. Manov, G. Arsov, M. Sarevski, D. Andonov, G. Rafajlovski, Z. Andonov, *Rational use of electric energy in AC drives* (3 years scientific investigation project financed of the R. Macedonia Ministry for education and science), 1994-96.
- [21] F. Saracevic, D. Miceski, A. Buckovski, Z. Andonov, S. Mircevski, Z. Kostic, *Rational usage of electrical energy in pump drives*, 6-th International Cultural and Academic Meeting of Engineering Students (ICAMES) Proceedings, Bogazici University, Istanbul, Turkey, 13-20 may, 2000 (pp.178-185).
- [22] The European Motor Challenge Programme, *Drives Module*, Brussels, 2003.
- [23] The European Motor Challenge Programme, *Pumping Systems Module*, Brussels, 2003.
- [24] The European Motor Challenge Programme, *Fan Systems Module*, Brussels, 2003.
- [25] The European Motor Challenge Programme, *Compressed Air Systems Module*, Brussels, 2003.
- [26] The European Motor Challenge Programme, *Active Systems for Refrigeration and Cooling Module*, Brussels, 2003.
- [27] Bonnet, Ch. Yung, *Increased Efficiency Versus Increased Reliability*, *IEEE Industry Applications Magazine*, January/February 2008, Vol. 14, No. 1 (pp. 29-36).
- [28] J. F. Fuchsloch, W. R. Finley, R. W. Walter, *The Next Generation Motor*, *IEEE Industry Applications Magazine*, January/February 2008, Vol. 14, No. 1 (pp. 37-46).
- [29] D. Evans, J. Crissman, J. Gobert, *Test Results for Energy Savings*, *IEEE Industry Applications Magazine*, January/February 2008, Vol. 14, No. 1 (pp. 44-49).
- [30] Lockley, B. Wood, R. Paes, F. De Winter, *Standard 1566 for (Un)Familiar Hands*, *IEEE Industry Applications Magazine*, January/February 2008, Vol. 14, No. 1 (pp. 21-28).
- [31] W.R. Finley, B. Veerkamp, D. Gehring, Ph. Hanna, *Improving Motor Efficiency Levels Globally*, *IEEE Industry Applications Magazine*, January/February 2009, Vol. 15, No. 1 (pp. 39-49).
- [32] Ch. Yung, *Tips for Improving Motor Efficiency*, *IEEE Industry Applications Magazine*, November/December 2007, Vol. 13, No. 6 (pp. 12-20).

Power Electronic Transformer Technology for Traction Applications – An Overview

Dražen Dujic, Frederick Kieferndorf, and Francisco Canales

Abstract—Combining modern high-power semiconductor devices with constantly improving magnetic materials opens up the possibility to replace bulky low-frequency transformers with a new medium voltage medium frequency conversion structure. While there are still challenges to be addressed related to these so called power electronic transformers, a steadily increasing development effort is evident and considered in various contexts. Traction applications seem to be the first ones where proliferation of these galvanically isolated power electronic converters is expected. In this application field, substantial weight and volume reduction can be achieved while providing additional functionality at the same time. In this paper a survey of recent R&D efforts in this field is presented.

Index Terms—Power Electronic Transformer, Railway, Medium Frequency Transformer, Multilevel Converter.

I. INTRODUCTION

NOWADAYS, conventional line frequency transformers (LFT) are widely spread in electrical systems providing basic functionalities such as voltage isolation and voltage adaptation. However, to deal with power quality problems (e.g., sags, swells, flicker and harmonics) at medium voltage (MV) levels, there is a need for the installation of additional equipment (usually some kind of power electronics converter operating at higher switching frequencies). This leads to a further increase of the installation volume, which in certain applications may not be feasible (traction, marine, wind, offshore). Recent trends in MV high power applications are replicating something that has already been achieved and put into practice in low voltage applications. There, line frequency operated transformers have mostly been replaced by medium frequency transformers (MFTs) where high frequency waveforms are applied directly to the transformer terminals, so that the overall magnetic volume is reduced and more compact converter designs are reached. Some of the results from this field are presented here, with the scope of this paper being

Manuscript received 30 May 2012. Accepted for publication 10 June 2012. Some results of this paper were presented at the 16th International Symposium Power Electronics, Novi Sad, Serbia, October 26-28, 2012.

D.Dujic, F.Kieferndorf and F.Canales are with the ABB Switzerland Ltd, Corporate Research, Segelhofstrasse 1K, Baden-Daettwil, 5405, Switzerland (+41 58 586 75 40; fax: +41 58 586 40 06; e-mail: drazen.dujic@ch.abb.com, frederick.kieferndorf@ch.abb.com, francisco.canales@ch.abb.com).

limited to railway applications (thus, single phase).

Traction applications are recognized as one of the likely early adopters of this emerging technology. Typical single phase railway AC lines found in Europe are 15kV, 16 $\frac{2}{3}$ Hz (originating from the use of cycloconvertors in the past and thus being one third of 50Hz) and 25kV, 50Hz. A conventional (state-of-the-art) approach to provide DC voltage to the variable speed drive on the locomotive is illustrated in a simplified manner in Fig.1. The primary winding of the LFT is connected directly to the AC catenary and active rectifier(s) are connected to the secondary winding(s) of the transformer where the voltage is stepped down. One or more inverter and motor units are further connected to the provided DC link (not illustrated in Fig.1). Since traction LFTs are usually optimized for minimum weight (2-4kg/kVA) and are heavily loaded, the resulting efficiency is rather poor and somewhere in the range of 90%-92%. Oil is customarily used for cooling and insulation, adding to the total weight and potential environmental issues (i.e. in case of leakage). The power of the system may vary from below 1MVA up to 10MVA for large cargo locomotives.

In a classical train arrangement, where the propulsion system is concentrated in the locomotive, the weight of a LFT is not necessary a problem, since a certain weight is required in any case in order to provide sufficient traction without slipping. However, in the case of electric multiple units (EMUs), where the propulsion system is distributed throughout the train, weight becomes an issue.

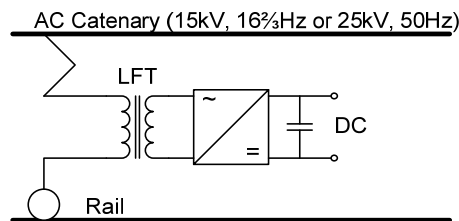


Fig. 1 AC-DC conversion with a line frequency transformer (LFT).

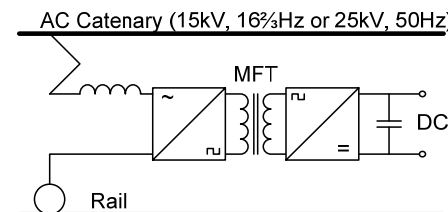


Fig. 2. AC-DC conversion with medium frequency transformer (MFT).

An alternative to the state-of-the-art solution is the use of a so called power electronic transformer (PET), consisting of a power converter in conjunction with MFT(s), as illustrated in Fig.2. Here, some sort of power electronic converter is connected directly to the AC catenary, while the MFT is providing voltage insulation and adaptation.

Present semiconductor devices are unable to work directly with these medium voltages and thus usually some of kind of series connection of a number of cells or modules is required in order to meet the voltage level of the MV line, resulting in a multilevel converter structure. The MFT from Fig.2 is usually realized not as one single transformer (although in some implementations it is), but rather as a number of transformers rated for a fraction of the total power and operating at a higher switching frequency (several kHz). Finally, rectification is required on the secondary side of the MFT in order to provide a DC link to the inverter(s).

This type of MV technology (although still under development) is becoming a reality with the advances in semiconductor technology (faster switching actions, higher blocking voltages and higher power densities) and the development of new magnetic materials with low loss densities at higher operating frequencies. Even though early considerations regarding PET can be traced back to the seventies [1], at the present time there are still no products of this kind offered by any of the key players in the traction market.

II. STATE-OF-THE-ART: PET ARCHITECTURES

Various architectures/topologies have been considered for the realization of a PET for tractions applications. Early works considered the use of thyristor based solutions [1], [2], as illustrated in Fig.3. The primary side of the MFT consists of two thyristor H-bridges connected in anti-parallel while the secondary side has a single phase forced commutated H-bridge. Thus, there is a cycloconverter at the input (HV side) and voltage source inverter (VSI) at the output (LV side).

In this implementation, the MFT is excited from the secondary side by the VSI and the MFT voltage is used to commutate the cycloconverter on the primary side. Use of thyristors limits the MFT frequency to a few hundreds of Hertz. In addition to low frequency, the circuit also generates fairly high line harmonics and improvements in this direction are reported in [3].

To mitigate some of the issues with the thyristor based approach and further increase the operating frequency of the MFT, the use of fully controllable devices such as IGBTs has been proposed [4], [5]. In [4], the cycloconverter from Fig.3 has been realized using IGBTs (series connection of two IGBTs with common emitter as a replacement for two anti-parallel thyristors) using at the same zero voltage switching (ZVS), while the VSI is realized as a standard IGBT H-bridge converter. However, to achieve the line voltage, a series connection of a number of IGBTs is required considering that, at present, the highest blocking voltage of commercially

available IGBTs is only 6.5kV.

Thus, a modular structure consisting of a number of cascaded cells (which are of the same nature as those in Fig.3, but realized with IGBTs) has emerged, as shown in Fig.4. In this arrangement, thanks to the voltage clamping of the secondary side DC voltage through the MFT to the primary side, voltage sharing among the different cells is achieved. At the same time, a multilevel voltage waveform at the input of the PET helps to reduce the line harmonics and the resulting filter requirements. In contrast to Fig.3, instead of having a single MFT, there is a need for a number of MFTs, each connected to an associated cell and rated for a fraction of the full power. However, insulation requirements are not relaxed and each MFT must be designed for the same dielectric stress as before.

A PET prototype based on the topology from Fig.4 has been presented in [5], targeting 15kV, 16 $\frac{2}{3}$ Hz railway network and with 1.2MVA ratings (continuous operation). The implementation had a total of 16 cells each consisting of a cycloconverter, MFT and VSI (rectifier). 3.3kV IGBTs were used on both primary and secondary sides, while the MFT was operated with 400Hz (see Fig.5).

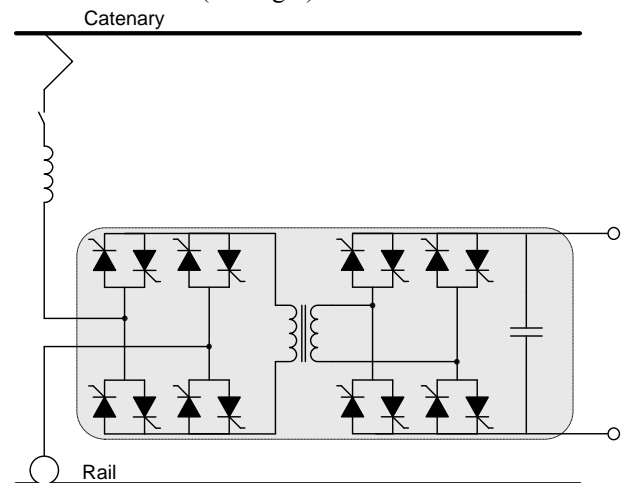


Fig. 3. PET topology with source commutated primary converter.

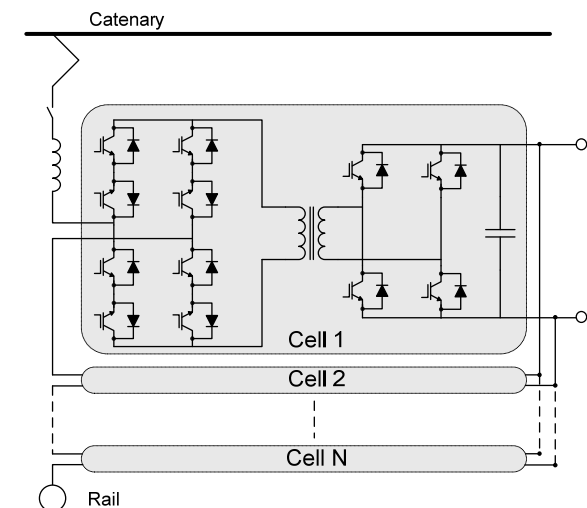


Fig. 4. PET topology with cascaded source commutated primary converters.



Fig. 5. ABB PET prototype (2006) using topology from Fig.4 [5].

To avoid the difficulties with cycloconverters on the primary side of the MFT and considering the fact that a number of cells is required anyhow, cascaded H-bridges (four quadrant converters) have been proposed by various research groups [6-10 all references]. In this way, a pure IGBT solution is achieved and the number of required cells is primarily related to the selected voltage class of the semiconductors.

In [6], a topology similar to the one shown in Fig.6, was proposed (the main difference is a lack of capacitors connected to the MFT, thus being a non-resonant converter). The input stages are realized with four quadrant converters and provide the intermediate DC links as well as a high resolution multilevel waveform at the input of the converter. DC/DC converters are connected to each of the floating DC links and provide galvanic isolation and voltage level adaptation to the secondary side (as before all converters are connected in parallel at the output). Power flow control is achieved through manipulation of the phase shift between the rectangular waveforms of the two sides of the DC/DC converter. Various reconfiguration possibilities of this kind of topology are discussed by the same group of authors in [7].

A topology identical to the one shown in Fig. 6 has been presented in [8], [9]. A series resonant DC/DC converter is proposed in order to reduce switching losses of the semiconductors (zero voltage switching (ZVS) and zero current switching (ZCS)) and allow for further increase of the MFT operating frequency. For a 15kV railway network using 6.5kV IGBTs, it was calculated that 7 cells would be required for nominal operation (although adding an extra cell for redundancy reasons is proposed) and the MFT frequency was expected to be in the range of 8-10 kHz. Some details about the control of this kind of PET can be found in [10].

More considerations regarding the topology of Fig.6 can be found in [11], [12]. Various arrangements have been analyzed and 6.5kV devices were selected as the most suitable ones, considering failure-in-time (FIT) rates and the number of devices needed. To increase the switching frequency, a soft switching series resonant DC/DC converter with half bridges on both sides of the MFT is considered. In addition to standard IGBTs, modified semiconductor devices were tested

as well. In particular, standard IGBTs were irradiated with electrons in order to move the device properties on the technology curve towards the area of lower turn off energies (reduction of carrier lifetime) but at the expense of higher on-state voltage drop and thus higher static (conduction) losses. Reported results emphasized the possible increase of the switching frequency in the range of 40-50% (at rated power). However, these kinds of devices are not commercially available yet, except for limited engineering samples.

A slightly different approach has been presented in [13]-[15] where multi-winding MFTs are used. The primary side is again realized with a series connection of H-bridges providing intermediate HV side DC links from which the primary windings of the multi-winding MFT are excited by half-bridge series resonant converters operating at 5kHz. The secondary side is realized using a single H-bridge converter with bidirectional power flow. A full scale 1.5MW PET prototype was realized featuring 8 cells in total (7 without redundancy). The mass of the PET prototype was reported as 3.1T, in comparison to 6.8T for a conventional LFT, however, at the expense of 50% higher cost and jeopardized reliability due to the use of 48 6.5kV IGBTs on the primary side of the multi-winding MFT. The authors advertised upcoming field trials using the developed PET prototype, but no further results were reported.

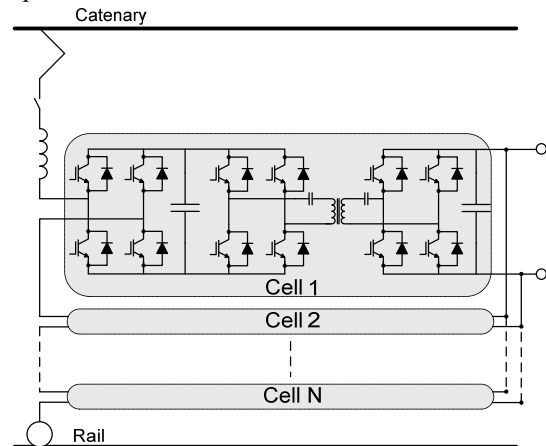


Fig. 6. PET topology with cascaded H-bridges and resonant/non-resonant DC-DC stages.

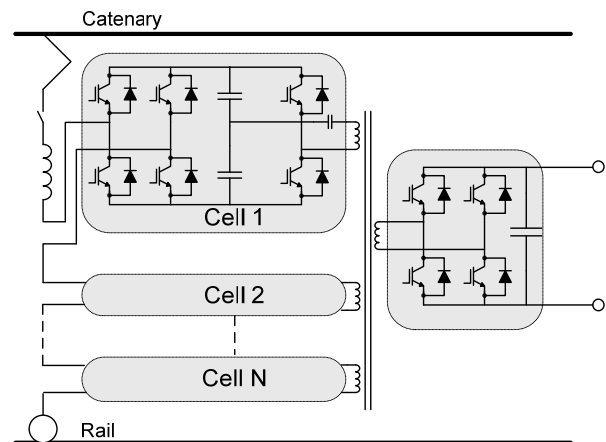


Fig. 7. PET topology with cascaded H-bridges and multi-winding MFT.

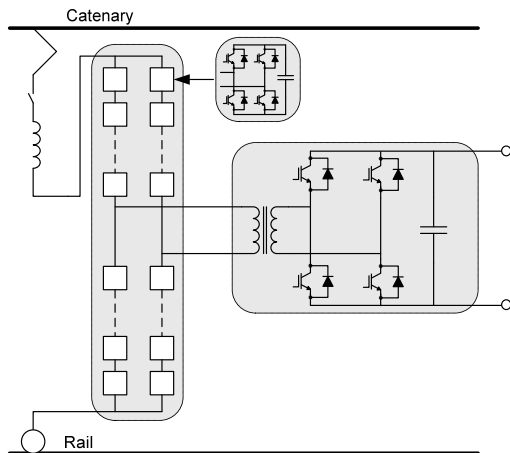


Fig. 8. PET topology using M2LC converter.

Use of a modular multilevel converter (M2LC) for traction applications has been presented in [16], [17]. A simplified layout is shown in Fig.8 (in the original publication there are multiple secondary windings of the MFT with dedicated active rectifiers, inverters and motors). M2LC is a highly modular topology and the basic building blocks (cells) for traction applications are H-bridges connected in series, each with its own DC capacitor bank, finally resembling a sort of large composite H-bridge, as shown in Fig.8. M2LCs are associated with large amounts of stored energy in each cell but with low energy density per cell, adding to the weight and volume of the whole system. So far, in real world applications M2LC has been successfully commissioned only for HVDC installations.

The most recent reports concerning PETs in traction application are reported in [18]-[20]. The topology is shown in Fig.9 and similar to the previous example it consists of cascaded H-bridges at the input and resonant DC-DC converters with the power stage realized using a half-bridge configuration. Also, in contrast to the LC series resonant tank employed in [8], [9] and [13]-[15], a LLC resonant tank is used. Thus, both the leakage inductance and the magnetizing inductance of the transformer are participating in the resonance. In this way ZVS is achieved during turn-on of the IGBTs while near ZCS is achieved during turn-off of the IGBTs. Some results regarding the design and preliminary testing of a DC/DC LLC resonant converter are presented in [18].

In [19] the development of a low voltage PET prototype is presented, focusing primarily on the control features required for characteristic operating regimes in traction applications. The LV PET, shown in Fig.10, was used as an analogue hardware simulator since the implemented control HW was identical to that used later in the full size PET reported in [20]. The full sized MV PET prototype, shown in Fig.11, is designed for a 15kV, 16 $\frac{2}{3}$ Hz railway network with a 1.2MVA power rating (1.5kV output voltage) and is realized with 8 cells (+1 for redundancy) and a MFT operating at 1.8kHz.

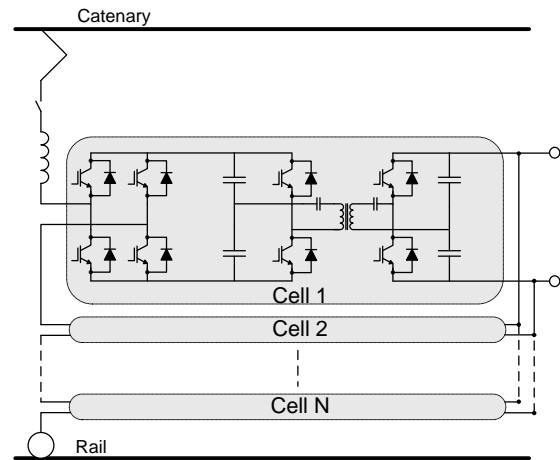


Fig. 9. PET topology with cascaded H-bridges and resonant (LLC) DC-DC stages.



Fig. 10. ABB low voltage PET prototype (2011) [19].



Fig. 11. ABB PET prototype (2011) [20].

A full set of experimental results is reported in the paper, illustrating various operating conditions in steady state and during transients as well. The PET prototype was developed for a field trial with Swiss Federal Railways and during the preparation of this paper it was already installed on the locomotive and electrically commissioned. Since February 2012, the PET prototype is in service for a one year field trial.

III. MEDIUM FREQUENCY TRANSFORMER

Details related to the MFT implementation were deliberately omitted from the previous section, since this topic is difficult enough on its own, and due to the space limitations it is discussed here on a rather general level. Therefore, the basic problems that are encountered in the design phase of an MFT are highlighted and some examples are illustrated.

The size of a transformer can typically be related to the area product, A_p , defined as [22]:

$$A_p = \frac{P_t}{K_f K_u B_m J f} \quad (1)$$

When designing a MFT, all of the parameters present in (1) must be carefully considered. The main idea behind the PET is to replace the bulky LFT with an overall more compact MFT or MFTs operating at a higher frequency (f), normally in the range of several kHz. While increasing the operating frequency (f) leads to a reduction of transformer size (A_p), high insulation requirements have a negative effect on the window utilization factor (K_u), resulting in a low filling factor of the window area due to the required amount of insulating material. This is especially true in the case of the MFT for PET, where due to the lack of applicable standards, the MFT is usually designed to meet the same requirements as the direct AC line connected LFT. Therefore, the required level of insulation is nearly independent of all the other parameters in (1) since it is purely related to the system requirements. Considering that the MFT is driven by rectangular rather than sinusoidal waveforms, the K_f factor which relates to the waveform shape is different relative to a LFT. At the same time, the Steinmetz parameters and associated core losses for the selected material at a particular frequency are determined assuming sinusoidal excitation, which makes preliminary loss estimations rather inaccurate, and experimental characterization is often required. Materials usually considered for the MFT are: nanocrystalline, amorphous iron and/or ferrites.

The winding current density (J) is directly linked to the required cooling effort to remove generated heat from the winding, thus having a huge impact on the selection of the cooling method. On the other hand, selection of different core materials leads to different maximum operating flux density (B_m) and has an impact on the MFT size as well. Finally, combining the requirements for high power (P_t), high insulation (K_u), simple cooling (J) and lower flux densities (B_m) of suitable materials for the frequencies (f) of interest the design of a high insulation, high power, MFT is not a straightforward task. On top of that, since it is desirable to integrate elements of the resonant tank into the MFT there is a need to precisely control transformer inductances (leakage and magnetizing) for proper resonant operation, which introduces further complications into the design. The need to operate at higher switching frequencies requires low leakage inductance which is at odds with the high insulation requirements which typically results in higher leakage.

Considering selection of different core materials, silicon

steel is used in [5], nanocrystalline in [20,24], ferrites in [13] while amorphous iron is used in [23]. Regarding the cooling and insulation, oil is used in both [5] and [20], de-ionized water for cooling of windings is used in [23,24], while insulation is also provided by oil in [24]. Two particular examples are illustrated in Fig.12 and 13.

The MFT shown in Fig.12 is realized using amorphous iron core material with a coaxial winding structure and active de-ionized water cooling through the space available between the primary and secondary windings. The prototype was designed for 350kW and 10kHz switching frequency. The respective insulation voltage testing is performed at 38kV and 50Hz for 60 seconds, while the rated impulse voltage is 95kV. The use of coaxial type windings limits the turns ratio to 1:1, which was acceptable in the case analyzed in [23]. Special attention was paid to properly assess the dielectric stress across the MFT in order to provide a design that could guarantee a long lifetime.

A different design is shown in Fig.13 [20]. It features an assembly with three MFTs, each rated for 150kW (with the ability to withstand 225kW overload for 60 seconds) and an operating frequency of 1.8kHz. The insulation test voltage and rated impulse voltage are similar to the previous case. The material used for the core is nanocrystalline and the oil direct air forced (ODAF) cooling method is applied (the whole structure being immersed into the oil), which solves the problem of insulation at the same time. This type of MFT was installed in the 1.2MVA PET prototype shown in Fig.11, in the oil filled tank visible at the bottom of the structure in Fig.11. The inductive elements required for proper resonant operation are realized as the leakage and magnetizing inductance of the MFT.

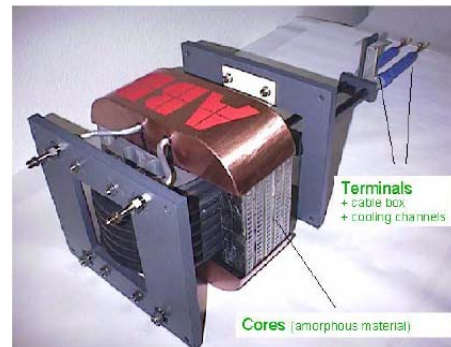


Fig. 12. ABB MFT prototype (2002) [23].

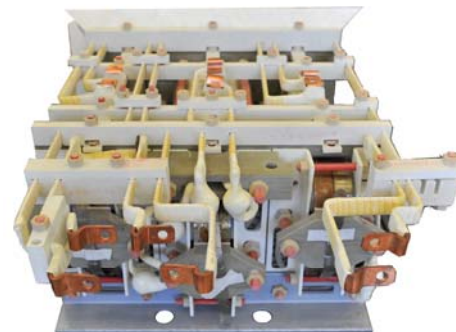


Fig. 13. ABB MFT prototype (3 pieces) (2011) [20].

IV. GENERAL REMARKS

Something that is not shown in any of the figures in section 2 and should be mentioned, since it is always considered in traction applications, is the presence of the 2nd harmonic ripple in the DC link, which is an inherent property of single phase systems. In the original publications, referenced throughout section 2, the 2nd harmonic filter (LC) is usually found on the low voltage secondary side of the MFT. As an example, in [13], the weight of the 2nd harmonic filter is 385kg, which compared to the weight of the rest of a system (around 3085kg) is more than 12%. The amount of the 2nd harmonic ripple is directly related to the power consumed during operation, and it can be partly suppressed by oversizing of the DC link capacitors and increasing the amount of energy stored locally.

At the input of the PET, there is a need for a line inductor, since the input stage is a four quadrant converter with power factor capability, in essence a boost type converter. Taking into account the frequency cancellation due to phase-shifted operation of the power modules, the resulting size of the inductor is minimized. However two additional considerations must be taken into account. The first one is related to the use of this inductor to also filter the line harmonics, for which a higher value is usually needed than that required for boost operation. In addition, if the line inductor is used to limit short circuit in case of a fault, the required value increases even further (e.g. in [20] 180mH air core inductor is used at the input of the PET prototype).

On a more general note, the main concerns preventing PET proliferation into the market are the reliability and cost of the technology. The reliability question comes simply from the fact that in order to realize a medium voltage multilevel converter, a high number of semiconductors is needed. Even if their FIT rates are reasonably low, there are other electronics boards (e.g. gate drivers, controls hardware, etc.) which have higher FIT rates (more prone to failure). One way to tackle this issue is to provide redundancy inside the converter and thus effectively increase the availability of the system. Since availability is driven by time lost (see (2)) and, if due to the high part count, the mean time between failure (MTBF) is low (reliability is low or FIT rates are high) then by making the mean time to repair (MTTR) as short as possible, one can still maintain a high availability.

$$A = \frac{MTBF}{MTBF + MTTR} \quad (2)$$

This implies that the converter should be as modular as possible so that the faulty part can be exchanged quickly. The philosophy behind the operation of a modular PET is that with all cells installed in the system, (minimum number +1), in the case of failure of any one cell, the faulty cell will be removed (bypassed) from the system. In this way, the system will continue operation with the remaining healthy cells. Note that while in operation with the minimum number of cells, the PET system can still deliver the full power to the output.

The cost issue is difficult to describe in simple terms since

it depends on many factors. In [14] a cost increase of around 50% compared to the conventional technology, was reported. This is not the whole story though, because a PET can provide more efficient energy conversion compared to the conventional solution, and this is in the range of 2-4%. Additionally the harmonic performance is improved when compared with the low frequency transformer approach. If this is provided in a smaller installed volume and with less weight than the conventional solutions, it creates further energy savings potential besides an improvement in passenger comfort, thus giving PET technology a strong potential in railway applications. The potential savings due to improved efficiency can also partly offset the higher cost of installation and for a clear understanding the total cost of ownership (TCO) must be considered. This issue is not simple and should be studied in more detail and will be addressed by the authors in the future.

V. CONCLUSION

Power electronic transformers, providing a reduction in weight and volume accompanied by additional functionalities, are considered a viable solution for the replacement of bulky low-frequency transformers. This is especially true for those operating from a 16 $\frac{2}{3}$ Hz railway grid. Designing such a converter system is not a straightforward task, and some of the challenges that are reported in the literature are presented here in this paper. PET offers certain advantages over the conventional solution, such as a reduction of weight and volume, improved efficiency and more control flexibility towards grid disturbances. Functional properties of this kind of technology have been demonstrated previously by many authors but still more integration work aiming at cost reduction is required before a first implementation will be seen on the market. In meantime, a great milestone has been achieved recently by successfully commissioning and putting into operation a world's first ever power electronic transformer on a locomotive that is in regular service [25].

REFERENCES

- [1] H.Meniken: "Stromrichtersystem mit wechsel-spannungs-zwischenkreis und seine anwendung in der traktionstechnik" PhD thesis, Fakultät für Elektrotechnik, RWTH Aachen, Aachen, Germany, 1978.
- [2] S.Östlund: "A primary switched converter system for traction applications" PhD thesis, Royal Institute of Technology, KTH, Stockholm, Sweden, 1992.
- [3] S.Östlund: "Reduction of transformer rated power and line current harmonics in a primary switched converter system for traction applications", *The 5th European Conf. on Power Electronics and Applications – EPE*, Brighton, UK, 1993, pp. 112-119.
- [4] P.C.Kjaer, S.Norrgra, S.Östlund: "A primary-switched line-side converter using zero-voltage switching", *IEEE Trans. on Industry Applications*, Vol. 37, No. 6, 2001, pp. 1824-1831.
- [5] N.Hugo, P.Stefanutti, M.Pellerin, A.Akdag: "Power electronics traction transformer", *The 12th European Conf. on Power Electronics and Applications – EPE*, Aalborg, Denmark, 2007, CD-ROM paper: 0715.
- [6] A.-C.Rufer, N.Schibli, V.Brignet: "A direct coupled 4-quadrant multilevel converter for 16 $\frac{2}{3}$ Hz traction systems", *The 6th International Conference on Power Electronics and Variable Speed Drives*, Nottingham, UK, 1996, pp.448-453.

- [7] A.Rufer, N.Schibli, C.Chabert, C.Zimmermann: "Configurable front-end converters for multicurrent locomotives operated on 16 2/3 Hz AC and 3kV DC systems", *IEEE Trans. on Power Electronics*, Vol. 18, No. 5, pp. 2003, 1186-1193.
- [8] M.Steiner: "Seriegeschaltete Gleichspannungs- zwischenkreis-umrichter in Traktionsanwendungen am Wechselspannungs-fahrdraht, Phd thesis, ETH, Zürich, Switzerland, 2000.
- [9] M.Steiner, H.Reinold: "Medium frequency topology in railway applications", *The 12th European Conf. on Power Electronics and Applications – EPE*, Aalborg, Denmark, 2007, CD-ROM paper: 0585.
- [10] H.Iman-Eini, Sh.Fahangi, J.L.Schanen, M.Khakhbazan-Fard: "A modular power electronic transformer based on a cascaded H-bridge multilevel converter", *Electric Power System Research*, vol. 79, no. 12, 2009, pp. 1625-1637.
- [11] J.Weigel, A.Nagel, H.Hoffmann: "High voltage IGBTs in medium frequency traction power supply", *The 13th European Conf. on Power Electronics and Applications – EPE*, Barcelona, Spain, 2009, CD-ROM paper: 0804.
- [12] H.Hoffmann, B.Piepenbreier: "High voltage IGBTs and medium frequency transformer in DC-DC converters for railway applications", *International Symposium on Power Electronics, Electrical Drives, Automation and Motion – SPEEDAM*, Pisa, Italy, 2010, pp. 744-749.
- [13] B.Engel, M.Victor, G.Bachmann, A.Falk: "15kV/16.7Hz energy supply system with medium frequency transformer and 6.5kV IGBTs in resonant operation", *The 10th European Conf. on Power Electronics and Applications – EPE*, Toulouse, France, 2003, CD-ROM paper: 1192.
- [14] J.Taufiq: "Power electronics technologies for railway vehicles", *International Power Conversion Conference – PCC*, Nagoya, Japan, 2007, pp. 1388-1393.
- [15] M.Mermet-Guyennet: "New power technologies for traction drives", *International Symposium on Power Electronics, Electrical Drives, Automation and Motion – SPEEDAM*, Pisa, Italy, 2010, pp. 719-723.
- [16] M.Glinka, R.Marquardt: "A new AC/AC-multilevel converter family applied to single-phase converter", *The 5th International Conf. on Power Electronics and Drive Systems, PEDS*, vol. 1, Singapore, 2003, pp. 16-23.
- [17] M.Glinka, R.Marquardt: "A new single phase AC-AC-multilevel converter for traction vehicles operating on AC line voltage", *The 10th European Conf. on Power Electronics and Applications – EPE*, Toulouse, France, 2003, CD-ROM paper: 0132.
- [18] D.Dujic, S.Lewdeni-Schmid, A.Mester, C.Zhao, M.Weiss, J.Steinke, M.Pellerin, T.Chaudhuri: "Experimental characterization of LLC resonant DC/DC converter for medium voltage applications", *International Power Conversion and Intelligent Motion Conference – PCIM*, Nürnberg, Germany, 2011, CD-ROM paper: 043.
- [19] D.Dujic, A.Mester, T.Chaudhuri, A.Coccia, F.Canales, J.Steinke: "Laboratory scale prototype of a power electronic transformer for traction applications", *The 14th European Conference on Power Electronics and Applications – EPE*, Birmingham, UK, 2011, CD-ROM paper: no. 0023.
- [20] C.Zhao, S.Lewdeni-Schmid, J.K.Steinke, M.Weiss, T.Chaudhuri, M.Pellerin, J.Duron, P.Stefanutti: "Design, implementation and performance of a modular power electronic transformer (PET) for railway application", *The 14th European Conf. on Power Electronics and Applications – EPE*, Birmingham, UK, 2011, CD-ROM paper. 0214.
- [21] A.Coccia, F.Canales, H.R.Riniker, G.Knapp, M.Kalbermatten, M.Baldinger, P.Barbosa: "Very high performance AC/DC/DC converter architecture for traction power supplies", *The 13th European Conf. on Power Electronics and Applications – EPE*, Barcelona, Spain, 2009, CD-ROM paper: 0384.
- [22] C.Wm.T.McLyman: "Transformer and inductor design handbook", *Marcel Dekker Inc*, 2004.
- [23] L.Heinemann: "An actively cooled high power, high frequency transformer with high insulation capability", *The 7th Applied Power Electronics Conf. and Exposition-APEC*, Dallas, TX, 2002, pp. 352-357.
- [24] H.Hoffmann, B.Piepenbreier: "Medium frequency transformer in resonant switching dc/dc-converters for railway applications", *The 14th European Conf. on Power Electronics and Applications – EPE*, Birmingham, UK, 2011, CD-ROM paper. 0541.
- [25] M.Claessens, D.Dujic, F.Canales, J.K.Steinke, P.Stefanutti, C.Vetterli: "Traction transformation – A power electronic traction transformer (PETT)", *ABB Review*, 1/12, 2012, pp. 11-17.

Modeling and Design of Passive Components for Flexible Electronics

Nikola Jeranče, Nataša Samardžić, Dragana Vasiljević, and Goran Stojanović

Abstract—In this paper, electromagnetic modeling of capacitors and inductors for printed electronic circuits is studied. Capacitors are successfully modeled by two-dimensional finite element software. Capacitive sensor for chemical detection is proposed and tested in water. Inductors are modeled by the integrating through the currents and obtained results have been compared with 3D finite element method. A capacitive sensor and an inductor on flexible substrate were fabricated. Simulation results have been validated through measurements.

Index Terms—Sensors, Capacitors, Inductors, Printed electronics.

I. INTRODUCTION

ELECTRONICS on flexible substrate is rapidly developing, promising new applications and low-cost components and circuits [1]. Although new applications with active components such as thin film transistors and organic light emitting diodes are very promising, the development of passive components is also important. Design of capacitors and inductors described in this paper is done for two purposes: circuit components needed to achieve desired response in frequency domain and variable capacitors and inductors for sensors application. For example, capacitive sensors can be used as chemical sensors in food intelligent packages [2]. Inductive position sensors are widely used in industrial and automotive applications. Accurate modeling of components in printed flexible circuits is the basis of their efficient design and development. The electromagnetic modeling methods, taking into account the specific properties of printed flexible circuits, are explored.

II. CAPACITORS ON A FLEXIBLE SUBSTRATE

In this paper, capacitors have been modeled in Comsol Multiphysics finite element software package as a classical electrostatics problem. Considered geometries allow us to do

Manuscript received 30 May 2012. Accepted for publication 10 June 2012. Some results of this paper were presented at the 16th International Symposium Power Electronics, Novi Sad, Serbia, October 26-28, 2012.

This work was financially supported by the Ministry of Science and Education of Republic of Serbia within the project no. TR32016, and equipment was provided within the FP7 REGPOT project APOSTILLE, grant no. 256615.

N. Jeranče, N. Samardžić, D. Vasiljević, and G. Stojanović are with the Faculty of Technical Sciences, University of Novi Sad, Novi Sad, Serbia.

the simulations in two dimensions (2D), which is faster and more convenient for electromagnetic design.

A. Selecting the Capacitor Structure

First simulated structures are capacitors in the shape of tube with electrode polarity shown on a cross section in Fig. 1. This figure presents the potential scale going from 0 (blue) to 1 V (red), whereas Fig.1(b)-Fig.1(d) show tube capacitors with different potential distributions obtained by electrodes on the outside wall. The results for capacitance for 20 mm length in third dimension (l) at $\epsilon_r = 1$, and the change for $\epsilon_r = 10$ in the tube, are given in Table I.

Another type of structures has been proposed, to fully exploit new possibilities with flexible substrate: spirally rolled capacitors. The electrodes were printed on a substrate

TABLE I
SIMULATION RESULTS FOR FLEXIBLE CAPACITORS

Design shown in figure	Outside diameter (mm)	C_0 (pF) for $\epsilon_r = 1$, $l = 20$ mm	$\frac{\Delta C}{C_0}$ for $\epsilon_r = 10$	Uniform field
1.(b)	3.2	1.08	128%	no
1.(c)	3.2	3.78	40%	no
1.(d)	3.2	4.08	29%	yes
2.(b)	7	58	900%	yes
2.(c)	9.5	24.2	900%	yes

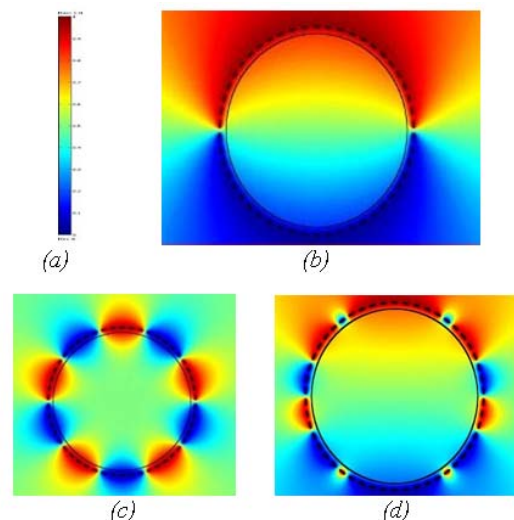


Fig. 1. Tube-shaped capacitors.

which is wound in a spiral shape so that positive and negative electrodes always come in front of each other.

The shape of substrate cross section is shown in Fig. 2(a) and first designs are shown in Fig. 2(b) and 2(c), whereas capacitance and its relative change are given in Table I.

These results are very encouraging: easily increased capacitance, very high sensitivity (following the change of ϵ_r) and very uniform electric field in the structure.

B. Spirally Capacitive Sensor – Simulations

To get a spiral shape of structure, at the beginning, an approximation with 8 straight lines per turn has been used. Cross section of that structure is shown in Fig. 3 and the results for capacitance for 10 mm length in third dimension (l), 0.5 mm distance between electrodes, inner diameter 3 mm and external diameter 5 mm at $\epsilon_r = 1$, and the change for $\epsilon_r = 10$ in the tube, are given in Table II.

W is electric energy in 2D (per length), and C is capacitance calculated as:

$$C = \frac{2 \cdot W \cdot l}{U^2} \quad (1)$$

U is voltage applied to the electrodes and its value was

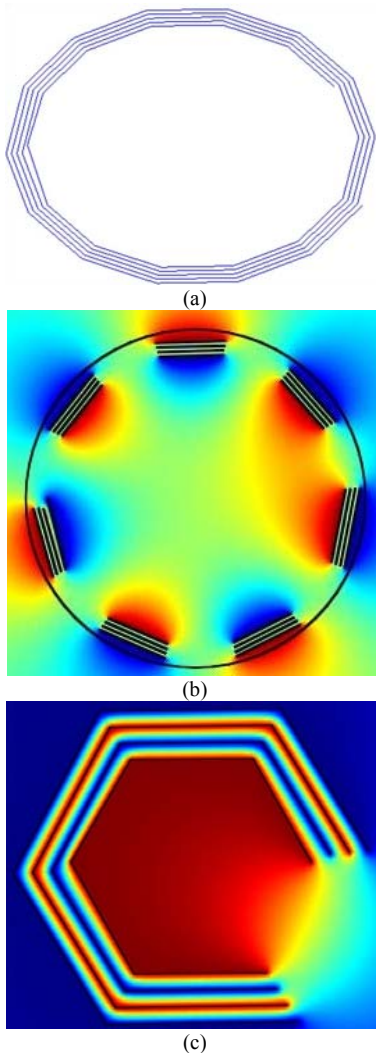


Fig. 2. Spirally-shaped capacitors.

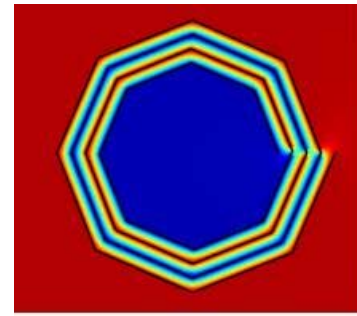


Fig. 3. Cross section of a spirally-rolled capacitor with 8 straight lines per turn.

TABLE II
SIMULATION RESULTS FOR CAPACITORS ON A FLEXIBLE SUBSTRATE DUE TO THE CHANGE OF ϵ_r

ϵ_r	W [N]	C [pF]
1	1.932751e-9	38.65502
10	1.932751e-8	386.5502

taken as 1 V, to make calculation easier.

After several simulations, for different number of straight lines per turn, it has been found that for more than 12 lines per turn, results do not change significantly, which it can be seen in Table III, therefore this number of straight lines was adopted as final.

The flexible substrate for manufacturing this capacitive sensor has $\epsilon_r=3$. For practical reasons, to prevent short circuit of the electrodes, gap between electrodes is left, which is shown in Fig. 4. Cross section of this structure and the results with the influence of the dielectric constant of substrate are shown in Fig. 4 and Table IV, respectively.

To make a constant distance between the electrodes we used a paper, which has a dielectric constant $\epsilon_r=3$. The paper would also allow water to enter between the electrodes and to change ϵ_r which will be measured. Simulation results for $\epsilon_r=3$ (ϵ_r of the paper between the electrodes) and variation for $\epsilon_r=80$

TABLE III
SIMULATION RESULTS FOR DIFFERENT NUMBER OF STRAIGHT LINES PER TURN (N), FOR $\epsilon_r = 1$

n	W [N]	C [pF]
8	7.021128e-10	14.04226
10	6.891024e-10	13.78205
12	6.836755e-10	13.67351

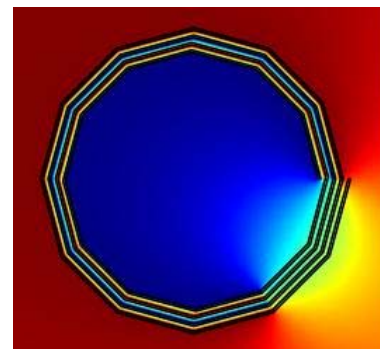


Fig. 4. Cross section of a spirally rolled capacitor with 12 straight lines per turn.

TABLE IV
SIMULATION RESULTS FOR CAPACITORS ON A FLEXIBLE SUBSTRATE WITH
INFLUENCE OF $\epsilon_r = 1$

ϵ_r	W [N]	C [pF]
1	1.725202e-9	34.50404
10	7.461256e-9	149.2251

(ϵ_r of water, where sensor would be placed) are given in Table V, for substrate thickness of 50 μm , paper thickness of 100 μm , and inner radius of 2.5 mm.

C. Spiral Capacitive Sensor – Measurements

Simulation results given in Table V have been verified by measuring the structure shown in Fig. 5 using the Impedance/Gain-Phase Analyzer HP4194A.

The first set of measurements presents capacitance variation at different frequencies. The capacitance was measured at five different frequencies and these results are shown in Fig. 6.

Fig. 6 also shows that changes in capacitance as a function of the frequency are very small so they can be neglected (the average value is considered). The next step was to verify how the dielectric constant affects the capacitance. Measurements were performed for two values of dielectric constants between electrodes, for $\epsilon_r=3$ (the dielectric constant of paper) and for $\epsilon_r=80$ (the dielectric constant of water). Those results are given in Table VI.

As it can be seen from Table V and VI the results of measurements are in very good agreement with the results obtained through the simulations. The next step was to test how putting Kapton film in water affects the capacitance. This test has been performed using the capacitor with the same design and dimensions as the previous one, but without the

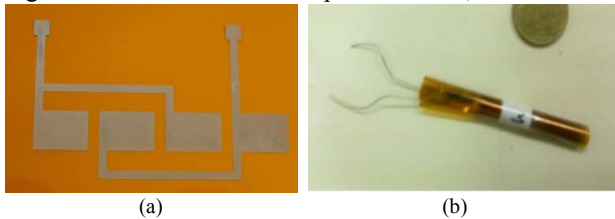


Fig. 5. Fabricated capacitive sensor (a) unwrapped and (b) wrapped.

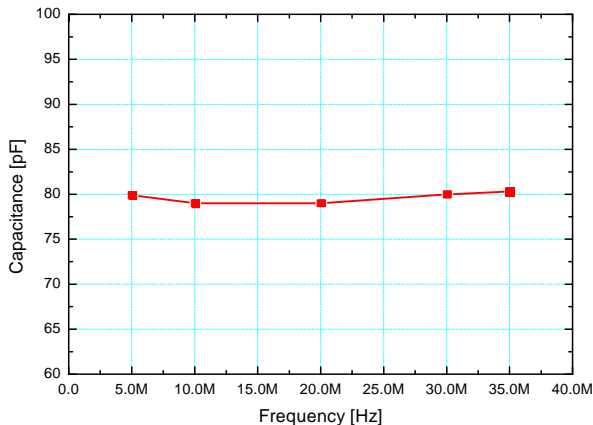


Fig. 6. Measured capacitance at different frequencies.

TABLE V
SIMULATION RESULTS FOR INFLUENCE OF ENVIRONMENT

ϵ_r	W [N]	C [pF]
3	3.996441e-9	79.92883
80	1.133231e-9	226.6462

TABLE VI
MEASUREMENT RESULTS FOR $\epsilon_r = 3$, AND ITS CHANGE FOR $\epsilon_r = 80$

ϵ_r	C [pF]
3	79.5573
80 (immediately)	217.196
80 (after 24 h)	268.010

paper between the electrodes. In the Table VII, measured capacitance results are given, when Kapton film is dry or exposed to the water for 24 h.

Bearing in mind that dielectric constant of water is much greater than dielectric constant of Kapton film, influence of the water layer (absorbed by paper) can be neglected. This can be seen in Table VI and VII. The presented results show that the sensor works properly, allowing measurement of changes in dielectric constant of the environment.

III. INDUCTORS ON A FLEXIBLE SUBSTRATE

Inductors can be modelled in finite element software, as three-dimensional (3D) magnetostatic problem. However, the absence of ferromagnetic materials in modelled circuits has allowed us to simplify the inductance calculation by integrating vector potentials in the circuit. In this manner, there is no need for time and memory consuming 3D finite element computation as well as the problem of domain truncation (which can affect finite element results) is avoided. The in-house developed program for inductance calculation has been validated through comparison with analytical expressions and also with finite element method.

A. Simulations by the Finite Element Method

Inductance calculations were firstly performed in COMSOL Multiphysics finite element software package. Simple conductive segments with rectangular shape were simulated as 3D magnetostatic problem using the method where the model is solved for magnetic potential and calculation has been performed through magnetic energy W_m :

$$L = \frac{2W_m}{I^2} \quad (2)$$

where: L – inductance, I – total current.

Current density is set as input parameter and adjusted so that total current through the structure is equal to 1 A.

The mesh for this type of problem (electronic circuits on flexible substrate) can contain many elements. This is due to

TABLE VII
THE EFFECT OF WATER ABSORBED IN KAPTON FILM ON MEASURED CAPACITANCE

$\epsilon_{r\text{Kapton}}$	C [pF]
dry	207.199
wet (after 24 h)	236.912

thin conductors and a lot of empty space around them which must be included in the model in order to represent the field correctly. In our models, we use thicker conductors, limiting the task to find the correct inductances in such cases, so that we can test our program.

Simulations were run for rectangle structures of different dimensions: 20 mm x 4 mm x 1mm, 10 mm x 1 mm x 1 mm and 10 mm x 2 mm x 0.5 mm (length x width x thickness).

Modeling was improved by using infinite elements: the studied domain is divided into two boxes – the inner box represents local domain and the external box represents infinity domain, thus avoiding huge number of elements, saving memory and time of computation. Default parameters for mapped infinite elements of Cartesian, cylindrical or spherical geometries are available in our software as an option, for the user to optimize calculations problem.

Simulations were run for different distances between box and the structure in Cartesian system and calculations of inductance were performed with energy density. Results were compared with those from analytical expression [4]:

$$L = 0.002 \left\{ \ln \left[\frac{2l}{w+t} \right] + 0.5 + \left(\frac{w+t}{3l} \right) \right\} \quad (3)$$

where w and t are dimensions of cross section, l stands for length of conductive segment in centimeters.

The best agreement has been obtained for inner box of 15 mm distance of every structure edge and 20 mm distance for larger box.

The same structures were calculated using our in-house developed program written in C++. The obtained values of inductances by analytical expressions, COMSOL and C++ simulations are given in the Table VIII.

After that, COMSOL Multiphysics was used for simulating spiral shaped inductor structure with initial radius of 3 mm which is increased for 0.5 mm at each full turn. Simulated structure corresponds to a half of one turn. Cylinders were used as boundaries for defining infinite elements. The simulation results for spirally rolled conductor obtained in COMSOL and by our program are given in Table IX.

B. Simulations by the Integrating

A computer program is written in C++ which calculates all inductances in a circuit. An inductor consists of straight conductive segments which can be printed on flexible substrate. Each straight segment is divided into small volume elements.

The inductance is calculated by integrating over the elements using the formula [3]:

$$L = \frac{1}{I^2} \int \vec{J} \cdot \vec{A} dv \quad (4)$$

where: \vec{J} – current density vector in the element; \vec{A} – vector potential at the center of element; dv – volume of the element. The vector potential at a point is computed by the formula [3]:

$$A = \frac{\mu}{4\pi} \int \frac{\vec{J}}{R} dv \quad (5)$$

TABLE VIII
RESULTS OF SIMULATION FOR RECTANGLE INDUCTANCE

Rectangle dimension (mm)	Analytical inductance value (nH)	COMSOL's inductance (nH)	C++ inductance (nH)
20 x 4 x 1	10.653	10.642	10.875
10 x 1 x 1	5.744	5.249	5.768
10 x 2 x 0.5	5.326	5.317	5.438

TABLE IX
SIMULATED ROLLED INDUCTANCE RESULTS

Software tool	Inductance, L (nH)
COMSOL	3.847
C++	4.03

where: R – distance to the point where \vec{A} is computed; μ – magnetic permeability.

The end point coordinates of the straight segments are entered in u-v plane, thus giving the initial coordinates and direction of (assumed to be parallel with the segment: a correct approximation if the segment is long enough) and vector normal to the surface for each element. These coordinates and vector directions are transformed into x-y-z Cartesian coordinate system by using appropriate mathematical expression to correspond to the shape of the twisted flexible substrate. In this manner, we avoid drawing complicated geometries in three dimensions and the component is described in the same way as it is fabricated afterwards. All self inductances and mutual inductances of individual segments and conductors are available in an output file, in order to make verification and circuit design easier.

In-house developed program has been tested for straight line segments (no twisting), circular conductors and spirally rolled conductors, which corresponds to the existing separate parts of the program code.

The results have been validated in three ways: through comparison with analytical expressions for self and mutual inductances where this was possible, through comparison with finite element results and, finally, through measurements.

A meander-shaped inductor shown in Fig. 7(a), were printed on a flexible substrate which is then wound into spiral shape to obtain the conductor geometry shown in Fig. 7(b). The spiral starts at radius 5 mm and 0.075 mm is added at each full turn, the vertical line segments are 10 mm long, all straight segments are 2 mm wide, 10 μ m thick. For the inductor in the plane we obtain the total inductance of 202 nH. For an illustration, self inductance of a straight 10 mm long segment obtained by the in-house developed program is 5.75 nH, while the value obtained by analytical expression (3) is 5.74 nH.

Total inductance of spirally rolled inductor calculated by our program is 514 nH.

We can simply test the part of the code describing circular conductors by calculating the inductance of a solenoid made of straight conductor printed on a flexible substrate and then wound around an axis. Line width is now the height of the solenoid and its length is equal to solenoid's circumference. For height equal to 100 mm and radius of 10 mm, the program calculates 4.06 nH inductance, compared to 3.95 nH obtained

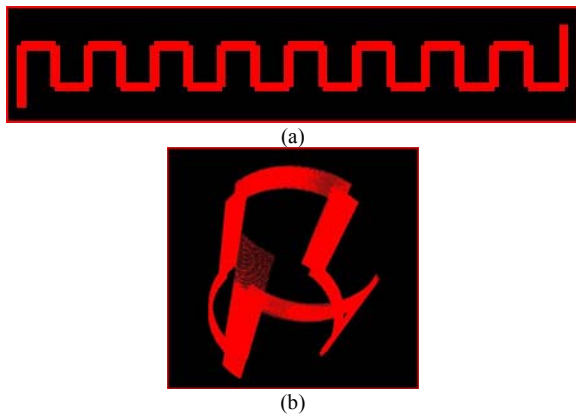


Fig. 7. (a) Meander inductor and (b) the spirally rolled inductor obtained by winding.

by well-known formula [4] for long solenoid.

Comparison with COMSOL finite element package has been done for straight rectangular segments (see Table VIII) and for spiral inductor for which the results are given in Table IX. Good agreement between finite element method and in-house developed program allows us to apply the program for more complex simulations and to adjust it to the needs of flexible circuit simulations.

C. Spirally Rolled Inductor – Measurements

In order to validate our simulation results, meander inductor in the plane and rolled were fabricated using ink-jet printing technology. The printed meander structure is the one presented in Fig. 7, with straight segments 2 mm wide, 10 mm length of vertical linear segments, while the rolled structure has 5 mm inner radius. The printing were done on Kapton film substrate with silver nanoparticle ink, using Dimatix DMP-3000 inkjet printer [5]. Thickness of the used substrate is 75 μm . Fig. 8 shows fabricated structure.

Measurements were performed with Impedance Analyzer HP4194A both for unwrapped and wrapped inductor. Inner radius of wrapping was 5 mm. The fabricated rolled meander inductor is shown in Fig. 9.

The simulation by the C++ program has given 202 nH for unwrapped and 514 nH as the inductance for the wrapped structure. It is known from simulation results that inductance value was around few hundreds of nH, thus we could conclude that copper wires' inductance used to connect testing component with Analyzer cannot be neglected. For that reason we measured wires' influence first and then subtracted those values from the total measured inductance to obtain the accurate inductance of the rolled structure.

Graphs from Fig. 10 represent changes of inductance as a function of frequency for unwrapped and wrapped meander



Fig. 8. Meander inductor on flexible Kapton substrate.

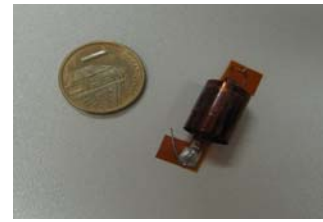


Fig. 9. The rolled meander inductor structure.

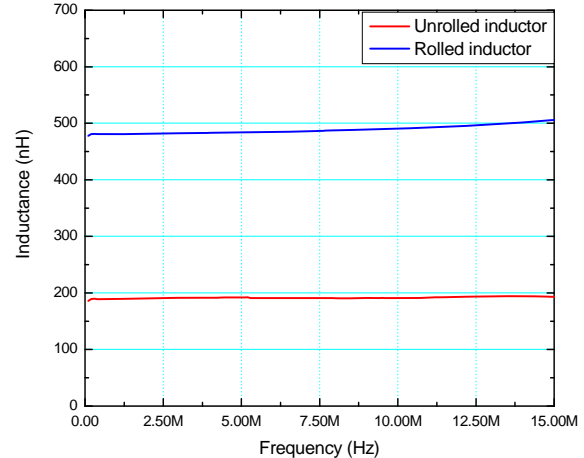


Fig. 10. Measured results of meander inductance for straight segments (red down line) and for wrapped structure (blue upper line).

inductor structure. Average value of total inductance in the first case is 190 nH and for wrapped case is 490 nH. As it can be seen, graphs showed a good agreement with simulated results.

IV. CONCLUSION

Modeling and design of capacitors and inductors printed on flexible substrates has been studied. Simulations of capacitive structures were done by 2D finite element software. Spiral sensor structures have been successfully simulated and a chemical sensor with high sensitivity has been designed. The sensor design has been validated through measurements. The time-consuming 3D finite element simulations of inductive structures were avoided by integrating vector potentials due to currents. The accuracy of the in-house developed program has been validated by comparison with analytical results, finite element results and measurements. The agreement of the obtained results is very good.

REFERENCES

- [1] Frances Gardiner, Eleanor Carter, "Polymer electronics – a flexible technology", iSmithers, 2009.
- [2] Mohd Syaifudin Bin Abdul Rahman, Subhas C. Mukhopadhyay, Pak Lam Yu, "Novel Sensors for Food Inspections", Sensors & Transducers Journal, Vol. 114, Issue 3, March 2010, pp. 1-40.
- [3] W.R. Smythe, "Static and dynamic electricity", 1950, McGraw-Hill Book Company.
- [4] H. Greenhouse, "Design of planar rectangular microelectronic inductors", IEEE Trans. Parts Hybrids, Packaging, Vol. PHP-10, pp.101-109.
- [5] www.dimatix.com.

Guest Editorial

IT is my pleasure now, after seven years, to play again the role of a guest editor of the “Electronics”. We are working in a fast changing world and that will be recognized by the content of the papers selected for this issue. These will, we hope, express the advance of the research community that is converging towards the journal “Electronics”.

When accepting the role of a guest editor of this issue we were aware of the importance of the moment for the promotion of „Electronics“. Here we try to support the efforts made by the Editorial board to improve the journal to the level that will bring it to the Thomson Reuters SCI list. We sincerely hope that „Electronics“ will become the first Serbian scientific journal of the field of electronics at that list.

Similarly to the situation we had in the year 2005 we have here an issue that is devoted to two distinguished international conferences that took place in the very near past. Those are the 4th Small Systems Simulation Symposium (SSSS) 2012 that took place on February 12-14, in Niš, and the 16th International Symposium on Power Electronics (EE) 2011, that took place on October 26-28, 2011. It is my pleasant duty to introduce you to the first one.

As it is well known now The SSSS, organized by the Faculty of Electronic Engineering in Niš, and the Yugoslav

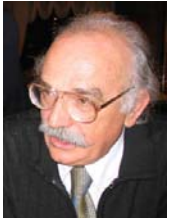
Simulation Society, became a traditional specialized event giving the opportunity to the researchers of any field to represent their scholar results in simulation methods or in methods based on simulation. We may say now that SSSS became the main event of the kind in the area of South East Europe. Participants to the symposium were from seven countries. The subjects of the reported papers were really spread over many filed of science and technology and it was a challenge to make a good selection. We are especially pleased to use this opportunity to promote international collaboration among research teams.

Here, while thanking to Prof. Branko Dokić, The Editor in Chief of “Electronics”, for the opportunity to express our views trough the choice of papers, we want to invite the scholar community to support his efforts to bring the journal to as high the level as possible.

Sincerely,

Prof. Vančo Litovski, Ph.D.
Guest Editor

Prof. dr Vančo Litovski Biography



Vančo Litovski was born in Rakita, South Macedonia, Greece, in 1947. He graduated at the Faculty of Electronic Engineering, University of Niš, Serbia in 1970. He received M. S. and Ph.D. degree in 1974 and 1977, respectively, from the same faculty. He is

founder and President of the Yugoslav Simulation Society. He is member of The Academy of Engineering Sciences of Serbia and Montenegro, and is author of about 400 publications. He received several awards for his scientific and educational achievements.

Energy Efficient Sensor Nodes Powered by Kinetic Energy Harvesters – Design for Optimum Performance

Tom J. Kaźmierski, Leran Wang, and Mansour Aloufi

Abstract—In an energy harvester powered wireless sensor node system, as the energy harvester is the only energy source, it is crucial to configure the microcontroller and the sensor node so that the harvested energy is used efficiently. This paper outlines modelling, performance optimisation and design exploration of the complete, complex system which includes the analogue mechanical model of a tunable kinetic microgenerator, its magnetic coupling with the electrical blocks, electrical power storage and processing parts, the digital control of the microgenerator tuning system, as well as the power consumption models of sensor node. Therefore not only the energy harvester design parameters but also the sensor node operation parameters can be optimised in order to achieve the best system performance. The power consumption models of the microcontroller and the sensor node are built based on their operation scenarios so that the parameters of the digital algorithms can be optimised to achieve the best energy efficiency. In the proposed approach, two Hardware Description Languages, VHDL-AMS and SystemC-A is used to model the system's analogue components as well as the digital control algorithms which are implemented in the microcontroller and the sensor node. Simulation and performance optimisation results are verified experimentally. In the development of the fast design exploration tool based on the response surface technique, the response surface model (RSM) is constructed by carrying out a series of simulations. The RSM is then optimised using MATLAB's optimisation toolbox and the optimisation results are presented.

Index Terms—Wireless sensor node, Energy harvesting, Performance optimisation, Simulation.

I. INTRODUCTION

WIRELESS sensor networks (WSNs) have attracted a great research interest in recent years. Since wireless sensor nodes can provide information from previously inaccessible locations and from previously unachievable number of locations, many new application areas are emerging, such as environmental sensing [1], structural monitoring [2] and human body monitoring [3]. Although

Manuscript received 1 May 2012. Accepted for publication 30 May 2012. Some results of this paper were presented at the 4th Small Systems Simulation Symposium, Niš, Serbia, February 12-14, 2012.

The authors are with the Faculty of Physical and Applied Sciences, University of Southampton, Southampton SO17 1BJ, UK, email: {tjk,lw04r,ma08r}@ecs.soton.ac.uk.

wireless sensor nodes are easy to deploy, the lack of physical connection means they must have their own energy supply. Because batteries have limited lifetime and are environmentally hazardous, it has become widely agreed that energy harvesters are needed for long-lasting sensor nodes [4]–[6]. The idea is to use energy harvester to capture small amounts of energy from the environment and use the generated energy to power the nodes in wireless sensor networks. Vibration-based energy harvesters are used in many commercial applications since mechanical vibrations are widely present. Most of the reported vibration energy harvester designs are based on a spring-mass-damper system with a characteristic resonant frequency. These devices normally have a high Q-factor and generate maximum power when their resonant frequency matches the dominant frequency of the input ambient vibration [7]. Consequently, the output power generated by the microgenerator drops dramatically when there is a difference between the dominant ambient frequency and the microgenerator's resonant frequency. Tunable microgenerators, which can adjust their own resonant frequency through mechanical or electrical methods to match the input frequency, are therefore more desirable than the fixed frequency microgenerators [8]. A wireless sensor node powered by tunable energy harvester typically has the following key components (Fig. 1) [9]: a microgenerator which converts ambient environment vibration into electrical energy, a power processing circuit which regulates and stores the generated energy, an actuator used for the frequency tuning mechanism, a digital controller that monitors and retunes the tunable energy harvesting system based on vibration

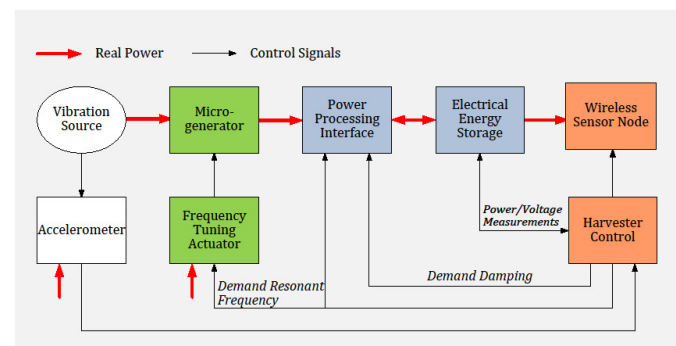


Fig. 1. Components of an energy harvester powered sensor node system [9].

measurements from an accelerometer, and the wireless transceiver or transmitter.

Hardware description languages, such as VHDL-AMS and SystemC-A, have been used to model energy harvesters in recent years [10], [11]. HDLs with mixed signal and multi-domain capabilities are suitable for energy harvester modelling because an energy harvester is naturally a mixed-physical-domain system. The technique outlined below models the complete system including the analogue mechanical, magnetic and electrical power storage and processing parts, the digital control of the microgenerator tuning system, as well as the power consumption models of sensor node. Additionally, the paper proposes a response surface based design space exploration and optimisation technique so that not only the energy harvester design parameters but also the sensor node operation parameters can be optimised in order to achieve the best system performance

II. PERFORMANCE OPTIMISATION

An automated energy harvester design flow must be implemented holistically and based on a single software platform that can be used to model, simulate, configure and optimise an entire energy harvester systems. Such a design flow is outlined in the pseudo-code of Algorithm 1 and also shown in Fig. 2. Naturally, the process starts with initial design specification, such as the available energy source (light, heat, vibration, etc), environmental energy density, device size, minimum voltage level/power output. According to these specifications, HDL models are constructed from component cells available in the component library. The component library contains parameterised models of different kind of micro-generator structures (solar cell, electromagnetic, piezoelectric, etc), various booster circuit topologies and storage elements. The outer loop in the algorithm represents this structure configuration process, which involves examining and comparing those HDL models from the library with the aim of identifying a set of components that meet specific user requirements. The inner design flow loop will then find the best performance of each candidate design by adjusting

Algorithm 1 Automated energy harvester design flow.

```

Initial design structure and specification
Structure configuration loop:
for all design structures do
  Build HDL model of design
  Optimisation loop:
  repeat
    Simulate and evaluate performance
    if best performance not achieved then
      Update design parameters
    end if
  until best performance achieved
  if there are more structures to try then
    Select new structure
  end if
end for

```

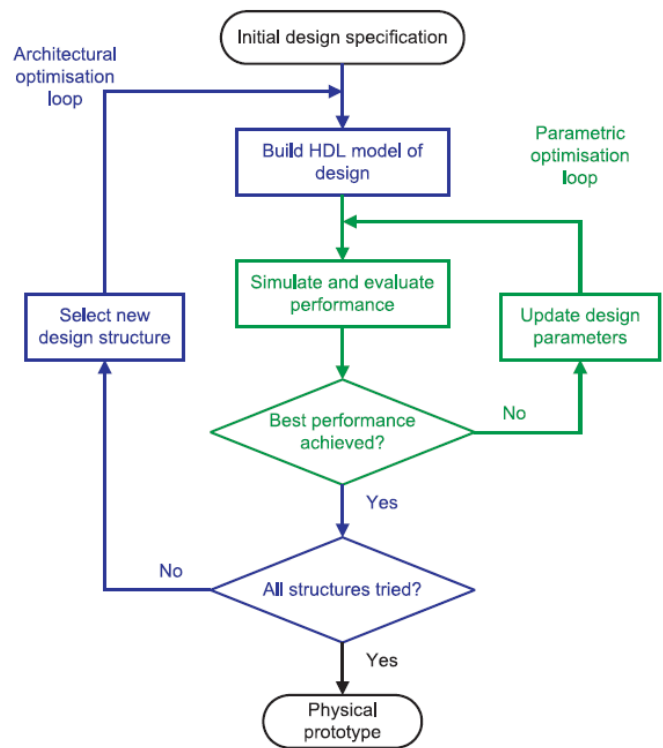


Fig. 2. Energy harvester design flow.

electrical and non-electrical parameters of the design's mixed-technology HDL model. The parametric optimisation of the generated structure will further improve the energy harvester efficiency by employing suitable optimisation algorithms. The design flow ends with the best performing design subject to user-defined performance characteristics.

Requirements for energy harvester component models are: 1) models need to be computationally efficient for fast performance optimisation when used in complete energy-harvester systems and yet accurate; these are conflicting requirements, 2) models need to capture both theoretical equations and practical non-idealities required for accurate performance estimation. The models should support different mechanical-electrical structures and will be expressed in terms of HDL descriptions. They will be able to predict the behaviour of the actual device accurately while remaining reconfigurable.

A small HDL model library of energy harvester components has been built. It contains two types of micro-generator, each of which can be configured with different coils (wire diameter of 12/16/25 μm), and two types of voltage multipliers that have three to six stages. The voltage transformer has not been included because it cannot be made and tested with available resources. But the simulation based optimisation of energy harvester with voltage transformer has been performed and will be discussed in Section II-A2. The configuration target has been set to find the set of components that can charge the 0.047F super capacitor to 2V in shortest time. These values were chosen because there has been reported energy harvester systems that use 0.047F storage capacitor and 2V working voltage [12]. Simulations of every available energy harvester

configuration were carried out simultaneously and a process has been developed to automatically track the best model. SystemVision VHDL-AMS simulator [13] has been used as the single software platform. The outcome design is listed in Table I.

It is no surprise that the micro-generator II has been chosen because it is larger and stores more kinetic energy. However, it is quite interesting that the coil with the largest wire diameter, which leads to the fewest number of turns, and the VM with the fewest stages have been chosen. To further investigate this result, more simulations have been done and an important trade-off between the electromagnetic micro-generator and the VM voltage booster has been found as explained below.

Fig. 3 shows the charging waveforms of Type I micro-generator connected to the same 5-stage VM but configured with different coils. At the beginning, the energy harvester with 25 μm wire diameter charges the quickest and the 12 μm configuration charges the slowest while the 16 μm one is in between. But the 25 μm configuration also saturates quickly and reaches the 2V mark slower than the 16 μm energy harvester. Due to simulation time limitation, the figure does not show how the other two waveforms end. But it could be foreseen that the 16 μm configuration will also saturate at some point while the 12 μm one reaches highest voltage.

Similar results have been obtained from the voltage booster end. Fig. 4 shows the charging waveforms of Type II micro-generator with 25 μm coil connecting with 3, 4 and 5 stages Dickson VMs. It can be seen that the energy harvester with the 3-stage VM charges the super capacitor to 2V first and the one with the 5-stage VM can reach the highest voltage.

The above results prove that when different components of an energy harvester are combined, the gain at one part may come at the price of efficiency loss elsewhere, rendering the

TABLE I
PARAMETERS OF THE CONFIGURATION RESULT

Micro-generator	Type II
Wire diameter	25 μm
Voltage booster	3-stage Dickson voltage multiplier

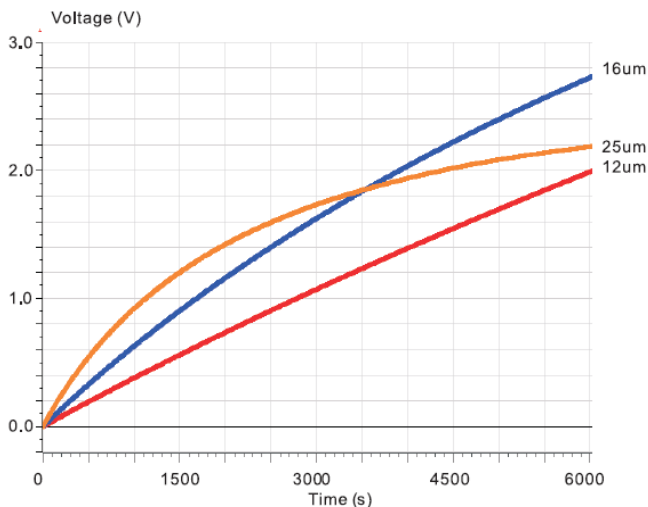


Fig. 3. Simulation of Type I micro-generator with different coils.

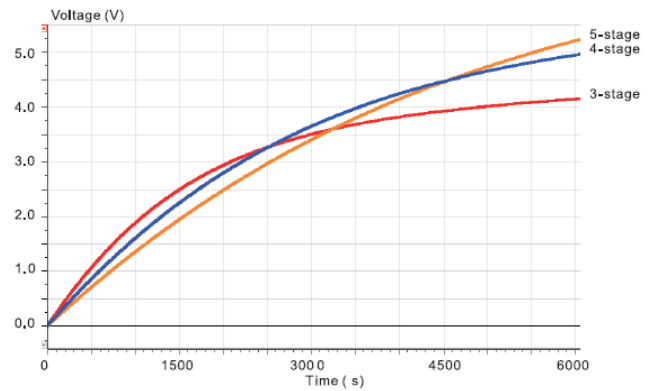


Fig. 4. Simulation of Type II micro-generator with different VMs.

whole system less efficient than expected. This observation is very useful for the development of future, more complicated systems and model libraries. Below we evaluate the performance loss due to the close mechanical-electrical interaction (micro-generator and voltage booster) that takes place in the energy harvester system.

A. Performance Optimisation

The loss expressed in terms of energy harvesting efficiency is:

$$\eta_{Loss} = \frac{E_{Harvested} - E_{Delivered}}{E_{Harvested}} \quad (1)$$

In the proposed design flow, the generated energy harvester design should be parameterised such that automated performance optimisation will be able to further improve the energy harvester efficiency by employing suitable optimisation algorithms. The optimisation objective investigated in the case study below is to maximise the charging rate of the super capacitor.

1) *Exhaustive search*: The micro-generator parameters that can be optimised are related to the coil size, i.e the thickness (t) and the outer radius (R). Other components such as the magnets and cantilever determine the resonant frequency of the micro-generator and thus should be determined from the application requirements. The optimised parameters of the voltage booster are the capacitor values of each VM stage. The entire energy harvester is optimised as an integrated model and the parameter search space is summarised in Table II.

The optimisation is based on the concurrent simulations of design instances from uniformly sample the search space and track the best result (Fig. 5). Other optimisation algorithms may also be employed and we show in Section II-A2 how a VHDL-AMS based genetic optimisation was successfully applied to the integrated optimisation of an energy harvester system.

To validate the effectiveness of the proposed approach, the

TABLE II
OPTIMISATION SEARCH SPACE

Coil thickness(mm)	1.0-1.3
Coil radius(mm)	2.0-2.45
Capacitor values(uF)	47/100/150

following simulations and experimental measurements have been carried out.

Original design: combines Type II micro-generator with a 5 stage Dickson VM. This VM has been reported in literature as the optimal configuration [14]. However, in the original design these two parts are optimised separately, which is quite common in existing energy harvester design approaches. Parameters of the original design are listed in Table III.

Optimised design: has been obtained using the proposed design flow (Fig. 5). Table IV gives the new micro-generator and voltage booster parameters.

The impact of these values on improving the energy harvester performance has been validated in both simulation and experimental measurements. According to the optimisation result, a new coil has been manufactured by Recoil Ltd, UK [15] which replaced the original one in the validation (see Fig. 6).

Simulation and experimental waveforms of the original and optimised design are shown in Fig. 7. As can be seen from the figure, there is good a correlation between the simulation and experimental waveforms in both of the energy harvester designs, which validates the effectiveness and accuracy of the proposed design flow. The energy harvester from original design can charge the super capacitor to 2V in 6000 seconds while the optimised design only uses 1500 seconds, which represents a 75% improvement.

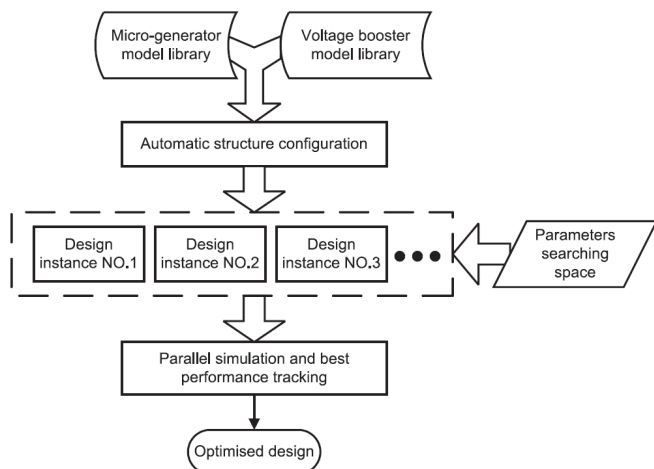


Fig. 5. Implementation of the proposed energy harvester design flow in VHDL-AMS.

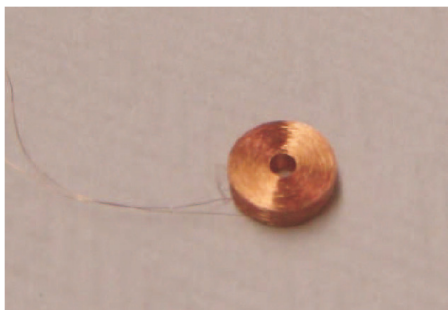


Fig. 6. New coil according to optimisation result ($R=2.0\text{mm}$, $r=0.5\text{mm}$, $t=1.3\text{mm}$, $d=25\mu\text{m}$).

TABLE III
PARAMETERS OF ORIGINAL ENERGY HARVESTER

Micro-generator	
Wire diameter(μm)	16
Coil thickness(mm)	1.3
Coil radius(mm)	2.45
Voltage booster	
VM configuration	5-stage Dickson
Capacitor values(C1-C5,uF)	47,150,150,47,150

TABLE IV
PARAMETERS OF OPTIMISED ENERGY HARVESTER

Micro-generator	
Wire diameter(μm)	25
Coil thickness(mm)	1.3
Coil radius(mm)	2.0
Voltage booster	
VM configuration	3-stage Dickson
Capacitor values(C1-C3,uF)	100,100,47

2) *Genetic optimization:* This section demonstrates another possible optimisation method to improve the energy harvester efficiency. Fig. 8 shows that in the proposed approach, not only the energy harvester model but also the optimisation algorithm is implemented in a single VHDL-AMS testbench. The parameters used for the optimisation are from both the micro generator and the voltage booster. The optimisation object is to increase the charging rate of the super capacitor. The optimisation algorithm generates design parameters to the model and obtains the charging rate through simulation. The optimisation loop runs continuously until the design parameters reach an optimum.

A super capacitor of 0.22F has been used in the performance optimisation experiment. The micro-generator parameters that can be optimised are the number of coil turns (N), the internal resistance (R_c) and the outer radius (R). The voltage booster circuit here is a voltage transformer. The optimisation parameters are the number of turns and the resistance of the transformer's primary and secondary windings. For proof of concept, a genetic algorithm (GA) [16] has been employed to optimise the energy harvester with a voltage transformer booster. The implemented GA has a population size of 100 chromosomes. Each chromosome has 7 parameters (3 from the micro-generator and 4 from the voltage booster). The crossover and mutation rate are 0.8 and 0.02 respectively. Other optimisation algorithms may also be applied based on the proposed integrated model. The "un-optimised" model parameters are given in Table V.

Applying the proposed modelling and performance optimisation, Table XIV gives the new micro-generator and voltage booster parameters which are referred to as the "optimized" design. The impact of these values on improving the charging of the super is shown in Fig. 9. As can be seen from the simulation results, in 150 minutes the un-optimised energy harvester charges the super capacitor to 1.5V and the optimised energy harvester reaches 1.95V, which represents a 30% improvement.

Performance of the developed GA has been further investigated by comparing the power transfer efficiency before and after optimisation. The maximum average power that can

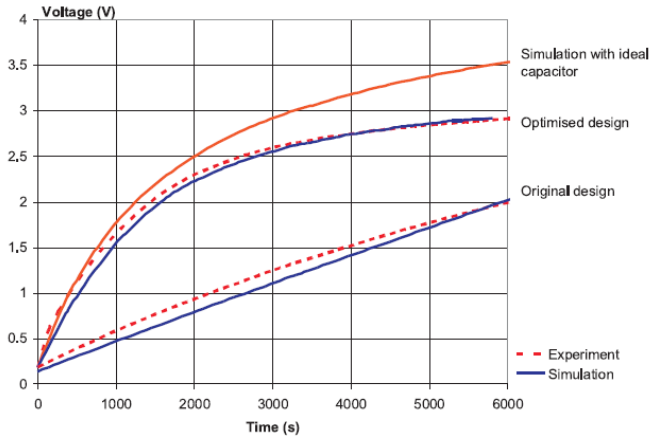


Fig. 7. Simulation and experimental waveforms of original and optimized energy harvesters.

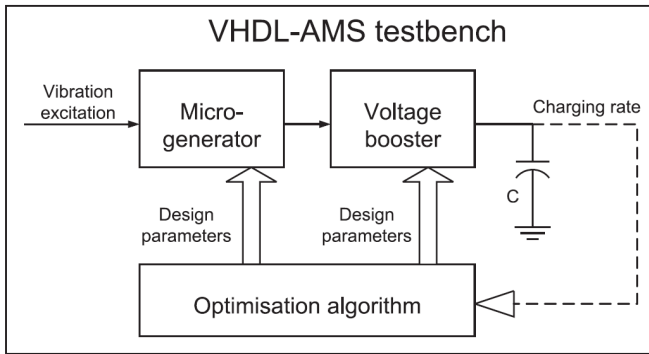


Fig. 8. Integrated performance optimisation in VHDL-AMS testbench.

be delivered to the electrical domain is about 144 μW . Table VII lists the average electrical power output from the micro generator and the voltage transformer. It can be seen that the optimisation improves the efficiency of both the micro generator and voltage booster, which validates the effectiveness of the developed genetic optimisation.

III. COMPLETE WIRELESS SENSOR NODE

Fig. 10 shows the diagram of the wireless sensor node system powered by tunable energy harvester. The wireless sensor node has a temperature sensor and a 2.4GHz radio transceiver. Once activated, the measured data are transmitted to another transceiver which is connected to a PC's USB port. The microgenerator converts the input vibration into electrical energy. The generated AC voltage is rectified by a diode bridge and stored in a 0.55F supercapacitor. The supercapacitor acts as the energy source for the microcontroller that controls the frequency tuning of the microgenerator and for the sensor node. In order to tune the resonant frequency of the microgenerator to match the frequency of the vibration source, the microcontroller uses two input signals, one from the microgenerator and one from the accelerometer. The operational amplifier acts as a comparator to generate square waves from the microgenerator output so that it is easy for the microcontroller to calculate the frequency. The detailed tuning algorithms are presented in

Micro-generator		
Outer radius of coil (R)	1.2 mm	
Coil turns (N)	2300	
Internal resistance (R_c)	1600 Ω	
Voltage transformer		
	Resistance(Ω)	No. of turns
Primary winding	400	2000
Secondary winding	1000	5000

Micro-generator		
Outer radius of coil (R)	1.1 mm	
Coil turns (N)	2100	
Internal resistance (R_c)	1400 Ω	
Voltage transformer		
	Resistance(Ω)	No. of turns
Primary winding	340	1900
Secondary winding	690	3800

	Generated power(μW)	Delivered power(μW)	Overall efficiency
Pre-optimisation	26.875	15.750	10.94%
Post-optimisation	29.250	19.625	13.63%

Section III-A3. The microcontroller also provides energy for the accelerometer, the operational amplifier and the actuator so that these devices can be turned off when not in use. Table VIII lists the type and make of the system components.

A. System Component Models

1) *Tunable microgenerator*: Fig. 11(a) shows a diagram of the electromagnetic microgenerator together with its tuning mechanism. The microgenerator is based on a cantilever structure. The coil is fixed to the base, and four magnets (which are located on both sides of the coil) form the proof mass. The tuning mechanism uses magnetic force to change the effective stiffness of the cantilever which leads to a change of resonant frequency. One tuning magnet is attached to the end of the cantilever beam and the other tuning magnet is connected to a linear actuator. The linear actuator moves the magnet to the calculated desired position so that the resonant frequency of the microgenerator matches the frequency of the ambient vibration. The control algorithm is modelled as a SystemC digital process described in Section III-A3. Fig. 11(b) shows a photo of the microgenerator which is used to validate the proposed technique [17].

The dynamic model of the microgenerator is [18]:

$$m \frac{d^2 z(t)}{dt^2} + c_p \frac{dz(t)}{dt} + k_s z(t) + F_{em} + F_{t-z} = F_a \quad (2)$$

where m is the proof mass, $z(t)$ is the relative displacement between the mass and the base, c_p is the parasitic damping factor, k_s is the effective spring stiffness, F_{em} is the electromagnetic force, F_{t-z} is the z component of tuning force F_t and F_a is the input acceleration force. The z component of tuning force is:

$$F_{t-z} = F_t \frac{z(t)}{l_c} \quad (3)$$

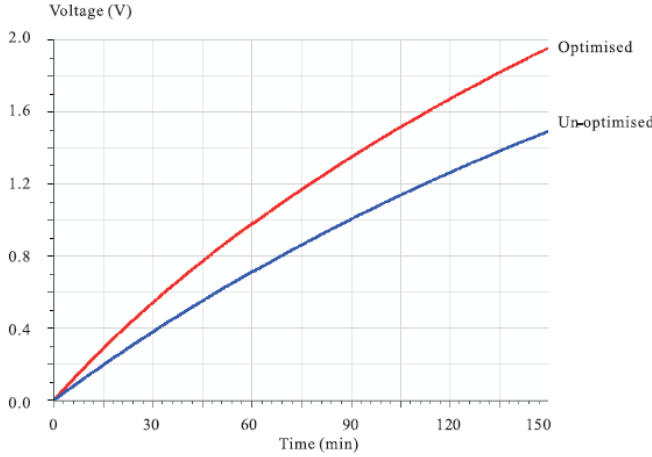


Fig. 9. Simulation waveforms of super capacitor charging by different energy harvester models.

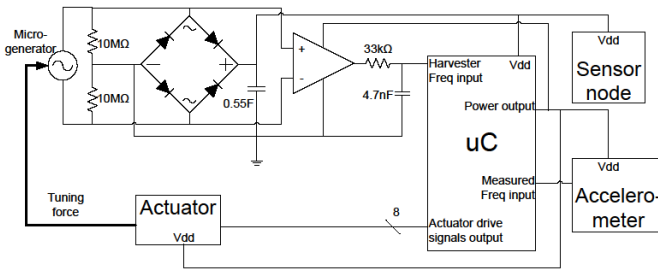


Fig. 10. System diagram of a tunable energy harvester powered wireless sensor node.

where l_c is the length of the cantilever. The resonant frequency ω_0 and damping coefficient ζ are:

$$\omega_0 = \sqrt{\frac{k_s}{m}} \quad (4)$$

$$\zeta = \frac{c_p}{2\sqrt{mk_s}}. \quad (5)$$

The resonant frequency of the tuned microgenerator (f_r') is:

$$f_r' = f_r \sqrt{1 + \frac{F_t}{F_b}} \quad (6)$$

where f_r is the un-tuned resonant frequency, F_t is the tuning force between two magnets and F_b is the buckling load of the cantilever. The electromagnetic voltage generated in the coil is:

$$V_{em} = -\Phi \frac{dz(t)}{dt} \quad (7)$$

where $\Phi = NBl$ is the transformation factor and N is the number of coil turns, B is the magnetic flux density and l is the effective length. The output voltage is:

$$V_m(t) = V_{em} - R_c i_c(t) - L_c \frac{di_L(t)}{dt} \quad (8)$$

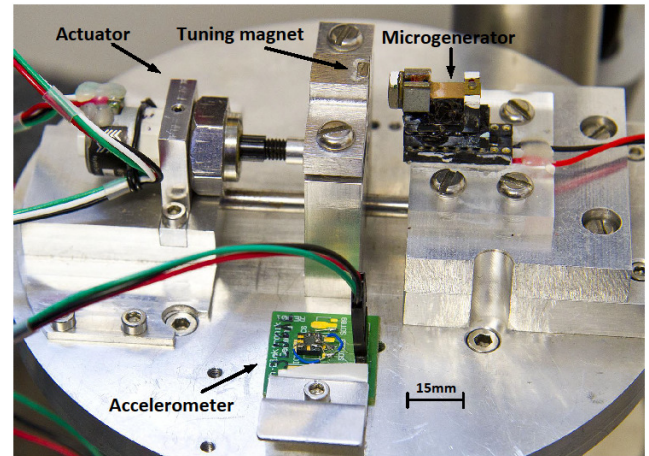
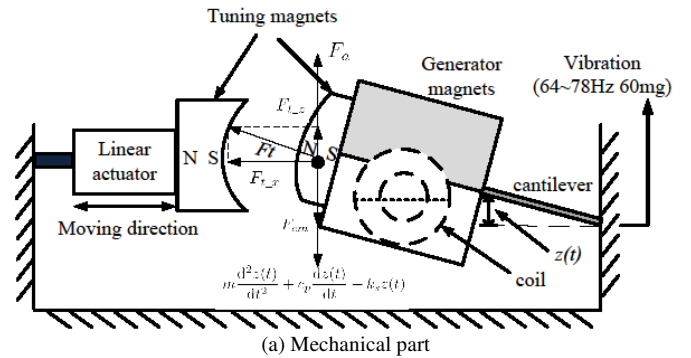
where R_c and L_c are the resistance and inductance of the coil respectively and $i_c(t)$ is the current through the coil. The electromagnetic force is calculated as:

$$F_{em} = \Phi i_c(t). \quad (9)$$

TABLE VIII
SYSTEM COMPONENTS POWERED BY THE ENERGY HARVESTER

Component	Type	Make
Microcontroller	PIC16F884	Microchip
Accelerometer	LIS3L06AL	STMicroelectronics
Linear actuator	21000 Series Size 8 stepper motor	Haydon
Sensor node	eZ430-RF2500	Texas Instruments

2) *Energy-aware sensor node behavior and power consumption model*: The eZ430-RF2500 wireless sensor node from Texas Instruments has been used in the system. The on-board controller is the MSP430F2274 and is paired with the CC2500 multi-channel RF transceiver, both of which are based on low-power design. The sensor node (Fig. 12) monitors the environment temperature as well as the supercapacitor voltage. Once activated, it transmits the temperature and voltage values through the radio link. Transmissions do not involve receiving acknowledgements. A program has been developed for the sensor control module to configure the sensor node in an energy-aware manner, namely that its transmission interval should depend on the available energy on the supercapacitor. The sensor node behaviour is summarised in Table IX. The transmission interval when the supercapacitor voltage is above 2.8V, i.e more energy stored, has been chosen as one parameter for optimisation. Although it is desirable to have as many transmissions as possible during a fixed time period, it may not always be the case that the transmission interval should be set as small as possible. This is because if the transmission is so frequency that the sensor node uses more energy than the harvester can generate, the supercapacitor



(b) Photo of tunable microgenerator
Fig. 11. Tunable electromagnetic microgenerator.

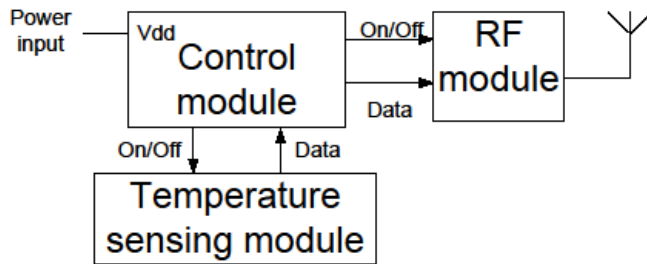


Fig. 12. Block diagram of the sensor node.

TABLE IX
SENSOR NODE BEHAVIOR BASED ON SUPERCAPACITOR VOLTAGE

Supercapacitor voltage	Wireless transmission interval
Below 2.7V	No transmission
Between 2.7 and 2.8V	Every 1 minute
Above 2.8V	Every 5 seconds (parameter for optimisation)

voltage will drop below 2.8V and the transmission interval will increase in order for the energy storage to recover. Other factors such as frequency tuning also uses stored energy and therefore will affect how much energy is available for the sensor node.

In order to characterise the power consumption model of the sensor node, the current draw of the sensor node has been measured during each transmission. The results are listed in Table X.

The supply voltage was kept at 2.9V. So during each transmission lasting 4.5 ms, the sensor node consumes 227 μJ of energy and the equivalent resistance of its energy consumption model is:

$$R_{node} = \begin{cases} 167 \Omega & \text{when in transmission} \\ 5.8 \text{ M}\Omega & \text{when in sleep} \end{cases} \quad (10)$$

3) *Tuning algorithms and power consumption models:* In order for a energy harvester powered wireless sensor node (Fig. 1) to work autonomously, all the system components need to be powered by the harvested energy. The pseudo code of the tuning algorithm is shown in Algorithm 2. Standard SystemC modules were used to model the digital control process and in the experimental verification the control algorithm was implemented in a PIC16F884 microcontroller. As can be seen in Algorithm 2, a watchdog timer wakes the microcontroller periodically and the microcontroller first detects if there is enough energy stored in the supercapacitor. If there is not enough energy, the microcontroller goes back to sleep and waits for the watchdog timer again. If there is enough energy, the microcontroller will then compare the frequency of the microgenerator signal, which is close to the input vibration frequency, to the microgenerator's resonant frequency. When a difference is detected between the vibration frequency and the resonant frequency, the microcontroller

TABLE X
CURRENT DRAW OF THE SENSOR NODE

Operation	Time	Current
Sleep mode	N/A	0.5 μA
Wake-up	1 ms	4.5 mA
Sensing	1.5 ms	13.4 mA
Transmission	2 ms	26.8 mA

Algorithm 2 Harvester tuning control algorithm

```

1: repeat
2:   Energy generation while waiting for watchdog timer:
   320 seconds (parameter for optimisation)
3:   if Enough energy stored in the supercapacitor
   ( $V_s \geq 2.6\text{V}$ , where 2.6V is the minimum voltage for
   the actuator to start) then
4:     Turn on Timer1 (clock frequency as parameter for
   optimisation)
5:     repeat
6:       Measure microgenerator period
7:     until 8 cycles have been measured
8:     Turn off Timer1
9:     Calculate input vibration frequency from 8 measure-
   ments
10:    Find optimum position (8-bit) of tuning magnet
   through look-up table which has been pre-obtained
   and stored in the microcontroller memory
11:    if Current position of tuning magnet matches opti-
   mum position (the accuracy is  $1/2^8$ ) then
12:      Goto 2
13:    else
14:      Perform rough tuning (Algorithm 3)
15:    end if
16:    Measure the phase difference between the accelerom-
   eter signal and the microgenerator signal
17:    if The phase difference is less than  $100\mu\text{s}$  then
18:      Goto 2
19:    else
20:      Perform fine tuning (Algorithm 4)
21:    end if
22:  end if
23: until Forever

```

retrieves the new desired position of the tuning magnet from a look-up table and begins a tuning process by controlling the actuator to move the tuning magnet to the new position (Fig. 11(a)). The watchdog timer and the microcontroller's clock frequency have been chosen as parameters for optimisation. Because these two parameters determine how much energy the microcontroller consumes and how quickly the system can response to the input vibration frequency change.

Algorithm 2 contains two subroutines: rough tuning (Algorithm 3) and fine tuning (Algorithm 4). The rough tuning measures the frequency of the microgenerator output and moves the actuator to the optimum position according to a predefined lookup table. However, the rough tuning alone cannot generate the best performance and a fine tuning algorithm is needed. This is because the measurement of the frequency of the microgenerator signal does not represent the input vibration frequency accurately enough and, in addition, there may also be a phase difference between the input vibration and the microgenerator motion that prevents the microgenerator from working at the resonance. The fine tuning takes another input, the raw vibration data from the accelerometer and moves the actuator to minimize the phase

Algorithm 3 Rough tuning algorithm

- 1: **repeat**
- 2: Send the optimum position as 8-bit control signal to the actuator
- 3: The actuator moves tuning magnet
- 4: Wait 5 seconds for the microgenerator signal to settle down
- 5: Compare the current position and optimum position
- 6: **until** Current position of tuning magnet matches optimum position

Algorithm 4 Fine tuning algorithm

- 1: **repeat**
- 2: Send the direction of movement that can reduce phase difference to the actuator
- 3: The actuator moves tuning magnet by 1 step
- 4: Wait 5 seconds for the microgenerator signal to settle down
- 5: Measure the phase of the accelerometer signal
- 6: Measure the phase of the microgenerator signal
- 7: Calculate the phase difference
- 8: **until** The phase difference is less than $100\mu\text{s}$

difference between the microgenerator signal and the accelerometer signal so that the microgenerator is working as resonance. It can be seen that the fine tuning algorithm requires more calculation (thus more energy) than the rough tuning and additional energy is consumed by the accelerometer (see Table XI). Therefore it is not so energy efficient to use only the fine tuning algorithm as the proposed two-subroutine method. In the two-subroutine method, the rough tuning moves the actuator to the approximate resonant position and the fine tuning finds the exact resonance.

To tune the resonant frequency of the microgenerator effectively, the system incorporates a microcontroller, a linear actuator and an accelerometer. These three components need to be powered by the energy harvester in order to make an autonomous system. To characterise the power consumption models of these components, current measurements have been taken and power/energy consumptions have been calculated (Table XI). According to the current and voltage values together with their operational times, the equivalent resistances for the power consumption models of these devices have been obtained.

IV. HDL IMPLEMENTATION

A. Analogue Part

The SystemC-A language [19] is used to build the system models. It is an extension to the SystemC language with analogue and mixed-signal (AMS) capabilities. The digital part is modeled using standard SystemC modules. The analogue part, consisting of non-linear differential and algebraic equations, is handled using the extended syntax where the user defines the behaviour of each analogue component by specifying the *build* methods that contribute to the analogue equation set of whole system. In Systemc-A, the

TABLE XI
POWER CONSUMPTION MODELS OF THE SYSTEM COMPONENTS

Component (action)	Operation time(ms)	Current (mA)	Power (mW)	R_{eq} (Ω)
Accelerometer	153	5.1	13.2	509
Actuator (1 step) (100 steps)	5 500	312 156	811 405	8.33 16.7
Microcontroller (Rough tuning) (Fine tuning)	149 325	1.9 5.1	5.0 6.5	1.38k 250

build method is provided to support the automatic equation formulation of the user-defined system models. It is a virtual method in the abstract *component* base class and inherited by all derived components. It consists of two functions, *BuildM()* and *BuildRhs()*. SystemC-A uses the *BuildM()* method to add the Jacobian entries to the analogue equation set and *BuildRhs()* method to build the equations, i.e. the right hand side of the Newton-Raphson linearized equation set. The microgenerator equations and corresponding Jacobian matrix entries to be included in the SystemC-A model are listed in Table XII.

The SystemC-A code of the tunable microgenerator model, which is according to Table XII, is listed below:

```

generator::generator(){} //constructor
generator::generator(char nameC[5],TerminalVariable
*node_a,TerminalVariable *node_b,double value,double
Freq): //node_a is Vm, node_b is Im, value is the
tuning force, Freq is the input frequency
component(nameC,node_a,node_b,value){
ztQ = new Quantity("ztQ");
//quantity zt is relative displacement
ytQ = new Quantity("ytQ");
//quantity yt is velocity
itQ = new Quantity("itQ");
//quantity it is inductor current
Fin=value; //tuning force
omega=Freq*2*3.14159;}

void generator::build(){ //model equations
t=TS->get_time(); //current time point
S=TS->get_S();
//time derivative, S=2/h for trapezoidal integration
mpytdotdot=-Mp*Yam*omega*omega*sin(omega*t);
//input acceleration force

zt=X(ztQ);
yt=X(ytQ); //X() return previous value
it=X(itQ);

ztdot=Xdot(ztQ); //Xdot() return previous time
derivative
ytdot=Xdot(ytQ);
itdot=Xdot(itQ);

BuildM(ztQ,ztQ,-Ks); //Jacobian of equation (2)
BuildM(ztQ,ytQ,-Cp-Mp*S);
BuildM(ztQ,itQ,-Phi);
BuildRhs(ztQ,mpytdotdot+Mp*ytdot+Cp*yt+Ks*zt+Phi*it)
;
//Right hand side of equation (2)

BuildM(ytQ,ztQ,S);
BuildM(ytQ,ytQ,-1);
BuildM(ytQ,itQ,0);
BuildRhs(ytQ,yt-ztdot);

BuildM(itQ,ztQ,0); //Jacobian of equation (8)
BuildM(itQ,ytQ,-Phi);
BuildM(itQ,itQ,Rc);
BuildRhs(itQ,-Rc*it-Lc*itdot-vt+Phi*yt);
//Right hand side of equation (8)
}

```

TABLE XII
EQUATION FORMULATION OF THE MICROGENERATOR MODEL

	$z(t)$	$\frac{dz(t)}{dt}$	$i_L(t)$	Equation
$z(t)$	$-k_s$	$-c_p - mS$	$-\Phi$	$m \frac{d^2 z(t)}{dt^2} + c_p \frac{dz(t)}{dt} + k_s z(t) + \Phi i_L(t) + F_{t_z} - F_a$
$\frac{dz(t)}{dt}$	S	-1	0	0
$i_L(t)$	0	$-\Phi$	R_c	$-R_c i_L(t) - L_c \frac{di_L(t)}{dt} + \Phi \frac{dz(t)}{dt}$

B. Digital Part

The pseudo code of the tuning algorithm is shown in Algorithm 2. Standard SystemC modules were used to model the digital control process and in the experimental verification the control algorithm was implemented in a PIC16F884 microcontroller. As can be seen in Algorithm 2, a watchdog timer wakes the microcontroller periodically and the microcontroller first detects if there is enough energy stored in the supercapacitor. If there is not enough energy, the microcontroller goes back to sleep and waits for the watchdog timer again. If there is enough energy, the microcontroller will then compare the frequency of the microgenerator signal, which is close to the input vibration frequency, to the microgenerator's resonant frequency. When a difference is detected between the vibration frequency and the resonant frequency, the microcontroller retrieves the new desired position of the tuning magnet from a look-up table and begins a tuning process by controlling the actuator to move the tuning magnet to the new position (Fig. 11(a)).

Algorithm 2 contains two subroutines: rough tuning (Algorithm 3) and fine tuning (Algorithm 4). The rough tuning measures the frequency of the microgenerator output and moves the actuator to the optimum position according to a predefined lookup table. However, the rough tuning alone cannot generate the best performance and a fine tuning algorithm is needed. This is because the measurement of the frequency of the microgenerator signal does not represent the input vibration frequency accurately enough and, in addition, there may also be a phase difference between the input vibration and the microgenerator motion that prevents the microgenerator from working at the resonance. The fine tuning takes another input, the raw vibration data from the accelerometer and moves the actuator to minimize the phase difference between the microgenerator signal and the accelerometer signal so that the microgenerator is working as resonance. It can be seen that the fine tuning algorithm requires more calculation (thus more energy) than the rough tuning and additional energy is consumed by the accelerometer (see Table XI). Therefore it is not so energy efficient to use only the fine tuning algorithm as the proposed two-subroutine method. In the two-subroutine method, the rough tuning moves the actuator to the approximate resonant position and the fine tuning finds the exact resonance.

V. SIMULATION RESULTS AND EXPERIMENTAL VERIFICATION

A SystemC-A model of the complete system has been built and simulated. The SystemC-A code of the top-level testbench

is listed below. The system components include the microgenerator, the diode bridge, the supercapacitor and the equivalent variable resistances of the actuator, the accelerometer, the microcontroller and the sensor node.

```
void testbench::system(){
```

```

ACT=new actuator;
ACM=new accelerometer;
uC=new control;
NODE=new sensor;
n0 = new Node("0");//don't write n0
n1 = new Node("n1");
n2 = new Node("n2");
n3 = new Node("n3");
n4 = new Node("n4");
n5 = new Node("n5");
n6 = new Node("n6");
//microgenerator generator *G1 =new
generator("G1",n1,n2,0.3192,64);
//diode bridge
diode *D1 =new diode("D1",n0,n1,2.117e-7,1.015);
diode *D2 =new diode("D2",n0,n2,2.117e-7,1.015);
diode *D3 =new diode("D3",n2,n3,2.117e-7,1.015);
diode *D4 =new diode("D4",n1,n3,2.117e-7,1.015);
resistor *R1 =new resistor("R1",n1,n0,10e6);
resistor *R2 =new resistor("R2",n2,n0,10e6);
//super capacitor model
resistor *Ri =new resistor("Ri",n3,n4,0.204);
resistor *Rd =new resistor("Rd",n3,n5,84.0);
resistor *Rl =new resistor("Rl",n3,n6,4375.0);
cap_ini *Ci0 =new cap_ini("Ci0",n4,n0,0.35,1.65);
cap_vary *Cil =new cap_vary("Cil",n4,n0,0.21,1.65);
cap_ini *Cd =new cap_ini("Cd",n5,n0,0.21,1.65);
cap_ini *Cl =new cap_ini("Cl",n6,n0,0.06,1.65);
//power consumption models for actuator,
accelerometer, microcontroller and sensor node
res_vary *RAct =new res_vary("RAct",n3,n0,1.0e9);
res_vary *RAcc =new res_vary("RAcc",n3,n0,1.0e9);
res_vary *RuC =new res_vary("RuC",n3,n0,1.0e9);
res_vary *RNode =new res_vary("RNode",n3,n0,1.0e9);
}

```

The test scenario has been divided into two parts. During the first half of the test, the input vibration frequency changes by 5Hz every 25 minutes (Fig. 13(a)). The main objective of this part of the test is to demonstrate the frequency tuning capability of the microgenerator. It can be seen that after the input frequency changes, the supercapacitor voltage drops because the generated voltage is not high enough to charge the supercapacitor. Then the microcontroller wakes up and tunes the resonant frequency of the microgenerator, which uses much of the energy stored on supercapacitor but the retuned microgenerator starts to charge the supercapacitor again. During the second half, the input frequency is fixed and the performance of the sensor node is being tested (Fig. 13(b)). The sensor node transmits at different time intervals according to the different voltage levels on the supercapacitor (Table IX). The transmission interval is reflected on the supercapacitor charging slope. The shorter transmission interval is, the more gradual charging slope gets. Experimental measurements have been carried out and the waveforms are also shown in Fig. 13. The comparison between the simulation and experimental waveforms of the supercapacitor voltage represents both the energy generation and consumption of the system. In both figures the simulation results correlate well with the experimental measurements which validate the presented technique.

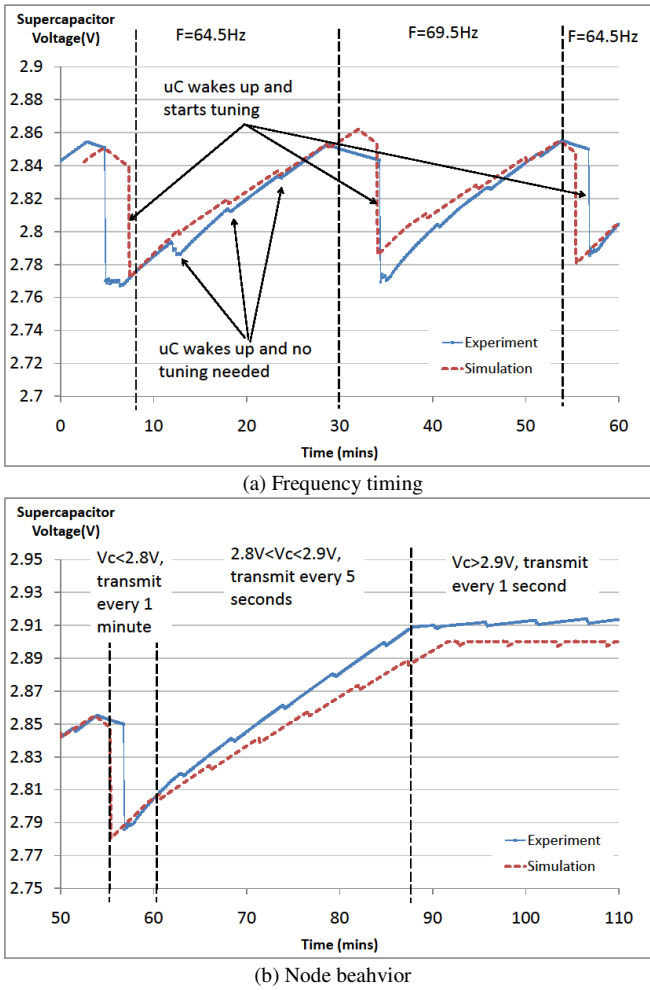


Fig. 13. Simulations and experimental measurements of the supercapacitor voltages.

VI. FAST DESIGN EXPLORATION USING A RESPONSE SURFACE MODEL

Response surface models are constructed from a data set extracted from either physical experiments or computer experiments (simulations) [20]. Due to space limitations, only two major steps of the methodology are given below, namely the formation of an approximated mathematical model by fitting the response under study in terms of design parameters using regression analysis (Section VI-A) and the design of a series of experiments or simulations based on design of experiments (DOE) methodology (Section VI-B). Discussions of the statistical assessment of the goodness of fit and the fitted model reliability are omitted in this paper.

A. Response Surface Mathematical Model

Suppose there is a dependant variable(s) ($y \in R^n$) where n is the number of observations, believed to be affected by a vector of independent variables ($a \in R^k$) where k is the number of independent variables, then the relationship between the dependent variable(s) and independent variables can be expressed as:

$$y = f(a_1, a_2, \dots, a_k) + \varepsilon \quad (11)$$

where ε represents the model errors, a_1, a_2, \dots, a_k are independent variables and $f()$ is called system function that relates dependant variable to independent variables. In most cases, the exact behavior of the system function is unknown especially in engineering problems, so the system function $f()$ may be approximated by an empirical model as:

$$y = \hat{y}(a_1, a_2, \dots, a_k) + \varepsilon \quad (12)$$

where \hat{y} are a low order polynomials or a multi-dimensional splines, and this is called the response surface model. The independent variables or design parameters in equation (12) (i.e a_1, a_2, \dots, a_k) are expressed in their corresponding physical units and must be converted to a dimensionless quantities with zero mean and the same standard deviation before proceeding with further RSM analysis such as regression. These new quantities are called coded variables (i.e x_1, x_2, \dots, x_k) of original design variables (parameters). The transformation process between natural representations and coded representations is achieved via equation (13):

$$x = \frac{a - [a_{\max} + a_{\min} / 2]}{[a_{\max} + a_{\min} / 2]} \quad (13)$$

where a_{\max} and a_{\min} are the maximum and minimum value in the range of that specific design parameter. Now the approximated function \hat{y} is expressed in term of coded variables (x_1, x_2, \dots, x_k) and how to choose such a model \hat{y} determines the success of applying RSM methodology. Typically, most engineering problems \hat{y} can be approximated by a quadratic multi-variable polynomials as follows:

$$\hat{y} = \beta_0 + \sum_{i=1}^k \beta_i x_i + \sum_{i=1}^k \beta_{ii} x_i^2 + \sum_{i < j} \beta_{ij} x_i x_j \quad (14)$$

where $\beta_0, \beta_i, \beta_{ii}, \beta_{ij}$ are the coefficients of the intercept, linear, quadratic and interaction in the regression model respectively, x_i, x_j are the design parameters in their coded format. The coefficients of the polynomial in equation (14) are determined through n simulation runs for the SystemC-A energy harvester model. The design points of the n runs are determined using DOE technique based on D-Optimal criteria. Using matrix notation, equation (14) can be written as:

$$\hat{y} = X\beta \quad (15)$$

where $X_{n \times p}$ is $n \times p$ design matrix, p is the number of coefficients in the approximated polynomial, n is the number of simulation runs. $\beta_{p \times 1}$ are the unknowns parameters need to be solved. The difference between the observed values y and fitted values \hat{y} for the i th observation $\varepsilon_i = y_i - \hat{y}_i$ is called the residual for that specific observation. The sum of the squares of the residuals (SSE) is defined as:

$$SSE = \sum_{i=1}^n \varepsilon^2 = \sum_{i=1}^n (y_i - \hat{y}_i)^2. \quad (16)$$

Combining equations (15) and (16) and differentiating with respect to β lead to:

$$\frac{\partial SSE}{\partial \beta} = \sum_{i=1}^n \left(\frac{\partial}{\partial \beta_i} (y_i - X\beta)^2 \right). \quad (17)$$

Solving equation (17) for each β_i using least square method

TABLE XIII
SYSTEM PARAMETERS FOR OPTIMISATION

Description	Value range	Coded symbol
Microcontroller clock frequency(Hz)	125k - 8M	x_1
Watchdog timer wakeup time(sec)	160 - 480	x_2
Transmission time interval(sec)	1 - 10	x_3

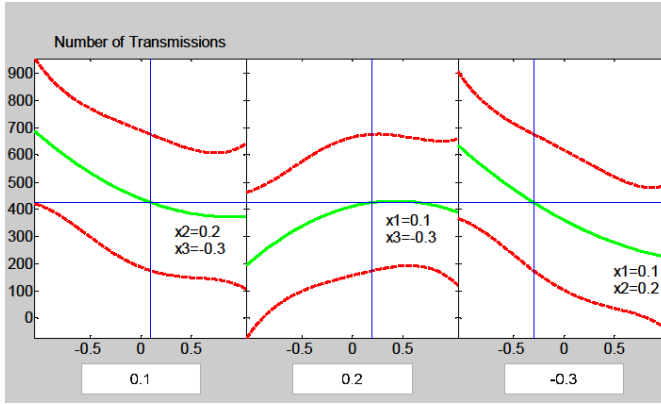


Fig. 14. The effect of each design parameter on system performance (total number of transmissions during one hour).

(LSM) will lead to an accurate model \hat{y} that satisfy the condition of minimum residuals (i.e best fit).

B. D-Optimal Experimental Design

In the design matrix $X_{n \times p}$, each specific run is represented by a single row and each column contains a specific design parameter that varies in each row based on predefined designed points. How to choose the predefined design points efficiently is called design of experiments (DOE) methodology. There are different types of design of experiments, such as full factorial, central composite design (CCD), Box Behnken designs (BBD) and computer generated designs, such as D-optimal design [20]. Because D-optimal DOE explores design parameters space efficiently with minimum number of run that enable model construction with good accuracy [21], it has be used for the study in this paper. The algorithm of D-optimal criterion optimise the feasible potential design points to form a subset of D-optimal points that will be used in simulation runs. This optimisation is based on maximizing the determinant of XX' , where XX' is called information matrix [21].

C. RSM Optimisation Results

As described in Section III-A, three parameters which affect the energy generation and consumption of the wireless sensor node system have been chosen for optimisation. Their value ranges and coded variable symbols are listed in Table XIII. Each of the three coded variables has three values [-1 0 1] which is the minimum number required to generate a quadratic approximation [20]. The full factorial design requires 27 (3^3) simulations while the D-optimal design only requires 10 simulations. As explained in Section VI-B, the D-optimal design points are obtained and 10 simulations have been carried out with the corresponding parameters. The

acceleration level of the input vibration is fixed as 60 mg and the input frequency changes by 5 Hz every 25 minutes. The optimisation aim has been chosen as to maximise the number of transmissions during one hour. The MATLAB response surface toolbox has been used to generate the quadratic equation and the response surface model is:

$$\hat{y}(x_1, x_2, x_3) = 469.167 - 108.833x_1 - 18.833x_2 - 209.5x_3 + 71.833x_1^2 + 90.5x_2^2 - 39.0x_3^2 - 32.333x_1x_2 - 71.333x_1x_3 + 43.333x_2x_3 \quad (18)$$

The fitted model in equation (18) reflects the effects of each design parameters as well as the interactions effects between design parameters. Fig. 14 plots each single design parameter against the total number of transmissions while holding other design parameters constant.

Two algorithms from the MATLAB optimisation toolbox have been used to maximise the number of transmission, i.e maximise equation (18). The chosen algorithms are Simulated Annealing and Genetic Algorithm, both of which are capable of global searching. The optimisation results, together with the original design, are listed in Table XIV. It can be seen that both of the optimised design improved the system performance massively. The total number of transmissions doubled with the optimised design, which validates our proposed technique.

VII. CONCLUSION

Wireless sensor networks are fast developing and energy harvester powered sensor nodes have attracted great research interest. In order to design energy efficient wireless sensor nodes, it is crucial to consider all the components in the context of energy consumption in a complete, autonomous wireless system. This paper presents such an HDL based modeling approach that links the system's energy generation and consumption with its analogue parts as well as digital processes. Simulation and optimisation results of the developed HDL models match well with the experimental measurements and correctly reflect the changing energy flow when the digital processes are carrying out different operations. Future work will focus on the optimisation of both the energy harvester and digital control algorithms so that the system's overall energy efficiency can be improved. This paper also presents an approach to fast design space exploration based on a response surface model. The RSM has been used to optimise a complete wireless sensor node syste using SystemC-A and MATLAB. SystemC-A has been used to

TABLE XIV
OPTIMISATION RESULTS

	Original design	Simulated Annealing	Genetic Algorithm
Microcontroller clock frequency(Hz)	4M	125k	125k
Watchdog timer wakeup time(sec)	320	160	480
Transmission time interval(sec)	5	1	1
Number of transmissions	405	869	809

model the system's analogue components as well as the digital processes and MATLAB to generate and optimise the response surface model. As demonstrated by the optimisation results, the proposed technique leads to an efficient optimisation process by combining the power of SystemC-A in modelling multi-domain systems and the power of MATLAB in computation.

REFERENCES

- [1] C. Alippi, R. Camplani, C. Galperti, and M. Roveri, "A robust, adaptive, solar-powered wsn framework for aquatic environmental monitoring," *Sensors Journal, IEEE*, vol. 11, no. 1, pp. 45–55, 2011.
- [2] Q. Ling, Z. Tian, Y. Yin, and Y. Li, "Localized structural health monitoring using energy-efficient wireless sensor networks," *Sensors Journal, IEEE*, vol. 9, no. 11, pp. 1596–1604, 2009.
- [3] A. Sapio and G. Tsouri, "Low-power body sensor network for wireless eeg based on relaying of creeping waves at 2.4ghz," in *Body Sensor Networks (BSN), 2010 International Conference on*, 2010, pp. 167–173.
- [4] S. Roundy, P. K. Wright, and J. M. Rabaey, *Energy scavenging for wireless sensor networks: with special focus on vibrations*. Springer, 2004.
- [5] M. P. Buric, G. Kusic, W. Clark, and T. Johnson, "Piezo-electric energy harvesting for wireless sensor networks," in *Wireless and Microwave Technology Conference, 2006. WAMICON '06. IEEE Annual*, 2006, pp. 1–5.
- [6] S. Ergen, A. Sangiovanni-Vincentelli, X. Sun, R. Tebano, S. Alalusi, G. Audisio, and M. Sabatini, "The tire as an intelligent sensor," *Computer-Aided Design of Integrated Circuits and Systems, IEEE Transactions on*, vol. 28, no. 7, pp. 941–955, 2009.
- [7] P. Mitcheson, T. Green, E. Yeatman, and A. Holmes, "Architectures for vibration-driven micropower generators," *Journal of Microelectromechanical Systems*, vol. 13, no. 3, pp. 429–440, 2004.
- [8] D. Zhu, J. Tudor, and S. Beeby, "Strategies for increasing the operating frequency range of vibration energy harvesters: a review," *Measurement Science and Technology*, vol. 21, no. 2, 2010.
- [9] *Energy Harvesting Systems: A Block Diagram* (2010, July 16), "Holistic energy harvesting," September, 2011. [Online]. Available: <http://www.holistic.ecs.soton.ac.uk/res/ehsystem.php>
- [10] H. Boussetta, M. Marzencki, S. Basrou, and A. Soudani, "Efficient physical modeling of mems energy harvesting devices with vhdl-ams," *Sensors Journal, IEEE*, vol. 10, no. 9, pp. 1427–1437, 2010.
- [11] L. Wang, T. Kazmierski, B. Al-Hashimi, A. Weddell, G. Merrett, and I. Ayala-Garcia, "Accelerated simulation of tunable vibration energy harvesting systems using a linearised state-space technique," in *Design, Test and Automation in Europe (DATE 2011), March 14-18, 2011*, pp. 1267–1272.
- [12] R. Torah, P. Glynne-Jones, J. Tudor, T. O'Donnell, S. Roy, and S. Beeby, "Self-powered autonomous wireless sensor node using vibration energy harvesting," *Measurement Science and Technology*, vol. 19, no. 12, pp. ISSN 1361–6501, 2008.
- [13] M. G. Corporation, *SystemVision User's Manual*, ser. Version 3.2, Release 2004.3, July 2004.
- [14] R. Torah, M. Tudor, K. Patel, I. Garcia, and S. Beeby, "Autonomous low power microsystem powered by vibration energy harvesting," *Sensors, IEEE*, pp. 264–267, 28-31 Oct. 2007.
- [15] Recoil Ltd, UK, <http://www.recoiltd.com/index.htm>, Sept. 2008.
- [16] M. Mitchell, *An Introduction to Genetic Algorithms*. Cambridge, Massachusetts: the MIT Press, 1996.
- [17] I. A. Garcia, D. Zhu, J. Tudor, and S. Beeby, "Autonomous tunable energy harvester," in *PowerMEMS 2009, 1-4 December 2009*, pp. 49–52.
- [18] D. Zhu, S. Roberts, J. Tudor, and S. Beeby, "Design and experimental characterization of a tunable vibration-based electromagnetic micro-generator," *Sensors and Actuators A: Physical*, vol. 158, no. 2, pp. 284–293, 2010.
- [19] H. Al-Junaid and T. Kazmierski, "Analogue and mixed-signal extension to SystemC," *IEE proc. Circuit Devices Systems*, vol. 152, no. 6, pp. 682–690, Dec. 2005.
- [20] J. Jacquez, "Design of experiments," *Journal of the Franklin Institute*, vol. 335, no. 2, pp. 259–279, 1998.
- [21] R. Unal, R. Lepsch, and M. McMillin, "Response surface model building and multidisciplinary optimisation using d-optimal designs," in *Proceedings of the 7th AIAA/USAF/NASA/ISSMO Symposium on multidisciplinary Analysis and optimisation*, 1998, pp. 405–411.

Pattern-Based Approach to Current Density Verification

Vazgen Melikyan, Eduard Babayan, and Ashot Harutyunyan

Abstract—Methodology of static verification of current density based on layout patterns common in IC designs is proposed. The methodology is based on pre-calculation of current density distribution for common layout patterns. Then using the obtained data to calculate current densities of large circuits by partitioning them to selected patterns. Presented experimental results show the effectiveness of the approach.

Index Terms—Current density, electromigration, verification, patterns.

I. INTRODUCTION

WITH increasing technology scaling, physical effects consideration and their impact priorities have changed. In particular, impact of electromigration (EM) increased [1-4]. EM is the mass transport in a conductor due to the momentum transfer between conducting electrons and diffusing metal atoms [1]. This effect damages interconnect because amounts of matter leaving and entering a given volume of interconnect are not equal, leading to accumulation or loss of material which results in damage [1]. When atomic flux into a region is greater than the flux leaving it, the matter accumulates in the form of a hillock. If the flux leaving the region is greater than the flux entering, the depletion of matter ultimately leads to a void (Fig. 1) [2].

Obviously, EM results in failure of IC which can be result not only of break or short-circuit, but also a significant increase in the interconnect resistance.

EM is defined as [3]:

$$J = -\frac{N_A}{kT} D_0 e^{-\frac{Q}{kT}} eZ^* \rho j \quad (1)$$

where N_A – density of atoms in the crystal lattice; D_0 – diffusion coefficient; Q – activation energy; eZ^* – resulting charge; ρ – resistivity; k – Boltzmann constant; T – absolute

Manuscript received 1 May 2012. Accepted for publication 30 May 2012. Some results of this paper were presented at the 4th Small Systems Simulation Symposium, Niš, Serbia, February 12-14, 2012.

Paper presents result of work implemented in the framework of project “11P5-002” jointly founded by Belarusian National Fundamental Research Found and State Science Committee of Ministry of Education and Science of Republic of Armenia.

Vazgen Melikyan and Eduard Babayan are with the Educational Department of Synopsys Armenia CJSC, 41 Arshakunyants ave., Yerevan, Armenia, (e-mail: {vazgenm,edbab}@synopsys.com).

Ashot Harutyunyan is with Microelectronics Circuits and Systems of State Engineering University of Armenia, 105 Teryan st., Yerevan, Armenia, (e-mail: harash@seua.am).

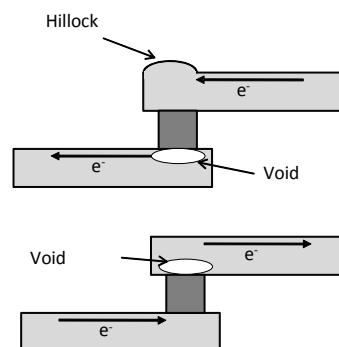


Fig. 1. Hillocks and voids.

temperature; j – current density.

During IC design it is required to check design against EM vulnerabilities. As it is seen from (1), such a check can be done by checking current density in interconnect against maximum allowable current density. Currently there are different current density verification EDA tools by different vendors. These tools have common disadvantages: they work only on chip level, require additional extraction and simulation steps, require large amount of background information, lack error correction, etc. [4,5]

This paper presents methodology of creation of current density verification tool based on common layout patterns which enables high verification performance without need of additional extraction and simulation steps.

II. METHODOLOGY

It is proposed to select common layout patterns (LP) (Fig. 2), taking into account the frequency of their use in real

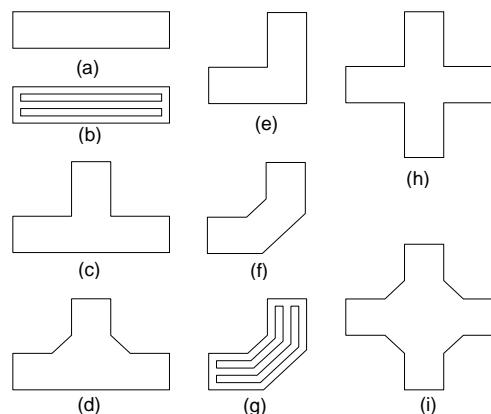


Fig. 2. Common layout patterns selected for modeling.

TABLE I
STATISTIC DATA FOR PATTERNS SELECTION

LP	IC A		IC B		IC C		IC D	
	Area, %	Count	Area, %	Count	Area, %	Count	Area, %	Count
a.	39	16643910	36	20582714	40	7374407	31	6583941
b.	10	9283	14	16700	0	0	0	0
c.	4	56859	2	13269	9	170152	5	8195
d.	0	0	4	2582	0	0	0	0
e.	16	341139	4	840437	11	166584	15	225007
f.	0	0	12	38474	2	39033	0	5
g.	1	28	1	56	0	0	0	64
h.	3	65401	3	26780	6	95161	2	16339
i.	0	0	5	1341	0	0	0	0
Total	73		81		68		53	

ICs and relative areas covered by them statistically (Table I).

Simulation of these patterns enables estimation of maximum current density in these patterns depending on their geometrical parameters.

For LP selection current density values in the direction of the normal were taken as boundary conditions. The dependence of the maximum current density on the boundary conditions and geometric parameters of the model was calculated.

The essence of the method is demonstrated below for the sample LP (Fig. 3). In this case currents distribution is uniform in the direction of normal, equal to j_n and $-j_n$ for

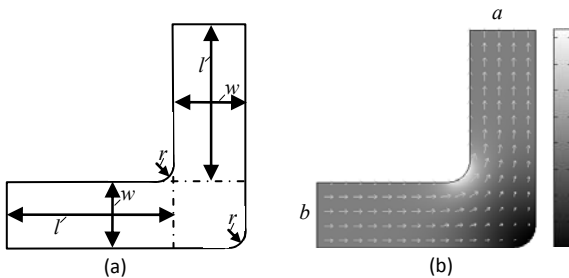


Fig. 3. For modeled LP: a – parameters; b – current density distribution.

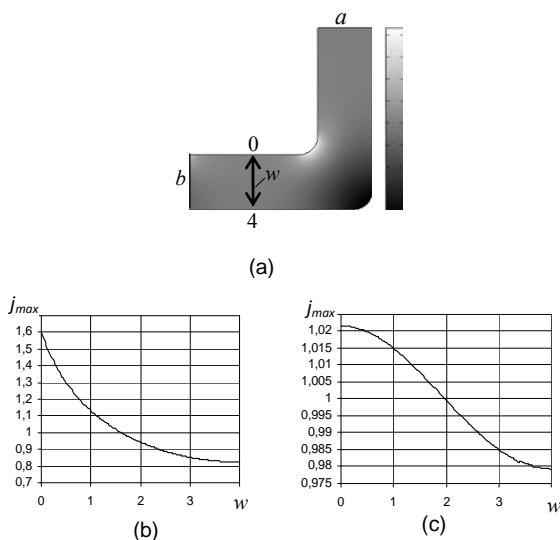


Fig. 4. Uneven distribution of boundary currents.

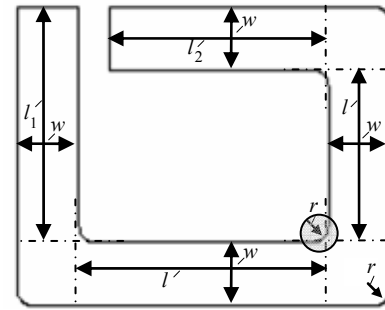


Fig. 5. The selected structure to obtain l_{min} .

edges a and b respectively, and 0 for the rest. Current density distribution map shows that in the inner corner of the LP current is thickened, and on the outside, on the contrary, is diluted. Simulation was performed to identify patterns of current distribution for non-uniform boundary conditions.

For edge a of LP in Fig. 4a, a boundary condition of uniform current distribution $j_n=l$ was set. Current distribution for edge b is shown on Fig.5b and it is mostly concentrated in upper corner. Current density reduces near upper corner and increases near bottom at a distance from edge b . In the middle of the straight segment the densities of these currents are most close to each other (Fig. 5c).

It was found out that with the increase of length of LP branches, the largest and smallest values in Fig.4c tend to 1. Consequently, it can be assumed that when length of branches l decreases in the considered model, the impact of boundary conditions distribution on the largest value of current density (LVCD) decreases. This allows neglecting boundary conditions distribution and its impact on current density distribution. The calculation of the boundary currents distribution leads to solution of differential equations. It is required to find a minimum length of branches l_{min} such that for branches with larger lengths, the relative difference between the maximum values of current density does not exceed the specified error ϵ at all possible r and w .

The length l_{min} should be found for boundary condition, assumed as such from a specific practical point of view. There could be other conditions at which smaller values of l_{min} are obtained for the same values of ϵ . As a result of investigations structure shown in Fig. 5 was chosen which provides the worst boundary conditions for the considered LP.

An experiment has been made to find the significance of changes of maximum values of current density, depending on the lengths l_1 and l_2 larger than l .

Given that with decrease of length l impact of boundary conditions on LVCD increases, for experiment the value of $l = 3 \cdot r$ was chosen for it to be as small as possible (it is the smallest, because at $l = 2 \cdot r$ the interior edges are equal to zero (Fig. 5))

The value of w was selected equal to l . This value of w can be viewed as practically the worst, because with increase of w the impact of boundary conditions on LVCD increases with unacceptably large error ϵ . Experimental results do not depend on the value of r . Setting r to 1, values $l=3$ and $w=3$ can be obtained. Due to position of branches values of l_1 and l_2 cannot exceed l . Thus, the value of one of them is fixed and

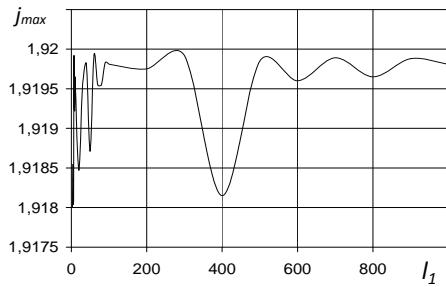


Fig. 6. Dependence of j_{max} on l_1 , for $l_1 \geq l$.

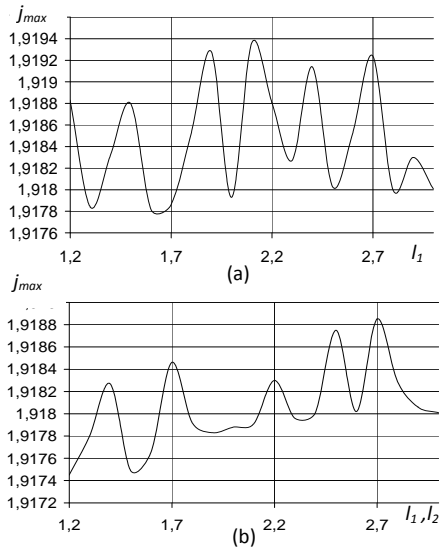


Fig. 7. Dependence of j_{max} a - on l_1 , for $l_1 \leq l$, b - on l_1 and l_2 ($l_1 \leq l, l_2 \leq l$).

only the value of another changes. Based on the dependence of LVCD on l_1 obtained through the experiment, it can be concluded that for l_1 nearly equal to l a value of LVCD is obtained which is by no more than 1% less than LVCD for larger l_1 (Fig. 6).

To find dependence of LVCD on simultaneous change of l_1 and l_2 , first l_1 was changed in the range less than l (Fig. 7a), then both l_1 and l_2 were changed (Fig. 7b). It can be stated that the LVCD values found for values larger than l will not change with increase of l_2 . Values of l_1 and l_2 can be taken equal to l during calculation dependence of LVCD on model parameters.

In the result of experiments it was found that for the worst selected values ($l/w=1.5$), the relative difference of obtained LVCD values is 0.5...0.6% compared to values obtained for values larger than l (Fig. 8).

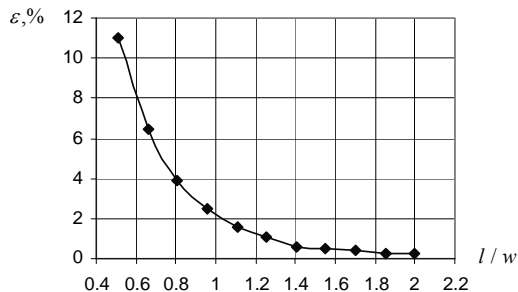


Fig. 8. Dependence of error ε on l/w .

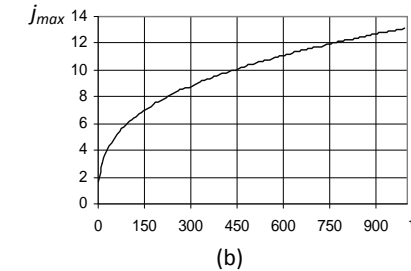
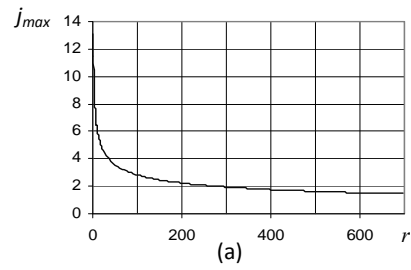


Fig. 9. Dependence of j_{max} on a - w , b - r

For considered LP, with the condition of $l/w \geq 1.5$ experiments were implemented to find the dependence of current density on parameters r and w . In the result it was obtained that j_{max} does not depend on w and r , thus it can be expressed as:

$$j_{max} = f(r) \cdot \varphi(w) \cdot j \tag{2}$$

where

$$j = I/w \tag{3}$$

is the current density in uniform area. Thus it is the boundary condition for those edges of the considered LP, which have nonzero current flowing in the direction of normal.

To obtain functions f and φ two experiments were implemented resulting in dependencies of j_{max} on w (Fig. 9a) and r (Fig. 9b) with fixed value of another variable.

In the result of approximation of dependence function, the following was obtained for considered LP:

$$j_{max} = (13,2 \cdot r^{-0,33} - 0,06368) \cdot (0,09743 \cdot w^{0,3365} + 0,0005986) \cdot j \tag{4}$$

Using expressions (2) and (3), for w this is obtained:

$$\frac{0,09743 \cdot w^{0,3365} + 0,0005986}{w} = \frac{j_{max}}{I \cdot (13,2 \cdot r^{-0,33} - 0,06368)} \tag{5}$$

The general flow of developed method of current density verification is presented on Fig. 10.

TABLE II.
COMPUTER TIME AND MEMORY REQUIRED
TO OBTAIN THE CURRENT DENSITY DISTRIBUTION

Parameters	Circuit 1	Circuit 2	Circuit 3	Circuit4
Time, s	0.125	0.391	1.734	7.984
Memory, kB	1.3	8.7	28.9	97.4

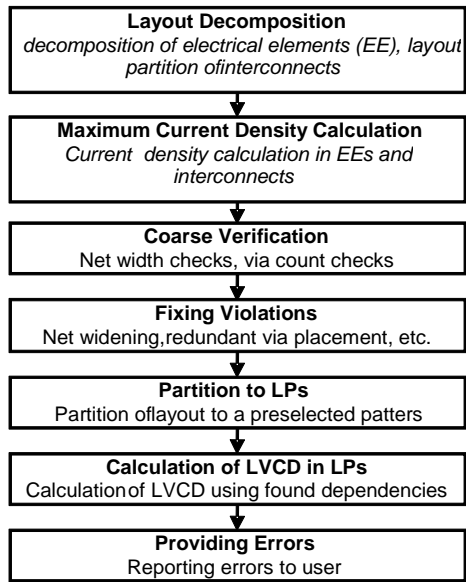


Fig. 10. General current density verification flow.

Experimental software implementing the proposed method was developed. Unlike industrial software, it does not need additional extraction and simulation steps. Experimental results obtained using software are shown in Table II.

For a circuit with 50000 LPs, 104 minutes were required for calculation with conventional software, whereas with proposed method it took only ~10 minutes.

III. CONCLUSION

The developed method of current density verification in ICs and the experimental software package have indisputable advantages over existing similar tools and meet practical requirements of modern IC design.

REFERENCES

- [1] H. Ceric, S. Selberherr, "Electromigration in submicron interconnect features of integrated circuits", *Materials Science and Engineering*, 2011, pp. 53-86.
- [2] L. Xiaoyu, S. Jiang, W. Yun, Z. Chenhui, "Research on failure modes and mechanisms of integrated circuits", *Prognostics and System Health Management Conference (PHM-Shenzhen)*, 2011, 2011, pp. 1-3.
- [3] M. Shao, et al., "Current calculation on VLSI signal interconnects", *Sixth International Symposium on Quality of Electronic Design, (ISQED)*, 2005, pp. 580-585.
- [4] B. Li, et al. "Statistical Evaluation of Electromigration Reliability at Chip Level", *IEEE Transactions on Device and Materials Reliability*, 2011, p. 1-11.
- [5] J.P. Gambino, T.C. Lee, F. Chen, T.D. Sullivan, "Reliability challenges for advanced copper interconnects: Electromigration and time-dependent dielectric breakdown (TDDB)", *16th IEEE International Symposium on the Physical and Failure Analysis of Integrated Circuits*, 2009, pp. 677-684.

Network Simulator Tools and GPU Parallel Systems

Leonid Djinevski, Sonja Filiposka, and Dimitar Trajanov

Abstract—In this paper we discuss the possibilities for parallel implementations of network simulators. Specifically we investigate the options for porting parts of the simulator on GPU in order to utilize its resources and obtain faster simulations. We discuss few issues which are unsuitable for the GPU architecture, and we propose a possible work around for each of them. We introduce a design of parallel module that interconnects with a network simulator, while maintaining transparency in aspect of the simulation modeler.

Index Terms—Network Simulator Tools, HPC, GPGPU, CUDA, OpenCL.

I. INTRODUCTION

NETWORK simulators are tools used by researchers in order to test new scenarios and protocols in a controlled and reproducible environment, allowing the user to represent various topologies, simulate network traffic using different protocols, visualize the network and measure the performances. Although network simulators are very useful, most of the widely used network simulators do not scale [1]. Simulation of medium to large networks results in a long simulation time which is not practical for investigating protocols.

With the development of parallel systems, significant processing power is becoming available. The single instruction, multiple data (SIMD) models of parallel systems, more particular the Graphics Processing Units (GPUs) have provided a massive acceleration. Additionally, the low cost of these units have brought a huge performance in the insides of regular personal computers (PCs). The first attempts for utilizing the GPU hardware for general purpose computing proved to be a very complicated process [2]. However, with development of the Compute Unified Device Architecture (CUDA) programming model in 2007 [3], and also with the publishing of the standard Open Computing Language (OpenCL) late 2008 [4], general purpose computing on

graphics hardware has significantly improved. Therefore, many general purpose applications have been ported for the GPU architecture.

Network simulators have traditionally been developed for execution on sequential computers. Developing a parallel implementation for a network simulator is not straight forward. There are many architectural issues that have to be taken in to account and they might prevent the complete utilizing of the GPU resources.

In this paper we review few of the most widely used network simulators. We also discuss the possibilities for parallel implementations of network simulators. Specifically we investigate the options for porting parts of the simulator on GPU in order to utilize its resources and obtain faster simulations. Additionally, we identify modules which carry the biggest workload as well as possible, issues that make the network simulators unsuitable for the GPU architecture, and we propose resolutions to work around these issues.

This rest of this paper is organized as follows: We review implementations of network simulator tools in Section 2, followed by a short overview of the GPU computing in Section 3. In Section 4 we identify which modules of the network simulator contain intensive workloads. Also in this Section we propose a framework which will utilize the GPU resources. In Section 5 we analyze performance, and we conclude and propose future work in Section 6.

II. RELATED WORK

There are two types of approaches for developing a parallel network simulator. One can create the parallel simulator from scratch, where all the simulation software is custom designed for a particular parallel simulation engine. For this approach a significant amount of time and effort are necessary to create a useable system. This is so, because new models must be developed, and therefore validated for accuracy.

An example of this approach is the Global Mobile Information System Simulator (GloMoSim), which is a scalable simulation library designed at UCLA Computing Laboratory to support studies of large-scale network models, using parallel and/or distributed execution on a diverse set of parallel computers [5]. GloMoSim beside sequential adopts parallel simulation model using libraries and layered API. The libraries are developed using PARSEC [6], which is a parallel C based programming language which uses message based

Manuscript received 1 May 2012. Accepted for publication 30 May 2012. Some results of this paper were presented at the 4th Small Systems Simulation Symposium, Niš, Serbia, February 12-14, 2012.

Leonid Djinevski, Sonja Filiposka and Dimitar Trajanov are with the E-TNC Research Group, Faculty of Computer Science and Engineering, Ss. Cyril and Methodius University, Rugjer Boshkovikj 16, 1000 Skopje, Macedonia, E-mail: {leonid.djinevski, sonja.filiposka, dimitar.trajanov}@finki.ukim.mk.

approach.

Another example is the Scalable Simulation Framework (SSFNet) which claims that is a standard for parallel discrete event network simulation [6, 7]. SSFNET's commercial Java implementation is becoming popular in the research community, but SSFNet for C++ (DaSSF) does not seem to receive nearly as much attention, probably due to the lack of network protocol models. It is a high performance network simulator designed to transparently utilize parallel processor resources, and therefore scales to a very large collection of simulated entities and problem sizes.

The second approach for developing parallel/distributed simulation involves interconnecting with existing simulators. These federated simulations may include multiple copies of the same simulator (modeling different portions of the network), or entirely different simulators. Few parallel implementations of this approach are presented in the following.

The NS-2 Simulator [8] is widely used in the networking research community and has found large acceptance as a tool to experiment new ideas, protocols and distributed algorithms. It is a discrete event driven sequential network simulator, developed at UC Berkeley by numbers of different researchers and institutions. NS-2 is suitable for simulating and analyzing either wired or wireless network sand is used mostly for small scale simulations. NS-2 is written in C++ and OTcl. The users define the network topology structure, the nodes, protocols and transmitting times in an OTcl script. The open source model of NS-2 encourages many researchers from institutions and universities to participate and contribute to improve and extend the project. NS-2 plays an important role especially in the research community of mobile ad hoc networks, being a sort of reference simulator [9]. Adding new network objects, protocols and agents requires creation of new classes in C++ and then linking them with the corresponding OTcl objects.

A parallel simulation extension for the traditionally widely used NS-2 simulator has been created at the Georgia Institute of Technology (PADS Research Group), but it is not in wide use. The Parallel/Distributed NS (*PDNS*) [10] was designed to solve the NS-2 problems with large scale networks by running the simulator on a network of workstations connected either via a Myrinet network, or a standard Ethernet network using the TCP/IP protocol stack. In that way the overall execution time of the simulation should be at least as fast as the original single workstation simulation, allowing simulating large scale networks.

Georgia Tech Network Simulator (GTNetS) is a network simulation environment which uses C++ as a programming language [11]. GTNetS is designed for studying the behavior of moderate to large scale networks. The simulation environment is structured as an actual network with distinct separation of protocol stack layers.

OMNeT++ is a network simulation library and framework, primary used for simulation of communication networks, but because of its flexible architecture can be used to simulate complex IT systems too. *OMNeT++* offers an Eclipse based

IDE and the programming language used is C++ [12, 13].

In this paper we introduce a different approach for parallelizing network simulators that is based on federation simulations. In order to fully utilize the available hardware we investigate the possibility to port the computing intensive network simulator modules to the GPU and thus obtain faster simulation time.

III. GPGPU, CUDA, AND OPENCL

In this section we summarize some key fact of the GPU architecture so we can provide and discuss information about parallel module implementation of a network simulator. The origin of General-Purpose computing on Graphics Processing Units (GPGPU) comes from graphics applications, so in similar fashion, CUDA or OpenCL applications can be accelerated by data-parallel computation [14] of millions of threads. A thread in this context means an instance of a kernel, which is a program that is running on the GPU. This way, the GPU device can be visualized as a SIMD parallel machine. Therefore, understanding of the graphics pipeline to execute programs is not needed. In a nutshell, CUDA or OpenCL provide convenient memory hierarchy, allowing maximizing the performance, by optimizing the data access. The memory hierarchy of a GPU device is presented in Fig 1.

The GPU device has off-chip memory, so called global memory. Since this memory is separated from the GPU, a single fetching of data takes at least 500 cycles. This is the slowest memory on the device, and therefore the most expensive performance wise.

The next level in the memory hierarchy is the local memory, which is shared by a number of threads organized in work groups. This memory is very small 16 – 48KB, and it can be accessed almost as fast as register memory denoted in Fig. 1 as private memory which is exclusive to a single thread. Therefore, a program will compute correctly if there is no data dependence between threads in different work groups.

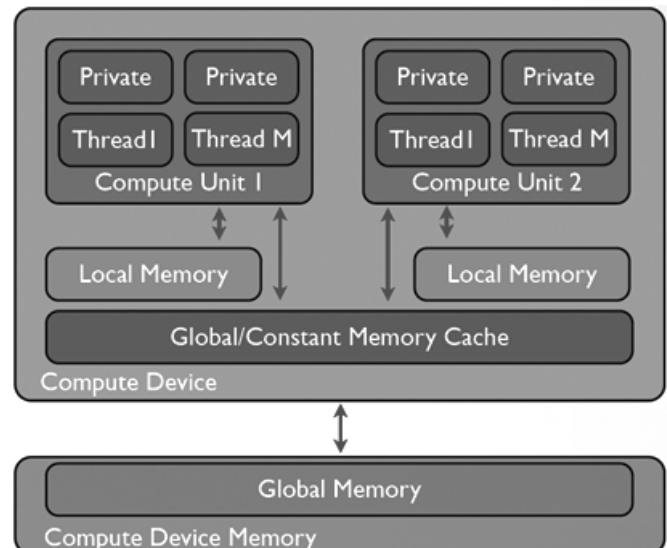


Fig. 1. GPU device memory hierarchy.

Exception is that within the same work group thread can have dependence because they can exchange data using the local memory.

IV. NETWORK SIMULATOR MODULES

Network simulator algorithms are usually not so straight forward for mapping on the GPU, therefore we need to identify the workload of each module. The modules with the biggest workload are candidates for parallelization. Since, the GPU is a SIMD, in order to utilize the architecture, we look for segments of the algorithm code which are repeated regularly. Usually, these code segments are for loops or loops for which control flow can be predicted.

Once we identify which modules to parallelize, few issues have to be taken in to account. If the code segment works with small amount of data, the GPU device parallelism cannot be expressed. Another major issue is the control flow divergence. If the code segment contains much branching, the parallel code gets serialized, thus minimal or no performance increase is achieved. Nevertheless, in order to tweak the algorithm, few methods can be used to decrease the divergence. However, the worst divergence situation is presented in Listing I.

LISTING I.
UNAVOIDABLE DIVERGENCE

```

if (condition 1)
  do this block of operations
else if (condition 2)
  do that block of operations
else if (condition 3)
  do some block of operations
else
  do any block of operations

```

In this case the divergence can cause up to 75% efficiency reduction, because the block of operation requires hundreds of instructions, thus making the algorithm unsuitable for SIMD parallel execution.

A. Program Transformations

In order to exploit more parallelism from the resources at hand, the program has to be transformed. The structure of the computations and their schedule need to be changes, so the program transformations will result with equivalent program which will have better performance.

Since data access is the most expensive part of the program execution, sometimes the program can be transformed so the data is not loaded from memory and calculated on the GPU device. In addition, another important factor is to have enough data to process in order to utilize the parallel resources. Therefore, it is prudent to introduce more calculation even if there are not needed at the moment, since in the following moments a requested calculation could already been obtained.

V. PERFORMANCE ANALYSIS

In order to obtain relevant results, we propose using a GPU device from the high-end segment. An example of a high-end

GPU device is the Nvidia Tesla C2070 GPU, which is the flag holder device for Nvidia at the moment of writing this paper.

Regarding parallelism, the Amdahl Law is plotted in Fig. 2, where the x-axis is the number of processors p , and the y-axis is the achieved speedup.

There are three segments that can be noticed on the plot. The segment I represents a relation between the speedup and the number of processors, where by increasing the number of processors. In the second segment, a saturation is achieved, so the speedup stays constant with the increasing the number of processors. The segment III, indicates that increasing of the number of processors, can lead to decreasing of the speedup, which is a consequence of much more communication between the processors and much less computing achieved.

Since for a given GPU device, the number of cores is constant, the plotted curve will depend of the amount of data that is being computed as it is presented in Fig. 3.

The curve 1 is the same curve as plotted in Fig 2. Curves 2 and 3 present the speedup for larger data quantities. Hence, we can conclude that for larger data quantities, the curve achieves saturation much slower.

Therefore, the network simulator parallel module, should scale well over different sizes of networks, in such a way that the simulation scenarios of interest are in the linear segment I, and possibly, if unavoidable in the saturation segment II.

The parallel module should achieve maximal speedup of at

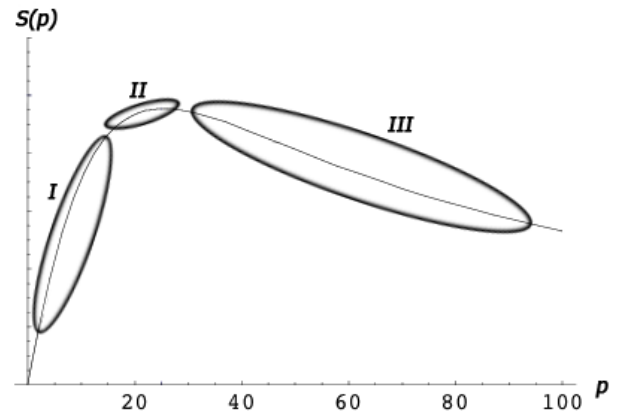


Fig. 2. Parallel speedup.

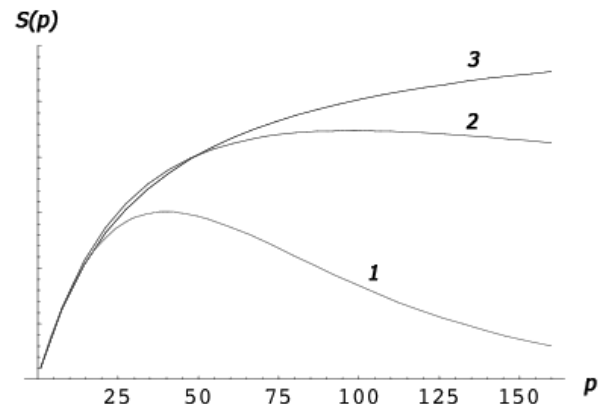


Fig. 3. Parallel speedups for different data amounts.

least x25 on a high-end TESLA C2070 GPU for the overall execution of the network simulator. This is a reasonable performance increase that is consistent with many real-life applications ported to the GPU platform, thus providing another example of achieved acceleration by utilizing the computational power of modern programmable GPU devices.

VI. CONCLUSION

Specific modules of the network simulators demand high computational resources. Therefore, we propose a parallel module for the network simulator in order to utilize the computational performance of GPU devices. Usually the network simulator algorithms run in single precision, so the GPU devices are suitable, although the fact that the GPUs support double precision which is still significantly slower.

In our future work, we intend to develop an implementation of a parallel module for one of the few most widely used network simulators. Also, we would like to evaluate how the GPU implementation of the network simulator extension can perform in specific case network topologies. In addition, we would like to search for the best suitable data structures that can provide further optimization. Beside the stand alone machine setup, we would like to test our parallel module on a multi-GPU setup. Additionally we would like to combine MPI and OpenCL, in order to investigate how parallel module will perform on a cluster of computers, where each computer has a multi-GPU setup.

REFERENCES

- [1] Weingartner, E., vom Lehn, H., Wehrle, K., "A Performance Comparison of Recent Network Simulators" in Conf. Rec. 2009. ICC '09. IEEE Int. Conf. Communications, pp. 1-5.
- [2] Harris, M.J., "General Purpose Computation on GPUs", retrieved June 2011 from <http://www.gpgpu.org/>.
- [3] NVIDIA CUDA, retrieved February 2010 from <http://developer.nvidia.com/object/cuda.html/>.
- [4] The OpenCL Specification, Version 1.0, document Revision 43, 2009, retrieved February 2010 from <http://www.khronos.org/opencl/>.
- [5] Zeng, X., Bagrodia, R., Gerla, M., "GloMoSim: A Library for Parallel Simulation of Large-Scale Wireless Networks", in Proc.12th Workshop on Parallel and Distributed Simulation, Banff, Alta.Canada, 1998, p. 154-161.
- [6] Parallel Simulation Environment for Complex Systems (PARSEC), retrieved June 2010 from <http://pcl.cs.ucla.edu/projects/parsec/>.
- [7] Cowie, J.H., Nicol D.M., and Ogielski A.T., "Modeling the GlobalInternet", Computing in Science and Engineering, 1999.
- [8] NS-2 Simulator, retrieved June 2010 from: <http://nslam.isi.edu/nslam/index.php>.
- [9] Di Caro, G. A., "Analysis of simulation environments for mobile adhoc networks", Technical Report No. IDSIA-24-03, IDSIA / USISUPSI,BISON project, Switzerland, 2003.
- [10] Riley, G., Fujimoto, R.M., Ammar, M., "A Generic Framework for Parallelization of Network Simulations", in Proc. 7th Int.Symposium on Modeling, Analysis, and Simulation of Computer and Telecommunication Systems, 1999, p. 128-135.
- [11] Riley, G.F., "The Georgia Tech Network Simulator", in Proc. of the Workshop on Models, Methods, and Tools for Reproducible Network Research (MoMe Tools), 2003.
- [12] Varga, A., "The OMNeT++ discrete event simulation system", Proc. of the European Simulation Multiconference (ESM '2001), Prague, Czech Republic, 2001.
- [13] Sekercioglu, Y. A., Varga, A., Egan, G. K., "Parallel Simulation Made Easy With Omnet++", in Proc. of the European Simulation Symposium (ESS2003), Oct. 2003, Delft, The Netherlands.
- [14] Grama, A., Gupta, A., Karypis, G., Kumar, V., Introduction to Parallel Computing, 2nd Edition, Addison-Wesley, Reading, MA, 2003.

The Decomposition of DSP's Control Logic Block for Power Reduction

Borisav Jovanović and Milunka Damjanović

Abstract—The paper considers the architecture and low power design aspects of the digital signal processing block embedded into a three-phase integrated power meter IC. Utilized power reduction techniques were focused on the optimization of control logic block. The operations that control unit performs are described together with power optimization results.

Index Terms—Digital signal processing, power optimization.

I. INTRODUCTION

NOWADAYS, most of electronic devices which are used for the measurement of power line parameters relays on single chip referred to as integrated power meter (IPM). An IPM usually embeds powerful digital signal processor block (DSP) performing various data-intensive calculations. This paper proposes a DSP core used in power metering applications, which enables high performances at the levels as those obtained with commercial DSP microprocessors, and, at the same time, operates at significantly reduced power consumption.

The paper explains the operations performed by DSP used for processing the instantaneous values of current and voltage signals including the digital filtering methods. The DSP calculates root mean square values of voltage and current, active, reactive, apparent power and energy. Besides, new circuit for distortion power measurement is presented.

Power dissipation is an important part of system-on-chip (SoC) design specifications. Low power design techniques, with an emphasis on modern standard cell technologies, are applied to the design of a DSP core. Effort is put into the dynamic power minimization. Since DSP's control unit is one of largest and most power consuming DSP's part, the paper presents the utilized low power techniques which are mainly focused on the optimization of control logic block.

The operation of DSP is discussed in the following section

Manuscript received 1 May 2012. Accepted for publication 30 May 2012. Some results of this paper were presented at the 4th Small Systems Simulation Symposium, Niš, Serbia, February 12-14, 2012.

The authors would like to thank the Serbian Ministry of Science and Technology Development for supporting the research reported in this paper within the project TR 32004.

B. Jovanović and M. Damjanovic are with the Faculty of Electrical Engineering, University of Niš, Aleksandra Medvedeva street 14, 18000 Niš, Serbia (phone: +38118529321; e-mails: {borisav.jovanovic, milunka.damjanovic}@elfak.ni.ac.rs).

of the paper. Then, in Section three, the architecture of the proposed core is given, with the description of utilized low power techniques. The implementation results are given in Section four.

II. DSP'S OPERATION

The proposed DSP circuit is incorporated into an IPM chip, the mixed-signal circuit consisting of analog and digital signal processing blocks. The analog part of IPM contains Sigma-Delta AD converters [1] for current and voltage signal conversion into digital words, Band-Gap voltage reference and PLL circuits.

The digital part is composed of digital filters [2], DSP block and 8052 microcontroller unit. From AD converters and digital filters [2] the DSP gets 16-bit digital samples of instantaneous voltage, current and phase-shifted voltage signals at data-rate of 4096 samples per second. Based on values of current and voltage, DSP calculates root-mean square (RMS) values of current I_{RMS} , and voltage V_{RMS} , active power P , reactive power Q , apparent power S and power-factor $\cos(\varphi)$ every second. The measurement range for current signal is from 10mA RMS to 100A RMS, and for voltage it is up to 300V RMS. Besides, DSP measures the instantaneous value of the power-network frequency with a maximum error of 0.01 Hz.

The measurement results are obtained for all three power line phases and three distinct result sets are provided, each dedicated to specific power line phase.

A short survey of used equations that explains the DSP's operation would be as follows.

A. The used equations

The instantaneous value of current, as function of time, can be represented in the form:

$$i(t) = \sqrt{2} I_{RMS} \cos(2\pi ft + \varphi) \quad (1)$$

After the discretization in time domain, it becomes:

$$i(n) = \sqrt{2} I_{RMS} \cos(n \cdot 2\pi f / fs + \varphi), \quad (2)$$

where f represents the power-line signal frequency equal to 50Hz, and fs is the AD converter sampling frequency, equal to 4096Hz.

Root-mean-square, I_{RMS} , is calculated once per second according to the expression (3):

$$I_{RMS} = \sqrt{\frac{\sum_{n=1}^N i(n)^2}{N}} \quad (3)$$

The DSP calculates new I_{RMS} value every second and value of parameter N in (3) is equal to 4096. Similar expression, like for I_{RMS} , is used for V_{RMS} calculation.

$$V_{RMS} = \sqrt{\frac{\sum_{n=1}^N v(n)^2}{N}} \quad (4)$$

If the instantaneous values of current and voltage are as follows,

$$i(t) = \sqrt{2}I_{RMS} \cos(2\pi ft + \varphi_1) \quad (5)$$

$$v(t) = \sqrt{2}V_{RMS} \cos(2\pi ft + \varphi_2) \quad (6)$$

the instantaneous active power $p(t)$ is:

$$p(t) = i(t) \cdot v(t) \quad (7)$$

After the discretization of the instantaneous power, the active power P is calculated according to:

$$P = \frac{\sum_{n=1}^N p(n)}{N} \quad (8)$$

The instantaneous reactive power $q(t)$ is obtained by multiplying current and phase-shifted voltage signals.

$$i(t) = \sqrt{2}I_{RMS} \cos(2\pi ft + \varphi_1) \quad (9)$$

$$v_p(t) = \sqrt{2}V_{RMS} \cos(2\pi ft + \varphi_2 + \pi/2) \quad (10)$$

The reactive power $q(t)$ is

$$q(t) = i(t) \cdot v_p(t) \quad (11)$$

The average reactive power Q is calculated according to:

$$Q = \frac{\sum_{n=1}^N q(n)}{N} \quad (12)$$

Apparent power S and power factor $\cos(\varphi)$ are calculated according to (13) and (14):

$$S = I_{RMS} \cdot V_{RMS} \quad (13)$$

$$\cos(\varphi) = P/S \quad (14)$$

$$S^2 = P^2 + Q^2 + D^2. \quad (15)$$

The relation (15) between apparent power S , active power P , reactive power Q and distortion power D , suggests us that it is enough to calculate P , Q and S and then use the (15) to find the distortion power D .

Possible sources of error in active power P calculation are the phase difference between voltage and current values and the fact that power-network frequency is slightly changed round the nominal (50Hz), so there are not an integer number of voltage half-periods in a second. Error eliminating is necessary, so after the multiplication of the current and voltage values, the values $i^2(t)$, $v^2(t)$, $p(t)$ and $q(t)$ are filtered, accumulated 4096 times per second and the achieved total is divided with 4096 every second.

III. DSP'S ARCHITECTURE

A. Controller/datapath architecture

The architecture of DSP [3], [4] utilizes controller/ datapath

architecture and consists of several blocks:

- Block 1 – the part which consists of arithmetical units used for I^2 , V^2 , P , Q accumulating and energy calculation
- Block 2 – including arithmetical operators used for calculation of current and voltage RMS, power factor, active, reactive, distortion and apparent power
- Block 3 – control unit that controls all other parts of DSP.
- Block 4 – frequency measurement circuit
- Block 5 – RAM memory block storing the measurement results.

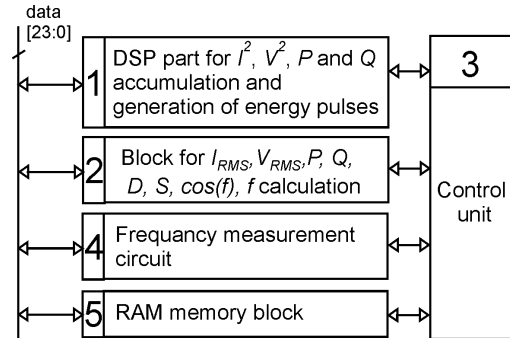


Fig. 1. DSP block diagram.

There is a single 24-bit data bus connecting these sub-blocks of DSP. The control path of DSP unit (Block 5) is implemented as a finite state machine (FSM) that generates a number of control signals. These signals determine what component can write to 24-bit data, what registers are loaded from the bus and what arithmetical operation is performed.

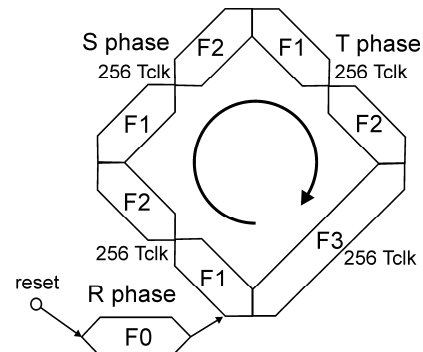


Fig. 2. The FSM state sequence.

During DSP's measurement operation, the control unit periodically executes main state sequence that lasts 1024 clock periods [5], repeated 4096 times during the time interval of one second. The sequence is divided into four sub-sequences called R, S, T and E that lasts 256 clock periods each. The first three sub-sequences R, S and T control the calculations made for each phase of the three-phase energy system. The fourth sub-sequence, denoted E, manages the calculations that are periodically repeated every second [5].

The control unit is composed of four smaller finite state machines: named F0, F1, F2 and F3. The reason for dividing the control unit is significant power consumption reduction which will be examined in following sections. Two sub-

FSMs, F1 and F2, perform arithmetical operations within the Block1 during the phases R, S and T, while sub-FSM F3 - performs operations within Block 2 during E period. The F0 is intended for RAM memory initialization and F0 is active only at the beginning of chip operation, after the main reset state. The operations that F1, F2 and F3 perform will be described in detail.

B. The operation of F1

The FSM F1 executes the state sequence during phases R, S and T and consists of one hundred and two different states. It is used for processing the squared value of instantaneous current and voltage AC signals (necessary for obtaining I_{RMS} and V_{RMS}) and instantaneous values of active and reactive power.

The operation sequence for current square accumulating is given in Fig. 3. The sequence is performed 4096 times every second.

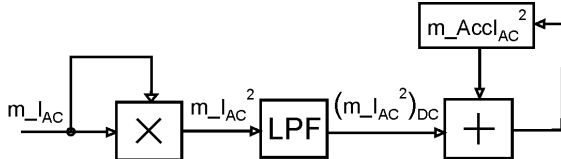


Fig. 3. Data processing chain for current-square accumulation.

At the beginning of the F1 operation sequence, the AC part of instantaneous current signal i_{AC} , stored in the 24-bit RAM register m_I_{AC} , is squared in the multiplication unit, which belongs to the Block1. Then, the squared value i_{AC}^2 is passed through the digital Low pass filter (LPF), and after, the DC value of squared value i_{AC}^2 signal, is accumulated into the 48 bit accumulation register $m_AccI_{AC}^2$. The register is stored in RAM memory and consists of two 24-bit register parts.

The LPF is implemented as a filter with Infinite impulse response (IIR) and helps in reducing the I_{RMS} calculation error. This error could exist because the time interval of one second (that is, accumulating time of i_{AC}^2 value) is not always equal to the integer number of power-line-signal half-periods.

The LPF takes at inputs the squared value i_{AC}^2 , which is stored in the register $m_I_{AC}^2$, and produces at output the DC value of i_{AC}^2 . The LPF has cut-off frequency of 10Hz and its transfer function is given by (16).

$$H_{LPF}(z) = \frac{(m_I_{AC}^2)_{DC}}{m_I_{AC}^2} = \frac{2^{-6}}{1 - z^{-1}(1 - 2^{-6})} \quad (16)$$

The transfer function $H_{LPF}(z)$ can be easily transformed into the equations in which the operands are expressed by registers:

$$(m_FI_{AC}^2 \times 64)_{NEW} = m_FI_{AC}^2 \times 64 \cdot (1 - \frac{1}{2^6}) + m_I_{AC}^2 \quad (17)$$

$$(m_I_{AC}^2)_{DC} = (m_FI_{AC}^2 \times 64) / 64 \quad (18)$$

The 48-bit LPF filter register $m_FI_{AC}^2 \times 64$, used in (2) and (3), consists of two 24-bit parts that are stored in the RAM memory block. The register contains the DC value of signal

i_{AC}^2 , multiplied by constant number 64.

The operations described by (2) and (3) are done by arithmetical circuits within the Block 1, which structure is given in Fig. 4, and includes one multiplication unit and one circuit for addition and subtraction. The intermediate results of operations (i_{AC}^2 and the DC value of i_{AC}^2) are temporarily stored in the registers RegA and RegB of Block1 (Fig.1). Only the AC part of instantaneous current signal i_{AC} (register m_I_{AC}) accumulation register $m_AccI_{AC}^2$ and LPF filter register $m_FI_{AC}^2 \times 64$ are located in RAM.

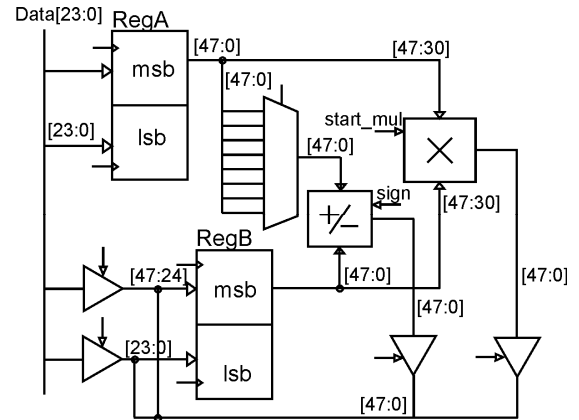


Fig. 4. The structure of Block 1.

The FSM sequence of operations for the accumulation of squared current values is given by the Fig. 5. The sequence consists of simple data transfer, shifting, multiplication and addition operations, performed at registers RegA and RegB.

```

m_I_AC → RegA_h, RegB_h
RegA_h × RegB_h → RegA
m_FI_AC^2 × 64_h → RegB_h
m_FI_AC^2 × 64_l → RegB_l
RegA - (RegB >> 6) → RegA
RegA + RegB → RegA
RegA_h → m_FI_AC^2 × 64_h, RegB_h
RegA_l → m_FI_AC^2 × 64_l, RegB_l
m_AccI_AC^2_h → RegA_h
m_AccI_AC^2_l → RegA_l
RegA + (RegB >> 6) → RegA
RegA_h → m_AccI_AC^2_h
RegA_l → m_AccI_AC^2_l

```

Fig. 5. The sequence of accumulation of squared current values.

The similar procedure is performed by Block 1 for processing the squared value of instantaneous voltage AC part signal v_{AC}^2 (necessary for obtaining V_{RMS}) and instantaneous values of active p and reactive power q . The results are stored in the RAM registers: $m_AccV_{AC}^2$, m_AccP

and m_AccQ . The difference is in used multiplication operands: the voltage samples are multiplied to obtain V_{RMS} ; voltage and current sample values for active power, and current-sample value is multiplied with phase-shifted voltage-sample for reactive power processing.

C. The operation of F2

The F2 is active during phases R, S and T and generates the energy pulses for measured active and reactive energy. The FSM consists of one hundred and ninety three states. A pulse is generated when measured energy exceeds predetermined energy level. The default energy level is one Watt-hour for active and VAR (Volt-Ampere reactive) for reactive energy.

The DSP has four outputs producing the narrow pulses: Ea_pos – for consumed active, Ea_neg – generated active, Eq_pos – inductive reactive, and Eq_neg – capacitive reactive energy. The energy level is stored in m_Whr register, the part of RAM memory block, and can be modified. The operations are carried out by Block 1 using the adder/subtractor and registers $RegA$ and $RegB$.

The sequence of operations is given in Fig.6. At the beginning of each sequence, performed exactly 4096 times during the time interval of one second, the active power value m_P , is added to the value of 48-bit register m_AccEa . The m_AccEa consists of two parts: the MSB part - m_AccEa_h and the LSB part - m_AccEa_l , both stored in RAM. After addition operation is done, the value of m_P and new value of m_AccEa are compared with zero. If value of m_P is positive and if new value of m_AccEa is greater than the energy level equivalent (given by m_Whr), a pulse on Ea_pos is generated and m_AccEa is subtracted by the m_Whr value. Else, if both m_P and m_AccEa are negative, a pulse on Ea_neg is generated, and value of m_Whr is added to m_AccEa .

The similar procedure stands for the reactive energy processing. Accompanied registers are m_AccEq_h and m_AccEq_l .

Besides dealing with energy pulses, the F2 eliminates DC offsets from instantiations current and voltage signals that are derived from digital filters. This is necessary for the calculation of current and voltage RMS value. The DC offset will give a additional DC component after squaring operation. Since this DC component is extracted by LPF, this offsets can induce the error to RMS values. This problem is avoided by introducing the HPF in voltage and current signal processing chains. The HPF, applied to instantaneous current and voltage signals, is implemented as IIR digital filter with cut-off frequency 5Hz and transfer function as given by:

$$H_{HPF}(z) = (1 - 2^{-10}) \frac{(1 - z^{-1})}{1 - z^{-1}(1 - 2^{-9})} \quad (19)$$

```

m_P → RegB_l
m_AccEa_h → RegA_h
m_AccEa_l → RegA_l
RegA + RegB → RegA
if (RegB > 0) {
    m_Whr → RegB_l
    if (((RegA - (RegB << 12)) > 0) {
        RegA - (RegB << 12) → RegA
        generate pulse for positive Ea;
    }
} else {
    if (RegA < 0) {
        m_Whr → RegB_l
        RegA + (RegB << 12) → RegA
        generate pulse for negative Ea;
    }
}
RegA_h → m_AccEa_h
RegA_l → m_AccEa_l

```

Fig. 6. The sequence of operations producing the energy pulses on Ea_neg and Ea_pos pins.

The HPF transfer function can be transformed into the equations (20) and (21) performed by DSP.

$$(m_FIx1024)_{NEW} = m_FIx1024(1 - \frac{1}{2^9}) + (2^{10} - 1)(m_I - m_I_p) \quad (20)$$

$$m_I_{AC} = m_FIx1024/1024 \quad (21)$$

The following registers values are used in the equations (20) and (21):

- m_I and m_I_p – two consecutive current samples obtained directly from digital filters
- $m_FIx1024$ is 48-bit HPF register, which contains the AC value of $i(t)$, multiplied by constant value 1024. The register consists of two parts: the MSB part – $m_FIx1024_h$ and LSB part - $m_Fix1024_l$.
- m_I_{AC} is AC part of instantaneous sample of current signal. It represents the result of filtering operation and it is further used by FSM F1.

The operation sequence for the offset elimination, performed by F2, is given in the Fig. 8. The operations are carried out by Block 1.

The similar procedure is made for processing of m_V_{AC} (necessary for obtaining V_{RMS}). The intermediate results are stored in 24-bit RAM registers: $m_FVx1024_h$ and $m_FVx1024_l$.

```

m_I_p → RegA_l
m_I → RegB_l
RegA_l - RegB_l → RegA_l
RegA → RegB
RegA - (RegB << 10) → RegA
m_Flx1024_h → RegB_h
m_Flx1024_l → RegB_l
RegA + RegB → RegA
RegA - (RegB >> 9) → RegA
RegA_h → m_Flx1024_h
RegA_l → m_Flx1024_l
RegA → RegB
0 → RegA_l
RegA + (RegB >> 10) → RegA
RegA_l → m_I_AC

```

Fig. 7. The sequence for high pass filtering of instantiations current sample signals, done by F2.

D. The operation of F3 FSM

The fourth sub-sequence of the control unit manages the calculations that are periodically repeated every second and consists of three hundred and four states.

Based on accumulating sums $m_{AccI_{AC}^2}$, $m_{AccV_{AC}^2}$, m_{AccP} and m_{AccQ} , arithmetical operations are performed by Block 2 to generate voltage and current root mean square values $m_{I_{RMS}}$ and $m_{V_{RMS}}$ and mean active and reactive power values m_P and m_Q . The sequence of operations is performed by FSM F3.

The interior structure of Block 2 is given in Fig. 8. It consists of two registers named RegC and RegD and arithmetical units that implement square rooting, subtraction, multiplication and division.

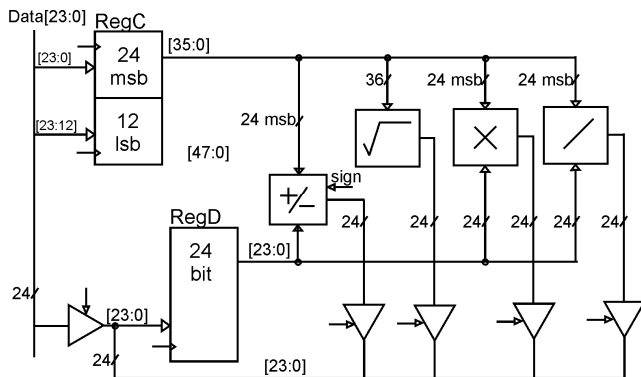


Fig.8 The structure of Block 2

The sequence, controlled by F3 that generates current root mean square $m_{I_{RMS}}$, is given in Fig. 9.

To generate value $m_{I_{RMS}}$, accumulated sum $m_{AccI_{AC}^2}$ is stored into RegC and then, it is divided by 4096. Next, square rooting operation is performed over the average value of voltage square. Then, current offset $m_{I_{ACoff}}$ is subtracted,

```

m_AccI^2_h → RegC_h
m_AccI^2_l → RegC_l
√RegC → RegD
0 → m_AccI^2
m_I_ACoff → RegC_h
RegC_h - RegD → RegD
m_Igain → RegC_h
RegC_h × RegD → RegD
RegD → m_I_RMS

```

Fig. 9. The sequence that generates current root mean square $m_{I_{RMS}}$.

multiplied with gain correction m_{Igain} and root mean square of current is obtained (Fig. 9).

The similar processing steps are conducted for $m_{V_{RMS}}$. For mean active and reactive power calculation the square root calculation is avoided. Apparent power m_S is obtained by multiplying $m_{I_{RMS}}$ and $m_{V_{RMS}}$, and power factor m_{CosF} – by dividing active m_P and apparent power m_S .

In addition to finding mean active (m_P), reactive (m_Q) and apparent power (m_S), the distortion power [6] (stored in the register m_D) calculation is provided. F3 controls the operations producing the m_D . Arithmetical operators used to calculate the value of m_D , belong to blocks 1 and 2. The structure of Block 1 had to be slightly modified. The new input is introduced to RegB (the part of Block 1) which makes the connection from the multiplication unit from Block 2. The result of multiplication operation, done by arithmetical operator within Block2, has to be transferred to the RegB. The sequence is given in Fig. 10.

At the beginning, the register RegA is reset to zero, and the content of register m_S is copied to both of the registers RegC and RegD. The squaring operation is performed and the result is moved to the RegA. Then, the active power m_P is moved to RegC and RegD, and the multiplication is performed. The result is subtracted from register RegA. The same operations

```

0 → RegA_h, RegA_l
m_S → RegC_h, RegD
RegC_h × RegD → RegB
RegA + RegB → RegA
m_P → RegC_h, RegD
RegC_h × RegD → RegB
RegA - RegB → RegA
m_Q → RegC_h, RegD
RegC_h × RegD → RegB
RegA - RegB → RegA
RegA → RegC
√RegC → RegD
RegD → m_D

```

Fig. 10. The sequence that generates distortion power m_D .

are done with the value m_Q . After, the content of RegA is moved to the RegC, and square root operation is performed. Finally, the result is moved from RegD into the m_D , which is stored in the RAM memory.

IV. THE IMPLEMENTATION RESULTS

Dynamic power dissipation of DSP block can be divided into three main areas: power consumed by memory blocks, arithmetical operators and by clock tree nets.

The first area is the power cost associated with accesses to the three data memories (represented by Block 5 in the Fig. 1). It is well known that memory accesses can form the largest component of power consumption in data-dominated applications. The power is consumed within the RAM units themselves, and also, during data transmission across the large capacitance of the 24-bit data bus. The control unit was modified to decrease the number of accesses to the RAM memory. Besides, the datapath was changed that the intermediate results, that DSP calculates, are stored in working registers of Block 1 and 2. Only the final measurement results are saved in RAM.

The second main area of power consumption comes from the energy dissipated in performing the actual operations on the data. This is made up of the energy dissipated by transitions within the datapath associated with the data (Block 1 and 2), and the control overhead (Block 3) required to perform the operations. In the proposed DSP, the most of dissipated power comes from large control unit and its power reduction will be further described.

Clock power is the third component of signal processing block power because the clock is fed to most of the circuit blocks in the processor and the clock switches every cycle. Considering all clock signals, the total clock power is a substantial 30% of the DSP's power. Clock gating is the efficient technique for dynamic power reduction. To avoid glitches, beside AND circuits, the level sensitive latches are used for clock gating circuit implementation.

The datapath of DSP incorporates several arithmetical units for multiplying, dividing and square rooting which are realized as sequential circuits. Since arithmetical blocks are not used all the time, their clock trees can be gated, reducing the power consumption. The DSP design was further power optimized. The gating signals are the only way to write data

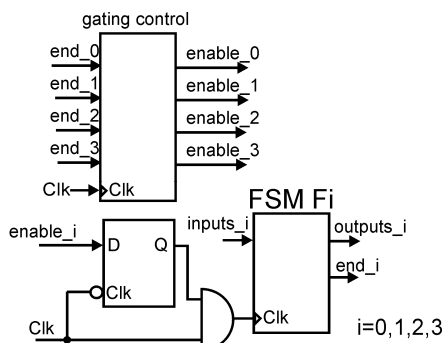


Fig. 11. The structure of Block 1.

into registers and memory blocks. For example, the clock signals of registers in the Block 1 and Block 2 were gated.

The rest of the optimization process considered the DSP's control unit. The control unit incorporates over six hundred states and required huge combinational logic within the synthesized FSM. The implementation of control logic block occupies large portion of DSP's area. Also, it represents one of the largest power consumers among DSP's blocks.

The following power minimization techniques were used: FSM decomposition [7, 8], clock gating and Grey code encoding [9]. The first technique divides large control unit into several smaller state machines, simplifying their combinational logic blocks. The division of control unit into smaller state machines has positive effect on power dissipation. After, the clock gating technique was used. The clock gating disables inactive parts of FSM by stopping its clock signal, and, reduces the switching activity within the combinational logic blocks. At the end, Gray binary encodings are assigned to the FSM's states to further reduce the power.

During FSM decomposition the transition graph of original FSM was considered first, and after, divided into four sub-graphs. Four sub FSMs were created, named with F0, F1, F2 and F3, which jointly produce the equivalent behavior as the original FSM. The decomposition is performed considering the datapath architecture. The states within one subset control the arithmetical operations performed by same part of DSP. For example, F1 and F2 perform the operations executed by Blocks 1 and 2, and state machine F3 - the operations done by Block 2.

After the FSM decomposition is done, the clock gating is introduced in the control unit implementation. The gating control circuit (shown in Fig. 11) is added to the control logic block. New circuit identifies the currently active FSM and enables the clock input signals to the active FSMs. When the clock signal is present at the input of active FSM, the other three state machines are blocked.

The DSP block was implemented in technology AMI CMOS 350nm with power supply voltage of 3.3V. The Cadence tools were used for implementation. First, the design was verified by RTL simulation, and synthesized by using

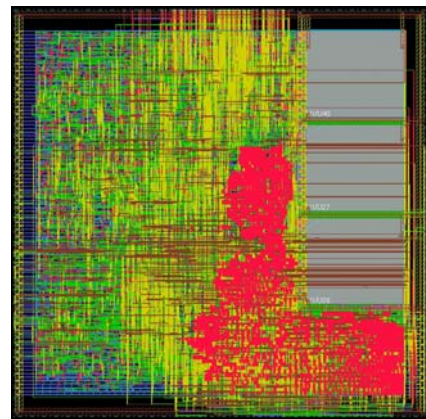


Fig. 12. The layout of DSP block. The red-highlighted section represents the area of huge control logic unit.

Cadence's RTL Compiler. Then, SoC Encounter has performed floor-planning, placement, routing, and clock and reset trees generation. At the end of logical verification process, the Verilog file was extracted from layout and brought back to NCsim simulator where final check of the total digital part of the IC was performed. During the post-layout simulation, switching activity file was obtained and the power consumption results are obtained by the SoC Encounter taking account the parasitic capacitances from layout and switching activity file.

The estimation of DSP's power consumption gave the valuable information about the energy budget and identified all power hungry components. Three power analyses were performed: for the: (a) original design (before the power minimization techniques were applied), (b) DSP design which is optimized by only gating and FSM decomposition, and finally, (c) design where all proposed techniques were applied: FSM decomposition, clock gating and Gray state encoding. The Table I gives the simulated power consumption values of different DSP cores, derived after layout generation. The power consumption of not optimized design was 1.82mW. When all these techniques were applied, the total power became only 1.043mW resulting in the 42% switching power reduction, compared to the non-optimized

TABLE I
THE RESULTS OF POWER OPTIMIZATION

Symbol	Not optimized	Decomposition & clock gating ^a	Decomposition, clock gating & Grey encoding
Area	1.84mm ²	1.831mm ²	1.823mm ²
Clock tree power	0.732mW	0.263mW	0.227mW
Control unit power	0.407mW	0.172mW	0.172mW
DSP's power	1.82mW	1.117mW	1.043mW

implementation.

V. CONCLUSION

The architecture and the low power design aspects of the digital signal processing block embedded into a three-phase integrated power meter IC, are considered. The operations that control unit performs are described together with power-optimization results.

The power reduction techniques were successfully implemented on the optimization of the control logic block. The control unit of DSP block, implemented as finite state machine, was decomposed into four smaller state machines, clock gating was completely introduced and Gray finite state machine encoding used. The resulting effect was the significant reduction of the power consumption.

REFERENCES

- [1] D. Mirković, P. Petković, "Multi channel Sigma-Delta A/D converter for integrated power meter", Proceedings of the Small Systems Simulation Symposium 2010, Niš, ISBN 987-86-6125-006-4, Feb., 2010, pp. 90-93.
- [2] M. Marinković, B. Andjelković, P. Petković, "Compact Architecture of Digital Decimation Filters in Solid-State Energy Meter", Electronics, Vol. 10, No. 2, University of Banja Luka, ISSN 1450, December 2006, pp. 28-32.
- [3] B. Jovanović, M. Damnjanović, P. Petković, "Digital Signal Processing for an Integrated Power Meter", Proceedings of 49. Internationales Wissenschaftliches Kolloquium, Technische Universitat Ilmenau, Ilmenau, ISBN 3-8322-2824-1, Vol.2, September, 2004, pp. 190-195.
- [4] B. Jovanović, M. Zwolinski, M. Damnjanović, "Low power digital design in Integrated Power Meter IC", Proceedings of the Small Systems Simulation Symposium 2010, Niš, ISBN 987-86-6125-006-4, Feb., 2010, pp. 49-55
- [5] M. Jevtić, B. Jovanović, S. Brankov, "Upravljačka jedinica sistema na čipu za registrovanje potrošnje električne energije", Zbornik radova XLVIII konferencije Etran 2004, Čačak, ISBN 86-80509-49-3, Vol.1, June, 2004, pp. 75-78
- [6] D. Stevanović, B. Jovanović, P. Petković, V. Litovski, "Korišćenje snage distorzije za identifikaciju izvora harmonijskog zagadenja na mreži", Tehnika - Elektrotehnika, 6/2011, Savez inženjera i tehničara Srbije, ISSN 0040-2176, 2011, accepted for publication.
- [7] S.H. Chow, H. Yi-Cheng, T. Hwang, "Low power realization of finite state machines - a decomposition approach", ACM Transactions on Design Automation of Electronic Systems (TODAES) Volume 1, Issue 3 (July 1996) pp.: 315 – 340, ISSN:1084-4309
- [8] W.K Lee, C.Y Chi-Ying Tsui, "Finite state machine partitioning for low power", Circuits and Systems, 1999. ISCAS'99, Proceedings of the 1999 IEEE International Symposium, Volume 1, June 1999, pp. 306 – 309
- [9] L. Benini, G. De Micheli, "State assignment for low power dissipation", Solid-State Circuits, IEEE Journal of Volume 30, Issue 3, Mar 1995 pp.:258 – 268

Data Privacy in Smart Electricity Networks

Slobodan Bojanić, Srdan Đorđević, and Octavio Nieto-Taladriz

Abstract—Smart Grids are amongst the most promising future developments to manage and control the energy consumption in the next decades. However, the integration and interdependencies that will evolve between the electricity power grid, telecommunication networks and ICT enable new threats and vulnerabilities to this critical infrastructure which must be addressed adequately with the right kind of security controls, balanced risk mitigation strategies and a continuous attention towards security, privacy and regulation aspects. It is an emerging area where new data privacy problems arise as mass rollout of smart meters is already happening.

Index Terms—Smart Grid, Data Privacy, Smart Meter, Privacy by Design.

I. INTRODUCTION

THE appearance of Smart Grids with intelligent meters alters the polling frequency of measurement and the coverage of the measurement at the consumer location. Namely up to now the measuring frequency is low and covers an area or larger number of energy users, the intelligent meter may change the frequency to minutes or real-time whereas the coverage is in the range of individual consumers or households. This implies that where up to now the operator has a large view of the energy behavior of a bigger set of consumers, this view will evolve to detailed information on the energy behavior of sole end consumers and most data from Smart Grids can be considered personal data [1]-[5].

Smart Grid applications are based on the advances the Electric Power System and increased integration with communications and information technology together with sensors and actuators for active monitoring and control. The potential benefits of the Smart Grids are far-reaching and significant like the opportunities for consumers to cut their bills by changing their habits, perhaps using energy at different times to take advantage of lower tariffs, as well as opportunities for industry to more accurately forecast demand, reducing expensive electricity storage costs and the realization

of climate change targets. However they also have the potential to process increasing amounts of personal data, unprecedented in this industry, and to make that personal data more readily available to a wider circle of recipients than at present.

The implementation of Smart Grids potentially connects location information to specific data that holds information on the use of electrical energy, and in the future possibly more. The fingerprint or contents of this data provides information on what is going on at the location at a specific moment, and may show patterns over longer time which may have great impact on the privacy and security of the consumer [14].

Thus it is necessary to deploy adequate measures to protect the contents and nature of this data in order to safeguard the privacy of the consumer. Without such protection there is a risk not only that processing of personal data will be in breach of national laws but also that consumers will reject these programmes on the basis that the collection of personal data is unacceptable to them. Such rejection may arise even if there is no breach of the law. Therefore it is necessary that all parties involved in the deployment of smart meters and the development of the smart grid ensure that the fundamental rights of individuals are protected and respected.

These concerns are also reflected in Strategic Research Agenda for the year 2035 of the European Technology Platform on Smart Grids [15]. That is an update of the Strategic Research Agenda 2007 for the needs by the year 2035. Namely regarding changes between 2007 and 2011 with sensitivity towards better predicting today the needs for the year 2035, it is obvious that Data and Information is becoming much more important. The amount of data that is available but also to be handled has increased very much since 2007 and continues to increase exponentially. One reason is the already wide penetration of smart meters which will increase dramatically within next years. This allows new business models but also increases the need for data security. Here, consumers became much more aware of this topic and became very concerned about the privacy of their data. The increased amount of data also increased the need to use the grid for data transport.

II. BACKGROUND

Privacy is normally assumed as the ability of an individual to be left alone, out of public view, free from surveillance or interference from others (individuals, organizations or the state) and in control of information about himself. Privacy is

Manuscript received 1 May 2012. Accepted for publication 30 May 2012. Some results of this paper were presented at the 4th Small Systems Simulation Symposium, Niš, Serbia, February 12-14, 2012.

This research was partially funded by The Ministry of Education and Science of Republic of Serbia under contract No. TR32004.

Slobodan Bojanić and Octavio Nieto-Taladriz are with Universidad Politécnica de Madrid, ETSIT Avenida Complutense n° 30, 28040 Madrid, Spain, e-mail: {slobodan, octavio}@die.upm.es.

Srdan Đorđević is with the Department of Electronics, Faculty of Electronic Engineering, University of Niš, Aleksandra Medvedeva 14, 18000 Niš, Serbia, e-mail: srdjan.djordjevic@elfak.ni.ac.rs.

not a plainly delineated concept and is not simply the specifications provided within laws and regulations. Furthermore, privacy should not be confused, as it often is, with being the same as confidentiality; and personal information is not the same as confidential information. Confidential information is information for which access should be limited to only those with a business need to know and that could result in compromise to a system, data, application, or other business function if inappropriately shared.

Privacy was not of particular concern for many decades in the electricity networks which have provided the vital links between electricity producers and consumers with great success. The basic architecture of these networks was developed in most countries to meet the needs of large, predominantly carbon-based generation technologies. Since Europe is committed to the 20-20-20 targets to reduce carbon emissions and to secure energy supply, energy efficiency and renewable energy are seen as solution to attain this goal. Both measures call for changes in the energy supply system leading to smart grids as key enablers for the required innovation.

The Smart grid is usually defined as an intelligent electricity network that combines information from users of that grid in order to plan the supply of electricity more effectively and economically that was possible in the pre-smart environment. It is a challenge to efficiently integrate the behavior and actions of all users connected to it – generators, consumers and those that do both – in order to ensure economically efficient, sustainable power system with low losses and high levels of quality and security of supply and safety. A further step will be energy optimization crossing the domains of electricity, gas and heat.

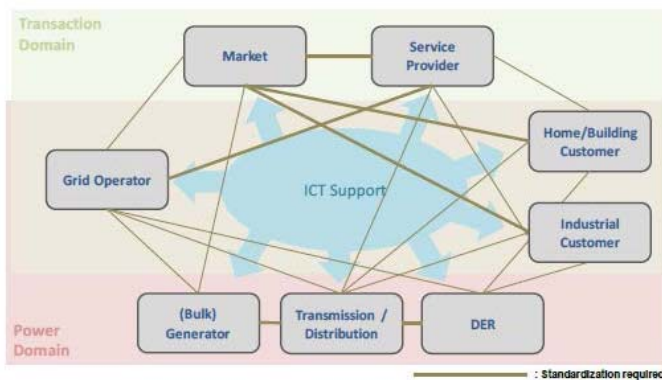


Fig 1. A conceptual model of the Smart Grid.

Key factors comprise the degree of decentralization of the system components and their interrelation with electricity networks, the variability of renewable generation, the increased distance between electricity generation and consumption, the intelligence level of the involved systems created by smart products and associated smart services, the legal framework, the associated regulation of market based product and service choices versus natural monopoly products and services and the business roles for actors involved in all

aspects of networks and intelligent electric systems.

Furthermore the integration requires fast data transfer architectures between grid control areas and between distribution and transmission system operators' systems: a huge amount of data has to be exchanged as much as possible in real time and with a high reliability between areas in order to promptly react to any change in the grid operation parameters. To exploit economies of scale and to provide scalable solutions, the deployed field devices and systems have to be as much as possible interoperable and standardized.

The introduction of smart meters makes the process more complex in that the data subject will provide suppliers with insights into personal routines. There is a big difference in circumstances between countries, ranging from those where rollout is largely complete following government mandate to those where no meters have been installed. Furthermore high volumes of data coming from smart monitoring devices and smart meters must be managed efficiently. Such growth in data flow needs to be organized and structured to be relevant information ready for distribution and communication.

The new approach in energy systems should be based on role based data access. Namely, data must be owned by and located at the data "originator" from where will be utilized for all relevant purpose - but with restricted access to what is relevant for the owner of the data. This calls for enhanced activities for ensuring high level of cyber security and respect of the privacy issue. One important step in this process is data minimization in respect of purpose and time limitation and data quality. Namely data should be collected for specific, explicitly defined and legitimate purposes and not further processed in a way incompatible with those purposes. Data quality supposes that they are adequate, relevant and not excessive in relation to the purposes for which they are collected and/or further processed as well as accurate and, where necessary, kept up to date. Furthermore data needs to be retained only for as long as is necessary to fulfill that purpose.

III. STAKEHOLDERS

Smart Grids include a much wider area than smart metering which is an important first step towards a Smart Grid. Smart meters bring intelligence to the 'last mile' between the grid and the final customer. Without this key element, the full potential of a Smart Grid may not be realized. Being that only few countries in Europe have undertaken a full deployment of smart meters actors involved in the sector should draw from existing experiences and take account of best practices in place.

The smart metering brings with it the potential for numerous novel ways for processing data and delivering services to consumers. Whatever the processing, whether it is similar to that which existed in the pre-smart environment, or unprecedented, the data controller must be clearly identified, and be clear about obligations arising from data protection legislation including Privacy by Design, security and the

rights of the data subject. Data subjects must be properly informed about how their data is being processed, and be aware of the fundamental differences in the way that their data is being processed so that when they give their consent it is valid.

Therefore the following Smart Grid stakeholders are:

- Grid users including/composed of grid operators, grid customers and meter operators
- End customer (domestic or commercial)
- Municipalities including energy retailers
- Politics
- Industries
- Consumer organizations
- Politics/society.

It can also be viewed through various domains interconnected by secure communication flows and flows of electricity as presented in Fig. 2.

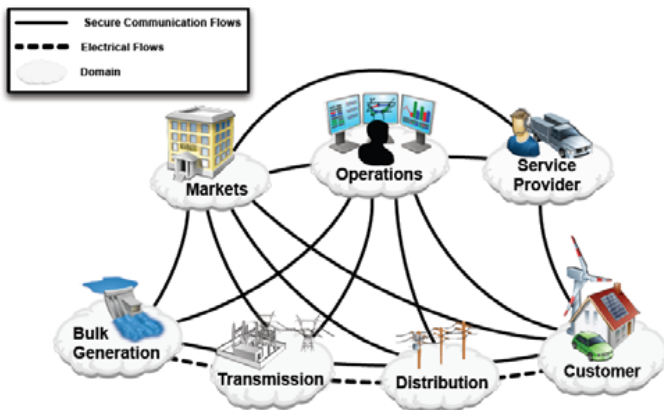


Fig. 2. Interaction among actors in Smart Grid.

Data processing service providers in provision of data processing services are in charge of respecting consumer privacy. Basically the smart meter takes a reading which reflects the energy usage at the property. At some point that reading, along with other information, can be transmitted outside the property. In some models it will be sent directly to a central communications hub where the smart meter data are managed. Once there, it can be accessed by DSOs, suppliers and ESCOs. It appears that the DSOs will have to face the greatest changes to make smart grids a reality. That is because of the growing distributed character (resulting in growing bidirectional power flow at all voltage levels) and variability of generation, customer privacy issues, system security, data and information processing for new applications and concepts such as Virtual Power Plants, etc.

Also multiple and complex methods of communication, with additional entry points and data paths creating complicated security challenges requiring solutions that encompass them all should be taken onto consideration. Given the complex and disparate landscape, the task of producing privacy solutions is quite challenging, and at this stage it seems that they can only be general, rather than specific.

The disparity of the current position does not allow

presenting a comprehensive view on all specific aspects of smart metering programs across the countries. There is a huge variation in circumstances between countries, ranging from those where rollout is largely complete following government mandate to those where no meters have been installed. There is also much variation in the level of involvement from DPAs and in the nature of the market across member states, and where responsibility lies with installation of meters. In some countries, publicly owned utility companies are responsible. Elsewhere, there is a competitive supplier market. Distribution system operators have a more prominent role in some countries.

The smart grid brings a completely new and complex model of inter-relationships that poses challenges for the application of data protection. In this emerging area it is fully expected that new data protection problems and solutions will evolve as more smart meters and smart grid components are installed. It is obvious is that mass deployment of smart meters is already happening, so there is urgency to comprehend the way that smart meters process personal data, and the issues that this raises. The issues of general concern warrant serious consideration by all those involved in this area. Since data in Smart Grids might contain privacy sensitive information the principles such as privacy by design and default should be involved. The personal data is being processed by the meters, so data protection laws apply.

Data controller must be clearly identified, and be clear about obligations arising from data protection legislation, security and the rights of the data subject whatever the processing, whether it is similar to that which existed in the pre-smart environment. Data subjects must be properly informed about how their data is being processed, and be aware of the fundamental differences in the way that their data is being processed so that when they give their consent it is valid.

IV. PRIVACY THREATS

The privacy implications are numerous for smart grid technology deployment centers on the collection, retention, sharing, or reuse of electricity consumption information on individuals, homes, or offices. Basically, smart grid systems will be multidirectional communications and energy transfer networks that enable electricity service providers, consumers, or third party energy management assistance programs to access consumption data. In addition, if plans for national or transnational electric utility smart grid systems proceed as currently proposed these far reaching networks will enable data collection and sharing across platforms and great distances [7]-[11].

As consumer privacy is a key factor in the change towards smart energy systems thus data access and ownership and the permission to gather data need to be very carefully considered. At the same time, consumers should be well informed about who deals with their data. It has to be emphasized that it is the consumer who owns his data, no one else, and therefore he is

entitled to appropriate rights and protections.

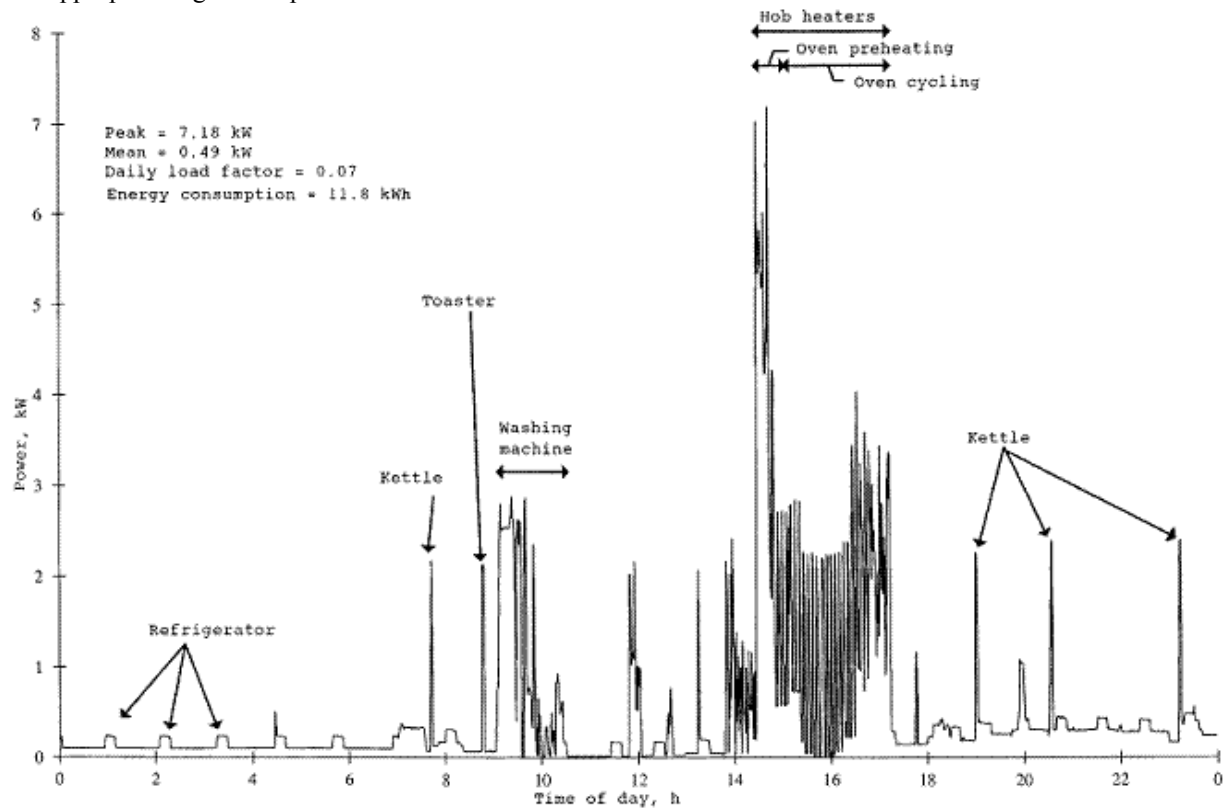


Fig. 3. Consumer profiling by energy.

A list of potential privacy concerns in Smart Grid systems include:

- Identity Theft
- Determine Personal Behavior Patterns
- Determine Specific Appliances Used
- Perform Real-Time Surveillance
- Reveal Activities Through Residual Data
- Targeted Home Invasions (latch key children, elderly, etc.)
- Provide Accidental Invasions
- Activity Censorship
- Decisions and Actions Based Upon Inaccurate Data Profiling
- Unwanted Publicity and Embarrassment
- Tracking Behavior of Renters/Leasers
- Behavior Tracking (possible combination with Personal Behavior Patterns)
- Public Aggregated Searches Revealing Individual Behavior.

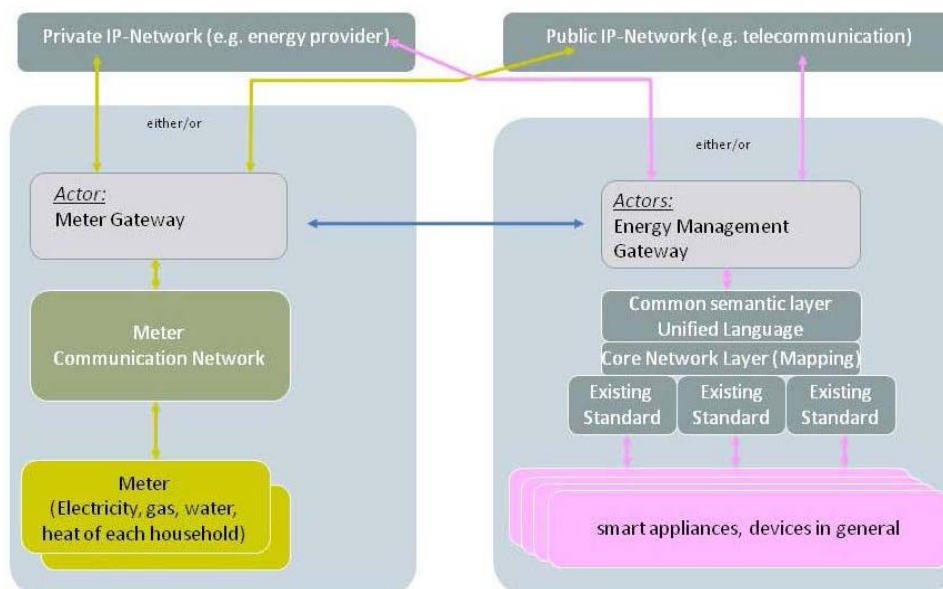


Fig. 4. Logical separation of metering and energy management.

Additionally, plans are underway to support smart grid system applications that will monitor any device transmitting a signal, which may include non-energy-consuming end use items that are only fitted with small radio frequency identification devices (RFID) tags may be possible. Whereas, in Europe energy theft and privacy are the most important concerns related to Smart Grid implementation, in other parts of the world (e.g. in the US) it is energy theft and malevolent attacks that are the main concerns.

V. PRIVACY PRINCIPLES

The increased amount of personal data being processed, the possibility of remote management of connection and the likelihood of energy profiling based on the detailed meter readings make it imperative that proper consideration is given to individuals' fundamental rights to privacy. The reference architecture for the home/building, pointing out the different logical blocks, and can be easily integrated in the whole system architecture is shown in Fig. 4. It is not related to a specific hardware design, but merely shows a logical separation of functions without predefining where and how those functions are implemented.

Privacy by Design (PbD) is a concept to address the ever-growing and systemic effects of Information and Communication Technologies, and of large-scale networked data systems [12]. The objectives of Privacy by Design — ensuring privacy and gaining personal control over one's information and, for organizations, gaining a sustainable competitive advantage — may be accomplished by practicing the following seven Foundational Principles:

1. Proactive not Reactive; Preventative not Remedial measures by anticipating and preventing privacy invasive events before they happen. PbD does not wait for privacy risks to materialize, nor does it offer remedies for resolving privacy infractions once they have occurred — it aims to prevent them from occurring. In short, Privacy by Design comes before the-fact, not after.
2. Privacy as the Default Setting i.e. ensuring that personal data are automatically protected in any given IT system or business practice. If an individual does nothing, their privacy still remains intact. No action is required on the part of the individual to protect their privacy — it is built into the system, by default.
3. Privacy Embedded into design and architecture of IT systems and business practices. It is not bolted on as an add-on, after the fact. The result is that privacy becomes an essential component of the core functionality being delivered. Privacy is integral to the system, without diminishing functionality.
4. Full Functionality — Positive-Sum, not Zero-Sum, by accommodating all legitimate interests and objectives in a positive-sum “win-win” manner, not through a dated, zero-sum approach, where unnecessary tradeoffs

are made such as privacy vs. security, demonstrating that it is possible to have both.

5. End-to-End Security — Full Lifecycle Protection extending securely throughout the entire lifecycle of the data involved — strong security measures are essential to privacy, from start to finish. This ensures that all data are securely retained, and then securely destroyed at the end of the process, in a timely fashion.
6. Visibility and Transparency — thus its component parts and operations remain visible and transparent, to users and providers alike. Remember, trust but verify.
7. Respect for User Privacy — Keeping it User-Centric appropriate notice, and empowering user-friendly options.

Yet, privacy concerns still need to be transposed into specific, precise and non-ambiguous technical requirements if they are to allow the security industry to competitively design and develop privacy-compliant solutions and services. The Privacy by Design concept should, at its turn, be better detailed in order to allow for its practical implementation in concrete cases.

There are also OECD Privacy Guidelines:

1. Collection Limitation Principle: There should be limits to the collection of personal data and any such data should be obtained by lawful and fair means and, where appropriate, with the knowledge or consent of the data subject.
2. Data Quality Principle: Personal data should be relevant to the purposes for which they are to be used and, to the extent necessary for those purposes, should be accurate, complete and kept up-to-date.
3. Purpose Specification Principle: The purposes for which personal data are collected should be specified not later than at the time of collection and the subsequent use limited to the fulfillment of those purposes or such others as are not incompatible with those purposes and as are specified on each occasion of change of purpose.
4. Use Limitation Principle: Personal data should not be disclosed, made available or otherwise used for purposes other than those specified in accordance with Principle 3 except — with the consent of the data subject; or by the authority of law.
5. Security Safeguards Principle: Personal data should be protected by reasonable security safeguards against such risks as loss or unauthorized access, destruction, use, modification or disclosure of data.
6. Openness Principle: There should be a general policy of openness about developments, practices and policies with respect to personal data. Means should be readily available of establishing the existence and nature of personal data, and the main purposes of their use, as well as the identity and usual residence of the data controller.
7. Individual Participation Principle: An individual should have the right: a. To obtain from the data controller, or otherwise, confirmation of whether or not the data

controller has data relating to him; b. To have communicated to him, data relating to him.

8. **Accountability Principle:** A data controller should be accountable for complying with measures that give effect to the principles stated above. Data can be sent to the controller in real-time or be stored in the smart meter. In both cases however, under the Data Protection Directive, it is considered that the data have been collected by the controller.

As part of the Privacy by Design process, security and privacy risk assessments will identify the potential risks to data security. Given the novel and vast prospect that is in store with the smart grid and its associated technologies, the task of anticipating security requirements is a challenging one. In order to mitigate risk, the approach should be end-to-end, incorporating all parties and drawing on a broad range of expertise. Security should also be designed in at the early stage as part of the architecture of the network rather than added on later. Appropriately robust security safeguards must be in place that should apply to the whole process including the in-home elements of the network, the transmission of personal data across the network and the storage and processing of personal data by suppliers, networks and other data controllers. Security is a path, not a destination. Security is about risk management and implementing effective counter measures.

The technical and organizational safeguards should cover at least the following areas:

- The prevention of unauthorized disclosures of personal data;
- The maintenance of data integrity to ensure against unauthorized modification;
- The effective authentication of the identity of any recipient of personal data;
- The avoidance of important services being disrupted due to attacks on the security of personal data;
- The facility to conduct proper audits of personal data stored on or transmitted from a meter;
- Appropriate access controls and retention periods;
- The aggregation of data whenever individual level data is not required.

One of the aspects which can cause public trust to diminish is the retention of data. Namely data retention for the purposes of smart metering needs an in depth analysis. since smart metering, by collecting and processing data on all electricity flows within the grid, is capable of contributing to ubiquitous surveillance of the energy consumers by collection of facts and details arising from consumption of electricity i.e. profiling. Depending on the actual technical design of a particular electricity grid, smart metering can have a profound negative impact on privacy. A suggestion that privacy is jeopardized may cause public trust to diminish unless proper transparent strategies are in place to convince the people.

Data retention covers storing data (personal or any other type) for meeting various legal and business data archival requirements, as well as backup and historical purposes.

There are several reasons for the retention of personal and technical data within smart metering. Depending on future developments and desired functionality there can be even more of them.

1. **Network Maintenance.** The utilities need some data, both personal and technical in nature, that is required for standard network operation. For this kind of data, in many cases there is little reason for long term retention – if it had not been used within a week, the data usually provides little benefit. For some long term maintenance functions, utilities need to store information for a longer period of time. In this case, the information could be aggregated, either over several users as to be large enough to ensure privacy, or by deriving very coarse grained information about a single customer (e.g. assigning one of ten customer profiles). Some cases (e.g. local legislation) may warrant the retention of more detailed data for a specific purpose. Some operators will need detailed data and some might be satisfied on aggregated or anonymised data. Hence, special attention must be paid to those operators who process personal data (i.e. non-aggregated and not anonymised).

2. **Billing and payments.** Certain data must be retained in order to compute the electricity bill. An estimate on the retention time is around a year, but depends on payment intervals. There is a difference among the countries between the current practices on frequency when the customer is billed.

3. **Taxation.** Utilities need to maintain some financial data (i.e. on their income) for tax purposes for a specified time (tax records). It seems that tax record can sufficiently rely only on the top-line figures (e.g. the final sum of bills/invoices). This would not include detailed data on electricity consumption (e.g. the 15-min interval meter readings.).

4. **Added Value Services.** These are additional services, apart from energy supply, provided by the utility and/or third parties on a commercial basis. These are of high business-related importance for distributors and suppliers. They are capable of providing more benefits for all Smart Grids actors (e.g. energy savings), but also of too big an intrusion to private live. At present, we do not know much exact examples of such services. Yet nobody can predict what market value for third parties can have the detailed data on energy consumption. Two simple examples can be given as the optimisation of energy consumption (e.g. ‘join the savings programme’) and goods or services offered thy third parties: (e.g. ‘since it is known that you do not use much electricity after 8 pm, go to the cinema half price’).

5. **Law enforcement.** There are a number of points of interest for law enforcement (e.g. police, intelligence, tax and customs authorities) in smart metering’s data retention. Here we are touching criminal law and thus the rules on due process (fair trial) and presumption of innocence must be observed.

6. Policy-Making. The state itself (as a regulator) might be interested in data retention for the policy-making purposes. It is a matter of energy security and production planning, among others.

7. Profiling, red-lining and discrimination. The detailed data on electricity consumption might interest various commercial actors outside the electricity market, among others. The retained data are vital for making a customer's profile, as the creation of a profile highly depends on retained personal data. The 'profiling' means 'an automatic data processing technique that consists of applying a 'profile' to an individual, particularly in order to take decisions concerning her or him or for analyzing or predicting her or his personal preferences, behaviors and attitudes.' A 'profile' is 'a set of data characterizing a category of individuals that is intended to be applied to an individual. Such profiling might lead to denial of services or increase their cost should a profile proves to be somehow dangerous or risky ('red-lining'). Furthermore, even a simple and non-detailed profile of energy consumption might facilitate commission of certain types of crimes.

VI. TECHNICAL SOLUTIONS

Final report of the CEN/CENELEC/ETSI Joint Working Group on Standards for Smart Grids [5] presents WAN interface to AMI subsystem & Head-End is used to connect the meter, a Local Network Access Point, or a Neighbourhood Network Access Point to a Central Data Collection system. Typical interface platforms for these interfaces are PSTN networks, public G2 (GPRS) and G3 (UMTS) networks, DSL or broadband TV communication lines, power line communications (PLC), either in narrowband or broadband.

The Head-End systems are the central Data Collection Systems for the Advanced Metering Subsystem. Head-end systems are typically part of an AMR (automatic meter reading) or AMM (automatic meter management) solution.

The interface towards the gateways and data concentrators (Network Access Points) is being standardized with Mandate M/441 whilst the interface from head-end systems towards central ERP and meter data management systems is covered by other IEC TCs, e.g. IEC TC 57 (61968-9).

Little work exists on the design of technical solutions to protect privacy in the smart grid [13]. Wagner et al. propose a privacy-aware framework for the smart grid based on semantic web technologies. Garcia and Jacobs design a multiparty computation to compute the sum of their consumption privately. The NIST privacy subgroup suggests anonymizing traces of readings, as proposed by Efthymiou et al., but also warns of the ease of reidentification. Molina et al. highlight the private information that current meters leak, and sketch a protocol that uses zero-knowledge proofs to achieve privacy in metering. Kumari et al. propose usage control mechanisms for data shared by smart meters connected to web based social networks.

It is equally important to make the principle of privacy by-design mandatory, including principles of data minimization and data deletion when using privacy enhancing technologies.

As it is currently almost impossible to ensure the full anonymisation of personal data and it is often possible to 're-identify' or 'deanonymise' individuals hidden in anonymised data with astonishing ease, only aggregated data should be used to the maximum possible extent. Considering significant privacy threats, we ask for privacy impact assessment to be conducted prior to the smart meter roll out.

Usually in data retention, data that is anonymised is considered non-personal because the data subject can no longer be identified and thus is not affected by the data protection framework. However, it is almost impossible to ensure the full anonymisation of personal data and it is often possible to 're-identify' or 'deanonymise' individuals hidden in anonymised data easily by using e.g. advanced algorithms or conjunction with other data sets. Therefore in some cases the means likely reasonably used for identification would allow for the identification of the data subject and in consequence would lead to the processing of personal data which are subject to data protection principles.

In respect with the aggregation of personal data, it is not clear how many persons one needs to aggregate on to protect individual data. This is also very context- and data dependent. Some research indicates that the minimum number of users is around 7 to 8, but in many circumstances it will be more. In case a meter is 'adjacent' to a household (i.e. majority of situations) we cannot say that we have any kind of data aggregation. There are simply too few inhabitants in such a household.

On the other hand, it is possible to have a smart meter that is able to 'tell' which exact device was used at a particular time. It is easy to build in and there is actually a lot of research in de-aggregating the readings. It is certainly easy to identify big devices like a washing machine, tea kettle, etc. But even if data is aggregated over devices, it is critical – you can tell when one comes home in the evening, even if one does not know whether the device one uses then is light, the tea-cooker, or a computer. Hence, the concept of data aggregation is here obstructed. Moreover, technical standards and systems should be developed with a focus on upgradeability to safeguard end-to-end security ensuring the overall intelligent metering system is future-proof and ready to cope with future challenges.

Standardization of smart grids is neither straightforward due to the huge number of stakeholders, the necessary speed, the many international activities and the still changing solutions make it a difficult task. Specific for the data privacy aspects, the consumer groups are asking for clear regulation around frequency of meter reading and usage of data. It is stressed that only data necessary to perform Smart Grid tasks should be collected and utilised. At the same time, whilst acknowledging benefits, Smart Grid/Meters should be designed for privacy and security.

Currently, there is no publically available reference architecture for Smart Grids with references to how privacy is designed into the core functionality, referring to all standards and principles for IT systems, business practices, and physical

designs and networked infrastructures.

Furthermore like in any other ICT-based infrastructure, cyber security has to be deeply analyzed. A single point of failure or back-door in the grid management system may be exploited to cut electrical supply to a country, resulting in enormous economic losses and endangering the whole community. Also, SmartGrids based ICT will transfer a lot of sensitive data that can be exploited to breach privacy, consequently, research has to ensure that state-of-the-art data-protection and data-privacy approaches are taken into account. To this end the communication systems and ICT should be upgraded to fast and diversified paths of data infrastructure.

Apart from consumer information handling in respect with security, privacy and data Protection, handling of huge amounts of data, the research issue is also the analysis of central versus decentral management.

Also Privacy Enhancing Technologies have to play significant role in the case of Smart Grids. While modern data mining technologies undermine classic protection, new advances in cryptographic techniques have become practical, and allow us to build systems that do not require the sharing of personal information. In a nutshell, it has become possible to compute almost arbitrary functions on encrypted data, i.e. the entity that handles the data never learns any input, only the result of the computation.

VII. CONCLUSION

Privacy and data protection challenge is arising in the move from the electricity grid towards the Smart Grid being unprecedented in terms of scale and complexity. This weighs even heavier dealing with critical infrastructure, in some cases unclear goals, some players moving into domains they have little experience in, a potentially huge privacy impact and an in-vivo implementation. An entirely new and complex model of inter-relationships poses challenges for the application of

data protection. The wide ranging nature of the issues presented by smart metering hinders to encompass an exhaustive list of privacy and security points. In this emerging area, it is fully expected that new data protection problems and solutions will evolve as more smart meters are installed. The massive rollout of smart meters is already happening, so there is urgency to manage the way that smart meters process personal data, and the issues of general concern which warrant serious consideration by all those involved in this area.

REFERENCES

- [1] ANEC/BEUC POSITION ON ENERGY EFFICIENCY, Joint ANEC/BEUC position paper on the Commission's Communication "Energy Efficiency Plan 2011"
- [2] Article 29 Data Protection Working Party, Opinion 12/2011 on smart metering, WP 183, 4.4.2011
- [3] BEUC Response To CEER Public Consultation On Demand Response Programmes
- [4] Cavoukian A., Privacy By Design ...Take The Challenge, Book.
- [5] CEN/CENELEC/ETSI Joint Working Group, Standards for Smart Grids, Final report, 4 May 2011.
- [6] Elster's White Paper, Privacy Enhancing Technologies for the Smart Grid, 4.10.2011
- [7] European Commission, COM(2010) 609, A comprehensive approach on personal data protection in the European Union Brussels, 4.11.2010
- [8] European Commission, COM(2011) 202, Smart Grids: from innovation to deployment, Brussels, 12.4.2011
- [9] European Technology Platform SmartGrids, Strategic Deployment Document for Europe's Electricity Networks of the Future
- [10] Kursawe, K., Danezis, G. and Kohlweiss, M., Privacyfriendly Aggregation for the Smart-grid.
- [11] NISTIR 7628, Guidelines for Smart Grid Cyber Security, September 2010
- [12] PbD, SmartPrivacy for the Smart Grid, November 2009.
- [13] Rial, R. and Danezis G., Privacy-Preserving Smart Metering, WPES11.
- [14] The Task Force Smart Grids Expert Group 2 report on "Essential Regulatory Requirements and Recommendations for Data Handling, Data Safety, and Consumer Protection". 06 June 2011.
- [15] European Technology Platform SmartGrids "Strategic Research Agenda for Europe's Electricity Networks of the Future - SmartGrids SRA 2035" March 2012.

Advanced DC Motor Drive for Haptic Devices

Miroslav Božić, Darko Todorović, Miloš Petković, Volker Zerbe, and Goran S. Đorđević

Abstract—Haptics covers many different forms of mechanical interaction with human senses by engaging, touch, vibrations and forces/torques, established for the purpose of augmenting the feedback structure during human-machine interaction. A haptic device has mechanical part, moved by actuators from one and human hand or fingers from the other, actuators, drives, sensing elements, as well as algorithms designed to control the interaction between human and machine in positioning and motion control tasks. With such a system, motors can be controlled in a way to simulate various environments, defined by their material and dynamics, for example pushing soft ball uphill. Haptic devices are becoming more popular in medical applications after introduction of modern medical robots with many different extensions for minimally invasive surgery or diagnostics based on palpation. This paper discusses one DC motor driver custom designed for the purpose of designing a haptic device for medical applications.

Index Terms—Haptics, DC motor drive.

I. INTRODUCTION

STEPPING out of industry was a challenging task for robotics scientists and engineer. Even now, after more than 25 years after establishing a first medical robot application where PUMA560 robot was placing a needle for brain biopsy using CT guidance, still we have no autonomous robot ready for any medical intervention. In reality, we are witnessing very effective robot installations reaching the level of restrained medical assistants, reliably and passively replicating or augmenting human manual commands presented at the handles, joysticks or specially designed mechatronic interfaces. The most prominent is Intuitive Surgical's da Vinci Surgical System. Simple but effective explanation is that living organisms are so complex in their structure and emerging forms, being healthy tissue or not, it requires another living organism with abundance of sensorimotor skills to perform even the simplest surgical intervention. From engineering point of view, it can be said we can have programmed elemental interaction but we cannot have a complete program

that will engage the skills in reliable manner of timing, sequencing or scaling. For that, we still need a surgeon that has all theoretical and practical knowledge while the robot will be only its extension to-wards better precision in positioning and applying force, less tremor, leading to successful and less invasive surgery. However, the most important achievement of robotic surgery is that it might help less trained surgeon to perform a standard surgery in a more reliable way but its overall success is limited within a scope of human skills. There is no surgery or diagnostics that robot can do while human can-not. Even worse for robotics, statistical evaluation of robotic-assisted surgery (RAS) vs. manual surgery shows no obvious benefit to patient's health, as RAS takes longer, it requires skills available only to additionally trained surgeons located at top-notch hospitals, and robotic surgery systems are still not developed enough at the point where human get hands on the robot. The weakest point of today's surgical robot technology is its human-machine interface part as the variety of interactions at that port is huge and so complex no modern technology tools and algorithms can provide its dependability.

The work presented in this paper aims the technology that will enable better HMI based on mechatronic system often called joystick, actuated with high performance DC motors. We developed Advanced Motor Drive for Haptic Devices (AMD-HD) with plenty of interfaces, functions, and processor support that can handle even motor skills of humans based on data after extensive exercising. The drive can be coupled with the other drives towards programmable bilateral interaction thus leaving a global control effort for the upper level where the strategy of interaction is considered. This paper describes the drive, its structure and purpose, accompanying software for drive programming to meet requirements needed for truly versatile haptic device.

II. AMD-HD DRIVE DESCRIPTION

The AMD-HD motor driver is designed to meet requirements such as precision, dynamics, reliability, connectivity, and scalability of high performance DC motors such as Maxon's RE series motors are. It supersedes generic Maxon drives well known as expensive and not so reliable drives. Among other, more expensive and reliable drives on the market, we did not find any driver that will naturally suit the needs in haptic devices for fast model-based control between the drive interactions due to the need of mechanical cross coupling required for achieving desired mechanical impedance projected at human hand in the whole workspace.

Manuscript received 1 May 2012. Accepted for publication 30 May 2012. Some results of this paper were presented at the 4th Small Systems Simulation Symposium, Niš, Serbia, February 12-14, 2012.

This paper is supported in part by PPP Mehmi project co-financed by DAAD and Ministry of Education and Science, Republic of Serbia, and in part by III44004-HUMANISM project financed by Ministry of Education and Science, Republic of Serbia.

Miroslav Božić, Darko Todorović, Miloš Petković, Goran S. Đorđević are with Department of Control Engineering, Faculty of Electronic Engineering, University of Niš, Serbia. goran.s.djordjevic@elfak.ni.ac.rs.

Volker Zerbe is with University of Applied Sciences, Erfurt, Germany. volker.zerbe@fh-erfurt.de.

The AMD–HD is based on micro-controller system that handles all: velocity and torque estimation, speed and torque control, position control, and even model-based control. Dedicated PC software handles GUI. The Driver and GUI software communicate via RS232/485 serial bus thus enabling multiple drive control within the same supervisory application at PC side.

A. Drive properties

The Drive nominal operating voltage is between 20 VDC and 90 VDC. Maximum output voltage is 72 VDC. Maximum output current 15 A (for less than 30 sec). Continuous output current is 10 A. Pulse Width Modulation frequency is 40 kHz. While the sampling rate is programmable and can be as low as 10 kHz, maximum motor speed is limited by maximum permissible speed (motor) and max. output voltage (controller). The dimensions of the drive are WxLxH: 148x148x40mm. Total weight with cooler is approx. 150grams.

Photo of the AMD–HD driver is shown on Fig. 1, with main modules numbered as:

1. Power Supply Unit
2. Control Unit
3. Motion Feedback Module
4. Analog-Digital IO module
5. Communication module
6. Motor current sensing module
7. H-bridge

The Drive has dedicated Power Supply Unit, with standard +5V, +12V, +V DC voltages for H-bridge. Noise is reduced by DC-DC converter with +V at input. Additional stabilization of voltage at the converter output supplies control circuitry. Microchip's PIC18F4431, besides its standard peripherals, has 4 independent complementary 14bit PWM modules; motion feedback module for data logging from quadrature signals of incremental optical encoder, 200 kbps 10bit AD converter; all making it almost perfect for the task we are targeting. Both,



Fig. 1. AMD-HD DC motor drive.

TTL and Differential inputs from encoders are handled by using 26LS32 line driver and 74HC157 Quad 2-Input Multiplexer as data selector. Encoder selection is possible within GUI software. Additional analog input 0 to 5VDC is available for position or velocity commands. Finally, two digital open collector inputs DI1 and DI2 are available for drive configuration from the GUI. The Drive communicates with GUI at PC level via RS232 point to point and RS485 multi point serial communication.

B. Current sensing

Current measurement is one of the most important properties of the Drive, as required for mechatronic technologies such as haptics. Precise current sensing can be related to the interaction force exerted between mechanics (linked to the motor) and human hand. For that to happen, it is crucial that mechanics efficiency of all transmissions (primarily, from gearbox, and secondary) is as low as possible and considerable amount of human machine interaction is feed back to the motor shaft for further estimation of current. The nature of such interaction points out sensitivity over bandwidth as hand movements are more soft and slow than strong and fast. Having that in mind we choose LEM HXS10-NP current sensing element. Sensor output is fed into non-inverting CMOS Op-Amp MCP601. The gain is set so that 1VDC corresponds to motor current of 1A. By setting up resistance the maximum gain is 2.5VDC/10A. The amplified signal is brought to analog input of micro-controller. The digital signal of current sensed is sent to GUI at PC.

Having in mind that output voltage of LEM sensor is:

$$V_{LEM} = V_{REF} \pm \frac{0.625 \cdot I_M}{I_{MAX}},$$

and the gain of amplifier is:

$$G = 1 + \frac{R_3}{R_2},$$

then, the voltage at the microcontroller input is

$$V_{MCU} = V_{REF} \pm \frac{0.625 \cdot I_M}{I_{MAX}} \cdot G.$$

C. GUI software

Dedicated GUI software, MCA-1 Monitor, handles all drive settings, PC peripheral configuration, data recording and visualization. Its main window is shown in Fig. 2.

This application handles:

1. COM port selection on PC where the driver is connected,
2. Address selection to be used by driver, for read and write of new parameters,
3. Free address assignment to non-configured driver
4. Inspection of Drive parameters such as: type, driver supply voltage, motor nominal voltage, maximal pulses of incremental optical encoder, encoder output signal type, motor brake operating voltage, gearbox ratio, digital input function selection.

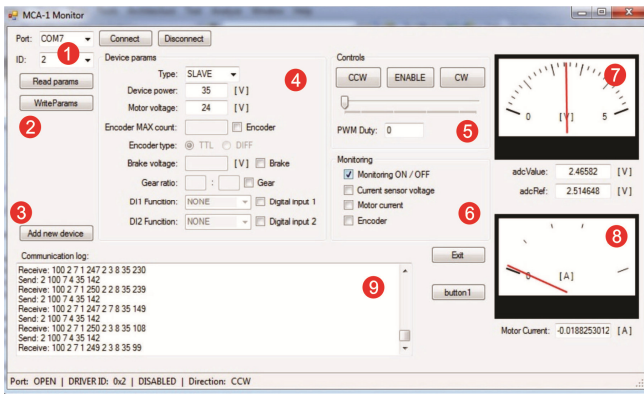


Fig. 2. Main window of MCA-1 monitor GUI

- 5. PWM duty cycle selection along with direction of rotation.
- 6. Motor parameter inspection
- 7. Current sensor voltage
- 8. Motor current sensing
- 9. Communication log.

This application also enables current data logging and graphical visualization in time-based diagrams, as shown in Fig. 3.

Arbitrary interaction with gearbox shaft with fingers produces the torques sensed and recorded by the driver. From Fig. 4, it is obvious that calculated motor current, shown with blue line, compared to LEM current sensor output, shown with red line, has very similar dynamics, almost without phase shift, and gain increase of approximately 82. The phase shift and filtering properties of the two signals should be correlated for further elaboration.

D. Communication Protocol

With rapid development of embedded systems, and significant price and development time reduction, distributed data gathering and local processing, based on reusable modules is becoming the mainstream model for rapid prototyping and final product development. In order to fulfill all the needs in matters of bandwidth, reliability and information security, appropriate protocol for communication between DC motor driver and PC, as well as between drivers themselves was defined, and communication libraries for .Net and microcontroller were developed.

The AMD-HD driver communicates with PC GUI software

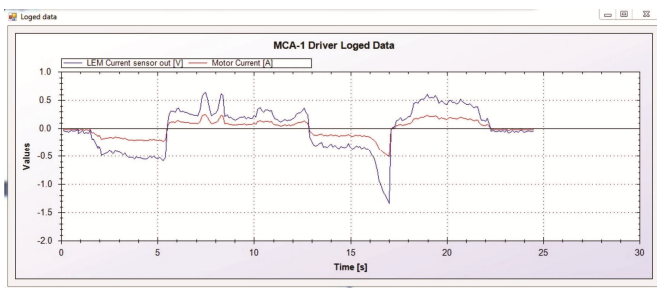


Fig. 3. Recorded voltage signal (at LEM sensor output) and calculated motor current.

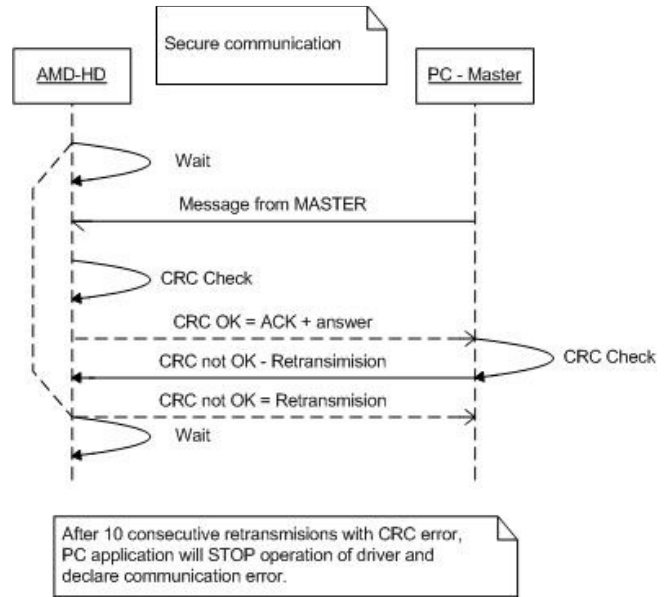


Fig. 4. Secure communication timing diagram.

via RS232 PTP or RS485 MP connection. Jumpers on the board are used for type selection. Also, two drives can be attached via I2C bus, but only the Master of the two drives can be controlled while the Slave will follow the Master. Message exchange protocol is explained with the timing diagram given in Fig. 4.

At first, we defined the time diagrams that describe the flow of messages and rules of communication between devices on global level shown on Fig. 4. Here we can see two timelines; first timeline is associated with AMD-HD (DC motor driver) and second is associated with PC which acts like a master device in communication. Because we use RS485 serial communication protocol on physical layer, we must have at least one master node at a time. As you can see on figure xx, the CRC is added at the end of each message and checked on each side. If CRC is not equal with calculated one, then the message retransmission is requested from both sides. In some modes, like PC monitoring, retransmission is not requested because the new driver state will be sent in next message again. The message with error will not be considered in that case. If 10 messages in a row come with errors then there is a communication failure and communication is stopped, to be sure not to make some damage.

Every message has defined structure and meaning. The structure of message is determined by the MUN (Message Unique Number) field. Based on this field, recipient can determine type of message, length and order of useful bytes. On Fig. 5 the structure of each message is shown.

Byte 0	Byte 1	Byte 2	Byte 2+n	Byte 2+n+1	Byte 2+n+2	Byte 2+n+3
ADR_REC	ADR_SEND	MUN	DATA_BYTES	NBR	#	CRC

Fig. 5. Message format.

First and second byte, define addresses of receiver and sender respectively. Third byte is already mentioned MUN byte, after which useful, data containing bytes are defined represented with DATA_BYTES. After useful data bytes, message length byte is placed and used for decoding purposes, after which termination byte represented with “#” character. At the end of the message calculated CRC is placed. Decoding on receivers side starts with finding the termination character and comparison between counted and the length of message in NBR byte. At the end CRC is checked and message is declared good or with errors.

E. Simulation

Modeling of H-bridge motor driver is considered trivial as extensive research was published in the last decades such as [1], and [2]. Modeling of Maxon DC Motors in Simulink is already done as well, and one of better models is found in [3] as a freeware. We have used that motor model but with catalogue data for Maxon motor RE40 [4, 5] as parameters. From practical point of view these simulations are not needed in haptic devices. Instead, for safety reasons we do need state transition diagrams of the drive for safe interaction with human operator. This should also include the safety system tailored for such purposes.

III. EXPERIMENTAL SETUP

This study and development has been undertaken for projects related to medical applications where human-machine interface is needed through controllable bilateral mechanical interaction. We chose high performance Maxon DC motor RE40, code 263075, operating on 48VDC, with 987 rpm no load speed, maximum continuous torque of 0.19Nm and torque constant of 461mNm/A, [4]. Such a motor is recognized among the others of the same family as the best transformer of output torque into motor current. Its low speed also makes it very suitable to be used in haptic interfaces. Even alone motor has enough torque to produce sensible force/torque on a standard mechanical device such as joystick. Here we added a high efficient planetary gearbox from the same manufacturer with 4.3:1 gear ratio and 9.4gcm² mass inertia [5]. Such a gearbox is very compliant backwards, meaning that motor can sense the torque applied on the gearbox shaft without considerable loss of information. The motor is also equipped with standard incremental optical encoder HEDS series with 500ppr. AMD-HD motor drive

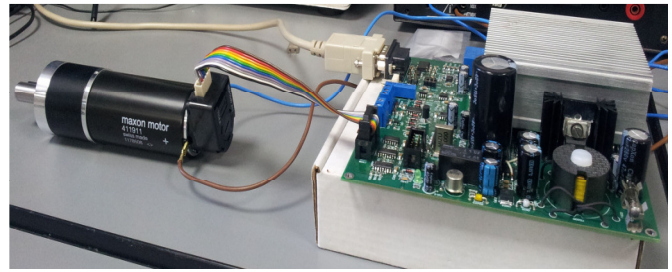


Fig. 6. Drive (to the left) and geared motor RE40.

along with gear-motor-sensor application is shown in Fig. 6.

IV. CONCLUSION

Advanced drive for DC motors is designed with focus on driving haptic devices with such system. It has several advantages as compared to the drives met on the market. First, it has high sensitive current sensor LEM HXS10-NP included meaning we can measure the interaction with environment (even through a gearbox of modest ratio) by measuring the current. Also, it can operate simultaneously with other drives, exchanging data on current, velocity, position and actual state of the motor. This makes it very useful in integrating it into a hierarchical control system where upper level of control is done at embedded controller while the motion itself along with interaction is left to be handled at the driver side. This is particularly useful in haptic devices where the interaction is complex dynamics and it requires special calculations. Finally, on-board processor can be used for customized model-based control (analytic or data-based) thus making this drive a perfect companion of the motor in the given mechatronic system.

REFERENCES

- [1] V. Gupta. “Working and analysis of the H - bridge motor driver circuit designed for wheeled mobile robots.” in Proc. Advanced Computer Control (ICACC), 2010 2nd International Conference, pp. 441 – 444, ISBN: 978-1-4244-5845-5, 27-29 March 2010
- [2] Wai Phyo Aung. “Analysis on Modeling and Simulink of DC Motor and its Driving System Used for Wheeled Mobile Robot” World Academy of Science, Engineering and Technology, ISSN 2010-37632, 2007
- [3] S. Kozola and D. Doherty. (2007, May). “Using Statistics to Analyze Uncertainty in System Models”, MATLAB Digest,
- [4] Maxon. “Maxon DC motor RE40 catalog page”, Internet: http://test.maxonmotor.com/docsx/Download/catalog_2005/Pdf/05_083_e.pdf [Oct. 12, 2011].
- [5] Maxon. “Maxon Planetary Gearhead GP 42 C catalog page”, Internet: http://www.electromate.com/db_support/downloads/244245.pdf [Oct. 12, 2011].

How To Measure Oscillator's Short-Term Stability Using Frequency Counter

Ivica Milanović, Snežana Renovica, Ivan Župunski, Mladen Banović, and Predrag Rakonjac

Abstract—In this paper a few methods of how to use frequency counter in time-domain frequency stability analysis are described. Three implemented methods are presented. As an experiment, a comparison of the realized methods in the Technical Test Center (TOC) and the “references” obtained in the Directorate of Measures and Precious Metals (DMDM) in Belgrade are accomplished. The measurement uncertainty estimation for time interval measurement with one frequency counter is presented as well.

Index Terms—Frequency, Frequency Counter, Oscillator, Short-Term Stability.

I. INTRODUCTION

Frequency stability is one of the most important specifications of an oscillator. Stability does not specify how much frequency is accurate, but how much it is stable during observed time interval. If considered time intervals up to 100 seconds (10 ms, 100 ms, 1 s, etc.), then we talk about so-called short-term stability. Otherwise, there is analysis of long-term stability, and then we specify the oscillator's stability for an hour, and more often for a day, a month, or a year [1].

Stability is defined as the statistical estimation of the frequency or time fluctuations of a signal over a given time interval. Statistical estimations can be presented in the frequency or, more often, in the time domain [2]. To achieve frequency stability in the time domain a set of a frequency offset measurements have to be carried out, along with the calculation of the collected data scattering.

II. THEORY OF FREQUENCY STABILITY MEASUREMENTS

Sine wave signal can be presented as:

$$V(t) = [V_0 + \varepsilon(t)] \sin[2\pi\nu_0 t + \varphi(t)] \quad (1)$$

where V_0 is nominal voltage, $\varepsilon(t)$ is amplitude deviation, ν_0 is

nominal frequency and $\varphi(t)$ is phase deviation.

In order to simplify further analysis, nominal voltage and nominal frequency will be assumed as being constant. Also, it is assumed that the amplitude deviation is negligible in comparison with nominal voltage [3]. Due to that, the instantaneous frequency is equal to:

$$\nu(t) = \nu_0 + \frac{1}{2\pi} \frac{d\varphi}{dt} = \nu_0 + \nu_\nu \quad (2)$$

and it is the sum of a constant nominal value ν_0 and variable term $\nu_\nu(t)$.

We are not interested in large frequency deviations because we are talking about reasonably stable oscillators. Therefore, another restriction is:

$$|\nu_\nu(t)| \ll \nu_0 \quad (3)$$

The objective of the frequency stability analysis is to characterize the phase and frequency oscillator fluctuations with time [4]. In spite of that, we are primarily concerned with the $\varphi(t)$ term.

The aim is to determine the fractional frequency offset of oscillator (device) under test (DUT) and reference oscillator:

$$\frac{\Delta f}{f} = \frac{\nu(t) - \nu_0}{\nu_0} = \frac{1}{2\pi\nu_0} \frac{d\varphi}{dt} = y(t) \quad (4)$$

Measuring of frequency stability is a process which can be divided into a few steps [3]:

- Preprocessing
- Collecting and storing data
- Outliers removal
- Noise type determination
- Data analysis (statistics)
- Results interpreting - reporting

A. Preprocessing

Oscillator's characteristics are highly dependent on environment conditions, like a temperature change. Preprocessing includes preparing and monitoring those conditions, and monitoring the electrical power quality [3].

B. Acquisition

Frequency stability is observed over some period of time. To determine it, we have to realize a set of frequency offset measurements equally-spaced in time. The essential data is an array of equally-spaced phase or frequency values taken at particular measurement interval. Phase data are preferred, because they can be used to obtain frequency data. This is not

Manuscript received 18 December 2011. Received in revised form 14 March 2012. Accepted for publication 28 March 2012.

Ivica Milanović is with the Technical Test Center, Serbian Armed Forces, Belgrade, Serbia (e-mail: milanovic_i@ikomline.net).

Snežana Renovica is with the Directorate of Measures and Precious Metals, Belgrade, Serbia (e-mail: renovica@dmdm.rs).

Ivan Župunski is with the Faculty of Technical Science, University of Novi Sad, Novi Sad, Serbia. (e-mail: zivan@uns.ac.rs).

Mladen Banović and Predrag Rakonjac are with the Technical Test Center, Serbian Armed Forces, Belgrade, Serbia (e-mail: metrologija@toc.vs.rs).

always true if we want reverse analysis – absolute phase cannot be reconstructed from frequency data, and all gaps in frequency data will lead to losing phase continuity [1]. In the literature the sampling time or the measurement interval is usually marked as τ_0 [4]. The averaging time (τ) is a multiple of the measurement interval (τ_0):

$$\tau = m \cdot \tau_0 \quad (5)$$

where m presents the averaging factor.

C. Outliers removal

System imperfection or some other external influences can produce abnormalities in collected and stored data - some values will significantly exceed expected quantities. Those data are called outliers, and they have to be removed from the collected array of data, before further analysis is carried out.

The median absolute deviation (*MAD*) is a robust way to set the criteria for an outlier [3]. It is the median of the absolute deviations of the data points from their median value (scaled), and is defined as:

$$MAD = Median \left\{ \frac{|y_i - m|}{0.6745} \right\} \quad (6)$$

where m is equal to $Median\{y(i)\}$. The factor 0.6745 makes the *MAD* equal to the standard deviation for normally distributed data.

An outlier criteria of $5 \cdot MAD$ [3] is usually a good choice.

Another, maybe more common way, is to use next criteria:

$$m + 3s < x(j) < m - 3s \quad (7)$$

where x are data, j is number of data points, m is the mean value of x , and s is the classical standard deviation of x .

D. Statistics – data evaluating

Frequency stability is a result of data taken in some period of time, yet the independent variable is not the running time t , but the averaging time τ . Regarding that, the experimental data cannot be accurately described as a stationary process, so the usual variances are not good way to express frequency stability – the stationary concept means that observed process has its beginning and its end. Limited time intervals of observation are the main reason for inventing a new statistical tool called Allan Variance [2].

It is developed in order to solve the problem that the standard variance doesn't converge to a single value for the non-white FM noises as the number of measurements is increased [1]. It is described as:

$$\sigma_y^2(\tau) = \frac{1}{2(M-1)} \sum_{i=1}^{M-1} (\overline{y_{i+1}} - \overline{y_i})^2 \quad (8)$$

where σ is Allan Variance, τ is averaging time, M is number of fractional frequency values, and y_i is i^{th} of M fractional frequency data averaged over the τ .

While standard deviation subtracts the mean from each measurement before squaring their summation, the Allan deviation subtracts the previous data point. This differencing of successive data points removes the time dependent noise contributed by the frequency offset.

The stability is being improved as the averaging time (τ) gets longer, because, in some cases, noises can be removed by averaging [1]. However, on some level further averaging no longer improves the results – that level is called the “noise floor”.

The non-overlapping Allan, or two-sample variance, is the standard time domain measure of frequency stability [3].

But, this kind of calculation can be performed by utilizing all possible combinations of data sets. This is so-called overlapping method [5]. It can be performed over the Standard Allan Variation in order to improve the confidence of a stability estimate:

$$\sigma_y^2(\tau) = \frac{1}{2m^2(M-2m+1)} \sum_{j=1}^{M-2m+1} \sum_{i=j}^{j+m-1} (\overline{y_{i+m}} - \overline{y_i})^2 \quad (9)$$

where σ is Overlapped Allan Variation, and m is averaging factor.

Allan Variance can be described both tabular or in log-log sigma-tau ($\sigma\tau$) diagrams. Those diagrams describe how much we need to average in order to get rid of the noise contributed by the reference and the measurement system.

There are several other variances which can be used, like Modified Allan, Hadamard, Total, Time Variance etc. However, Overlapping Allan Variance should be used as the first choice [3].

E. Confidence Intervals

Sample variances are distributed according to:

$$\chi^2 = \frac{edf \cdot s^2}{\sigma^2} \quad (10)$$

where χ^2 is Chi-square probability, *edf* is Equivalent number of Degrees of Freedom, s^2 is the sample variance, and σ^2 is the true variance.

The *edf* depends of number on data samples and the noise type. The lower and the upper bound of the sample variance are:

$$\sigma_{\min}^2 = \frac{edf}{\chi^2(p, edf)}, (0 < p < 1) \quad (11)$$

$$\sigma_{\max}^2 = \frac{edf}{\chi^2(1-p, edf)}, (0 < p < 1) \quad (12)$$

where p is desired confidence factor.

F. Noise type determination

The instability of the most frequency sources can be modeled by a combination of their frequency fluctuations $S_y(f)$. Measure of frequency stability versus the time over which the frequency is averaged can be presented as:

$$S_y(f) \approx f^\alpha \quad \text{or} \quad \sigma_y(\tau) \approx \tau^{\mu/2} \quad (13)$$

where $S_y(f)$ is power spectral density, α is the parameter that defines the noise model in a frequency domain, $\sigma_y(\tau)$ is frequency stability vs averaging time, and μ is the parameter that defines the noise model in a time domain, and it is equal to $\mu = -\alpha - 1$.

Some typical noises with α parameter values are shown in Fig.1.

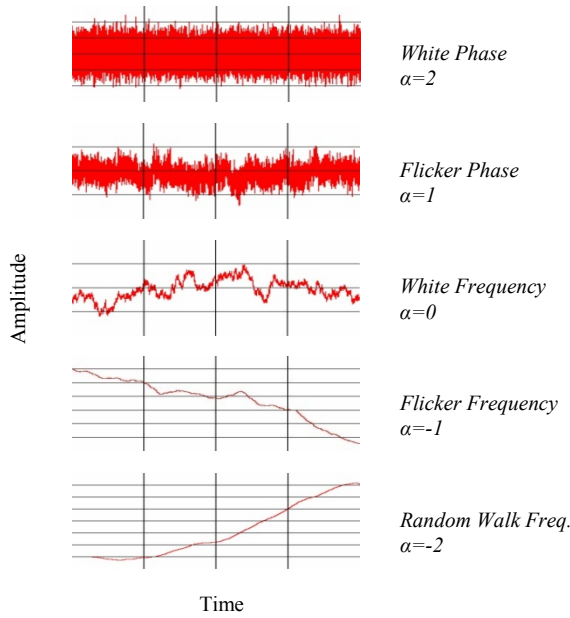


Fig. 1. Simulated Noises in the Time Domain.

White PN – usually exists as a result of signal amplifying, and has no relation with resonance mechanism.

Flicker PN – it is related to resonance mechanism, and it is usually made by noisy electronics.

White FN – it is a common type for passive resonator frequency standards (cesium or rubidium). They contain slave (usually quartz) oscillators whose frequency is “locked” to a resonance feature of another device.

Flicker FN – its physical cause is typically related to the physical resonance mechanism of an active oscillator, electronics parts, or environmental properties. It is common in high-quality oscillators, but it can be masked by white FN or flicker PN in lower-quality oscillators.

Random Walk FN – it usually exists very close to the carrier [6], and it is related to an oscillator’s physical environment – mechanical shock, vibration, temperature, etc.

In a σ - τ diagram those simulations can be presented as in Fig.2.

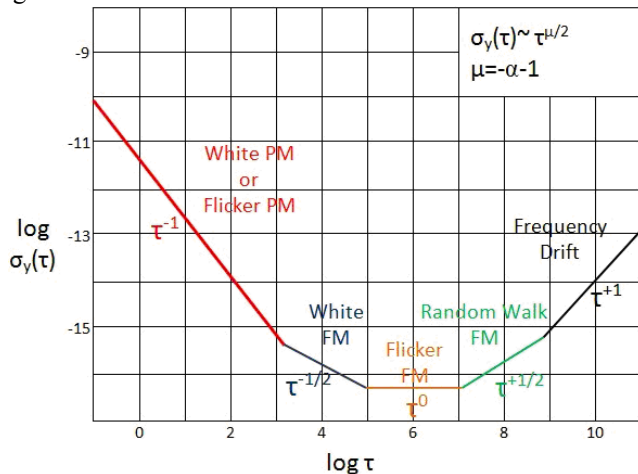


Fig. 2. Noises in the Time-Domain – σ - τ diagram.

So, if we calculate the slope of the derived Allan variation

curve, we can determine the dominant noise type of the measured oscillator.

III. ELECTRONIC COUNTERS IN TIME INTERVAL MEASUREMENTS

Frequency difference measurements can be carried out with time interval counters – devices with two inputs (signal in one input starts the measurement, and signal in second input stops it). In this case we have a comparison between two signals: the output signal from the reference oscillator and the output signal from the oscillator under calibration (device under test – DUT).

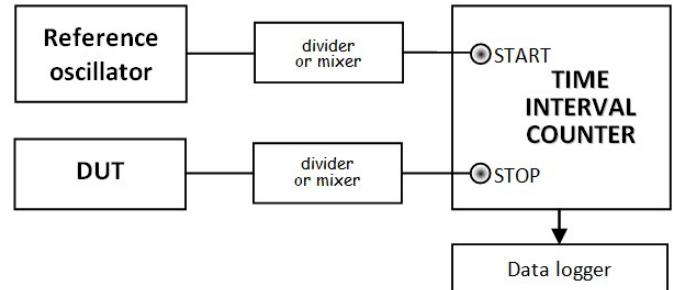


Fig. 3. Using the time interval (or frequency) counter for frequency stability measurements – basic idea.

This is the scheme which presents the basic idea of the stability measurements [7]. A few methods are realized according to that principle.

A. Reference oscillator

A measurement compares the DUT to a reference or standard. The standard should have better short-term characteristic – the test uncertainty ratio (TUR) should be 10:1, or even higher. When we talk about short-term stability, the most common types of oscillators can be arranged in ascending order: like the best quartz, then rubidium and then the cesium commercial oscillators. Nowadays, the best standards for short-term stability are so-called BVA quartz oscillators (“*Boitier a Vieillessement Ameliore*”). For example, Oscilloquartz BVA OCXO, type 8607 with option 15 (short term option) has $\sigma(\tau)$ better than $1.5 \cdot 10^{-13}$, for τ from 1 to 30 seconds.

B. Frequency counters

The frequency difference between DUT and standard is detected by a time interval counter. Frequency counters are most commonly used instruments with capabilities of the time interval measuring. There are conventional counters, reciprocal counters, counters with digital interpolation scheme, etc. [8]. However, when we are talking about the time interval measurements, a few characteristics of the counters are dominant:

- Single-shot time interval resolution. It represents the number of digits that counter can display. This characteristic limits counter’s ability to measure frequency offset, and determines the smallest frequency change that can be detected without averaging,

- Accuracy in the time interval measurements,
- Dead time. It represents instrumentation delay between successive measurements,
- Trigger level timing error,
- Trigger offset,
- Internal noises,
- Aging of the oscillator and its temperature changes,
- Asymmetry between channels (mismatch),
- Averaging capabilities, etc.

Some of those characteristics can be suppressed or even overcome, and some of them cannot. The measuring uncertainty calculation will show their effects on the short-term stability measurements. This will be discussed later on in a chapter VI.

C. Frequency dividers or frequency mixers

Most common output frequencies of oscillators are 5 MHz or 10 MHz. Since they are not practical to measure with frequency counters, frequency dividers or frequency mixers are used to convert them to lower frequencies.

Despite the greater simplicity of the frequency dividers, frequency mixers are more used [1]. They are more expensive, require more hardware and additional oscillator, but they have a much higher signal-to-noise ratio, and this is the main reason for their usage.

D. Data logging

As a result, frequency counters give a set of frequency offset measurements. Those data can be written to a paper, or stored into some external memory space, in order to be analyzed later.

In order to avoid extra usage of counter hardware resources, and to suppress the measuring uncertainty and the dead time, some external accumulators can be used. At the beginning, analog plotters were used. They are changed with the accumulators – while the dead time data are sent to the accumulator's memory. After the measurement, the data can be read out later on. The main disadvantage is memory space.

Nowadays, the interfaces between the counters and personal computers extend the capability to store data directly to PC memory.

IV. REALIZED METHODS FOR SHORT-TERM STABILITY MEASUREMENTS

Two methods are realized in Technical Test Center laboratory: Direct time interval measurement and dual mixer time difference method.

A. Direct time interval measurement method

In this method Hewlett Packard 5370A universal time interval counter is used. It has good time interval resolution – 20 ps in a single-shot. Also, it has capability to work in a binary mode of operation for time interval measurements – minimum time between measurements is 165 μ s instead of 330 μ s (like in a normal mode). This way counter does not perform any type of statistical measurement (mean, standard

deviation, etc.). Instead, counter outputs raw data – five binary data form one decimal data (information of time interval value).

HP 5370A is connected to a PC USB port with Agilent 82357A GPIB/USB interface. Short-time stability measurement is automated with Agilent VEE Pro 7.0 software. Minimum sample time is 100 ms.

When the measurement is finished program transforms binary data into decimal values, calculates Allan deviation and draws σ - τ diagram. Frequency offset is calculated as:

$$\frac{\Delta f}{f} = -\frac{\Delta t}{t} \quad (14)$$

where Δt is time interval between two successive measurements, t is averaging time, and $\Delta f/f$ is the fractional frequency offset.

Further data analysis is carried out with the AlaVar 5.2 software. It removes outliers (according to (7)), gives Allan variation table results and charts, and can determine dominant noise type (five noise types, as is described in the chapter II-F).

B. Dual mixer time difference method

This method is realized with: HP 5345A frequency counter, two HP 10830A frequency mixers, HP 5358A accumulator (as an additional plug in the HP 5345A), and HP 59308A timing generator for HP 5345A external arming.

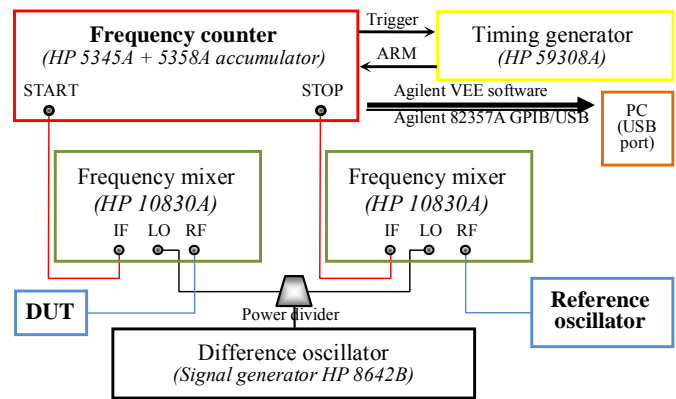


Fig. 4. Dual Mixer Time Difference Method with HP 5345A.

As a difference oscillator HP 8642B signal generator is used. It provides $v_b = 6$ kHz beat frequency (6 kHz sine wave signal). External arming of HP 5345A is with 200 μ s pulses from HP 59308A.

The difference oscillator's output ($v_0 \pm v_b$) is split by a power divider, and applied to each mixer. Further measurement is taken over 6 kHz IF signals.

To calculate $\sigma(\tau)$ formulas (15) and (16) are used:

$$\Delta f_i = \frac{v_b}{\tau} [(t_{i+1} - t_i) - (t_i - t_{i-1})] \quad (15)$$

$$\sigma_y(\tau) = \sqrt{\frac{1}{2N} \sum_{j=1}^N \frac{(\Delta f_j)^2}{v_0^2}} \quad (16)$$

where t_i is time interval between 2 successive measurements,

ν_b is beat frequency, τ is averaging time, ν_0 is nominal (carrier) frequency, and N is number of samples.

This measuring method is also automated with Agilent VEE Pro 7.0.

Because of the HP 5345A poor time interval measurement resolution (2 ns), this method is also configured with HP 5370A frequency counter. The configuration is the same, but timing generator was not used, because HP 5370A has no capability of the external arming.

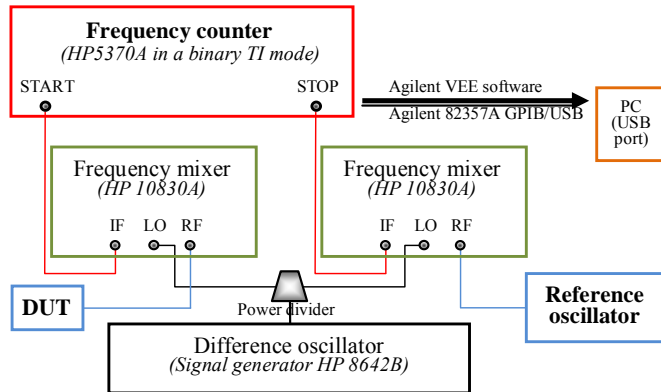


Fig. 5. Dual Mixer Time Difference Method with HP 5370A.

Three of these methods were compared with the “reference” method realized in the Directorate of Measures and Precious Metals. DMDM uses specially designed for time interval analysis, TSC 5110A Time Interval Analyzer. It is designed to measure the phase difference between two signals, to measure frequency, to determine and draw Allan deviation and to draw phase and frequency plots. Optionally, it can determine SSB (single-sideband) phase noise.

This time interval analyzer is based on the heterodyne method (method with two mixers), and uses intermediate frequency (IF) of approximately 100 Hz (when equal frequency oscillators are compared). The smallest sampling interval is one period of the IF or 10 ms.

For the frequency standard DMDM uses Oscilloquartz BVA OCXO 8607 (described in the chapter III-A), which is one of the best commercial short-term stability standards.

V. EXPERIMENTAL RESULTS

Three different types of oscillators are used for short-term stability measurements: HP 105B and HP 5061A quartz oscillators, Racal Dana 9475 rubidium oscillator and Oscilloquartz 3210 cesium frequency standard. They are compared with three realized methods: with HP 5370A universal time interval counter - direct method (in binary mode of operation) and dual mixer method, and dual mixer method with HP 5345A frequency counter.

The environmental conditions were $23^{\circ}\text{C}\pm 1^{\circ}\text{C}$, and humidity $50\%\pm 10\%$.

In order to compare them, measurements are also taken with TSC 5110A and frequency references BVA 8607 and the

Symmetricom 5071A high performance cesium standard, in DMDM’s time and frequency laboratory. This method was assumed “reference”, which will be shown in the charts below.

In Fig.6 the σ - τ diagram (Allan variance chart) for rubidium oscillator stability is shown. It was compared with two different quartz oscillators for 5 MHz outputs, measured with HP 5370A (direct measurement). In the range from 0.1 to 4 seconds the difference between DMDM and TOC results is significant. For $\tau=1\text{s}$ DMDM result is $5\cdot 10^{-12}$, and with direct measurement $2\cdot 10^{-11}$. Nevertheless, as manufacturer specifies Allan variance better than $5\cdot 10^{-11}$, the conclusion for the averaging time 1s will not be wrong.

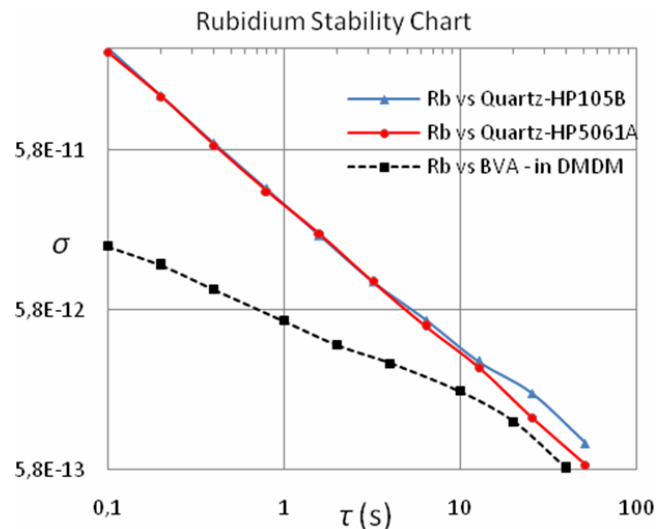


Fig. 6. Direct method with HP5370A in a binary mode.

The same measurement was made using the cesium 3210. The results are given in Fig.7. For $\tau = 1\text{s}$ they are practically the same. Still, under 1s difference is bigger as τ gets smaller.

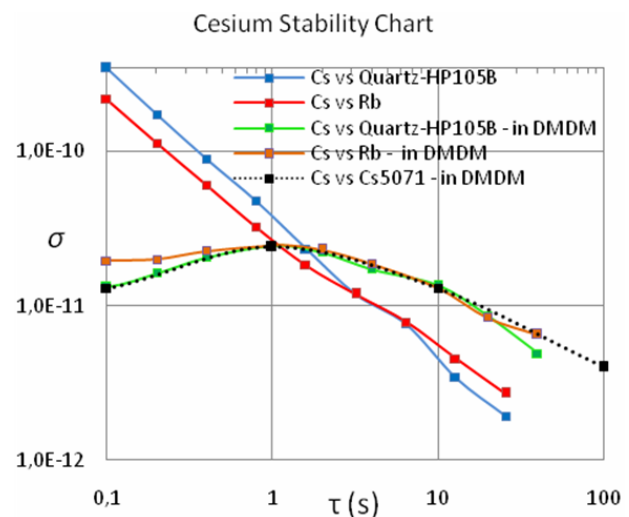


Fig. 7. Direct method with HP5370A in binary mode.

As we introduced mixers in the measurements, the results became better (Fig.8).

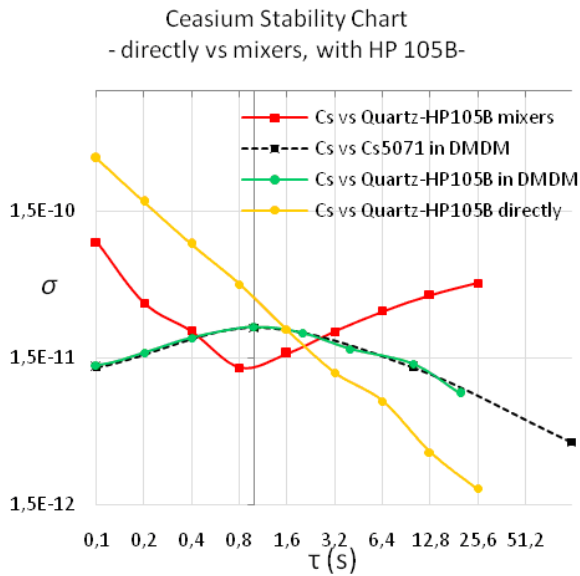


Fig. 8. Use of HP5370A in binary mode – directly and with mixers.

Mixing 10 MHz with 6 kHz signal improves system capabilities, especially in a band below 1 second.

In Fig. 9 we can clearly see the improvements made by using time difference method, and with use of good standards.

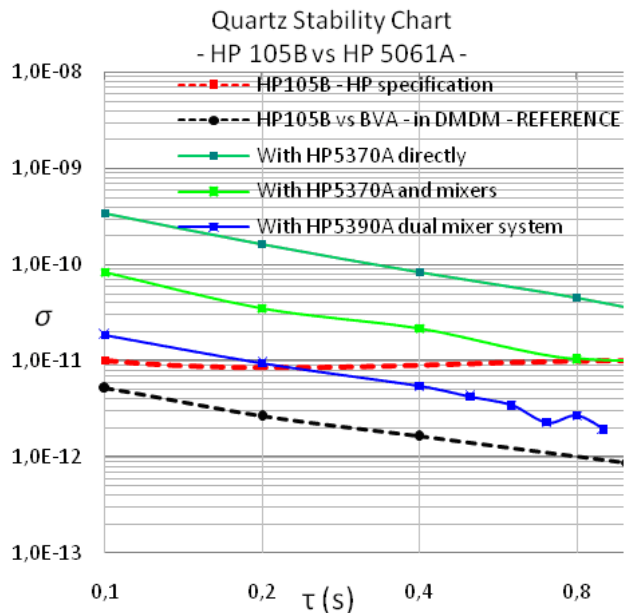


Fig. 9. HP 105B quartz oscillator stability measured with direct and dual mixers methods – comparison.

Two quartz oscillators were compared (HP 105B and HP 5061A). The “worst” results were achieved with the direct method.

Even the better counter was used (20 ps HP 5370A), because of the lack of the timing generator, dual time difference method realized with HP 5345A gave better results. That shows the importance of the counter’s accurate arming.

The conclusion is that for oscillators with high short-term stability, only dual time difference method can produce

reliable results.

VI. MEASURING UNCERTAINTY

Regarding previous chapters it is obvious that counter’s specifications are dominant in measuring uncertainty contribution. All of those methods are based on time interval measurements. Like an example, the measuring uncertainty estimation for direct measurement with HP 5370A time interval counter will be discussed.

A. Random Effects – Uncertainty Type A

The random effects vary in an unpredictable way each time you make a measurement. They produce an unstable reading on the counter’s display. This uncertainty is often assumed to have an approximately normal distribution.

1. Resolution or Quantization uncertainty

This is uncertainty due to single-shot time interval resolution of a counter [9]. For HP 5370A this resolution is 20 ps, and producer defines this uncertainty like:

$$\delta_r = \frac{\pm 20 ps}{\sqrt{\text{sample size}}} \pm 2 ps \quad (17)$$

If we choose sample size 1, this contribution is ± 22 ps.

2. Accuracy of a time interval measurement

Because of a great influence of jitter Hewlett Packard defines uncertainty due to time interval measurement accuracy as:

$$\delta_a = \text{jitter} \quad (18)$$

HP 5370A has typical jitter of 100 ps, so, total amount of this contribution is ± 100 ps.

3. Start/stop trigger point uncertainty due to noise

This uncertainty occurs when a time interval measurement starts or stops too early or too late because of noise on the input signal [9], as shown in Fig. 10.

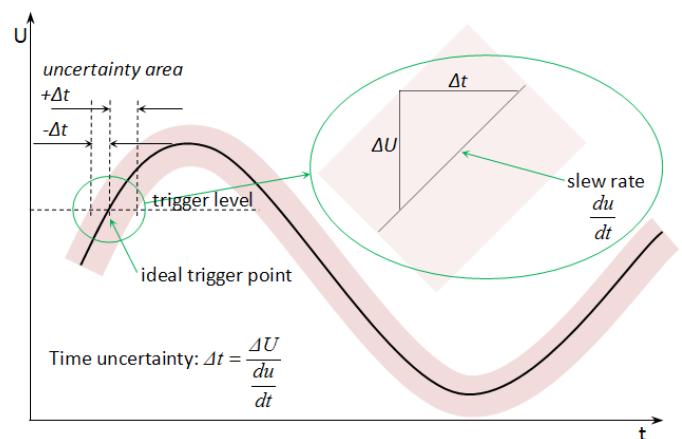


Fig. 10. Start trigger points uncertainty due to noise.

There are two sources of the noise: noise on the signal being measured and noise added to this signal by the counter’s input circuitry:

$$\delta_{in} = \frac{\sqrt{V_{ni}^2 + V_{ne}^2}}{\frac{du}{dt}} \quad (19)$$

where V_{ni} is internal noise, V_{ne} is external noise, and du/dt is signal slew rate at trigger point.

The slew rate (du/dt) for sine-wave signal at the zero-crossing is:

$$\frac{du}{dt} = u \cdot \omega \cdot \cos(0) = 2 \cdot \pi \cdot f \cdot U_{RMS} \cdot \sqrt{2} \quad (20)$$

The internal noise for HP 5370A is 150 μ V. If we assume that input is 10 MHz sine-wave signal, with $U_{RMS} = 1$ V, and signal to noise ratio (SNR) 60 dB, formula (20) now is:

$$\delta_{in} = \frac{\sqrt{\left(\frac{150\mu V}{U_{RMS}}\right)^2 + \left(\frac{1}{SNR}\right)^2}}{2 \cdot \pi \cdot f \cdot U_{RMS} \cdot \sqrt{2}} = \frac{\sqrt{\left(\frac{150\mu V}{1V}\right)^2 + (0.001)^2}}{2 \cdot \pi \cdot 10MHz \cdot 1V \cdot \sqrt{2}} \quad (21)$$

Finally, for start trigger point, measuring contribution is ± 11 ps.

If we assume the same U_{RMS} for both signals at the counter inputs, the uncertainty for stop trigger point will be the same as for start trigger point, so we have $\delta_{in-start} = \delta_{in-stop} = \pm 11$ ps.

B. Systematic Effects – Uncertainty Type B

Uncertainty type B is unchanged when a measurement is repeated under the same conditions. Instead, those effects cause an offset of the measurement result from the true value.

4. Start/stop trigger points uncertainty due to trigger level offset or Trigger level timing uncertainty

This measuring uncertainty results from trigger level setting uncertainty due to deviation of the actual trigger level from the indicated, and from input amplifier hysteresis if the input signals do not have equal slew rates [9][10].

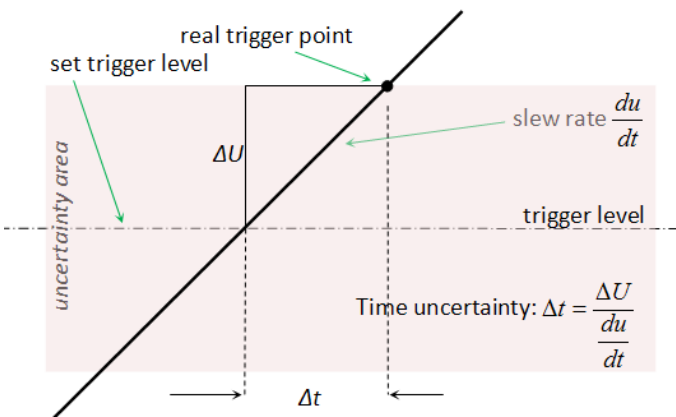


Fig. 11. Start trigger point uncertainty due to trigger level offset.

This uncertainty can be presented as:

$$\delta_{io} = \frac{\Delta U}{\frac{du}{dt}} \quad (22)$$

where ΔU is offset from zero.

For HP 5370A this offset from zero is less than 2.5 mV, so:

$$\delta_{io} = \frac{2.5mV}{2 \cdot \pi \cdot 10MHz \cdot 1V \cdot \sqrt{2}} \quad (23)$$

As the input signals are equal we have:

$$\delta_{io-start} = \delta_{io-stop} = \pm 28 \text{ ps}$$

If we assume a rectangular distribution [10], the corresponding standard uncertainty can be calculated by dividing by $\sqrt{3}$, so we will have:

$$\delta_{io-start} = \delta_{io-stop} = \pm 16 \text{ ps}$$

5. Channel asymmetry uncertainty or Channel mismatch uncertainty

This uncertainty is a result of unequal propagation delays in the two counter's inputs, and differences in rise times of the input amplifiers.

Hewlett Packard for 5370A defines asymmetry better than 700 ps. Assuming a rectangular distribution this measuring uncertainty contribution is $\delta_{asymm} = \pm 404$ ps.

6. Timebase uncertainty

This uncertainty is frequency deviation from its nominal value (10 MHz in this example). HP 5370A uses external reference from cesium frequency standard, so, the uncertainty is the result of two main sources:

- aging of the oscillator (stability) – ε_a
(for Oscilloquartz 3210 Allan deviation for 0.1 s is: $1.3 \cdot 10^{-11}$ for 2σ , or $0.65 \cdot 10^{-11}$ for 1σ)
- temperature changes – ε_t
(for Oscilloquartz 3210 temperature changes are defined as: $2 \cdot 10^{-12}$ in the range -5 °C to 55 °C)

The timebase uncertainty [9] is defined by:

$$\delta_{TB} = TI \cdot \sqrt{\frac{\varepsilon_a^2 + \varepsilon_t^2}{3}} \quad (24)$$

where TI is measured time interval (in this example it is sampling interval of 100 ms), so, this contribution is: $\delta_{TB} = \pm 0.4$ ps.

The influence of type A measuring uncertainty can be reduced by averaging [5]. Experimental measurements are realized within 90 s, 100 s, 180 s and 360 s, or 900, 1000, 1800, 3600 or 9000 samples, respectively. The summary contribution of type A measuring uncertainty is calculated using formula 25:

$$u_{RAND} = \frac{\sqrt{\delta_r^2 + \delta_a^2 + \delta_{m-start}^2 + \delta_{m-stop}^2}}{\sqrt{N}} = 3 \text{ ps} \quad (25)$$

where N stands for the number of samples.

Finally, the expanded uncertainty for $k=2$ is equal to:

$$U(k=2) = 2 \cdot \sqrt{u_{RAND}^2 + \delta_{io-start}^2 + \delta_{io-stop}^2 + \delta_{asymm}^2 + \delta_{TB}^2} \quad (26)$$

$$U(k=2) = 0.809 \text{ ns}$$

The influence of channel asymmetry is dominant one, and it is shown that bigger averaging time does not result in reducing measuring uncertainty.

In deciding which counter should be used, the user has to pay particular attention on: channel asymmetry, accuracy of

the time interval measuring, and time base uncertainty of a counter.

This way of estimating measuring uncertainty can be used for all time interval measurements which are carried out with a frequency counters.

VII. THE CONCLUSION

In this paper the oscillator's short-term stability and procedure of it's measurement in the time domain was described, in short. Particular phases of measurement, and the way for a data analysis are given, too.

Three methods realized with frequency counter HP 5345A, and time interval counter HP 5370A are described. The results of real measurements are given in graphs. They are compared with the results acquired in DMDM which are considered referent ones. In the DMDM measurement was carried out using the time interval analyzer with two standards: BVA quartz oscillator and ultra stable cesium frequency standard. The shot-term stability was measured for quartz oscillator HP 105B, rubidium frequency standard Racal Dana 9475 and cesium frequency standard Oscilloquartz 3210.

The comparisons are presented in graphs. It is shown that methods based upon the frequency counters can be used to determine short-term stability for averaging time of one second, or more. For smaller averaging intervals, more reliable is method realized with time interval analyzers in accordance with ultra stable oscillators like a references.

Direct measurements with counters are possible, but if we want to improve measuring system capabilities, it is better to compare IF frequencies, rather than their nominal values. These methods can be realized either with dividers or

frequency mixers. Advantages and disadvantages are shown in this paper.

The measurement of short-term stability is, basically, measurement of time interval between two sinusoidal signals. According to that, the measurement uncertainty estimation for time interval measurement using frequency counter is given. The analysis shows that the mismatch between counter channels has the greatest influence to total measuring uncertainty. For counters which are going to be used in frequency stability measurements, this analysis shows what are the most important characteristics we have to pay attention on.

REFERENCES

- [1] M.A.Lombardi, "Fundamentals of Time and Frequency", NIST, 2002.
- [2] P.Kartashoff, "Frequency and Time", Monographs in Physical Measurement, 1978.
- [3] W.J.Riley, "Handbook of Frequency Stability Analysis", Hamilton Technical Services, July 2007.
- [4] Rohde&Schwarz, "Time Domain Oscillator Stability Measurement Allan Variance", Application Note, Feb.2009.
- [5] W.J.Riley, "The Averaging of Phase and Frequency Data", Hamilton Technical Services, Nov.2010.
- [6] D.A.Howe, D.W.Allan, J.A.Barnes, "Properties of Oscillator Signals and Measurement Method", NIST
- [7] Hewlett Packard, "Fundamentals of Time Interval Measurements", Application Note 200-3, June1997.
- [8] Hewlett Packard, "Fundamentals of the Electronic Counters", Application Note 200, Mar.1997.
- [9] Fluke, "Sources of Error in Time Interval Measurements", Application Note
- [10] Pendulum Instruments, "Accurate Phase Calibration", Application Note CNT-81, AN-07

Corrigendum

After the publication of the previous “Electronics” issue (Vol. 15, No. 2, December 2011) authors Abdel Hakeim M. Husein and Fady I. EL-Nahal of the paper “Schematic Representation for Illustrating the Procedure of Optical Noise Figure in Erbium-doped Fiber Amplifier (EDFA) and Praseodymium-doped Fiber Amplifier (PDFA)” (pp. 98–102) have noticed that they made a mistake in equation (4) on page 99. The equation should be:

$$N_2 = N \frac{R_p + R_s}{R_p(1 + 2\beta) + R_s(2 + \beta) + \gamma_{21}} \quad (4)$$

“Electronics” journal

Instructions for Authors

First A. Author, Second B. Author, and Third C. Author

Abstract—These instructions give you guidelines for preparing papers for ELECTRONICS journal. Use this document as a template if you are using Microsoft *Word* 6.0 or later. Otherwise, use this document as an instruction set. The electronic file of your paper will be formatted further. Define all symbols used in the abstract. Do not cite references in the abstract. Do not delete the blank line immediately above the abstract; it sets the footnote at the bottom of this column.

Index Terms—About four key words or phrases in alphabetical order, separated by commas.

I. INTRODUCTION

THIS document is a template for Microsoft *Word* versions 6.0 or later.

When you open the file, select “Page Layout” from the “View” menu in the menu bar (View | Page Layout), which allows you to see the footnotes. Then, type over sections of file or cut and paste from another document and use markup styles. The pull-down style menu is at the left of the Formatting Toolbar at the top of your *Word* window (for example, the style at this point in the document is “Text”). Highlight a section that you want to designate with a certain style, then select the appropriate name on the style menu. The style will adjust your fonts and line spacing. **Do not change the font sizes or line spacing to squeeze more text into a limited number of pages.** Use italics for emphasis; do not underline. The length of the manuscript is limited to the maximum of 15 pages.

To insert images in *Word*, position the cursor at the insertion point and either use Insert | Picture | From File or

copy the image to the Windows clipboard and then Edit | Paste Special | Picture (with “float over text” unchecked).

We will do the final formatting of your paper.

II. PROCEDURE FOR PAPER SUBMISSION

A. Review Stage

The manuscripts are to be delivered to the editor by e-mail: electronics@etfbl.net. Prepare it in two-column format as shown in this template. Place all figures and tables at the end of the paper (after the references) on separate page(s). Figures and tables must have the same caption names as referenced in the text. Only PDF format of the manuscript is allowed at the review stage. Please, check if all fonts are embedded and subset and that the quality of diagrams, illustrations, and graphics is satisfactory. Failing to provide above listed requirements is a valid reason for rejection.

B. Final Stage

When you submit your final version (after your paper has been accepted), prepare it in two-column format, including figures and tables in accordance with this template. Pack all of your files (manuscript source file in *Word*, figures, and manuscript PDF form) within one archive file (you may use any of the available file compression tools: *WinZip*, *WinRAR*, *7-Zip*, etc.). Do not forget to provide the manuscript converted in PDF format that will be used as a reference for final formatting of your paper. Figures should be named as referenced in the manuscript (e.g. *fig1.eps*, *fig2.tif*, etc.)

C. Figures and Tables

Format and save your graphic images using a suitable graphics processing program and adjusts the resolution settings. We accept images in the following formats: PS, EPS, TIFF, GIF, and PNG. Additionally, it is allowed to use images generated by using one of the following software tools: Microsoft Word, Microsoft PowerPoint, or Microsoft Excel. The resolution of a RGB color file should be 400 dpi. Please note that JPG and other lossy-compressed image formats are not allowed. Use available software tools to convert these images to appropriate format.

Image quality is very important to how yours graphics will reproduce. Even though we can accept graphics in many formats, we cannot improve your graphics if they are poor quality when we receive them. If your graphic looks low in quality on your printer or monitor, please keep in mind that cannot improve the quality after submission.

Manuscript received 15 September 2011 (write the date when you have first sent the manuscript for review). Received in revised form 20 October 2011 (write the date when you have sent the manuscript in its revised form if revisions required for your paper after review).

(Place here any sponsor and financial support acknowledgments).

F. A. Author is with the Faculty of Electrical Engineering, University of Banja Luka, Banja Luka, Bosnia and Herzegovina (corresponding author to provide phone: +387-51-222-333; fax: +387-51-111-222; e-mail: author@etfbl.net).

S. B. Author was with Faculty of Technical Sciences, University of Novi Sad, Novi Sad, Serbia. He is now with the Institute “Mihailo Pupin”, Belgrade, Serbia (e-mail: author@pupin.rs).

T. C. Author is with the School of Electrical Engineering, University of Belgrade, Belgrade, Serbia, on leave from the Faculty of Electronic Engineering, University of Niš, Niš, Serbia (e-mail: author@elfak.ni.ac.rs).

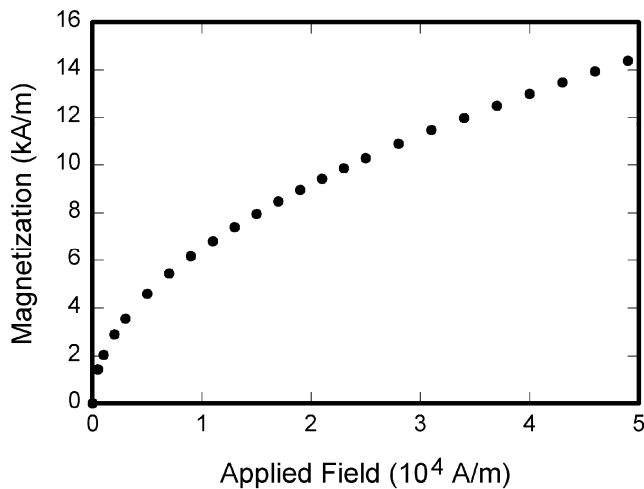


Fig. 1. Magnetization as a function of applied field. Note that “Fig.” is abbreviated. There is a period after the figure number, followed by two spaces. It is good practice to explain the significance of the figure in the caption.

If you are importing your graphics into this Word template, please use the following steps:

Under the option EDIT select PASTE SPECIAL. A dialog box will open, select paste picture, then click OK. Your figure should now be in the Word Document.

If you are preparing images in TIFF, EPS, or PS format, note the following. High-contrast line figures and tables should be prepared with 600 dpi resolution and saved with no compression, 1 bit per pixel (monochrome).

Photographs and grayscale figures should be prepared with 300 dpi resolution and saved with no compression, 8 bits per pixel (grayscale).

Most charts graphs and tables are one column wide (3 1/2 inches or 21 picas) or two-column width (7 1/16 inches, 43 picas wide). We recommend that you avoid sizing figures less than one column wide, as extreme enlargements may distort your images and result in poor reproduction. Therefore, it is better if the image is slightly larger, as a minor reduction in size should not have an adverse affect the quality of the image.

III. MATH

If you are using *Word*, use either the Microsoft Equation Editor or the *MathType* add-on (<http://www.mathtype.com>) for equations in your paper (Insert | Object | Create New | Microsoft Equation *or* MathType Equation). “Float over text” should *not* be selected.

IV. UNITS

Use either SI (MKS) or CGS as primary units. (SI units are strongly encouraged.) English units may be used as secondary units (in parentheses). **This applies to papers in data storage.** For example, write “15 Gb/cm² (100 Gb/in²).” An exception is when English units are used as identifiers in trade, such as “3½-in disk drive.” Avoid combining SI and CGS units, such as current in amperes and magnetic field in

TABLE I
UNITS FOR MAGNETIC PROPERTIES

Symbol	Quantity	Conversion from Gaussian and CGS EMU to SI ^a
Φ	magnetic flux	1 Mx \rightarrow 10^{-8} Wb = 10^{-8} V·s
B	magnetic flux density, magnetic induction	1 G \rightarrow 10^{-4} T = 10^{-4} Wb/m ²
H	magnetic field strength	1 Oe \rightarrow $10^3/(4\pi)$ A/m
m	magnetic moment	1 erg/G = 1 emu \rightarrow 10^{-3} A·m ² = 10^{-3} J/T
M	magnetization	1 erg/(G·cm ³) = 1 emu/cm ³ \rightarrow 10^3 A/m
$4\pi M$	magnetization	1 G \rightarrow $10^3/(4\pi)$ A/m
σ	specific magnetization	1 erg/(G·g) = 1 emu/g \rightarrow 1 A·m ² /kg
j	magnetic dipole moment	1 erg/G = 1 emu \rightarrow $4\pi \times 10^{-10}$ Wb·m
J	magnetic polarization	1 erg/(G·cm ³) = 1 emu/cm ³ \rightarrow $4\pi \times 10^{-4}$ T
χ, κ	susceptibility	1 \rightarrow 4π
χ_ρ	mass susceptibility	1 cm ³ /g \rightarrow $4\pi \times 10^{-3}$ m ³ /kg
μ	permeability	1 \rightarrow $4\pi \times 10^{-7}$ H/m = $4\pi \times 10^{-7}$ Wb/(A·m)
μ_r	relative permeability	$\mu \rightarrow \mu_r$
w, W	energy density	1 erg/cm ³ \rightarrow 10^{-1} J/m ³
N, D	demagnetizing factor	1 \rightarrow $1/(4\pi)$

Vertical lines are optional in tables. Statements that serve as captions for the entire table do not need footnote letters.

^aGaussian units are the same as cgs emu for magnetostatics; Mx = maxwell, G = gauss, Oe = oersted; Wb = weber, V = volt, s = second, T = tesla, m = meter, A = ampere, J = joule, kg = kilogram, H = henry.

oersteds. This often leads to confusion because equations do not balance dimensionally. If you must use mixed units, clearly state the units for each quantity in an equation.

The SI unit for magnetic field strength H is A/m. However, if you wish to use units of T, either refer to magnetic flux density B or magnetic field strength symbolized as $\mu_0 H$. Use the center dot to separate compound units, e.g., “A·m².”

V. HELPFUL HINTS

A. Figures and Tables

Because we will do the final formatting of your paper, you do not need to position figures and tables at the top and bottom of each column. In fact, all figures, figure captions, and tables can be at the end of the paper. Large figures and tables may span both columns. Place figure captions below the figures; place table titles above the tables. If your figure has two parts, include the labels “(a)” and “(b)” as part of the artwork. Please verify that the figures and tables you mention in the text actually exist. **Please do not include captions as part of the figures. Do not put captions in “text boxes” linked to the figures. Do not put borders around the outside of your figures.** Use the abbreviation “Fig.” even at the beginning of a sentence. Do not abbreviate “Table.” Tables are numbered with Roman numerals.

Color printing of figures is not available Do not use color unless it is necessary for the proper interpretation of your figures.

Figure axis labels are often a source of confusion. Use words rather than symbols. As an example, write the quantity

“Magnetization,” or “Magnetization M ,” not just “ M .” Put units in parentheses. Do not label axes only with units. As in Fig. 1, for example, write “Magnetization (A/m)” or “Magnetization ($A \cdot m^{-1}$),” not just “A/m.” Do not label axes with a ratio of quantities and units. For example, write “Temperature (K),” not “Temperature/K.”

Multipliers can be especially confusing. Write “Magnetization (kA/m)” or “Magnetization (10^3 A/m).” Do not write “Magnetization (A/m) \times 1000” because the reader would not know whether the top axis label in Fig. 1 meant 16000 A/m or 0.016 A/m. Figure labels should be legible, approximately 8 to 12 point type.

B. References

Number citations consecutively in square brackets [1]. The sentence punctuation follows the brackets [2]. Multiple references [2], [3] are each numbered with separate brackets [1]–[3]. When citing a section in a book, please give the relevant page numbers [2]. In sentences, refer simply to the reference number, as in [3]. Do not use “Ref. [3]” or “reference [3]” except at the beginning of a sentence: “Reference [3] shows” Please do not use automatic endnotes in *Word*, rather, type the reference list at the end of the paper using the “References” style.

Number footnotes separately in superscripts (Insert | Footnote).¹ Place the actual footnote at the bottom of the column in which it is cited; do not put footnotes in the reference list (endnotes). Use letters for table footnotes (see Table I).

Please note that the references at the end of this document are in the preferred referencing style. Give all authors’ names; do not use “*et al.*” unless there are six authors or more. Use a space after authors’ initials. Papers that have not been published should be cited as “unpublished” [4]. Papers that have been accepted for publication, but not yet specified for an issue should be cited as “to be published” [5]. Papers that have been submitted for publication should be cited as “submitted for publication” [6]. Please give affiliations and addresses for private communications [7].

Capitalize only the first word in a paper title, except for proper nouns and element symbols. For papers published in translation journals, please give the English citation first, followed by the original foreign-language citation [8]. All references **must be** written in Roman alphabet.

C. Abbreviations and Acronyms

Define abbreviations and acronyms the first time they are used in the text, even after they have already been defined in the abstract. Abbreviations such as IEEE, SI, ac, and dc do not have to be defined. Abbreviations that incorporate periods should not have spaces: write “C.N.R.S.,” not “C. N. R. S.” Do not use abbreviations in the title unless they are unavoidable (for example, “IEEE” in the title of this article).

¹It is recommended that footnotes be avoided (except for the unnumbered footnote with the receipt date and authors’ affiliations on the first page). Instead, try to integrate the footnote information into the text.

D. Equations

Number equations consecutively with equation numbers in parentheses flush with the right margin, as in (1). First use the equation editor to create the equation. Then select the “Equation” markup style. Press the tab key and write the equation number in parentheses. To make your equations more compact, you may use the solidus (/), the exp function, or appropriate exponents. Use parentheses to avoid ambiguities in denominators. Punctuate equations when they are part of a sentence, as in

$$\int_0^{r_2} F(r, \varphi) dr d\varphi = [\sigma r_2 / (2\mu_0)] \cdot \int_0^\infty \exp(-\lambda |z_j - z_i|) \lambda^{-1} J_1(\lambda r_2) J_0(\lambda r_i) d\lambda. \quad (1)$$

Be sure that the symbols in your equation have been defined before the equation appears or immediately following. Italicize symbols (T might refer to temperature, but T is the unit tesla). Refer to “(1),” not “Eq. (1)” or “equation (1),” except at the beginning of a sentence: “Equation (1) is”

E. Other Recommendations

Use one space after periods and colons. Hyphenate complex modifiers: “zero-field-cooled magnetization.” Avoid dangling participles, such as, “Using (1), the potential was calculated.” [It is not clear who or what used (1).] Write instead, “The potential was calculated by using (1),” or “Using (1), we calculated the potential.”

Use a zero before decimal points: “0.25,” not “.25.” Use “ cm^3 ,” not “cc.” Indicate sample dimensions as “0.1 cm \times 0.2 cm,” not “0.1 \times 0.2 cm^2 .” The abbreviation for “seconds” is “s,” not “sec.” Do not mix complete spellings and abbreviations of units: use “Wb/m²” or “webers per square meter,” not “webers/m².” When expressing a range of values, write “7 to 9” or “7-9,” not “7~9.”

A parenthetical statement at the end of a sentence is punctuated outside of the closing parenthesis (like this). (A parenthetical sentence is punctuated within the parentheses.) In American English, periods and commas are within quotation marks, like “this period.” Other punctuation is “outside”! Avoid contractions; for example, write “do not” instead of “don’t.” The serial comma is preferred: “A, B, and C” instead of “A, B and C.”

If you wish, you may write in the first person singular or plural and use the active voice (“I observed that ...” or “We observed that ...” instead of “It was observed that ...”). Remember to check spelling. If your native language is not English, please get a native English-speaking colleague to carefully proofread your paper.

VI. SOME COMMON MISTAKES

The word “data” is plural, not singular. The subscript for the permeability of vacuum μ_0 is zero, not a lowercase letter “o.” The term for residual magnetization is “remanence”; the adjective is “remanent”; do not write “remnance” or “remnant.” Use the word “micrometer” instead of “micron.” A

graph within a graph is an “inset,” not an “insert.” The word “alternatively” is preferred to the word “alternately” (unless you really mean something that alternates). Use the word “whereas” instead of “while” (unless you are referring to simultaneous events). Do not use the word “essentially” to mean “approximately” or “effectively.” Do not use the word “issue” as a euphemism for “problem.” When compositions are not specified, separate chemical symbols by en-dashes; for example, “NiMn” indicates the intermetallic compound $\text{Ni}_{0.5}\text{Mn}_{0.5}$ whereas “Ni–Mn” indicates an alloy of some composition $\text{Ni}_x\text{Mn}_{1-x}$.

Be aware of the different meanings of the homophones “affect” (usually a verb) and “effect” (usually a noun), “complement” and “compliment,” “discreet” and “discrete,” “principal” (e.g., “principal investigator”) and “principle” (e.g., “principle of measurement”). Do not confuse “imply” and “infer.”

Prefixes such as “non,” “sub,” “micro,” “multi,” and “ultra” are not independent words; they should be joined to the words they modify, usually without a hyphen. There is no period after the “et” in the Latin abbreviation “*et al.*” (it is also italicized). The abbreviation “i.e.,” means “that is,” and the abbreviation “e.g.,” means “for example” (these abbreviations are not italicized).

An excellent style manual and source of information for science writers is [9].

VII. EDITORIAL POLICY

Each manuscript submitted is subjected to the following review procedure:

- It is reviewed by the editor for general suitability for this publication
- If it is judged suitable, two reviewers are selected and a single-blinded review process takes place
- Based on the recommendations of the reviewers, the editor then decides whether the particular paper should be accepted as is, revised or rejected.

Do not submit a paper you have submitted or published elsewhere. Do not publish “preliminary” data or results. The submitting author is responsible for obtaining agreement of all coauthors and any consent required from sponsors before submitting a paper. It is the obligation of the authors to cite relevant prior work.

Every paper submitted to “Electronics” journal are single-blind reviewed. For conference-related papers, the decision to accept or reject a paper is made by the conference editors and publications committee; the recommendations of the referees are advisory only. Undecipherable English is a valid reason for rejection.

VIII. PUBLICATION PRINCIPLES

The contents of “Electronics” are peer-reviewed and archival. The “Electronics” publishes scholarly articles of archival value as well as tutorial expositions and critical reviews of classical subjects and topics of current interest.

Authors should consider the following points:

- 1) Technical papers submitted for publication must advance the state of knowledge and must cite relevant prior work.
- 2) The length of a submitted paper should be commensurate with the importance, or appropriate to the complexity, of the work. For example, an obvious extension of previously published work might not be appropriate for publication or might be adequately treated in just a few pages.
- 3) Authors must convince both peer reviewers and the editors of the scientific and technical merit of a paper; the standards of proof are higher when extraordinary or unexpected results are reported.
- 4) Because replication is required for scientific progress, papers submitted for publication must provide sufficient information to allow readers to perform similar experiments or calculations and use the reported results. Although not everything need be disclosed, a paper must contain new, useable, and fully described information. For example, a specimen’s chemical composition need not be reported if the main purpose of a paper is to introduce a new measurement technique. Authors should expect to be challenged by reviewers if the results are not supported by adequate data and critical details.
- 5) Papers that describe ongoing work or announce the latest technical achievement, which are suitable for presentation at a professional conference, may not be appropriate for publication in “Electronics”.

IX. CONCLUSION

A conclusion section is not required. Although a conclusion may review the main points of the paper, do not replicate the abstract as the conclusion. A conclusion might elaborate on the importance of the work or suggest applications and extensions.

APPENDIX

Appendixes, if needed, appear before the acknowledgment.

ACKNOWLEDGMENT

The preferred spelling of the word “acknowledgment” in American English is without an “e” after the “g.” Use the singular heading even if you have many acknowledgments. Avoid expressions such as “One of us (S.B.A.) would like to thank” Instead, write “F. A. Author thanks” **Sponsor and financial support acknowledgments are placed in the unnumbered footnote on the first page, not here.**

REFERENCES

- [1] G. O. Young, “Synthetic structure of industrial plastics (Book style with paper title and editor),” in *Plastics*, 2nd ed. vol. 3, J. Peters, Ed. New York: McGraw-Hill, 1964, pp. 15–64.
- [2] W.-K. Chen, *Linear Networks and Systems* (Book style). Belmont, CA: Wadsworth, 1993, pp. 123–135.
- [3] H. Poor, *An Introduction to Signal Detection and Estimation*. New York: Springer-Verlag, 1985, ch. 4.

- [4] B. Smith, "An approach to graphs of linear forms (Unpublished work style)," unpublished.
- [5] E. H. Miller, "A note on reflector arrays (Periodical style—Accepted for publication)," *IEEE Trans. Antennas Propagat.*, to be published.
- [6] J. Wang, "Fundamentals of erbium-doped fiber amplifiers arrays (Periodical style—Submitted for publication)," *IEEE J. Quantum Electron.*, submitted for publication.
- [7] C. J. Kaufman, Rocky Mountain Research Lab., Boulder, CO, private communication, May 1995.
- [8] Y. Yorozu, M. Hirano, K. Oka, and Y. Tagawa, "Electron spectroscopy studies on magneto-optical media and plastic substrate interfaces (Translation Journals style)," *IEEE Transl. J. Magn.Jpn.*, vol. 2, Aug. 1987, pp. 740–741 [Dig. 9th Annu. Conf. Magnetics Japan, 1982, p. 301].
- [9] M. Young, *The Technical Writers Handbook*. Mill Valley, CA: University Science, 1989.
- [10] J. U. Duncombe, "Infrared navigation—Part I: An assessment of feasibility (Periodical style)," *IEEE Trans. Electron Devices*, vol. ED-11, pp. 34–39, Jan. 1959.
- [11] S. Chen, B. Mulgrew, and P. M. Grant, "A clustering technique for digital communications channel equalization using radial basis function networks," *IEEE Trans. Neural Networks*, vol. 4, pp. 570–578, Jul. 1993.
- [12] R. W. Lucky, "Automatic equalization for digital communication," *Bell Syst. Tech. J.*, vol. 44, no. 4, pp. 547–588, Apr. 1965.
- [13] S. P. Bingulac, "On the compatibility of adaptive controllers (Published Conference Proceedings style)," in *Proc. 4th Annu. Allerton Conf. Circuits and Systems Theory*, New York, 1994, pp. 8–16.
- [14] G. R. Faulhaber, "Design of service systems with priority reservation," in *Conf. Rec. 1995 IEEE Int. Conf. Communications*, pp. 3–8.
- [15] W. D. Doyle, "Magnetization reversal in films with biaxial anisotropy," in *1987 Proc. INTERMAG Conf.*, pp. 2.2-1–2.2-6.
- [16] G. W. Juette and L. E. Zeffanella, "Radio noise currents in short sections on bundle conductors (Presented Conference Paper style)," presented at the IEEE Summer power Meeting, Dallas, TX, Jun. 22–27, 1990, Paper 90 SM 690-0 PWRS.
- [17] J. G. Kreifeldt, "An analysis of surface-detected EMG as an amplitude-modulated noise," presented at the 1989 Int. Conf. Medicine and Biological Engineering, Chicago, IL.
- [18] J. Williams, "Narrow-band analyzer (Thesis or Dissertation style)," Ph.D. dissertation, Dept. Elect. Eng., Harvard Univ., Cambridge, MA, 1993.
- [19] N. Kawasaki, "Parametric study of thermal and chemical nonequilibrium nozzle flow," M.S. thesis, Dept. Electron. Eng., Osaka Univ., Osaka, Japan, 1993.
- [20] J. P. Wilkinson, "Nonlinear resonant circuit devices (Patent style)," U.S. Patent 3 624 12, July 16, 1990.
- [21] *IEEE Criteria for Class IE Electric Systems* (Standards style), IEEE Standard 308, 1969.
- [22] *Letter Symbols for Quantities*, ANSI Standard Y10.5-1968.
- [23] R. E. Haskell and C. T. Case, "Transient signal propagation in lossless isotropic plasmas (Report style)," USAF Cambridge Res. Lab., Cambridge, MA Rep. ARCRL-66-234 (II), 1994, vol. 2.
- [24] E. E. Reber, R. L. Michell, and C. J. Carter, "Oxygen absorption in the Earth's atmosphere," Aerospace Corp., Los Angeles, CA, Tech. Rep. TR-0200 (420-46)-3, Nov. 1988.
- [25] (Handbook style) *Transmission Systems for Communications*, 3rd ed., Western Electric Co., Winston-Salem, NC, 1985, pp. 44–60.
- [26] *Motorola Semiconductor Data Manual*, Motorola Semiconductor Products Inc., Phoenix, AZ, 1989.
- [27] (Basic Book/Monograph Online Sources) J. K. Author. (year, month, day). Title (edition) [Type of medium]. Volume (issue). Available: [http://www.\(URL\)](http://www.(URL))
- [28] J. Jones. (1991, May 10). Networks (2nd ed.) [Online]. Available: <http://www.atm.com>
- [29] (Journal Online Sources style) K. Author. (year, month). Title. Journal [Type of medium]. Volume(issue), paging if given. Available: [http://www.\(URL\)](http://www.(URL))
- [30] R. J. Vidmar. (1992, August). On the use of atmospheric plasmas as electromagnetic reflectors. *IEEE Trans. Plasma Sci.* [Online]. 21(3), pp. 876–880. Available: <http://www.halcyon.com/pub/journals/21ps03-vidmar>

Instruction for Authors

Editorial objectives

In the journal "Electronics", the scientific papers from different fields of electronics and electrical engineering in the broadest sense are published. Main topics are electronics, automatics, telecommunications, computer techniques, power engineering, nuclear and medical electronics, analysis and synthesis of electronic circuits and systems, new technologies and materials in electronics etc. The main emphasis of papers should be on methods and new techniques, or the application of existing techniques in a novel way.

The reviewing process

Each manuscript submitted is subjected to the following review procedures:

- It is reviewed by the editor for general suitability for this publication;
- If it is judged suitable, two reviewers are selected and a double-blind review process takes place;
- Based on the recommendations of the reviewers, the editor then decides whether the particular paper should be accepted as it is, revised or rejected.

Submissions Process

The manuscripts are to be delivered to the editor by e-mail: electronics@etfbl.net.

Manuscripts have to be prepared in accordance with the instructions given in the template for paper preparation that can be found on the journal's web page (www.electronics.etfbl.net).

Authors should note that proofs are not supplied prior to publication and ensure that the paper submitted is complete and in its final form.

Copyright

Articles submitted to the journal should be original contributions and should not be under consideration for any other publication at the same time. Authors submitting articles for publication warrant that the work is not an infringement of any existing copyright and will indemnify the publisher against any breach of such warranty. For ease of dissemination and to ensure proper policing of use, papers and contributions become the legal copyright of the publisher unless otherwise agreed.

ELECTRONICS, VOL. 16, NO. 1, JUNE 2012

SPECIAL SECTION ON 16th INTERNATIONAL SYMPOSIUM ON POWER ELECTRONICS – EE2011

GUEST EDITORIAL	1
PROF. DR VLADIMIR KATIĆ BIOGRAPHY	2
<hr/>	
BIDIRECTIONAL AC DC CONVERTER FOR REGENERATIVE BRAKING	3
Predrag Pejovic, Johann W. Kolar, and Yasuyuki Nishida	
ANALYSIS OF SINGLE COIL PM-BLDC MOTOR	9
Boguslaw Grzesik and Mariusz Stepień	
IPMSM MODEL INCLUDING MAGNETIC SATURATION AND CROSS-COUPLING	12
Darko P. Marčetić, Roberto M. Varga, and Mile B. Božić	
COMPARISON OF METHODS FOR ON-LINE HARMONIC ESTIMATION	16
Jovan M. Knežević and Vladimir A. Katić	
PWM ALGORITHMS FOR MULTILEVEL INVERTER SUPPLIED MULTIPHASE VARIABLE – SPEED DRIVES	22
Martin Jones, Obrad Dordevic, Nandor Bodo, and Emil Levi	
SOME EXAMPLES THAT USE THE FEM IN PM GENERATORS ANALYSIS	32
Marian Greconici	
INFLUENCE OF A THIN COPPER SHIELD ON A BLDC MOTOR PARAMETERS	37
Nándor Burány, Dejana Herceg, and Neda Pekarić-Nad	
HIGH FREQUENCY MODEL OF EMI FILTER	42
Szymon Pasko and Boguslaw Grzesik	
ENERGY EFFICIENCY IN ELECTRIC DRIVES	46
Slobodan Mirchevski	
POWER ELECTRONIC TRANSFORMER TECHNOLOGY FOR TRACTION APPLICATIONS – AN OVERVIEW	50
Dražen Dujčić, Frederick Kieferndorf, and Francisco Canales	
MODELING AND DESIGN OF PASSIVE COMPONENTS FOR FLEXIBLE ELECTRONICS	57
Nikola Jeranče, Nataša Samardžić, Dragana Vasiljević, and Goran Stojanović	
<hr/>	
SPECIAL SECTION ON 4 th SMALL SYSTEMS SIMULATION SYMPOSIUM (SSSS) 2012	
GUEST EDITORIAL	63
PROF. DR VANČO LITOVSKI BIOGRAPHY	64
<hr/>	
ENERGY EFFICIENT SENSOR NODES POWERED BY KINETIC ENERGY HARVESTERS – DESIGN FOR OPTIMUM PERFORMANCE	65
Tom J. Kaźmierski, Leran Wang, and Mansour Aloufi	
PATTERN-BASED APPROACH TO CURRENT DENSITY VERIFICATION	77
Vazgen Melikyan, Eduard Babayan, and Ashot Harutyunyan	
NETWORK SIMULATOR TOOLS AND GPU PARALLEL SYSTEMS	81
Leonid Djinevski, Sonja Filiposka, and Dimitar Trajanov	
THE DECOMPOSITION OF DSP'S CONTROL LOGIC BLOCK FOR POWER REDUCTION	85
Borisav Jovanović and Milunka Damjanović	
DATA PRIVACY IN SMART ELECTRICITY NETWORKS	92
Slobodan Bojanić, Srdan Đorđević, and Octavio Nieto-Taladriz	
ADVANCED DC MOTOR DRIVE FOR HAPTIC DEVICES	100
Miroslav Božić, Darko Todorović, Miloš Petković, Volker Zerbe, and Goran S. Đorđević	
<hr/>	
PAPERS	
HOW TO MEASURE OSCILLATOR'S SHORT-TERM STABILITY USING FREQUENCY COUNTER	104
Ivica Milanović, Snežana Renovica, Ivan Župunski, Mladen Banović, and Predrag Rakonjac	
<hr/>	
CORRIGENDUM	113
INSTRUCTIONS FOR AUTHORS	115

ISSN 1450 -5843

UDK 621.38